Studies on hydrothermally processed Zinc oxide nanostructures for optical, wettability and sensing applications

Submitted to the

University of Hyderabad

Towards partial fulfilment for the degree of

Doctor of Philosophy in Physics

By

Yalambaku Rajesh

Regd. No: 15PHPH10



Under the supervision of

Prof. M. Ghanashyam Krishna

School of Physics,

University of Hyderabad

Hyderabad-500 046.

Telangana, India.

(December-2021)

Declaration

I, YALAMBAKU RAJESH hereby declare that this Ph.D. thesis entitled "Studies on Hydrothermally processed Zinc Oxide nanostructures for Optical, wettability and sensing applications" Submitted by me under the guidance and supervision of Professor. M. Ghanashyam Krishna is a bonafide research work. I also declare that it has not been submitted previously in part or in full to this University or any other University or Institution for the award of any degree or diploma.

Date: 23-12-2021

Name: YALAMBAKU RAJESH

Signature of the Student: J. Rojedy

Regd. No. 15PHPH10



Certificate

This is to certify that the thesis entitled "Studies on Hydrothermally processed Zinc Oxide nanostructures for Optical, wettability and sensing applications" submitted by YALAMBAKU RAJESH bearing Reg. No. 15PHPH10 in fulfilment of the requirements for the award of Doctor of Philosophy in Physics is a bonafide work carried out by him under my supervision and guidance.

This thesis is free from plagiarism and has not been submitted previously in part or in full to this or any other university or institution for the award of any degree or diploma.

Further, the student has the following publications before the submission of the thesis for adjudication.

- Y. Rajesh, S.K. Padhi, and M.G. Krishna, "ZnO thin film-nanowire array homo-structures with tunable photoluminescence and optical band gap" RSC Adv. 10(43), pp.25721-25729 (2020). [Chapter-4 (Part-A)]
- Y. Rajesh, D.D. Purkayastha, and M.G. Krishna, "Seed layer mediated wettability and wettability transition of ZnO nano/micro-rod arrays" J. Alloys Compd. 857, p.157617 (2021). [Chapter-5]
- 3. Y. Rajesh, M.S.S. Bharati, S.V. Rao, and M.G. Krishna, "ZnO nanowire arrays decorated with titanium nitride nanoparticles as surface-enhanced Raman scattering substrates" Appl. Phys. A, 127(4), pp.1-8 (2021). [Chapter-6]

 Y. Rajesh, Md. Ahamad Mohiddon., and M.G. Krishna "Shape evolution and optical response of ZnO nanostructures grown on thermally evaporated ZnO and Au thin films" Materials Chemistry and Physics, 125448 (2021). [Chapter-4 (Part-B)]

Further, the student has passed the following courses towards the fulfilment of course-work required of Ph.D.

S. No.	Course Code	Name	Credits	Pass/Fail
1.	PY801	Advanced Quantum Mechanics	4	Pass
2.	PY803	Advanced Statistical mechanics	4	Pass
3.	PY804	Advanced Electromagnetic Theory	4	Pass
4.	PY821	Research methodology	4	Pass

M. Thanashyam . Prof. M. Ghanashyam Krishna

Thesis Supervisor,

School Of Physics,

University of Hyderabad.

Prof. M. GHANASHYAM KRISHNA
Centre for Advanced Studies in
Electronics Science & Technology
School of Physics, University of Hyderabad
HYDERABAD-500 046. Telangana, India.

Place: Hyderabad

Date: 23.12.2021

Prof. K.C. James Raju

Dean

School Of Physics,

University of Hyderabad.

School of Physics
University of Hyderabad
Hyderabad-500 046, INDIA

Acknowledgement

Undertaking this Ph.D. has been a truly life-changing experience for me and it would not have been possible to do without the support and guidance that I received from many people. It's my pleasure to express my sincere gratitude to one and all who have helped me for the successful completion of this thesis. Many people helped me directly and indirectly to complete this thesis and I thank all of them.

First and foremost, I would like to express my heartfelt gratitude to my supervisor, **Prof. M. Ghanashyam Krishna Sir**, for his invaluable guidance, love, and incredible support throughout my Ph.D. From day one onwards, I received his valuable suggestions, and encouragement in research inspired me to work hard to complete this work. Without his motivation and help, this research task and thesis will be difficult. I am immensely thankful to him for giving me a platform for my carrier in the research field. And also, I am very happy & thankful to him for allowing him to become a member of his research lab. Finally, I want to say that I am grateful to be your student.

I sincerely thank my doctoral committee members Prof. G. Rajaram, Prof. Ashok Chatterjee and Prof. S. Srinath for their valuable suggestions, discussions, encouragement, and support throughout my Ph.D.

I thank former Deans, Prof. R. Singh, Prof. Bindu A. Bamba, Prof. V. Seshu Bai, Prof. Ashok Chatterjee and present Dean Prof. K. C. James Raju, for providing the necessary facilities in the school.

I would also like to thank SoP & CASEST faculty members and staff for their valuable suggestions.

I thank Prof. M. Ghanashyam Krishna and Prof. S.V.S. Nageswara Rao of (Prof. In-charges of Centre for Nanotechnology) allowed me to use cleanroom, experimental lab and instrumental facilities.

I would like to thank Prof. E. Hari Kumar, Prof. M. Sivakumar, Prof. S. Chaturvedi, Prof. Bindu Bambah, Prof. Surajit Dhara and Dr. Swati Ghosh Acharyya for their teaching, support and encouragement in my course work.

I would like to express my sincere thanks to Prof. Soma Venugopal Rao for his encouragement and providing lab facilities.

I am grateful for the funding for my Ph.D. from NFST fellowship under UGC and Non-Net fellowship from UoH.

I express my sincere thanks to Dr.Debarun (NIT Nagaland) for contact angle measurements and Dr. V.Madhurima (CUTN) for allowing me to work in her lab, and Dr. Venkata Saravanan (CUTN) help and suitable suggestions.

I am indebted to Dr. Varma and Dr. Ahamad Mohiuddin for their Love, encouragement, valuable suggestions, and help in my research work. Dr. Varma, thank you so much Anna for your fellowship and presence to gain technical experience in instruments.

I thank Prof. M.V.Ramana Reddy for his good suggestions and encouragement.

I want to thank Dr. Santanu for his help and good suggestions in my work.

I express my sincere thanks to Dr. Senthil Nathan (SoC) for his great help and loveable friendship.

I am pleased to express appreciation to all my seniors for creating a productive research environment for Dr. Varma, Dr. Santanu, Dr. Ummer Pasha, Dr. Shankernath, Dr. Akshara Dr. Lakshun, Dr.Ch Ravi Kumar, Shivaramkrishna, Dr.Syed Hamad, Dr. Pundareekam, Dr. Sandeep, Dr.Pavan Kumar naik, Dr.Alkathy, Dr. Sivanaga Reddy, Dr. Arun nimmala.

I express my sincere thanks to Dr. Lokesh, Dr.Rambabu, Dr. Dr.Suresh P, Dr. Nagarjuna, Dr. Dhanasekhar, for their help and encouaragment in my research work.

I express my sincere thanks to my labmates M.Rahul and Ravinder.T for their help, support, and fruitful interactions. I had a Joyful journey with you people. Once again, thank you, guys.

I thank Sravani, Rowtu Srenu, Krishna Teja, Sai, Mangababu, B Venkatesulu Reddy, Ravi, Mr. Debanth, Saidulu for their help and support. I feel happy to have nice working lab mates.

My sincere gratitude to all my 2015 batch mates: Sujai, Rama Krishna, Naresh, Rashmi, Devesh, Sravanthi, Manasa, Leela, Praneetha, Avisek, Zahid, Nilanjan, Bappaditya, Abu Taher, Hemant, Vinod, Dr. Bharathi, Dr. Krishna Kanth, John, Yelliah, Dr. Moses, Prathap, Subratho, Mrs. Pani. Without all of them, all these years would not have been the same, including the time we spent at university. Once again, thank you all for an incredible journey with all.

I express thanks to technical staff from the school of physics and center for Nanotechnology, namely Mr. Abraham, Mr. Sudarsan Singh, Mr. Sekhar, Ms. Deepika, Mrs. Sasikala, Ms. Sunitha and Mr. Santhosh (FESEM), Mr. Naresh (GI-XRD), Ms. Jyothi & Mr. Uday(P-XRD), Dr. Balaji (Raman), Dr.Sai (PL) for their help and support. From CFN Mr. Prasanth, Mr. M Durga Prasad & Pankaj (TEM), Mrs. B. Sandya, Mr. Ravibabu, Mrs. Grace, and Mr. Sreekanth for the help and support.

I thank Clean Room maintenance staff Mr. T. Rajiv, Mr. Tyagaraju, and Mr. Balaram for support related to cleanroom in other technical works.

My sincere gratitude to all my HCU friends.

I thank all research scholars from ACRHEM, SOP, SOC and SEST.

The strength of a building lies in its basement, I am indebted to all my teachers from childhood to M.Sc. They were directly or indirectly the reason for my excellence in education.

I thank all my school, inter B.Sc.and M.Sc. friends who were directly or indirectly part of this success. Especially my B.sc. Friends G.Venky and K.Siva Mr. Reddy Sekhar Naidu, Mr. Muni. Mr. Kishore. I thank Guravaiah anna for your encouragement. I joined M.Sc Physics. And also, thank Mr. J. Rajesh, Mr. Subba Reddy, Mr. BVR, and Mr. Prasanth, who are the main reason to join in HCU.

Lastly, I dedicate this thesis to my family members and teachers for their encouragement and Support to undertake the decision to enter into studies.

I express my sincere gratitude towards my parents **Y. Ramamurthy Garu** and **Y. Anasuyamma Garu**, for their love, affection, valuable support, and encouragement helps lot me to full fill my thesis work. The way they have guided me was awesome, and also, they have given me ultimate freedom. And also, thank my loving brother P. Sai Balakrishna for his great help and support. I thank my sister. Santhi and Bava for your support.

I express my sincere thanks to all my relatives Mrs. Papulamma (Grandmother), Mr.E. Rajagopal and Mrs. E. Vijaya Lakshmi's family & E. Siddaiah's family. Especially Mrs. E. Vijaya Lakshmi Garu for great help, support, and encouragement towards my studies. Thank you so much attha.

And also, I would like to express my sincere thanks to I. Gurrappa & Mrs. I. Annapurna Garu, Mr. Chandu, and Ms. Purnima for encouragement in my research work.

I want to thank especially & sincere gratitude to my EU & EGF friends. I learned so many things from you. My Ph.D. journey went well & joyfully because of you people. I will never forget your love, help, support, and encouragement.

Finally, I thank God almighty for giving me immense strength to achieve this.

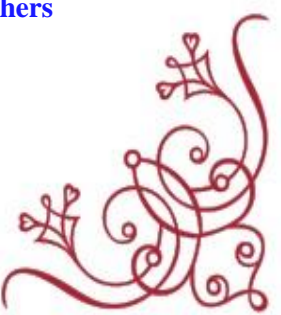






Y. Ramamurthy Garu and Y. Anasuyamma Garu & All My Teachers









Abbreviations

BSG Borosilicate glass

ZnO Zinc oxide

In₂O₃ Indium Oxide

SnO₂ Tin Oxide

Au Gold

In Indium

Sn Tin

InA Indium as deposited films

SnA Tin as deposited films

InO Indium oxidized

SnO Tin oxidized

TiN Titanium nitride

SERS Surface-enhanced Raman scattering

EF Enhancement factor

WCA Water Contact angle

PL Photoluminescence

UV Ultraviolet

Vis Visible

LSPR Localized Surface Plasmon Resonance

NMRAs Nano/micro-rod arrays

ZnAcD Zinc acetate dehydrate

ZnNH Zinc nitrate hexahydrate

HMTA Hexamethylenetetramine

XRD X-ray diffraction

FESEM Field emission scanning electron microscopy

EDX Energy Dispersive X-ray Spectroscopy

TEM Transmission electron microscope

CCD Charge Coupled Device

UV-NBE Ultraviolet-Near band edge

V_o Oxygen vacancies

AR Aspect ratio

HP Hydrothermal process

MAHP Microwave assisted hydrothermal process

MB Methylene blue

NB Nile blue

NPs Nanoparticles

ZNW Zinc oxide nanowires

T-ZNW TiN nanoparticles decorated ZnO nanowires

RSD Relative standard deviation

CONTENTS OF INDEX

	Page No.
Declaration	ii
Certificate	iii
Acknowledgements	v
Abbreviations	ix
Chapter 1: Introduction	01
Abstract	2
1 Background	03
1.1 Metal oxide based nanostructured materials	03
1.2 Synthesis of nanomaterial	04
1.3 Growth techniques	05
1.3.1 Liquid-Solid transformation based techniques	05
1.4 Hydrothermal synthesis of nanostructured materials	07
1.4.1 Introduction	07
1.4.2 Normal Hydrothermal method	08
1.4.2.1 The crystal growth mechanism and reaction kinetics in the hydrother method	rmal09
1.4.2.2 The role of water in hydrothermal synthesis	09
1.4.2.3 The role of Mineralizer hydrothermal synthesis	09
1.4.3 Microwave hydrothermal method	10
1.4.3.1 Reaction Mechanism of Microwave hydrothermal method	10
1.5 The role of seed-layer in hydrothermal method	11
1.6 Nanostructures based on Metal oxides	12
1.6.1 Overview of ZnO	12
1.6.1.1 Properties of ZnO	13
1.7 Applications of ZnO	15
1.7.1 Wettability studies and Self-cleaning applications	15
1.7.2 Influence of surface roughness on wettability	16
1.8 Surface-Enhanced Raman Scattering (SERS) application of ZnO	18
1.8.1 Surface-enhanced Raman scattering (SFRS) mechanisms of Enhancement	19

	1.9 Photoluminescence	20
	1.10 Motivation	21
	1.11 Objectives	24
	1.12 Thesis organization	25
C	Chapter 2: Materials: processing techniques, parameters and characterization	26
Α	Abstract	27
	2.1 Background	28
	2.2 Materials: Processing techniques and parameters	29
	2.2.1 Seed layer thin film deposition: process flow	29
	2.2.2 Hydrothermal synthesis: Process flow	30
	2.3 Materials: Characterization Techniques	31
	2.3.1 Thickness measurement of thin-films	32
	2.3.2 Structural studies	32
	2.3.3 Microstructural studies by Field Emission Scanning Electron Microscopy	
	(FESEM)	34
	2.3.4 Transmission electron microscope	35
	2.3.5 Ultraviolet-visible-Near Infrared (UV-Vis-NIR) spectrophotometry	36
	2.3.6 Raman spectroscopy	37
	2.3.7 Photoluminescence spectroscopy	38
	2.3.8 Surface enhanced Raman scattering (SERS) measurements	39
	2.3.8.1 SERS Enhancement factor calculations	39
	2.4 Wettability studies by Contact angle goniometry	41
	2.5 Summary	43
C	Chapter 3: Deposition and characterization of seed layers	44
Α	Abstract	45
	3.1 Background	46
	3.1.1 Microstructure and structure ZnO thin films	46
	3.1.2 Photoluminescence, Raman spectroscopy, and Optical properties of ZnO seed Layers	50
	3.2 Microstructure and structure of Indium (In) and Tin (Sn) seed layers	52
	3.2.1 Ontical properties of InO and SnO seed layers	59

3.3 Microstructure and structure of gold (Au) seed layer	60
3.3.1 Optical properties of gold (Au) seed layer	61
3.4 Conclusion	62
$ \begin{array}{llllllllllllllllllllllllllllllllllll$	nal and 63
Abstract	64
Part-4A (Conventional Hydrothermal synthesis)	65
4.1 Background	65
4.1.1 Effect of precursor concentration on microstructural evolution of ZnO Homo-structures	65
4.2 Effect of thickness of ZnO seed layers and duration of synthesis on the growth of Nanorods	68
4.3 Effect of hydrothermal synthesis temperature on the growth of nanorods and wires	71
4.4 Transmission electron microscopy of ZnO nanowires	73
4.5 Photoluminescence, Raman spectroscopy, and Optical properties of ZnO homo- Structures	75
4.6 Microstructure and structure of ZnO nanostructures on Gold (Au) seed layers	80
4.7 Raman spectroscopy of ZnO nanostructures on Au seed layer	83
4.8 Microstructure and structure of ZnO nanostructures on glass substrate (Seedless gro	owth).84
4.9 Raman spectroscopy and Optical properties of ZnO micro/nanostructures on BSG Substrate	86
4.10 Discussion on the mechanisms of the growth of ZnO nanostructures	88
4.11 Summary	92
Part-4B (Microwave Hydrothermal synthesis)	93
Abstract	93
4.12 Background	94
4.12.1 Microstructural shape evolution and crystal structure	94
4.12.2 Raman spectra, photoluminescence and optical transmission	97
4.13 Role of different parameters on shape evolution	100
4.14 Summary	103
Chapter 5: Effect of different metal and metal oxides seed layers on the grow wettability of ZnO nano/ microstructures	vth and 104

Abstract	105
5.1 Background	106
5.1.1 Growth patterns and crystallographic texture of ZnO structures	106
5.2 Raman spectroscopy	120
5.3 Photoluminescence	124
5.4 Optical transmission studies	132
5.5 Wettability studies	134
5.6 Conclusion	141
Chapter 6: Application of Titanium nitride nanoparticle decorated Z surface enhanced Raman scattering substrates	inO nanowires as142
Abstract	143
6.1 Background	144
6.1.1 Microstructure	144
6.1.2 Crystal structure	145
6.1.3 Raman spectroscopy	146
6.1.4 Optical properties	147
6.2 SERS studies	148
6.2.1 The SERS Enhancement factor calculations	155
6.3 Summary	157
Chapter 7: Summary, Conclusion, Scope for future work	158
7.1 Summary and Conclusions	159
7.2 Scope for future work	162
Publications	XV

Chapter

1

Introduction

Abstract

This chapter presents an overview of various applications, physical and chemical properties of metal-oxide nanostructures with particular focus on ZnO. The hydrothermal route for synthesis of nanostructures is discussed. Based on the literature, applications of ZnO nanostructures in self-cleaning, surface enhanced Raman scattering and photoluminescence are reviewed. Finally, motivation of the present work based on research gaps and objectives of the thesis are presented.

1. Background

In the past few years, the study of nanostructured materials has become highly popular in physics, chemistry, engineering and biology [1-3]. These materials are geometrical entities with a defined shape having nanoscale dimensions (1-100 nm). According to the dimensions, nanomaterials are classified into 4 types of materials: Zero (0-D), One (1-D), Two (2-D) and Three –dimensional (3-D) [4]. The most common examples of 0-D nanomaterials are quantum dots [5]. 1-D nanomaterials have only one parameter such as length or breadth in the range of 1-100 nm like nano tubes, nano rods, nano wires, nano belts, nano fibers. They are popular due to their unique physical properties and applications in nanoscale electronics, optoelectronics, nano composites and alternative energy sources. 1-D nanostructures such as p-n diodes, light emitting diodes (LED's), ultraviolet (UV) detectors, field-effect transistors (FETs), single nanowire solar cells, chemical sensors and integrated nanowires devices have been developed [6-8]. 2-D nanomaterials are generally single layer materials such as nano layers, nano coatings, semiconductor thin film devices and also optical films. 3-D nanomaterials are not confined to the nanoscale in any dimension such as bulk single crystal of silicon material [4, 8]. In this thesis the focus is on 1-D nanomaterials.

1.1 Metal oxide based nanostructured materials

Metal oxide nanomaterials show good performance compared to their corresponding bulk materials due to high surface to volume ratio and confinement effects resulting from the nanoscale dimensions [9]. In technological applications, these materials are used in the fabrication of microelectronic circuits, piezoelectric devices, film coatings as passive structures against surface corrosion, fuel cells and as catalysts. In nanotechnology, the main objective is to grow nano-arrays or nanostructures with exclusive properties compared to single particle species or bulk. Oxide based nanoparticles show unique physical, mechanical and chemical properties because of size dependence and high density of edge surface sites [10]. Oxide nanomaterials play an important role in various applications like gas sensors, photovoltaics, and photonic devices. Metal oxide nanostructures have guided a revival of interest in them for a wide range of applications in energy conversion and storage [11], harvesting such as Li-ion batteries [12], surface plasmon resonance in noble metal nanoparticles and enhanced band gap due to quantum confinement effect in semiconductor nanomaterials. Some of the most commonly used metal oxide nanomaterials are Zinc Oxide (ZnO), Tin Oxide (SnO₂), Indium Oxide (In₂O₃), Titanium dioxide (TiO₂), Copper

Oxide (CuO), nickel oxide (NiO), and Iron oxide (Fe₃O₄). These metal oxide-based nanostructures have been prepared by different methods which are discussed in the next section.

1.2 Synthesis of nanomaterials

Two main approaches for the synthesis of nanomaterials and fabrication of nanostructures are known: (i) Top-down and (ii) Bottom-up approach.

(i) Top-down approach

This approach involves the breaking-down the bulk size of material into microstructures, nanosized structures and particles. These methods remove thin layers and particles of bulk solid materials using techniques like ball milling and lithography as shown in figure 1.1. The main disadvantage in this approach is that it requires extensive post-process to achieve the desired dimensions, making it very expensive. However, the precise control over dimensions is very attractive for many applications.

(ii) Bottom-up approach

This approach involves the building of a material from the bottom level: atom-by atom, molecule-by-molecule, or cluster-by cluster. Bottom- up approach has the potential of being more economical and creating less waste than top-down approach. Hydrothermal synthesis, organometallic chemical route, reverse-micelle route, sol-gel synthesis, template assisted sol-gel, and electrodeposition colloidal precipitation are some of the popular bottom-up approach techniques. Schematic representation of bottom-up approaches for growth/synthesis of nanoscale materials shows in figure 1.1.

The synthesis of nanostructured materials with pre-defined shape, size, morphology, and composition is one of the most major challenges in the both approaches. Depending on the application a number of techniques have been explored such as thermal evaporation [14-16], hydrothermal synthesis [17-19], metal organic and chemical vapor deposition [20-21], template-based synthesis [22-23] can be used. Synthesis of these materials result in different kinds of nanostructures such as nanorods, nanowires, nanoparticles, nanobelts, nanoflowers, nano-rings, nanotubes, nanosheets, nano-combs, nano-spirals, and nano-springs, [24-25]. The present work focuses on 1-D nanowires due to the very large range of applications in optical and optoelectronics, solar cells, sensors and self-cleaning applications.

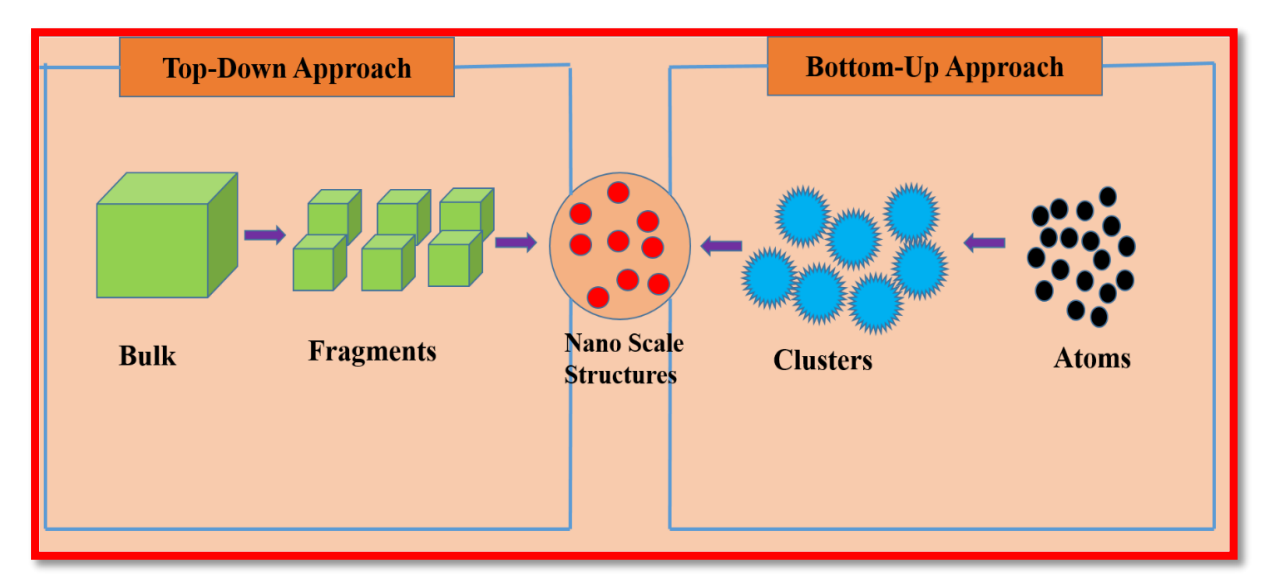


Figure 1.1: Schematic diagram of Top-Down and Bottom-up approaches [13].

1.3 Growth techniques

Methods of nanostructured material synthesis may be grouped into two broad categories based on:

1. The liquid-solid [26] and 2. Gas-solid [27] transformation based techniques. The liquid-solid transformation techniques include hydrothermal processes, electrodeposition, and sol-gel synthesis. Chemical vapor deposition (CVD) using catalyst metals, chemical vapor transport, reactive vapor transport, carbothermal reduction, laser ablation, thermal evaporation and thermal decomposition, chemical beam epitaxy (CBE) come under gas-solid based transformation techniques [28]. Liquid phase techniques generally make use of templates for producing 1-Dimensional materials. However, techniques without use of templates are also being developed. A detailed overview of these techniques is shown in figure 1.2.

1.3.1 Liquid-Solid transformation based techniques

There are a number of approaches for nanorods/nanowires synthesis using liquid-solid transformation techniques. These can be classified into two sub-categories: (i) template based and (ii) template free approaches.

(i) Template based methods

These kinds of methods require the use of a basic template to guide the growth of 1-D nanostructures. There are three types of templates: Surface step, positive template and negative template types [28].

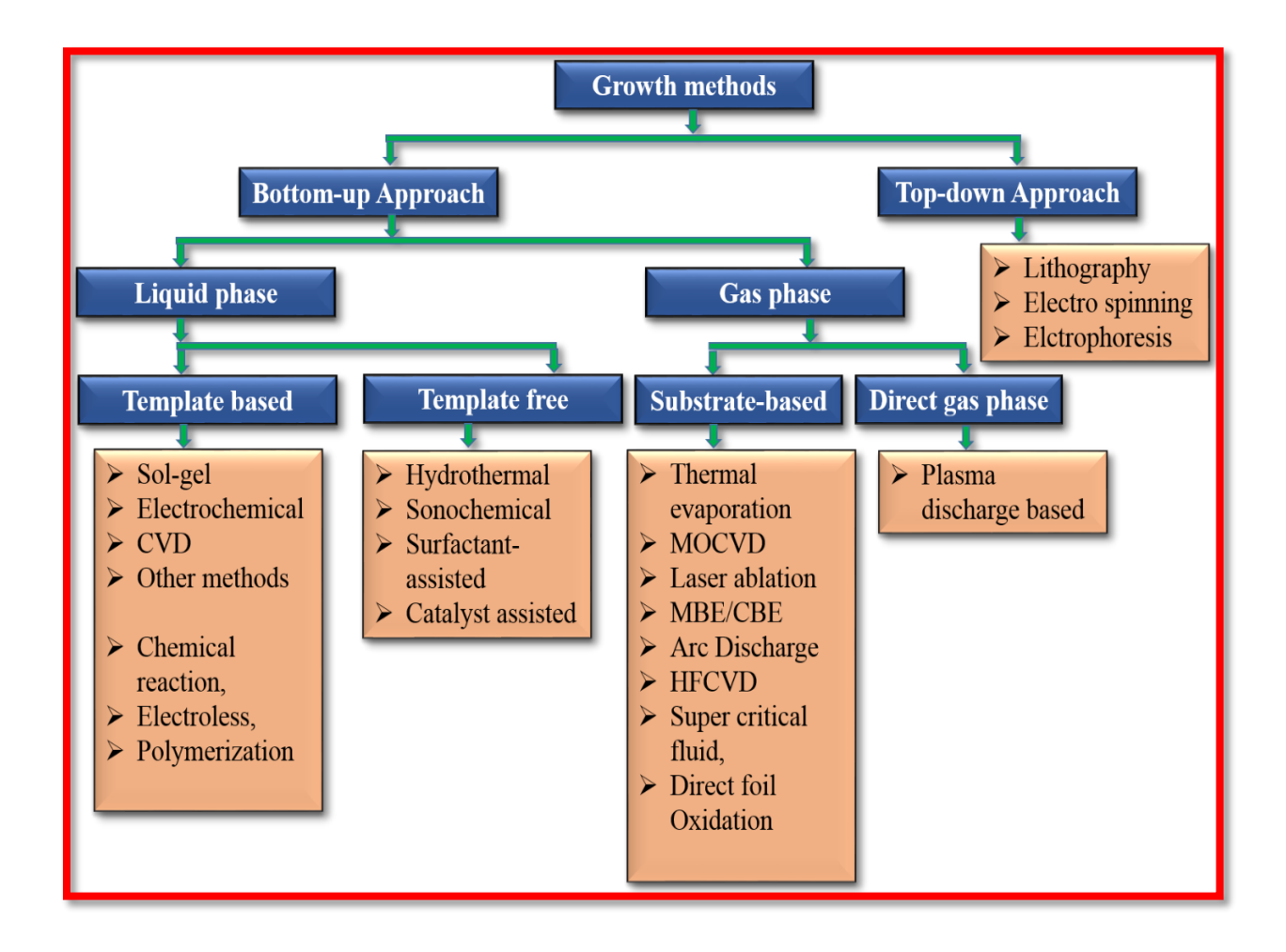


Figure 1.2: Summary tree chart of various growth techniques for 1-Dimensional nanomaterials (wires, rods, tubes) from the gas phase and solution [28].

Among the three, the most common is the negative template method used in chemical vapor deposition, electro deposition and sol-gel methods.

(ii) Template free methods

In the template based methods, the growth of 1-Dimensional nanowires/nanorods is followed by template and growth depends mainly on the boundary between bulk liquid and template, which occupies a small fragment of total system volume. In contrast, nanowire synthesis using template-free methods from solutions can create conditions to promote 1-D growth from the entire bulk liquid. These conditions are available in methods such as hydrothermal synthesis, using surfactant or catalyst seeds and sono-chemical growth, using stirring and ultrasound. In the present thesis,

the focus is on hydrothermal synthesis and the role of catalyst seed layers in the growth of nanostructured materials.

1.4 Hydrothermal synthesis of nanostructured materials

1.4.1 Introduction

The search for a nanomaterials synthesis method which has easy operation, low pollution, low production cost and excellent product performance has been going on many years [29-31]. The focus is mainly on liquid phase method including the sol-gel process [32-34], Hydrothermal Synthesis method [35-37], colloidal, and precipitation methods [38-41]. The main advantages of these methods are simple synthesis process, convenient operation, and controllable particle size. The term "Hydrothermal" means a system of water pressure and high temperature. Hydrothermal synthesis includes the growth and crystallization of a material in a high-temperature aqueous solution of soluble metal-organic and metal salts at high pressures.

The hydrothermal method is a soft chemical synthesis process simulating the process of ore formation in nature. It is used to fabricate single crystals to prepare less or ultrafine agglomerated crystallites as nanomaterials at a relatively low temperature. In recent days, the technology of hydrothermal synthesis has found its place in variety of science and technology branches as shown in figure 1.3. Hydrothermal synthesis is divided into two categories: Normal Hydrothermal and Microwave Hydrothermal synthesis.

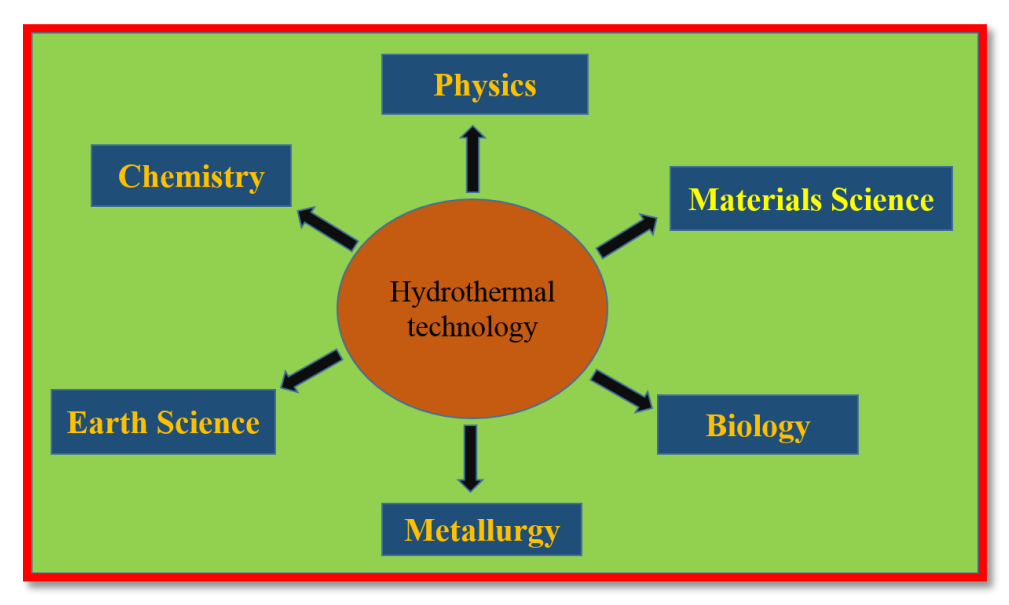


Figure 1.3: The Hydrothermal technology in different fields.

1.4.2 Normal Hydrothermal method

In the normal hydrothermal method, the aqueous solution is placed in an autoclave reactor at temperatures between 90-200 °C and at pressures higher than atmospheric for different time duration. At different temperatures employed in the closed reaction vessel, the higher pressure preventing aqueous solution evaporation. Usually, an autoclave is a closed cylindrical steel pressure vessel capable of withstanding high pressures and high temperatures for prolonged time duration and is also inert to the aqueous solution. The inner lining of the steel is pressure vessel is made up of different materials such as quartz, Teflon and glass depending on requirement. The vessel has two ends, one of which is closed while the other end is open. The aqueous solution is poured into the autoclave from the open end after which it is closed tightly with cap. The temperature gradient is maintained between the two ends wherein one end is the hotter zone and other end is the cooler zone. The hotter end also denoted as nutrient zone will create solute dissolution. In contrast, the cooler zone also denoted as growth zone is where the precursor is deposited on seed crystal leading to the growth of the desired crystal. The supersaturated solution of precursor gives precipitation which is useful for growth to occur. The general processing steps of the normal hydrothermal method are shown in Figure 1.4.

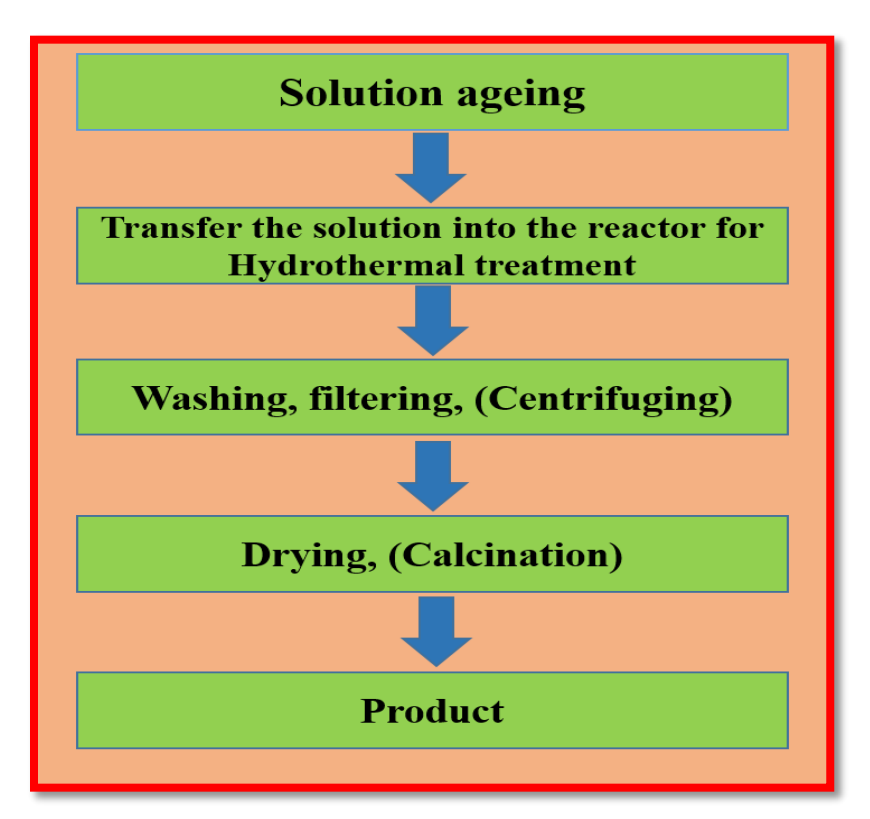


Figure 1.4: The general processing steps of the Normal hydrothermal synthesis [42].

1.4.2.1 The crystal growth mechanism and reaction kinetics in the hydrothermal method

Under hydrothermal conditions there are four main steps of crystal growth which are (1) the reactants are dissolved in the solution in the form of molecular groups or ions. (2) the molecules or ions are separated between the hotter zone and cooler zone portions of the autoclave by temperature difference. At the low temperature region the molecular groups or ions are transported, where the growth of the seed crystal forms a supersaturated solution. (3) at the growth interface the molecular groups or ions are decomposed, adsorbed, and desorbed. (4) Finally, at the interface the adsorbed material moves and the dissolved matter crystallizes. Significantly, under different hydrothermal conditions, the same crystals show different morphologies. Therefore, it is most important to study the crystal growth mechanism in hydrothermal synthesis [43-44].

1.4.2.2 The role of water in hydrothermal synthesis

In the hydrothermal reactions water participates as a chemical component or as a reaction accelerator or it can be a solvent [45]. Water will create the following variation at high-pressure and high-temperature: (a) an increase in temperature and pressure instantly, rapidly increasing the ionic product. Therefore, the ion reaction and the hydrolysis reaction rates will increase under high-pressure and high temperature. (b) Increase in the temperature decreases the surface tension and viscosity of water. Due to decreased viscosity of water, the movement of ions and molecules significantly increases, compared to other conditions. Hence, the crystals grow more quickly under the hydrothermal system. (c) The dielectric constant of water is strongly influenced by temperature and pressure. The dielectric permittivity decreases with increasing temperature and increases with increase in pressure. Therefore, at a fixed pressure the reaction is mostly influenced by temperature and the dielectric permittivity of water at that temperature. (d) The dielectric constant viscosity, solubility, diffusion coefficient of precursor in water are also important.

1.4.2.3 The role of Mineralizer hydrothermal synthesis

One of the major disadvantages of using water as the solvent is the low solubility of precursor in water, even at high temperature. To enhance the solubility and increase the rate of crystal growth, a mineralizer is used. Generally, mineralizers are a class of compounds such as low melting salts, bases, and acids. Suitable mineralizers increase solubility and also change the temperature coefficient of solubility and accelerate the nucleation rate of crystal [46-49]. Examples of

commonly used mineralizers are HMTA, KOH, NaOH, NH₃, and NH₄OH. A Schematic diagram of the hydrothermal reactor is shown in figure 1.5.

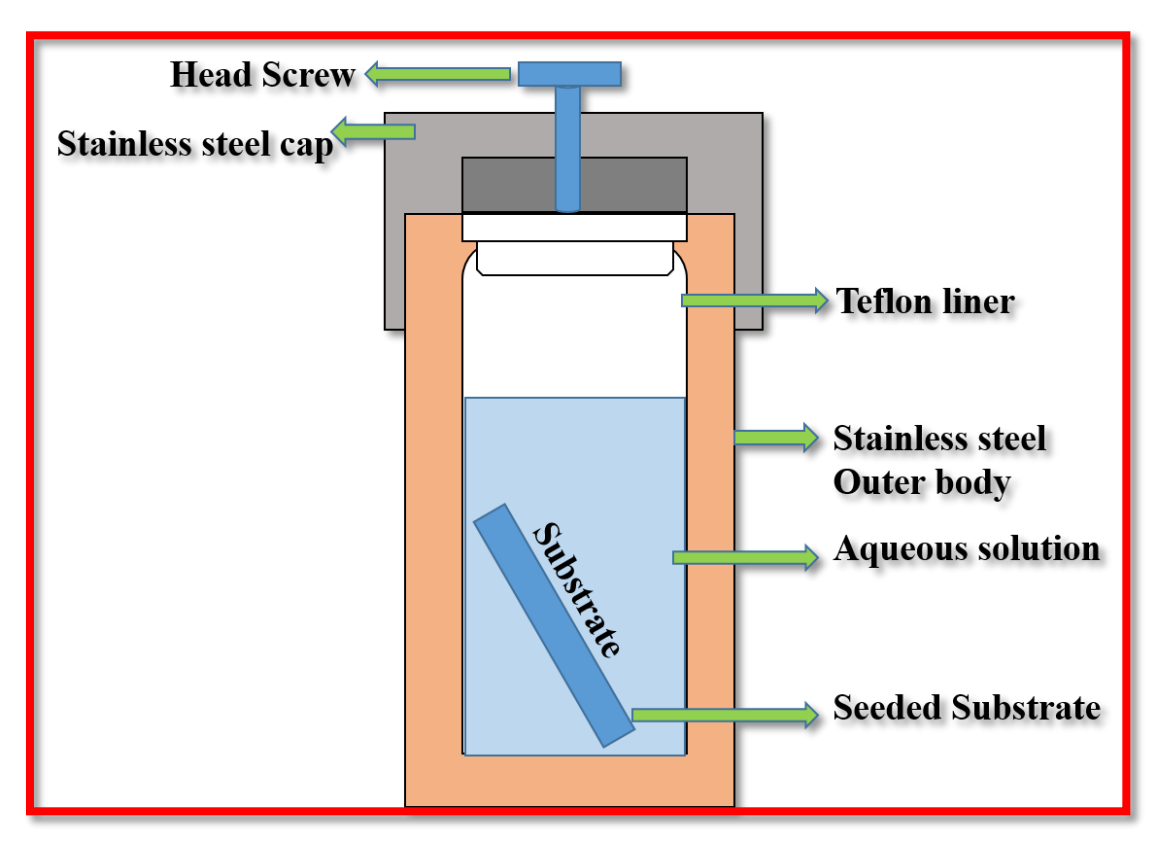


Figure 1.5: Schematic diagram of closed vessel hydrothermal Reactor (Autoclave).

1.4.3 Microwave hydrothermal method

A major disadvantage of normal hydrothermal synthesis is the slow kinetics of chemical reactions and high temperatures (>120 °C) required to grow nanostructures. To overcome these problems, microwave hydrothermal synthesis method was developed. In the microwave hydrothermal method high power and rapid heating is used to reduce reaction times and temperatures as microwaves directly transfer heat to the reactants whereas in normal hydrothermal method, heat transfer is by convention.

1.4.3.1 Reaction Mechanism of Microwave hydrothermal method

The frequency at which microwave hydrothermal synthesis is carried out is 900 MHz - 2.45 GHz. When microwaves irradiate a material surface, a small part will get reflected. Most of it can pass through the material or is absorbed by it. The absorbed component of microwave radiation is

converted into heat energy. The reaction mechanism mainly depends on the interaction between the material and microwaves, in microwave heating. The material particles can be polarized under the electromagnetic field. This polarization can be atomic, electronic, space charge polarization, and orientation polarization. Newalkar et al. [50] demonstrated that the microwave hydrothermal method is a more advantageous approach for making nanophase materials with different shapes, sizes in addition to being environmentally friendly and saving energy. Furthermore, the microwave hydrothermal synthesis method has attractive characteristics such as sensitive reaction, uniform heating system, and a fast heating speed. These characteristics can rapidly produce nanoparticles with consistent morphology and a narrow particle size distribution [42, 51].

A schematic view of the process of nanorod arrays synthesized by microwave hydrothermal method is shown in figure 1.6.

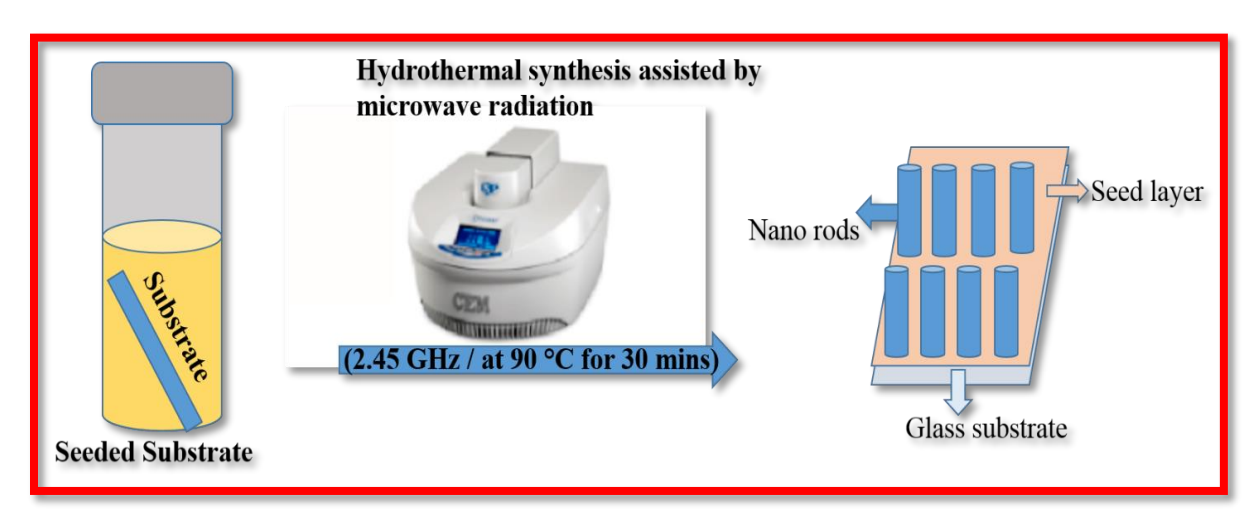


Figure 1.6: ZnO nanorod synthesized by hydrothermal method assisted by microwave radiation [51].

1.5 The role of seed-layer in hydrothermal method

Several synthesis methods have been utilized for the growing nanowires and nanorods such as vapor phase transport [52], metal-organic chemical vapor deposition [53], electrochemical deposition [54], Normal hydrothermal synthesis [55], and microwave hydrothermal synthesis [51]. The growth of nanorods and nanowires is mainly affected by various parameters such as the concentration of precursor salts, reaction agents, growth temperatures, pH, and growth time. These parameters are useful to control the morphology of nanostructures. However, it is also reported that the seed layers are a suitable catalyst for the development of nanowires and nanorods. Seed

layers are metal-oxide and metallic seed layers such as ZnO, In₂O₃, SnO₂, In, Sn and Au. The seed layer of crystalline quality firmly controls the quality of structural nanowires and nanorods. The nanoparticle size on the seed layer in turn influences the size of nanorods and nanowires. The presence of seed layer materials has enhanced the capability of growing of nanowires and nanorods by hydrothermal synthesis. These seed layers mainly catalyze and control the dimension, shape, size, and growth [51, 56]. However, the role of seed layers in the growth of nanowires and nanorods is not completely understood. Therefore, in this thesis, different seed layers are deposited on glass substrate and their roles in determining the growth of nanostructures are investigated. Many other chemical and physical techniques such as vapour-phase, solution-liquid-solid, vapour-liquid-solid and vapour-solid growth, and physical vapor deposition techniques (Thermal evaporation, pulsed laser deposition, sputtering technique, chemical vapor deposition, and molecular beam epitaxy) are also used to for producing nanostructured materials [57-71].

1.6 Nanostructures based on Metal oxides

As stated earlier, metal oxide materials are more attractive in all functional applications. They have a wide variety of exciting mechanical, optical, magnetic, electrical, and other properties. The metal oxide nanostructures have potential applications in self-cleaning, optical and optoelectronic devices, molecule detection by surface-enhanced Raman scattering, solar cells and sensors. There are many metal oxide materials researched for applications in nanotechnology and nanostructured devices. One of the most popular multifunctional metal oxide material is Wurtzite zinc oxide (ZnO) and, therefore, it has been selected as the material for investigation in the present thesis. Some of the properties of ZnO are discussed in the next sections.

1.6.1 Overview of ZnO

ZnO is a II-VI group compound semiconductor material with a direct wide-bandgap of 3.33 eV and is transparent in the 400-700nm wavelength range with large exciton binding energy (60 meV) [72-74]. ZnO has interesting optical, mechanical, electrical, and structural properties. The band gap in the UV and blue region of wavelengths makes it suitable for optoelectronic devices. ZnO exhibits defects like zinc interstitial, zinc vacancies, oxygen vacancies and oxygen interstitials. These properties are useful for fabricating electrodes, LEDs, sensors, and solar cells.

1.6.1.1 Properties of ZnO

(i) Crystal structures

ZnO typically has three crystalline structures: (a) Hexagonal wurtzite, (b) cubic zinc blende-type structure, and (c) rock salt structure (This structure is observed only under high pressure). Wurtzite structure and cubic zinc blende structures of ZnO possess sharp polar symmetry with hexagonal axes. The commonly observed structure is the hexagonal wurtzite form and it is more stable in ambient conditions. The wurtzite structure has space group (C6mc) and lattice parameters a = 0.3296 and c = 0.52065 nm. The tetrahedral unit of the wurtzite structure has Zn cations and O_2 anions. This structure consists of a number of alternating planes that are tetrahedrally- coordinated with Zn^{2+} and O^{2-} ions alternately stacked along the c-axis [75-77]. The ZnO crystal structures are shown in figure 1.7.

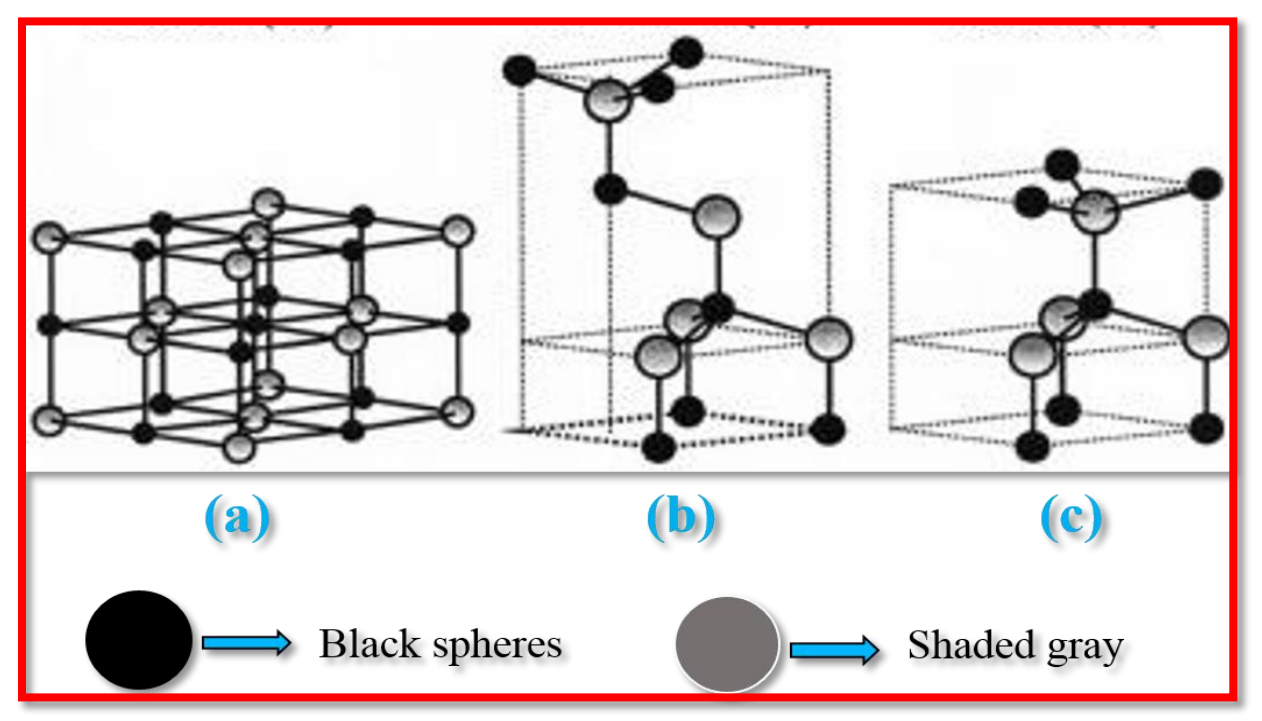


Figure 1.7: Stick and ball representation of ZnO crystal structures: (a) cubic rocksalt, (b) cubic zinc blende, and (c) hexagonal wurtzite. The shaded gray and black spheres denote Zn and O atoms, respectively [73].

(ii) Mechanical and thermal properties of ZnO

Compared to other metal oxides Zinc oxide is very soft with a hardness value of 4.5 Mohs scale. ZnO has good heat conductivity, high heat capacity, high melting temperature and low thermal expansion. These properties are useful for ceramic applications [72].

(iii) Optical properties of ZnO

ZnO is a direct wide-bandgap semiconductor with value of 3.33 eV, large exciton binding energy (60meV), large refractive index and high transparency in the visible region. These properties lead to luminesce in the range of near UV (380 nm). ZnO shows three photoluminescence peaks; a red emission around 650 nm, a green emission near 510 nm and UV near band-edge emission peak near 380 nm [78-80]. In addition, deep-level emissions in the green zone show a broad band emission from 505 to 550 nm which are assigned to defects, Zn interstitials, Zn vacancies, oxygen vacancies and oxygen interstitials [81].

(iv) Electronic properties of ZnO

ZnO has a piezoelectric coefficient of 1.29 C/m² which makes it suitable for piezoelectric applications that require large electro mechanical coupling [72]. The wide-bandgap enables it to sustain high electric fields leading to the possibility of high-temperature operation and lower

Table-1: The physical properties of ZnO.

S.No.	Properties			
1	Chemical formula ZnO			
2	Molar mass	81.4084g/mol		
3	Appearance Amorphous white solid			
4	Density 5.606g/cm ³			
5	Odor Odorless			
6	Boiling point 2360 °C			
7	Melting point 1,975 °C			
8	Band gap 3.37 eV (direct)			
9	Solubility in water 0.16mg/100 mL			
10	Refractive index 2.0			
	Structure			
11	Crystal structure Wurtzite			
12	Space group C_{6v}^4 - $P6_3mc$			
13	Lattice constant $a = 0.32 \text{ nm}, c = 0.52 \text{ nm}$			
14	Coordination geometry Tetrahedral			

Electronic noise. One of the disadvantages of the ZnO is that it is challenging to produce p-type ZnO. The physical properties of ZnO are briefly presented in table-1.

1.7. Applications of ZnO

ZnO has many applications out of which three are discussed (1) Self-cleaning applications (2) Surface-enhanced Raman scattering (SERS) and (3) photoluminescence. These applications are focused upon in the present thesis.

1.7.1 Wettability studies and Self-cleaning applications

There is a lot of interest in studying the wettability of surfaces by liquids inspired by many water repellent properties of surfaces in nature, such as rice leaves, lotus leaf and animal skin. Wettability is a surface property that exploits the interaction between a liquid and a solid surface. It is dependent on many properties like surface roughness, surface energy, surface tension, and nature of liquids. This process is recorded by measuring the contact angle between the liquid droplet and solid surface. The wetting mechanism has two interactions: cohesive interactions and adhesive interactions which explain about the behavior of fluids on the solid surface and the interactions of solid-liquid and liquid-liquid. The classification of these interactions is presented in table-2. The wetting property of a surface is measured by the contact angle (CA).

If the contact angle is $> 90^{\circ}$ then the surface is called hydrophobic while, if it is $< 90^{\circ}$, the surface is of hydrophilic nature. If the contact angle is $> 150^{\circ}$ the surface nature is super-hydrophobic, and when the contact angle $< 10^{\circ}$, the surface nature is super-hydrophilic. The best example for the super hydrophobic surface is lotus leaf in nature. In this, the micro/nanostructures on the surface capped by hydrophobic wax crystals leads to smaller contact area in between lotus leaf and water droplet resulting in super-hydrophobic behavior. Surface wettability studies are useful for self-cleaning applications in industrial and daily life such as textiles, roof tiles, car mirrors, solar cells, utensils, interior furnishing materials and interior furnishing materials [82-84].

Table-2: Wetting classification in liquid-liquid and solid-liquid interactions.

		Strength of		
Contact Angle (CA (θ))	Property of wetting	Liquid-liquid interaction	Solid-liquid interaction	
heta=0 °	Perfect wetting	Very Weak	Very Strong	
$ heta=180^{ extsf{o}}$	Perfect non-wetting	Very Strong	Strong	
0 < θ <90°	High wettability	Weak	Weak	
90° θ <180°	Low wettability	Strong	Very Weak	

1.7.2 Influence of surface roughness on wettability

The contact angle is given by Young's equation.

$$\cos\theta = \frac{Y_{SV} - Y_{SL}}{Y_{LV}} \qquad (1.01)$$

Where,

 θ =Contact angle

Y_{SV} =Solid-vapor interfacial tension.

 Y_{SL} =Solid-liquid interfacial tension.

 Y_{LV} =Liquid-vapor interfacial tension.

The three interfacial tensions through Young's equation are measured by the tangent angle at the base of the liquid droplet. The surface wettability is not only dependent on the chemical composition but also depends on the surface roughness. Two other models, Wenzel model (equation (1.02)), and the Cassie-Baxter model (equation (1.03)) have also been developed to describe the wettability of rough surfaces.

$$\cos \theta_{w} = r_{w} \frac{(\gamma_{sv} - \gamma_{sv})}{(\gamma_{lv})} = r_{w} \cos \theta_{Y}$$
 (1.02)

Where, r_w is the Wenzel's roughness factor.

$$\cos \theta_{CB} = (r_f f \cos \theta_Y + f - 1) \qquad \longrightarrow \qquad (1.03)$$

Where, θ_Y is the Young contact angle, f is the fraction of the projected area of the solid surface that is wetted by the liquid and r_f is the roughness ratio of the wetted area.

In the Wenzel model, the liquid droplet interacts at all points on the solid surface and assumes homogeneous microstructure on the solid surface. In the Cassie-Baxter process, the liquid droplet perfectly sits on the surface protrusions, and this method reveals the understanding of the role of a heterogeneous surface structure on the wettability. Although these methods demonstrate the behavior of liquid droplets on composite solid surface and vapor state, they are useful to illustrate the study of wettability behavior [82,85-87]. One of the important wettability phase transition is the reversible transition (metastable to stable). The transition state happens from Cassie–Baxter to Wenzel state or Wenzel state to Cassie–Baxter state. In this process, the liquid droplet cannot sit for a long time on the surface protrusions due to the energy barrier and thermodynamic parameters such as pressure, temperature other external forces (like an electric field). Therefore, the wettability transition is reversible [88-94].

Metal oxide materials have an exciting role in self-cleaning applications. The self-cleaning mechanism process was based on the photocatalytic and photo-induced hydrophilicity nature of thin-film and changing structural properties on the surface. If UV radiation is incident on the metal-oxide nanostructured layers (on the surface) or if they are stored in dark, the wettability property changes from hydrophobic to hydrophilic nature and hydrophilic to hydrophobic. Thus, wettability displays a reversible transition. Application of UV irradiation on these metal-oxide surfaces creates holes and electrons. The surface trapped electrons generated due to collision between metal and electrons results in the binding energy decrease between the oxygen atom and metal. In this process, lattice oxygen and holes are generated because of oxygen ion vacancy. The oxygen ion vacancy is useful for hydroxyl absorption. After UV exposure on metal-oxide nanostructure surface, the substrate changes into hydrophilic nature. If the oxygen replaces the adsorbed hydroxyl ions there is a transition from hydrophilic to a hydrophobic state [95-98]. A schematic diagram of self-cleaning surfaces is shown in figure 1.8.

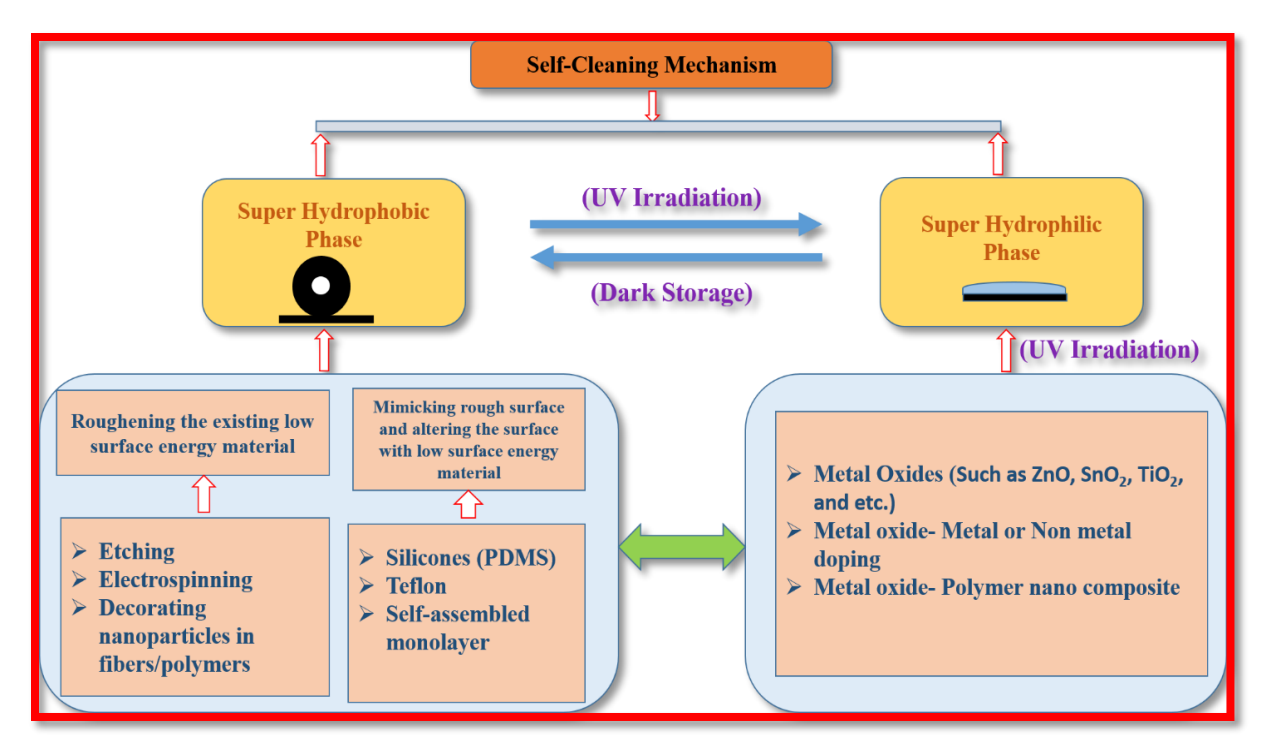


Figure 1.8: Schematic diagram of self-cleaning surfaces by various methods [82].

1.8. Surface-Enhanced Raman Scattering (SERS) application of ZnO

Surface-enhanced Raman scattering (SERS) plays a significant role in chemical and biomolecular sensing at the trace level. In this technique, analytes are adsorbed onto metal nanostructures (e,g. Ag, Au, and Cu). These metal nanostructures can enhance weak Raman signals by coupling with the excitation wavelength, which is in the visible range [99-100]. These is due to the presence of localized surface plasmon resonance (LSPR) of metal nanoparticles at the excitation wavelength. Mainly, the LSPR is dependent on the dielectric environment, size, and shape of the metal nanoparticles and these parameters can be used to control the enhancement of SERS signal intensity [101].

SERS is a surface sensitive technique for detecting single molecules and trace level detection of various analytes on the surface [102-108]. It is the most sensitive technique for explosive-agent detection [109], environmental monitoring, glucose sensing [110], stimulant detection of chemical warfare [111], the monitoring of heterogeneous catalytic reactions [112-113], corrosion, bacterial detection and detection of bio-molecules [114-121].

1.8.1 Surface-enhanced Raman scattering (SERS) mechanisms of Enhancement

There are two main mechanisms of enhancement of signals in SERS: (1). Electromagnetic enhancement and (2) Chemical enhancement. It has been shown that electromagnetic enhancement is due to the excitation of localized surface plasmons of the metal nanoparticles. The chemical enhancement effect attributes the SERS effect to the charge transfer from the adsorbed molecule to the surface [122].

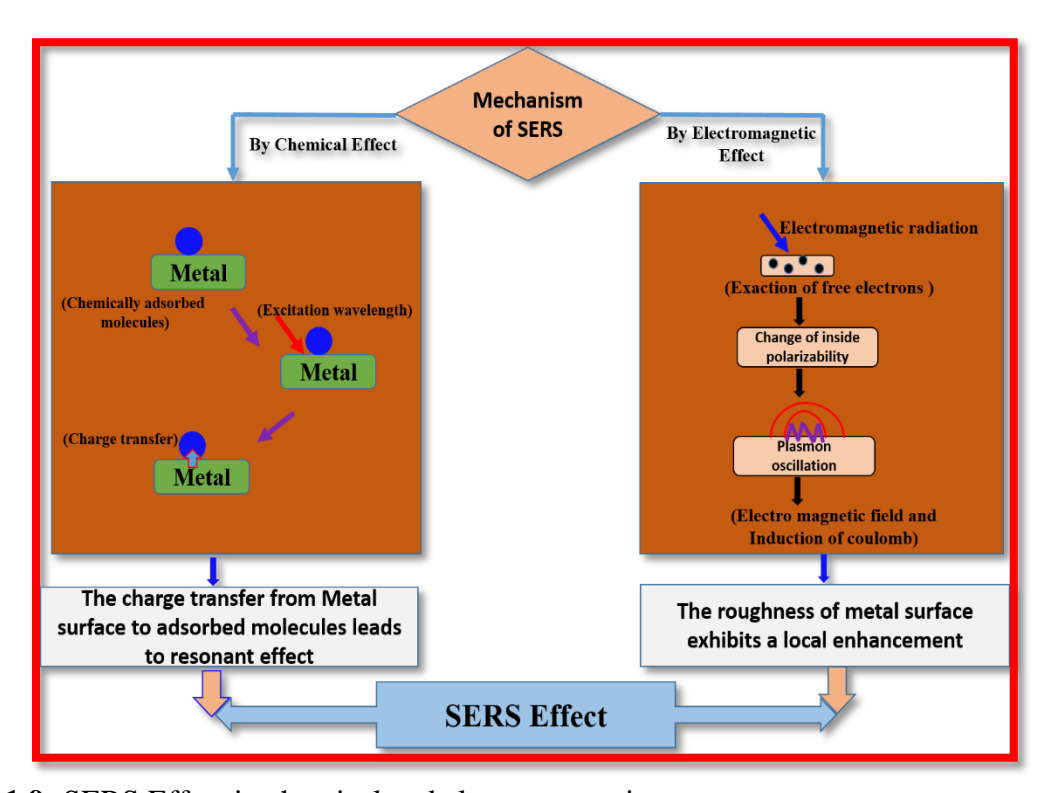


Figure 1.9: SERS Effect in chemical and electromagnetic process.

It is reported that a dominant contributor in Surface-enhanced Raman scattering processes is the electromagnetic enhancement mechanism. The electromagnetic radiation interacts within the crevices, gaps, and sharp features of plasmonic nature materials such as Au, Ag, and Cu [123-124]. Many groups theoretically calculated electromagnetic enhancement factors for SERS can be as large as $10^{10} - 10^{11}$ [125-126]. The theoretically calculated chemical enhancement factors for SERS are is around 10^3 [127-129]. It is thus inferred that electromagnetic enhancement is a much stronger effect than chemical enhancement. Brief details of the mechanisms are shown in figure 1.9.

1.9 Photoluminescence

When an incident beam of photons interacts with a sample surface, the light is absorbed and imparts the additional energy into the material in a process termed as photo-excitation. The material can dissipate this excess energy through the emission of light by a process called photoluminescence. The schematic diagram of Photoluminescence spectrometer shown in figure 1.10. The wavelength of emitted light is proportional to the difference in energy levels between the two electronic states that take part in the transition between the higher energy and low energy states [130].

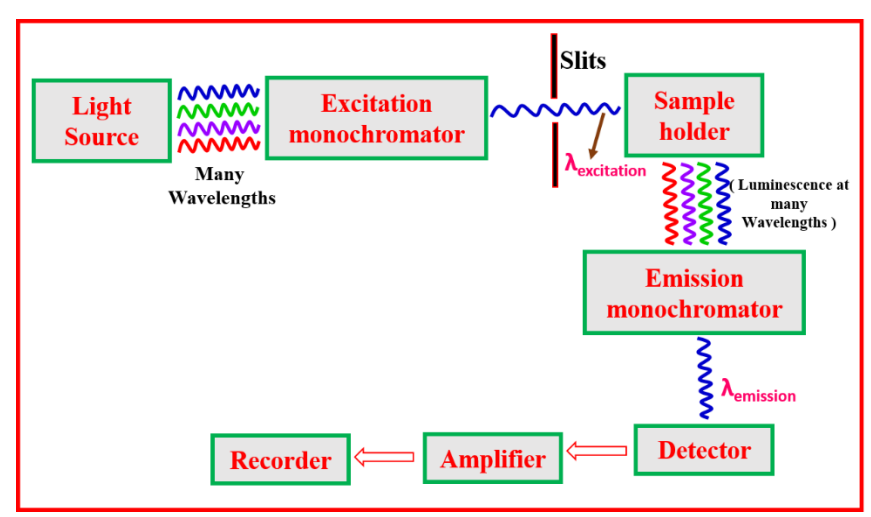


Figure 1.10: Schematic diagram of Photoluminescence spectrometer.

Photoluminescence (PL) spectroscopy is a sensitive non-destructive method for characterizing inorganic and organic materials such as semiconductors and insulators. The PL spectra from a semiconductor can be analyzed to determine the electronic bandgap.

Significantly, the radiative transitions in semiconductors arise from local defect levels. The PL energy associated with these levels is used to identify specific defects and their concentration.

Photoluminescence spectroscopy is routinely applied to microscopic imaging in single molecules and biological environment, for example, fluorescent dye molecules nanoparticles or quantum dots. Furthermore, the PL spectroscopy of various nanomaterials is of scientific and industrial interest because it is essential for the development of display panels in electronic equipment, light-emitting diodes, fluorescent lamps, scintillation detectors, thermoluminescence dosimeters, bio sensors, paints, inks and dyes [130, 131-138].

1.10 Motivation

Nanostructured materials and devices are, thus, of interest due to the wide variety of applications and insights into the science of nanoscale behavior they provide. It appears that one of the most popular materials for applications at the nanoscale is ZnO because of the ease with which it can be synthesized and many attractive properties. These properties, in turn, lead to a large range of optical, optoelectronic, electronic, energy harvesting, photocatalytic and sensing applications. Vertically aligned ZnO nanowires are of great technological interest. Physical techniques of fabricating vertically aligned ZnO nanostructures use expensive lithographic methods that also suffer from limitations of scale-up. In contrast, chemical methods can be employed for fabrication on large areas more easily and at lower cost. [139-148].

A facile and cost-effective method for the synthesis of ZnO nano/micro-rod arrays (NMRAs) is the hydrothermal process [149-153]. Xu et al showed the importance of growth time, concentration and temperature on the dimensions of the nanorods [154]. Similarly, Boercker et al [155] and Tsangarides et al. [156] synthesized hydrothermally processed ZnO nanowires on ZnO platelets and ink-jet printed Zinc acetate dihydrate layers, respectively. This study demonstrated the role of the seed layer. There are other studies on growth patterns of ZnO nanowire arrays and their dependence on seed layers as well as promoters such as NH₄OH, KOH, NaOH and NH₃ [149-159]. Majority of the work focuses on ZnO seed layers. However, there are reports of seedless growth, *i.e.* on layers other than ZnO. For example, Wen et al [159] grew ZnO nanowire arrays on patterned metal surfaces to achieve vertical alignment and application as electrochemical switch. Geng et al. [160] grew vertically aligned ZnO NMRAs on e-beam evaporated Ag and ZnO seed layers. The motivation for the present work is the fact that hydrothermal processing of ZnO on the metal or metal oxide seed layers leads to vertical alignment.

The fabrication of ZnO based homo-junctions for light emitting diodes has been of interest [160, 161-173]. Sun *et al.* observed good light emission properties in a homo-structure comprising p-ZnO film/n-ZnO nanowire with turn-on voltage of 8V. Su *et al.* demonstrated that homo-junctions of Sb doped ZnO nanowires on single crystal Ga doped ZnO substrates display a low turn on voltage and sharp near band edge emission. Kampylafka *et al.* fabricated p and n-type ZnO thin film homo-junctions with turn-on voltage of 1.5 V and transmittance of 75-85 %. Baek *et al.* fabricated, hydrothermally synthesized, Sb doped ZnO nanorod array-based homo-junctions for LED applications. The turn on voltage was 3.7 V with a near band edge emission accompanied by

a peak centred around 730 nm. These examples indicate that homo-junctions possess several advantages over more conventional hetero-junctions due to the ease and few number of steps of fabrication and control over growth patterns. As a result, they continue to generate interest for applications. However, there are only a few reports on the use of ZnO nanowire based homo-junctions on thick ZnO films for luminescence applications.

In earlier work, by our research group, it was demonstrated that thermal oxidation of Zn-In and Zn-Sn bilayers leads to the formation of horizontal and doped ZnO nanowires [174]. Therefore, the possibility of using In and Sn as seed layer thin films for the growth of vertically aligned ZnO nano/micro rods is studied in the present work. In and Sn, both, possess several advantages like low melting point, ease of deposition by thermal evaporation and crystallization at room temperature which may accelerate the crystallographic evolution of ZnO.

Hydrothermally grown ZnO nanowires by seeded or seedless techniques find applications as active materials for gas sensing, photo-catalysts and Light emitting diodes [139-148]. An application that has attracted attention is the self-cleaning property of ZnO nanowire arrays. Li et al [175] fabricated ZnO nanowire arrays on AZO/FTO and FTO thin film coated substrates and demonstrated superhydrophobic behaviour. Shape controlled wettability (hydrophobic or hydrophilic) of ZnO nanostructures was shown by synthesizing them in the form of solid or hollow flower-like structures [176]. Microflowers, nanorods, microspheres synthesized under similar conditions also exhibited variations in water wettability [177]. It is also indicated that roughness, in addition to shape, of the ZnO nanorods on Si substrate influence the wettability behavior [178]. The addition of SiO₂ thin films on ZnO nanoflakes controlled the wettability and the contact angle did not change even after 40h of UV exposure [179]. ZnO nanowires on soft surfaces such as fibers and cellulose are also interesting from a wettability perspective [180-181]. Our research group have also shown the reversible wettability transitions of ZnO nanowires and nanorods under UV irradiation [168, 182]. The focus of work in this area, evidently, remains on controlling the wettability by changing the shape, dimensions, inter-wire/rod spacing and surface roughness of the nano/micro-rod arrays (NMRAs). There has been some interest in controlling the reversible wettability by tailoring the concentration of defects such as oxygen ion vacancies in metal oxides [183-184]. The change in wetting state is due to adsorption of hydroxyl radicals in vacancy sites [185]. On ZnO surface, doping with metal, forming a heterostructure with another material, variation in annealing temperature were adopted to alter the surface oxygen vacancies [186-203].

A motivation of the current study is, therefore, to fabricate ZnO nano/micro rod arrays (NMRAs) by hydrothermal synthesis on different metal and metal oxide seed layer thin films to investigate the effect on the wettability of the arrays. The metal layers are Au, In, and Sn and the oxide layers are In₂O₃, SnO/SnO₂ and ZnO. The In and Sn oxides are prepared by post-deposition annealing of the corresponding In and Sn films. In contrast, the ZnO films are prepared directly by thermal evaporation of a ZnO source, followed by annealing. The study of (1) hydrothermal growth of ZnO nanostructures on non-patterned as-deposited and annealed In and Sn seed layers and (2) their wettability and wettability transitions under UV irradiation has not been reported earlier.

Hydrothermal synthesis provides the possibility of realizing the nanostructures at low temperatures of the order of 90°C. However, the requirement of a seed layer and the slow kinetics are often cited as limitations of the process. The use of ZnO itself as a seed layer is an approach that alleviates the problem. Metals such as Au have also been used as seed layers to produce vertically aligned nanowires and nanorods [150, 204-210]. The slow kinetics, that necessitates processing for long durations of time of the order of several hours, is overcome by carrying out the process at high temperatures of the order of 150°C or using microwave assisted hydrothermal synthesis. The latter approach not only reduces the duration of the process of nanostructures but also the temperature at which it is carried out [211-224].

Hence, another motivation of the present work is to investigate both these issues. In normal hydrothermal synthesis it was found that shorter duration and lower temperature processing does not lead to formation of nanostructures. Hence, in this work, the effect of microwave assistance during hydrothermal synthesis on the formation of ZnO nanostructures on ZnO films is investigated. The synthesis temperature and duration are fixed at 90°C and 30 min, respectively. The ZnO nanostructures are also grown on 100 nm thickness Au films to compare and understand the role of the surface of the films on the nanostructuring process. A third experiment conducted is to study the role of precursor i.e. zinc acetate or zinc nitrate on the shapes of the nanostructures. A possible mechanism for the growth patterns observed and the role of each processing variable in determining them is also presented. As stated earlier, Surface enhanced Raman scattering (SERS) and Surface enhanced resonance Raman scattering (SERS) are important probes for the detection of chemical and biological molecules. Enhancement of the Raman signals is obtained by decorating surfaces with Au, or Ag nanoparticles. Most of the SERS enhancement occurs in the top layer of the nanostructured metals. Therefore, the approach is to employ metal nanoparticle

decorated surfaces wherein LSPR can be tuned by varying the shape, size and inter-particle distance [225-234]. Recent work has shown that titanium nitride (TiN) thin films display a strong absorption peak that can be attributed to plasmonic resonance at approximately 530 nm, which is very close to that of Au nanoparticles [235-236]. TiN thin films and nanostructures can, as a result, be used as SERS substrates which demonstrated by the detection of molecules such as R6G [237-244]. Complex processing techniques such as sputter deposition are required to produce the reported materials. It is quite well-known that TiN has numerous sub-stoichiometric compositions and the growth of the stoichiometric form requires precise process control [245]. Thus, while the promise of TiN for SERS applications is established, previous work also points to the need for different techniques to expand the applicability. The motivation of the current work is, therefore, to overcome the issue of non-stoichiometry by producing nanoparticles from commercial stoichiometric TiN powders and grinding them for several hours to produce nanoparticles. They are then dispersed in acetone and drop cast on hydrothermally synthesized ZnO nanowire arrays. Decoration of the ZnO nanowire arrays with TiN nanoparticles takes place at room temperature. This novel approach is used to demonstrate proof-of-concept application as SERS substrates.

1.11 Objectives

The objectives of the present work formulated based on the research gaps are

- 1. Investigate the role of precursors, temperature and duration of processing, and seed layers (ZnO, Au, In, Sn, In₂O₃ and SnO) on the growth of ZnO nanostructures.
- 2. Establish the role of process parameters and surface conditions in the growth of vertically aligned ZnO nanowires and nano/ micro rods by hydrothermal synthesis.
- Compare the normal and microwave-assisted hydrothermal processes for the growth of ZnO nanostructures
- 4. Demonstrate the control of photoluminescence behavior of ZnO nanostructures grown by hydrothermal synthesis.
- 5. Demonstrate the use of ZnO nanostructures for wettability and self-cleaning applications
- 6. Demonstrate the use of Titanium nitride (TiN) nanoparticle decorated ZnO nanostructures for sensing applications by the surface enhanced Raman scattering process.

1.12 Thesis organization

The remainder of the thesis is organized as follows

- ❖ Chapter-2: Materials: processing techniques, parameters and characterization.
- ❖ Chapter-3: Deposition and characterization of seed layers.
- ❖ Chapter-4: Comparison of growth of ZnO nanowires/ nanorods by conventional and microwave hydrothermal synthesis.
- ❖ Chapter-5: Effect of different metal and metal oxides seed layers on the growth and wettability of ZnO nano/ microstructures.
- ❖ Chapter-6: Application of Titanium nitride nanoparticle decorated ZnO nanowires as surface enhanced Raman scattering substrates.
- ❖ Chapter-7: Summary, Conclusion, Scope for future work.

Chapter

2

Materials: processing techniques, parameters and characterization

Abstract

In this chapter, the techniques used to process the different materials studied in the present thesis are described. The methodology of varying the parameters related to each process and techniques for characterization of the samples are also presented. The process of synthesizing ZnO nanostructures involved two steps: (1) deposition of seed layer by thermal evaporation and (2) hydrothermal synthesis of ZnO on the seed layer thin films. The seed layer thin films of Au, In, Sn and ZnO are deposited on glass substrates by thermal evaporation. The ZnO nanostructures are obtained by changing the precursor, temperature and duration of hydrothermal processing. The obtained materials are characterized by x-ray diffraction, field emission-scanning electron microscopy, energy dispersive x-ray spectroscopy, transmission electron microscopy, UV-VIS-NIR spectrophotometry, Raman spectroscopy, Photo Luminescence spectroscopy and contact angle meter.

2.1 Background

As stated in the introduction chapter, the aim of the present thesis is to study the role of seed layers on the growth of ZnO nanostructures synthesized by the hydrothermal process. Another objective is to investigate the potential of these ZnO nanostructures for photoluminescence, wettability and surface enhanced Raman scattering applications. For this purpose, based on literature, the steps given below were followed

- 1. Seed Layer deposition: The seed layers selected were Au, In and Sn as the metals and In₂O₃, SnO/SnO₂ and ZnO as the oxides. Thermal evaporation was selected as the deposition technique based on work done previously in our research group. To achieve oxides of In and Sn the metal films were annealed after deposition in air. Similarly, ZnO films were post-deposition annealed to achieve better stoichiometry. The substrate was glass in all cases.
- 2. Hydrothermal processing: The ZnO nanostructures were obtained by hydrothermal processing. A detailed study of the role of precursor (Zinc Nitrate hydrate or Zinc acetate hydrate), mineralizers (HMTA, KOH, NaOH and NH₃), duration (10 min to 10hrs) and temperature (90 to 180 °C) on the nanostructuring process was carried out. Comparison with microwave assisted hydrothermal synthesis was also studied.
- 3. Characterization: All the samples were characterized by x-ray diffraction for structure, scanning electron microscopy for microstructure, Energy dispersive analysis of x-rays (EDAX) for composition, Raman spectroscopy for electronic structure and defects, Photoluminescence spectroscopy to understand the nature of emission, UV-Visible-NIR spectrophotometry for band gap estimation, contact angle measurement for wettability. Some of the samples were characterized by Surface enhanced Raman scattering measurements to investigate possible sensing applications. Some of the samples were characterized by transmission electron microscopy.

Details of materials processing techniques used and parameters varied as well as characterization techniques are provided in the following sections.

2.2 Materials: Processing techniques and parameters

2.2.1 Seed layer thin film deposition: process flow

Thin films of Au, In, Sn and ZnO were deposited by thermal evaporation in a home-built vacuum system equipped with a diffusion pump and rotary pump to create vacuum. A photograph of the system is shown in figure 2.1. Typically, the process of thin film deposition is carried out in the following steps.

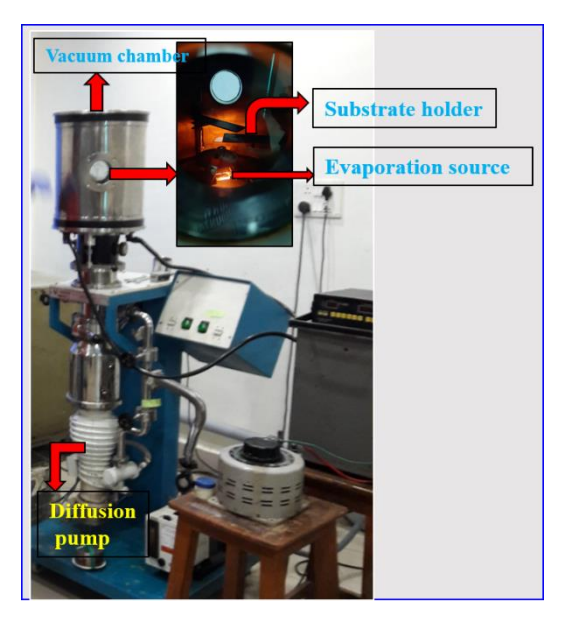


Figure 2.1: Photograph of thermal evaporation coating unit used.

- 1. First, A rough vacuum is created in the chamber by a mechanical rotary pump (chamber pressure 5×10^{-2} millibar).
- 2. This is followed by creation of high vacuum using a diffusion pump (chamber pressure 5×10^{-6} millibar).
- 3. In the case of Au, In and Sn, evaporation is from a W spiral while in the case of ZnO, the powder is evaporated from a Mo boat.
- 4. The substrate was glass for all the films. The source-substrate distance was varied from 5 cms to 11 cms and after optimization of rate of deposition, it was fixed at 8 cms.
- 5. The substrates were not heated during deposition. However, in the case of In films they were post-deposition annealed at 200 °C for 2 hrs and the Sn films were post-deposition

- annealed at 300 °C for 2 hrs in air to achieve oxidation. The ZnO films were annealed in air at 400 °C for 2 hrs, to improve stoichiometry and achieve crystallinity.
- Based on previous work, the thickness of In and Sn films was 10, 20, 30,40 and 50 nm, the
 Au thin films were 100 nm thick and the thickness of ZnO films was 100,150, 200 and 400
 nm.

2.2.2 Hydrothermal synthesis: Process flow

ZnO nanostructures are synthesized mainly by the normal hydrothermal synthesis process. Microwave assisted hydrothermal synthesis was used to establish if the lowest temperatures required to obtain nanostructures are the same in both processes (i.e. normal and microwave assisted). The photograph and schematic view of the two types of hydrothermal reactors are, respectively shown figure 2.2(a) and (b). Two precursors Zinc acetate dihydrate [Zn(O₂CCH₃)₂(H₂O)₂, 99.0%] and zinc nitrate hexahydrate [Zn(NO₃)₂(H₂O)₆, 98.0%] with Hexamethylenetetramine (HMTA) [(CH₂)₆N₄, 99.0 %] as the alkaline reagent were used.

Although most of the steps are the same for both precursors, they are listed separately to highlight the differences. All chemicals were purchased from Sigma-Aldrich (Steinheim, Germany) and used without further purification. In the rest of the thesis zinc acetate dihydrate is referred to as ZnAcD and zinc nitrate hexahydrate as ZnNH.

The typical process flow for hydrothermal synthesis using ZnAcD is presented in detail below

- (1) The seed layer thin film deposited glass substrate is introduced into the reactor containing the aqueous solution of ZnAcD and the alkaline reagent (hexamethylenetetramine (HMTA).
- (3) The experiments were carried out at a fixed concentration of HMTA (25mM) and three different concentrations of ZnAcD: 15mM (precursor-deficient), 25mM (equal concentration) and 35mM (precursor rich).
- (4) Experiments were also carried out by replacing HMTA with NaOH and NH₃.
- (5) The synthesis was carried out at 90, 120,150 and 180 °C for durations of 10min, 30min, 60min, 180min, 360 min and 600mins.
- (6) After each synthesis process, the substrate and growth layer is rinsed and dried.

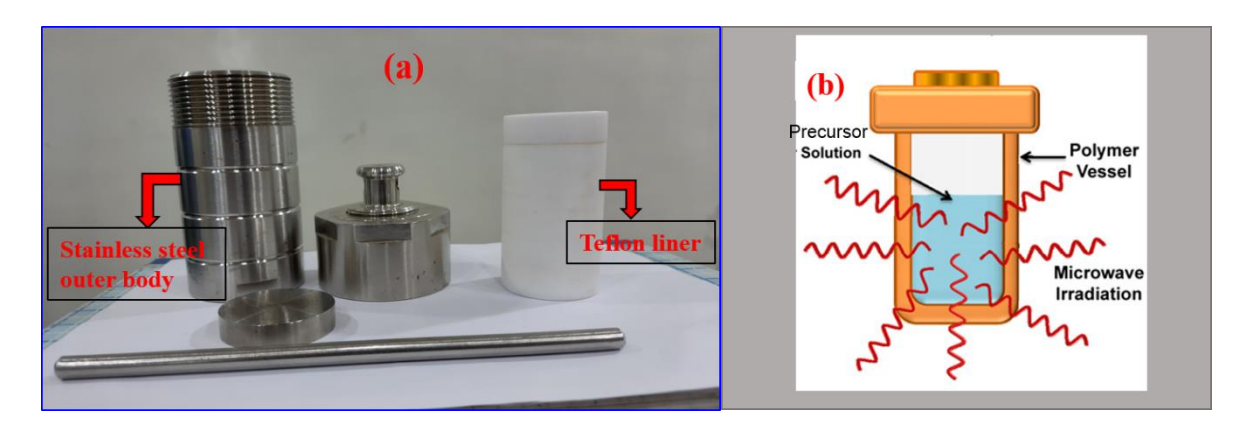


Figure 2.2: (a) Hydrothermal Synthesis Autoclave Reactor with PTFE Lined Vessel Teflon Chamber (b) Schematic illustration synthesis of the Microwave-assisted hydrothermal reactor.

The typical process flow for microwave hydrothermal synthesis using ZnNH and ZnAcD is presented in detail below

- (1) The seed layer thin film deposited on glass substrate is introduced into the microwave reactor containing the aqueous solution of ZnNH or ZnAcD and the alkaline reagent (hexamethylenetetramine (HMTA).
- (2) 25mM of Zinc acetate dihydrate $[Zn(O_2CCH_3)_2(H_2O)_2, 99.0\%]$ or 25mM of zinc nitrate hexahydrate $[Zn(NO_3)_2(H_2O)_6, 98.0\%]$ were mixed with 25 mM of hexamethylenetetramine (HMTA) $[(CH_2)_6N_4, 99.0\%]$ to obtain an aqueous solution.
- (3) The substrates coated with the ZnO or Au thin films were then dipped into the aqueous solutions
- (4) The process is carried out in a microwave oven (2.45 GHz) operated at 700 W at a fixed temperature of 90 °C and duration of 30 minutes for all the cases.
- (5) After each synthesis process, the substrate and growth layer is rinsed and dried.

2.3 Materials: Characterization Techniques

Two types of materials have been synthesized in the present thesis: (1) thin films that act as seed layers. These materials are characterized for thickness, microstructure and structure only, since their role is limited and (2) ZnO nanostructures that are grown on these seed layers. Since the aim of the work is to investigate them for applications, they are characterized for microstructure, crystal structure, chemical structure, optical transmission, photoluminescence, wettability and surface

enhanced Raman scattering. The techniques used to obtain the relevant information are discussed in the following sections.

2.3.1. Thickness measurement of thin-films

The thickness of thin films was measured in a Stylus Profilometer (Model XP-100, Ambios technology, USA). The schematic diagram and photograph of the equipment are shown in figure 2.3 (a) and (b). The technical specifications of the instrument are given below.

Profilometer provides following features:

- Scan Length range: 30-55 mm maximum
- Minimum resolution step:- 10 A°
- Vertical range:- 1200 µm maximum
- Step height repeatability:- 5 A°
- Stylus tip radius:- 2.5 μm
- Stylus force range: 0.03 10 mg

The parameters used in the present study are

Scan range ~2.5 - 800 microns

Stylus force 0.03mg

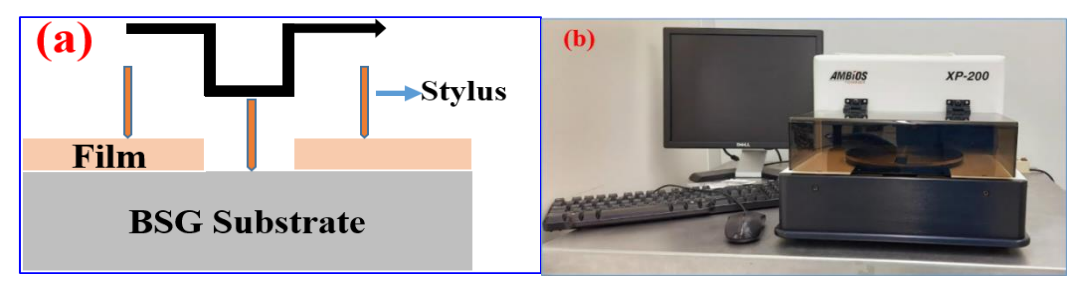


Figure 2.3: (a) Illustration of stylus profilometry to measure film thickness (b) Stylus Profilometer (XP-200, Ambios Technology, USA).

2.3.2 Structural studies

In the present thesis, the used X-ray diffractometer is Bruker- D8 Discover and PANalytical X-ray diffractometer with Cu K α radiation (λ =0.15408 nm) 40 kV and 30 mA. The GI-XRD pattern is recorded at a grazing incidence angle of 0.5°. The calibration is done by silicon standard, which accounts for the instrumental line broadening, the value is approximately 0.10° for Bruker-D8

Discover diffractometer. The XRD phase patterns are recorded in the range of 20° - 80° and diffraction phase patterns were identified using the JCPDS (Joint Committee of Powder Diffraction Standard) files [246]. The X-ray Diffractometers are shown in figure 2.4(a)-(b).

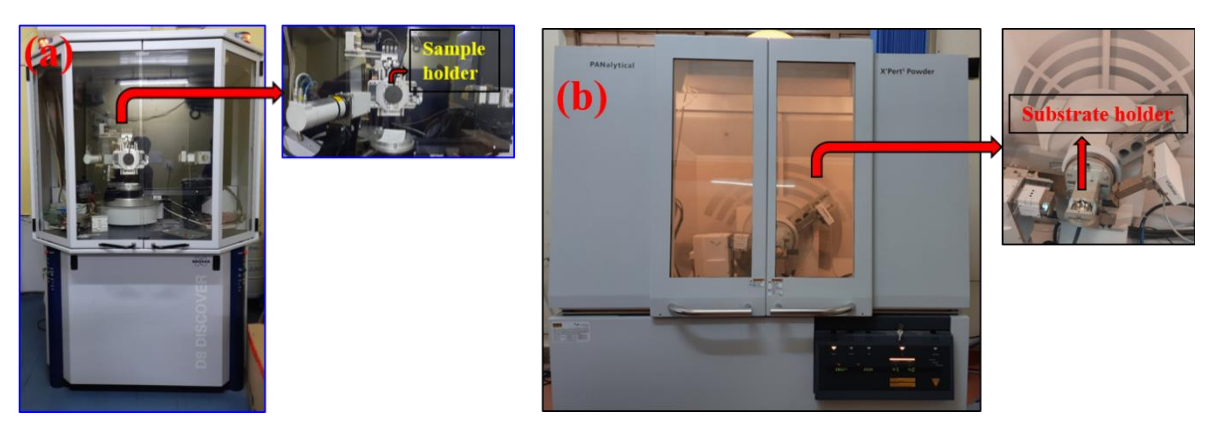


Figure 2.4: (a) Bruker D8-Discover for thin films (GIXRD) and (b) PANalytical X-ray diffractometer.

Crystallite Size

The crystallite sizes are calculated by the line profile quantitative analysis of the peak broadening of diffracted peaks using Debye-Scherrer Formula.

$$D = \frac{\kappa \lambda}{\beta \cos \theta} \quad \to (2.01)$$

Where, k=0.94, λ is the X-ray wavelength (Cu-K_{\alpha} radiation, $\lambda=0.15405$ nm), and β is full width at half maximum (FWHM) of the peak and Θ is the Bragg's angle. The lattice strain is calculated by using the below equation.

$$strain = \frac{d - d_0}{d_0} \longrightarrow (2.02)$$

Where, d= is the interplanar distance,

 $d_{o}=$ is the standard value of diffraction peak position taken from the JCPDS file. Negative strain is considered compressive while positive strain is termed as tensile strain.

The texture coefficient (TC (h,k,l)) calculated by using the following formula

$$TC_{(hkl)} = \frac{\frac{I(hkl)}{I_o(hkl)}}{\frac{1}{N} \sum_n \frac{I(hkl)}{I_o(hk)}} \rightarrow (2.03)$$

Where, I (hkl) is the intensity that is experimentally determined for a specified plane, while I₀ (hkl) is the standard intensity obtained from JCPDS files corresponding to the same plane (hkl). N is the total number of reflections, while n is the number of diffraction peaks.

2.3.3 Microstructural studies by Field Emission Scanning Electron Microscopy (FESEM)

Field emission scanning electron microscopy (FESEM) is used to study surface morphology, microstructures, chemical composition, and particles' size and shape. In Field emission scanning electron microscopy, the acceleration voltage of electrons is 0.5 - 30 kV and all the process happens under high vacuum, of the order of 10⁻⁶ millibar. In the present work, the FESEM images were recorded in a Ultra-55, Carl Zeiss microscope shown in figure 2.5.

The specifications of the instrument are

- (1) Emitter type: Schottky field-emitter type
- (2) Accelerating voltage range: -5 kV 20 kV
- (3) Detector types: In specimen chamber ET-SE detector, High efficiency In-lens detector (SE detector), and Energy selective backscattered electron (EsB detector).
- (4) Probe current: 4pA to 10 nA
- (5) Resolution (at different voltages):- 0.1kV- 15kV
- (6) Magnification (in different modes):- 12 900,000X in SE mode

100 - 900,000X with EsB detector

(7) Number of axes:-5 (X-axis- (L-R movement), (Y-axis (forward-backward movement), Z-axis (height), R (rotation), T (Tilt)).

The elemental composition of some of the samples was determined using Energy Dispersive X-ray Spectroscopy (EDS). The specimen's chemical composition and microstructural information are obtained at operating voltage 5 kV-20 kV with a working distance of 4.5 mm.

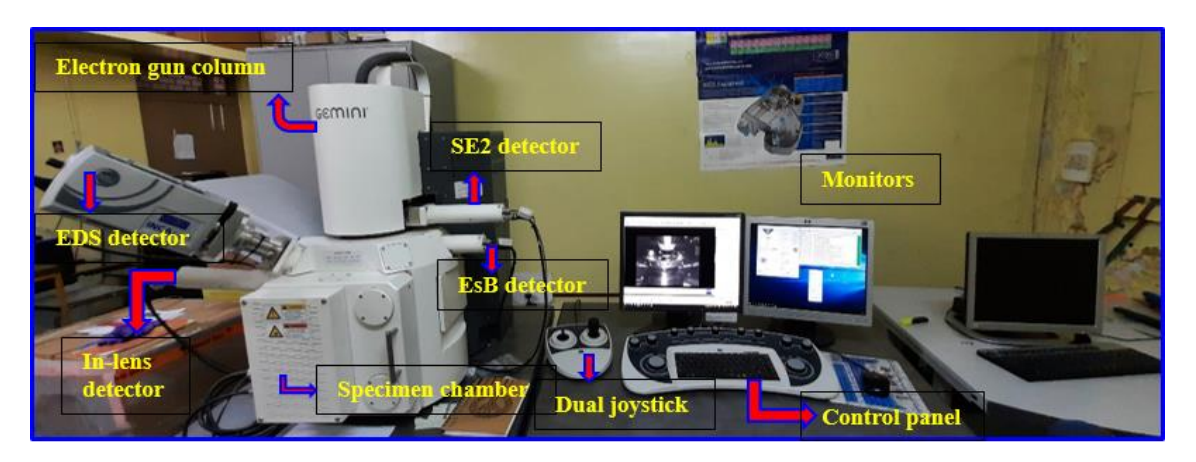


Figure 2.5: (a) Photograph of the Field emission scanning electron microscope (model: Carl ZEISS, Ultra55, Germany).

2.3.4 Transmission electron microscope

The growth of ZnO nanowires, in a few cases, was also determined using transmission electron microscope (model: FEI Tecnai G² S-Twin, FEI electron microscope operated at 200 kV using Gatan CCD camera). Photograph of the Transmission electron microscope shown in figure 2.6. High resolution TEM images were also recorded in the same instrument. Selected area Electron diffraction (SAED) patterns were recorded with a Gatan CCD camera. A 10 nm gold film deposited on the grid was used for camera length calibration purposes. Some of the technical specifications are given below:

1. Acceleration voltage: 200kV

2. Electron source: LaB₆

3. TEM point resolution: 0.24nm

4. TEM line resolution: 0.14nm

5. TEM magnification range: $25 \times -1030 \text{k} \times$

6. Imaging: 4K×4K CCD camera and EDX detector of Energy resolution: 136eV



Figure 2.6: Photograph of the Transmission electron microscope.

2.3.5 Ultraviolet-visible-Near Infrared (UV-Vis-NIR) spectrophotometry

The optical properties of thin-films and nanostructures were characterized using the JASCO V-670 UV-Vis-NIR double beam spectrophotometer shown in figure 2.7.



Figure 2.7: Photograph of the UV-VIS-NIR spectrophotometer (JASCO V-670).

The spectral data were recorded in 190- 2500 nm wavelength range with air as reference. The UV-Vis-NIR spectrophotometer system operates in the double-beam mode with single monochromatic

light sources. The deuterium lamp source is used for wavelengths ranging between 190-350 nm, and the halogen lamp range is 330-2700 nm. The detectors are a photomultiplier tube and PbS photoconductive cell. These detectors have quantitative response, high sensitivity and low level noise. The UV-VIS-NIR spectrophotometer is used to determine the optical properties such as transmittance (T %), absorption (abs), and reflectance (R) of the films and nanostructures. The spectrophotometer has a resolution limit of ± 0.2 nm and a sampling interval of 2 nm. In the present study, the bandgap was calculated from Tauc's relation [247-250].

$$\alpha\hbar\omega = B(\hbar\omega - E_g)^n \rightarrow (2.04)$$

Where, the exponent n is $\frac{1}{2}$ or 2 depending on the nature of the gap (indirect or direct), $\hbar\omega$ is photon energy, E_g is optical bandgap, α is absorption coefficient, α is obtained with Beer Lambert's law mentioned below

$$I = I_0 e^{-\alpha d} \longrightarrow (2.05)$$

Where, I_o and I are the incident intensity and transmitted intensity of photons respectively, d is thickness of the film.

2.3.6 Raman spectroscopy

Raman spectra of all the samples was recorded in air using a neodymium-doped yttrium aluminum garnet (Nd: YAG) laser with 532 nm wavelength, in the backscattering geometry in a CRM spectrometer attached with a confocal microscope and 100X objective lens with CCD detector located on a model alpha 300 platform of WiTec Germany. The photograph is shown in figure 2.8. The specifications of the instrument are

- (1) Laser Source: 532 nm
- (2) Objective lens:- 100X
- (3) Detector:- CCD detector
- (4) Spectral range: 130-3700 cm⁻¹
- (5) Pixel resolution: -<0.09 < 3.

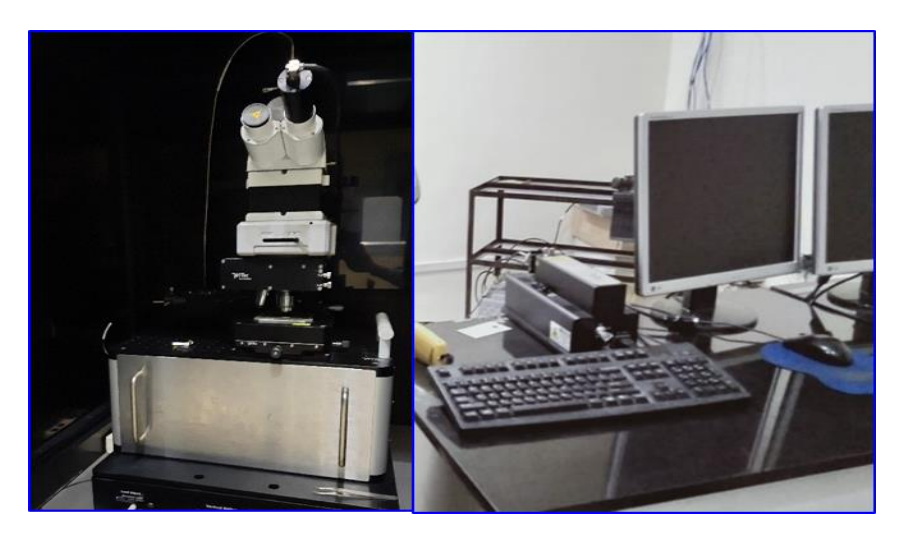


Figure 2.8: Photograph of the Raman spectrometer (Witec Alpha 300).

2.3.7 Photoluminescence spectroscopy

The Photoluminescence (PL) spectra of the samples were recorded at room temperature using a Horiba JobinYvon model FL3-22 spectrometer shown in figure 2.9. The specifications of the instrument are

- (1) Model:- Horiba Jobin Yvon model FL3-22 spectrometer
- (2) Light source: 450-W Xe
- (3) Excitation spectrometer:- Double
- (4) Sample compartment:- T-Box
- (5) Emission spectrometer:- Double
- (6) Detector:- PMT



Figure 2.9: Horiba Jobin Yvon model FL3-22 spectrometer.

2.3.8 Surface enhanced Raman scattering (SERS) measurements

SERS measurements were performed with a LabRAM-Horiba Jobin Yvon spectrometer with a 50X objective lens and 532 nm wavelength laser and displayed in the figure 2.10. The specifications of the instrument are

(1) Laser Source: - 532 nm

(2) Objective lens: 50X, 0.5 NA

(3) Detector: CCD detector (pixel size 26 µm X 26 µm)

(4) Spectral range: 50 cm⁻¹ to 4000 cm⁻¹

(5) Scan table: X-Y stage is used to scan the sample

(6) Accumulations: - 3

(7) Acquisition time: - 8 sec

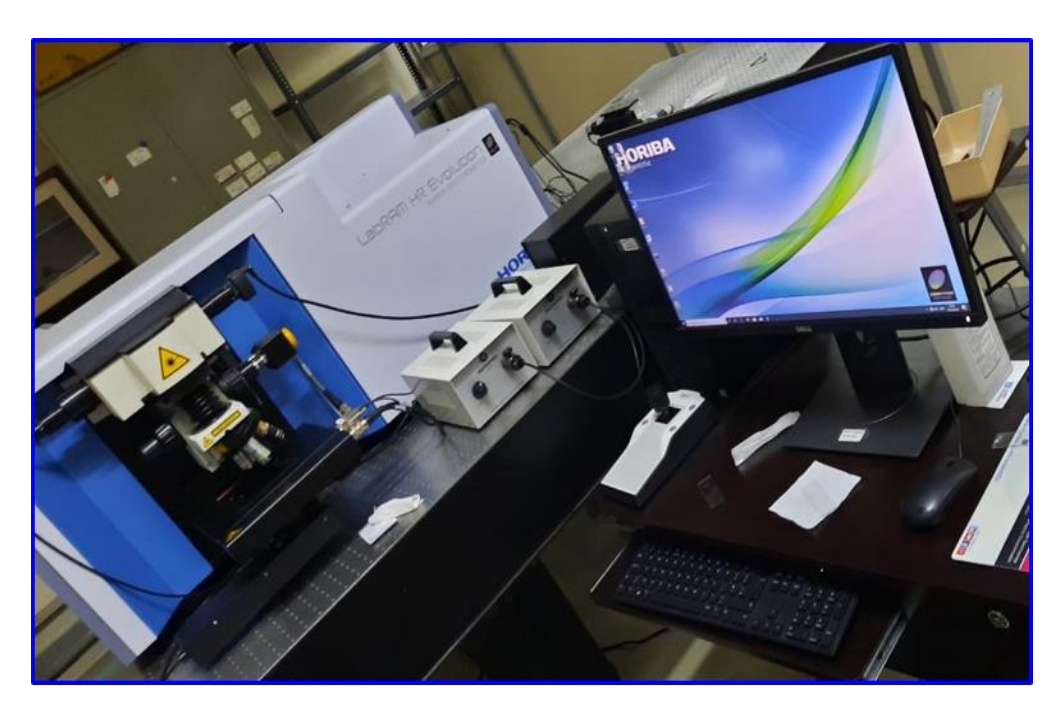


Figure 2.10: (a) Photograph of the LabRAM-Horiba Jobin Yvon spectrometer with a 50X objective lens and 532 nm wavelength laser.

2.3.8.1. SERS Enhancement factor calculations

The SERS enhancement factor (EF) measures the Raman signal amplification created by the substrate from a specific Raman mode of the analyte molecule. The enhancement factor quantifies

the performance of a SERS active substrate. This can depend on the analyte, incident wavelength, microstructure of the substrate, and probe molecule on the SERS substrate.

SERS enhancement factor (EF) was calculated using this formula [251-253]

$$EF = \frac{I_{SERS}}{I_{Raman}} \frac{N_{Raman}}{N_{SERS}}$$
 (2.06)

Here, N_{Raman} and N_{SERS} are the number of molecules contributing to the SERS and Raman signal. I_{SERS} is the enhanced Raman intensity at the lower concentration on SERS substrate. I_{Raman} is the average Raman intensity at a higher concentration measured over the surface. In the calculation of the EF, N_{SERS} and N_{Raman} can be determined by the following equations

$$N_{SERS} = \eta N_A C_{SERS} V_a \frac{A_{laser}}{A_{NS}}$$
 (2.07)

$$N_{SERS} = \eta N_A C_{SERS} V_a \frac{A_{laser}}{A_{NS}}$$
 \longrightarrow (2.07)
 $N_{Raman} = N_A C_R V_a \frac{A_{laser}}{A_{substrate}}$ \longrightarrow (2.08)

Here, N_A is Avogadro's number. Laser parameters (effective area of the laser spot size), analyte volume V_a utilized are kept equal in collecting the SERS and Raman spectra. Therefore,

$$EF = \frac{I_{SERS}}{I_{Raman}} \frac{C_{Raman}}{C_{SERS}} \times \frac{1}{\eta}$$
 (2.09)

The adsorption factor estimation was performed with the Langmuir isotherm model, in which the lower η (0< η <1) value reflects more favorable adsorption. From the linearized form of Freundlich adsorption isotherm, i.e., log C versus log I plot of the particular vibrational mode, the slope is a measure of adsorption intensity [251-253]. Generally, the obtained slope ranges between 0 and 1 and, therefore

$$EF = \frac{I_{SERS}}{I_{Raman}} \frac{C_{Raman}}{C_{SERS}} \rightarrow (2.10)$$

Here we have assumed $\eta=1$. Therefore, the achieved EF values are generally under-estimated [251-253].

2.4. Wettability studies by Contact angle goniometry

Wetting studies were performed using a contact angle meter (DMs-401, Kyowa Interface Science CO LTD, Japan). The measurement of contact angle was performed in an ambient atmosphere. At first, in the experimental arrangement, a 2 µl pendant drop of water was created, and the substrate stage raised so that the droplet would touch the substrate surface. The sessile drop's contact angles were recorded using a high-speed camera and analyzed using FAMAS software integrated with the system.

The instrument also has an automated software-driven dispensing system with a nozzle and a piping system fitted to it for producing precise pendant and sessile drops. The contact angle is calculated by drop shape analysis of the software. The principal assumptions of this analysis are as follows.

- 1) The drop is assumed to be symmetric about a central vertical axis. This means that it is irrelevant from which direction the drop is viewed.
- 2) The drop is not in motion and viscosity and inertia play a role in determining its shape.

As stated in the introduction chapter, liquid droplets form the contact angle at the three-phase boundary where a liquid, gas, and solid intersect on the surface.

Contact angle goniometer (Figure 2.11) is an instrument used for measuring the contact angle between the liquid and the substrate. The contact goniometer consists of

- (a) A Charge Coupled Device (CCD) camera
- (b) A flat stage table to place the solid substrate
- (c) A stand fitted with a clamp to hold the goniometer microsyringe
- (d) A variable fiber-optic-illuminator and
- (e) A straight needle for manual dispensing.

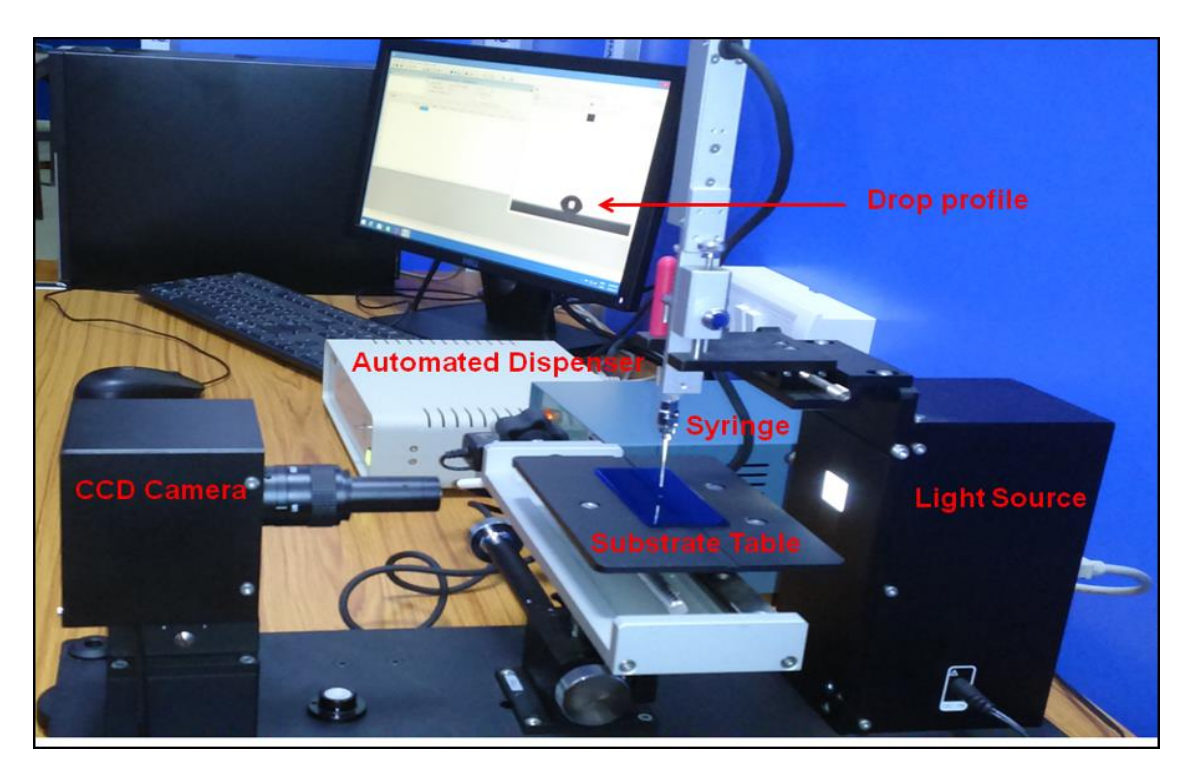


Figure 2.11: Photograph of contact angle goniometer.

A small drop of the liquid is dropped on a substrate placed on the goniometer's flat stage table in the study. The CCD camera captures the liquid drop profile over the substrate and the video presented on the screen—the contact angle calculated by drop shape analysis of the software manager. The contact goniometer used to measure the static contact angle, receding contact angles and advancing surface tension of liquid droplet by pendant drop method and the surface energy, adhesive energy of the solid substrate from measured contact angles. The self-cleaning application was established by irradiating the nanostructured surfaces with UV light of wavelength 254 nm.

2.5 Summary

In summary, Zinc oxide (ZnO), Gold (Au), As deposited Indium (InA), As deposited (SnA) seed layers were deposited on BSG substrate by thermal evaporation. After this, Indium oxide (InO) was obtained by annealing InA films at 200°C for 2 hours, Tin oxide (SnO) by annealing SnA films at 300°C for 2 hours, and Zinc oxide (ZnO) by annealing the as-deposited films at 400°C for 2 hours. These seed layers are used for hydrothermal synthesis. The protocol followed for hydrothermal processing is described in detail. The metal and metal oxide seeded layers as well as the hydrothermally processed ZnO nanostructures were characterized by x-ray diffraction, Raman and PL spectroscopy, UV-Vis-NIR spectrometry, Scanning and Transmission electron microscopy and contact angle measurements for optical, wettability and SERS applications. Details of the instruments used along with their technical specifications are also presented.

Chapter

3

Deposition and characterization of Seed layers

Abstract

One of the most important factors that determines the growth of nanostructures by hydrothermal synthesis is the nature of the seed layers. In this thesis, the aim is to examine the role of the seed layer thin films on structure, microstructure, optical, sensing and wettability properties of the ZnO nanostructures grown over these layers. Two types of seed layers, metal and metal oxides, were studied to establish their efficacy. The metals studied are In, Sn and Au while the oxides are thermally oxidized In and Sn and ZnO. All the thin films are deposited by thermal evaporation. The metal thin films are obtained by evaporating the corresponding metals. In the case of ZnO thin films, the source is the corresponding oxide while to achieve In and Sn oxides the metal films are thermally oxidized in air. In this chapter, the details of the processing parameters, structure and microstructure of the seed layer films is presented in detail. The characterization helps in correlating the role of the seed layers with the growth and properties of the ZnO nanostructures presented in the next chapters

3.1 Background

As stated in the introduction chapter one of the objectives of the present study is to examine, in detail, the role of seed layers in determining the growth patterns of the ZnO nanostructures processed by hydrothermal synthesis over them. As a first step the structure and properties of the seed layers is discussed in this chapter. The seed layers are In, Sn and Au metals and oxides of In, Sn and Zn. In and Sn oxides are prepared by annealing the corresponding metal films in air while the ZnO films are prepared by evaporating ZnO itself, followed by thermal annealing in air to achieve stoichiometry. The films are characterized by x-ray diffraction, scanning electron microscopy and optical methods.

3.1.1. Microstructure and structure ZnO thin films

The X-ray diffraction (XRD) patterns of the as-deposited films taken at two different locations are shown in figure 3.1(a) and (b). The corresponding FESEM images are displayed as insets. It is observed that the as-deposited films are a combination of Zn and ZnO. There is one peak assigned to the (0 0 2) plane of the wurtzite ZnO and two peaks that are assigned to the (0 0 2) and (1 0 1) planes of Zn metal. The surface morphology is very non-uniform with spherical particles of diameter in the order of 50 -70 nm (figure 3.1(a)) and densely packed spherical particles of diameter in the order of 40 -50 nm, superposed on which are smaller particles of 10-30 nm diameter in figure 3.1(b).

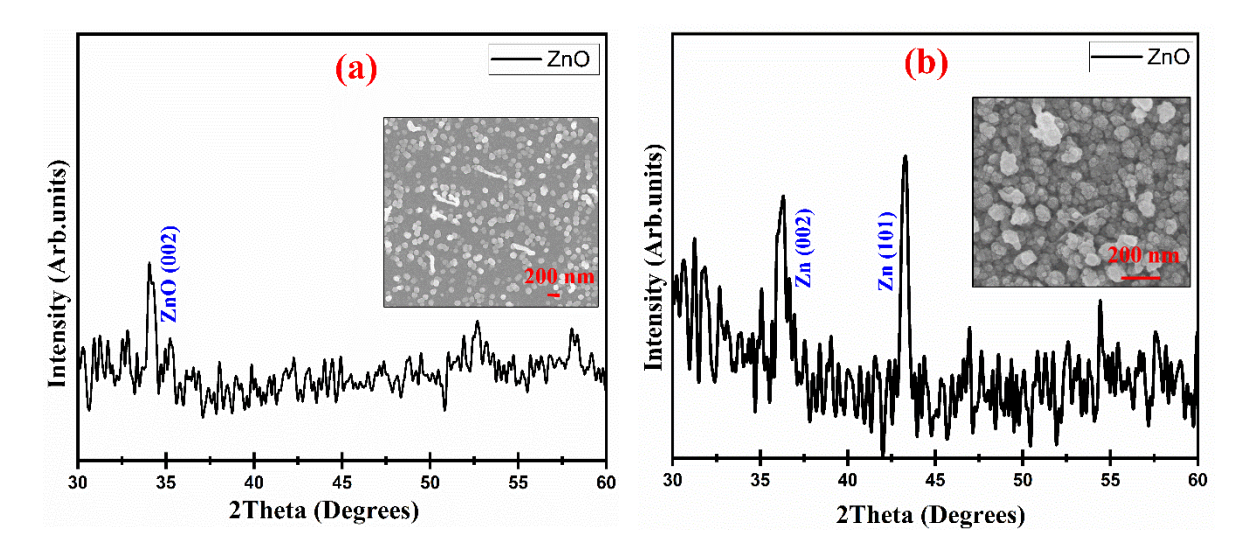


Figure 3.1: XRD patterns and FE-SEM images of ZnO seed layers (a) and (b) as-deposited

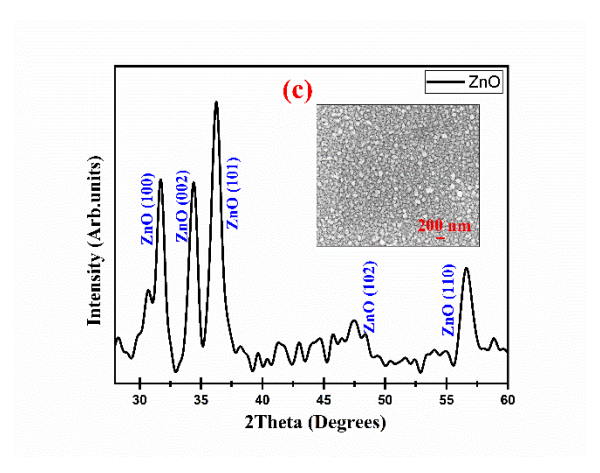


Figure 3.1: XRD patterns and FE-SEM images of ZnO seed layers (c) annealed at 400 °C for 2 hours.

Since the films were a mixture of metal and metal oxide, they were annealed at 400 °C for 2 hours to completely oxidize them. The XRD pattern in figure 3.1 (c) shows that, after annealing, peaks related to metallic Zn disappear and only the diffraction peaks relating to the (100), (002), (101), (102) and (110) planes of wurtzite ZnO remain. All diffraction peaks are indexed to ZnO with a hexagonal wurtzite crystal structure using JCPDS file no: 80-0074. The ZnO surface microstructure is more uniform with densely packed spherical particles in the 30-50 nm diameter range. The ZnO crystal structure does not exhibit a preferential orientation. This optimized protocol to obtain stoichiometric ZnO was used in all further experiments.

The effect of different thickness of seed layers, from 100-400nm, deposited by thermal evaporation under high vacuum on structure and microstructure is presented next. The surface microstructure of ZnO thin films of approximate thickness 100 nm, 150 nm, 200 nm, and 400 nm is shown in Figure 3.2 to 3.5. The microstructure of the 100 nm thickness ZnO at different magnifications shown (Figure 3.2 (a-c) consists of densely packed spherical particles of diameter 30-50 nm.

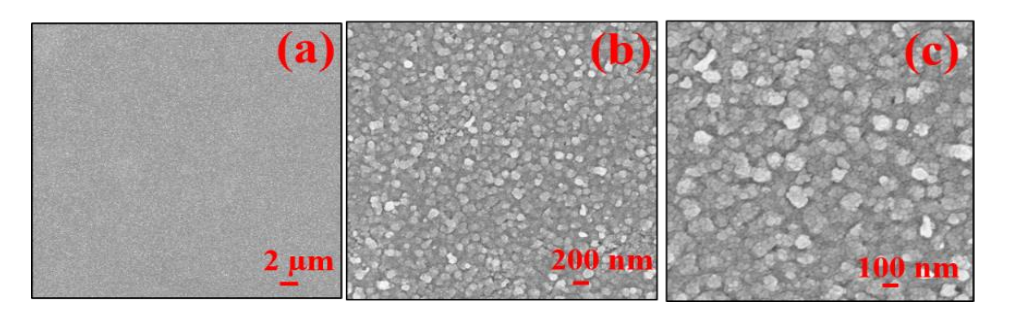


Figure 3.2 (a-c): FE-SEM images of 100 nm ZnO thin film at different magnifications.

The edges of the spherical particles are sharpened to give various non-spherical shapes when the thickness is increased to 150 nm (figure 3.3(a-c)).

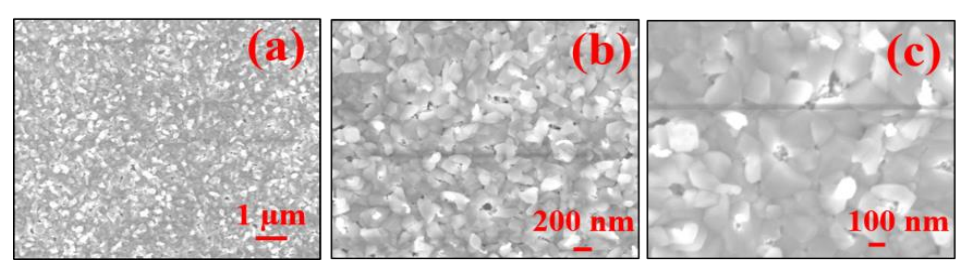


Figure 3.3 (a-c): FE-SEM images of 150 nm ZnO thin film at different magnifications.

Few of the particles are elongated in one direction providing rectangular shapes. The elongation of these particles extended out of the plane's surface, resulting in three-dimensional (3D) microstructures. Due to this 3D arrangement, micron-sized voids are developed at the interfaces. These particles transform into large spherical particles of 200 nm size by increasing the thickness of the films to 200 nm (figure 3.4(a-c).

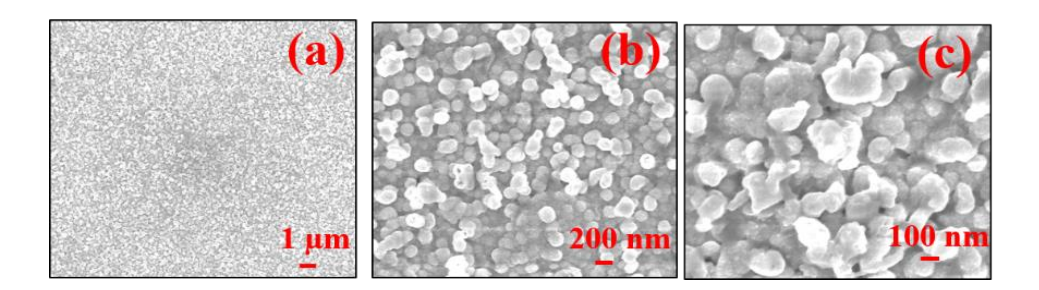


Figure 3.4 (a-c): FE-SEM images of 200 nm ZnO thin film at different magnifications

This is accompanied by a decrease in packing density of the particles, as evidenced by the voids between them. The 400 nm thickness film has an entirely different microstructure. The surface comprises twisted flakes of length 30-50 nm and width of 400-500 nm that is vertically oriented (figure 3.5(a-c).

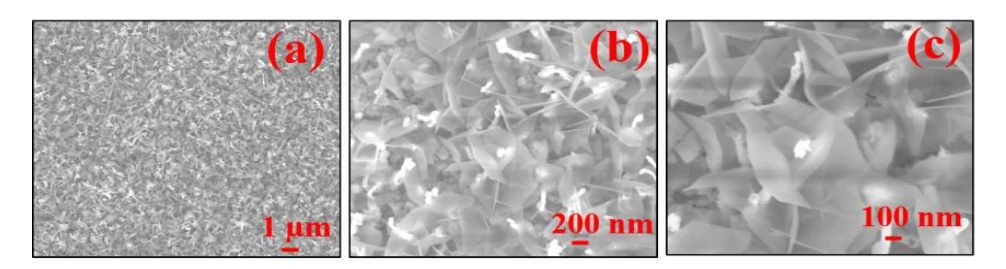


Figure 3.5 (a-c): FE-SEM images of 400 nm ZnO thin film at different magnifications

Thus, the ZnO film thickness increase has brought a profound change on the surface microstructural development and the packing density of the evolved microstructures. The contribution of surface roughness to the evolution of the nanowires cannot be neglected [254]. It would thus appear that variation in thickness causes changes in surface microstructure and roughness of the ZnO films. Apart from this, smaller grain size may lead to nanowires with smaller dimensions [255-256].

The phase formation and crystallographic information of the thin films investigated using XRD are presented in Figure 3.6(a-d). All diffraction peaks are indexed to ZnO with a hexagonal wurtzite crystal structure using JCPDS file no: 80-0074. This observation suggests that the changes in the thickness of ZnO thin films has modified the microstructure, but remained structurally phase pure. No un-reacted metallic Zn is observed. The prominent diffraction peaks at 2θ =31.64, 34.12, 36.2 and 56.6 ° are indexed to (100), (002), (101) and (110) planes of hexagonal wurtzite phase of ZnO respectively.

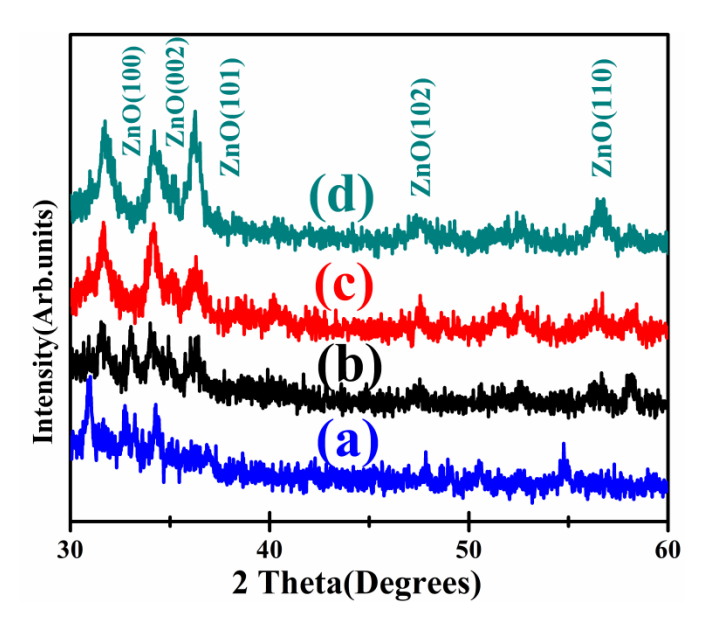


Figure 3.6: X-ray diffraction patterns of ZnO seed layers of (a) 100 nm, (b) 150 nm, (c) 200 and (d) 400 nm thickness respectively.

The very diffuse nature of peaks for the 100 nm samples can be attributed to the nano-crystalline nature of the films. There is a slight decrease in the relative intensities of the different ZnO peaks indicating the change in the preferred orientation of the ZnO film. In the 200 nm film, there is a relative drop in the intensity of the (101) peak while, for the 400 nm film, there is an increase in

the peak intensity of the (110) plane. Significantly, there are no peaks related to metallic Zn, indicating that the films are stoichiometric ZnO (within the detection limits of XRD). It is known that crystallization of ZnO thin films prepared by thermal evaporation either from a Zn or ZnO source requires post-deposition heat treatment [257]. The films in the present case are also nanocrystalline with a crystallite size of 20-25 nm, as estimated from Scherrer's formula. In addition, there is a shift in the peak positions to higher 20 values with an increase in thickness, indicating a change in the residual stresses within the ZnO films at different thicknesses. These residual stresses are likely to originate from a mismatch in the thermal expansion coefficient of ZnO and glass substrate. Liu et al. [258-259] attributed this deviation to surface effects which cause lattice deformations and reduction in the lattice parameter. This could also be the reason for the observed variations in microstructures as a function of thickness.

It is evident that the 100 nm ZnO film, thus, has a comparatively smooth surface, densely packed spherical nanostructures, and nano-crystalline nature. Based on these observations and literature mentioned above, it was inferred that the 100 nm ZnO film would be optimal in providing the nucleating sites for developing vertically aligned ZnO based nanostructural-1D entities.

3.1.2. Photoluminescence, Raman spectroscopy, and Optical properties of ZnO seed layers

Photoluminescence and Raman spectroscopy are very powerful probes to investigate the presence of defects in the ZnO films. It is observed that the PL spectra of the different thickness ZnO seed layers, shown in figure 3.7(a), display a prominent peak centred around 550 nm and a comparatively weaker peak centred around 380 nm. It is well documented that ZnO exhibits a near band-edge (NBE) PL peak at around 380 nm and defect related peak at approximately 550 nm. While the UV-NBE is attributed to the exciton–exciton scattering process from the n=1 state to the exciton continuum state (P-line), the emission near 550 nm is generally assigned to oxygen vacancies (V_0) [260].

Significantly, in the present case, UV-NBE is of much lower intensity than the visible-region emission. This would imply the existence of a large volume of defects in the films in the form of oxygen vacancies or Zn interstitials. Another interesting aspect is the decrease in intensity of the defect related peak and corresponding increase in intensity of the UV-NBE with increase in thickness. This phenomenon is accompanied by a red-shift in both peak positions. The red-shift of the band edge emission has been attributed to the Burstein– Moss band filling effect or a band gap shrinkage due to charge transfer from un-reacted Zn to ZnO.

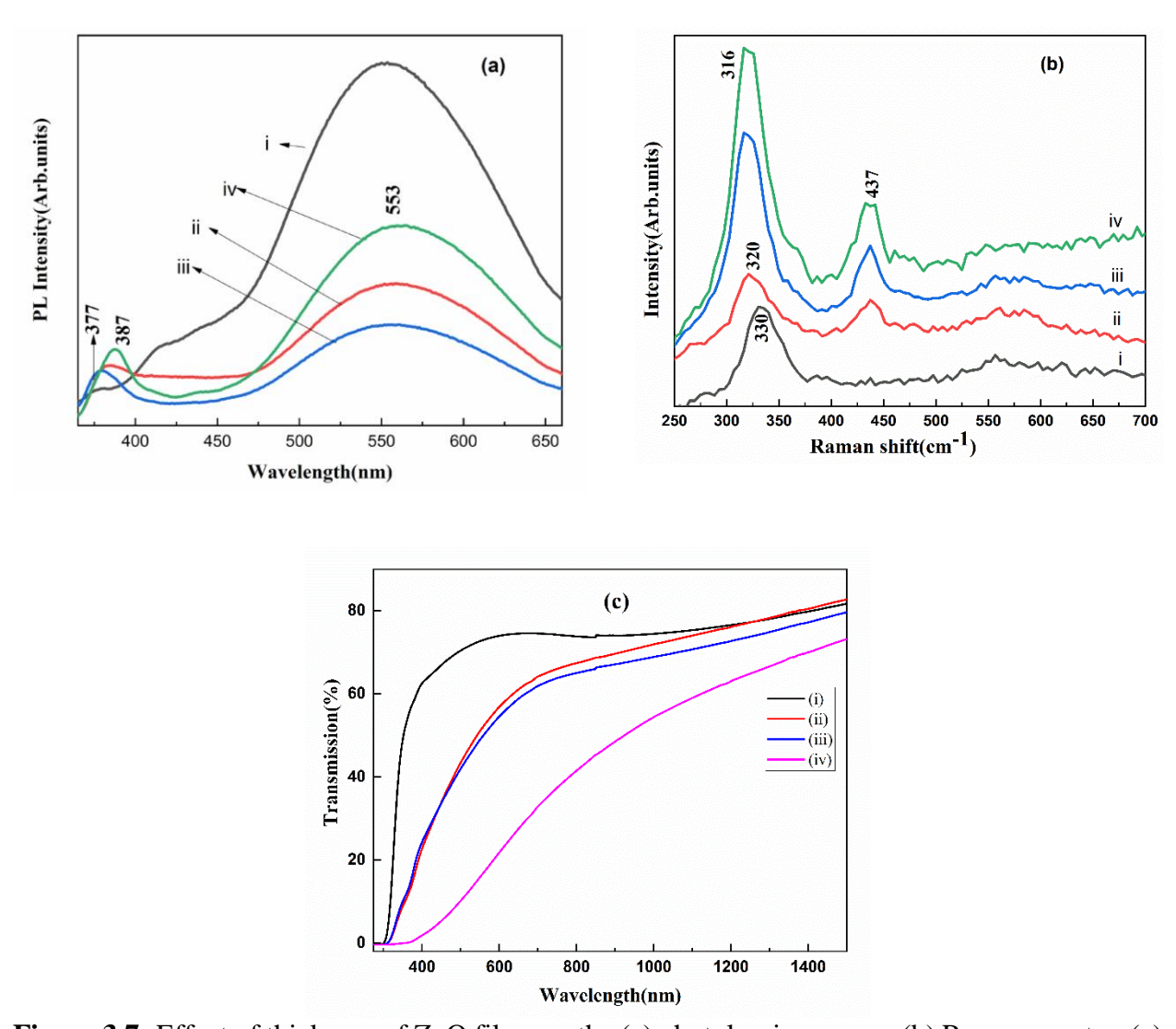


Figure 3.7: Effect of thickness of ZnO films on the (a) photoluminescence, (b) Raman spectra, (c) Optical spectra i=100 nm; ii=150 nm; iii=200 nm; iv=400 nm.

Raman spectra of these films displayed in figure 3.7(b) confirm these observations. There is a strong Raman band centred at 330 cm⁻¹, which blue-shifts (to 316 cm⁻¹) and gets strengthened with the increase in thickness. The most intense Raman band of ZnO, which is known to be centred around 437 cm⁻¹, is very weak for the 100 nm thickness film.

With increase in thickness the intensity of the peak increases and its existence is very evident for the 400 nm thickness film. The relative intensities of the high wavenumber to low wavenumber peaks increases with increase in thickness of the film. The low wavenumber peak at 330 cm⁻¹ has been interpreted earlier as being a second order Raman scattering peak originating from multiphonon scattering processes [261-263]. This is ascribed to the E_2 (high) - E_2 (low) mode of ZnO,

related to the zone boundary phonons, similar to GaN [264]. The presence of these modes in undoped ZnO thin films is unusual, since the majority of the observations on this low wavenumber peak have been in the case of metal-doped ZnO. For example, in Mn doped ZnO there is clear evidence of the intensity of the peak increasing with increased dopant concentration [261]. Multiphonon processes are generally linked to the presence of disorder (such as defects and vacancies) in the material, which allows phonons of different symmetries to be scattered leading to the enhancement of their peak intensity. The blue-shifting of this peak can be attributed to increase in strain at the interface between the film and substrate due to heat treatment [264-266]. Thus, the PL and Raman spectroscopy observations indicate the existence of defects in the thin films used to support the nanowire arrays.

The optical transmission spectra, in figure 3.7 (c), revealed that ZnO seed layers transmission in the wavelength range of 300–1500 nm is 60% - 80%. The transmission of ZnO nanostructures increases as the thickness of seed layers decreases. The band gap, as a consequence of increased thickness, decreases from 3.9 eV to 3.4 eV. The transmission spectrum of these different thicknesses of ZnO seed layers demonstrates a high absorbance and sharp absorption shoulder in wavelengths between 300 and 400 nm (UV region). This is due to the quantum confinement effect of the ZnO nanostructures [267-268].

The picture that emerges from these studies is that the ZnO thin films show a large density of defects at lower thickness, which decrease as the thickness is increased. The origin of these defects can be traced to the process used for preparation of thin films, i.e. thermal evaporation. Thermal evaporation of high melting point materials such as ZnO induces non-stoichiometry in the deposited films [269]. Heat treatment is attempted to reduce defects, which is partially successful as evidenced by the PL and Raman spectra displayed earlier. The 100 nm thickness film is selected for study of HP of ZnO nanostructures due to the fact that the surface had smallest size nanoparticles, which are densely packed. It is, however, seen that density of defects on the surface of the films, as evidenced by PL and Raman spectra, is high.

3.2. Microstructure and structure of Indium (In) and Tin (Sn) seed layers

The morphology of the seed layers plays an important role in determining the growth patterns of the ZnO structures grown on top of them. The surface of the 10 nm thickness as-deposited In (InA) film shows large agglomerates of 100 nm diameter superposed on which are smaller particles of

10-20 nm diameter (figure 3.8(a-c)). The annealing of the In seed layers (InO) at 200°C for 2hrs (figure 3.8(d-f)) results in a more uniform morphology, consisting of 30 nm particles.

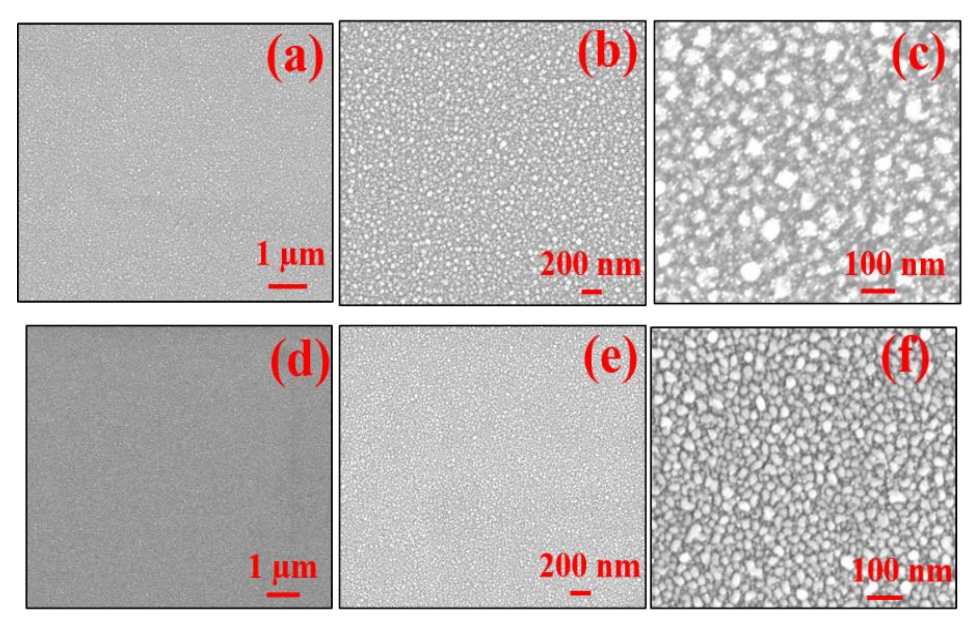


Figure 3.8: FE-SEM images of the top surface of the 10 nm InA film (a-c), InO film (d-f) at different magnifications.

In the case of Sn seed layers the as deposited films (SnA) display large cuboidal particles (Figure 3.9(a-c)). Annealing of the Sn seed layers (SnO) at 300°C for 2hrs resulted in breaking up of these particles into spherical agglomerates of the order of 30-50 nm (figure 3.9(d-f)).

The surface of the 20 nm thickness as deposited In (InA) film shows large agglomerates of 80-100 nm diameter superposed on which are smaller particles of 10-20 nm diameter (figure 3.10 (a-c)). The annealing of the In seed layers (InO) at 200°C for 2hrs (figure 3.10 (d-f)) results in a more uniform morphology, consisting of 20-30 nm particles. In the case of Sn seed layers the as deposited films (SnA) display large cuboidal particles (figure 3.11(a-c)).

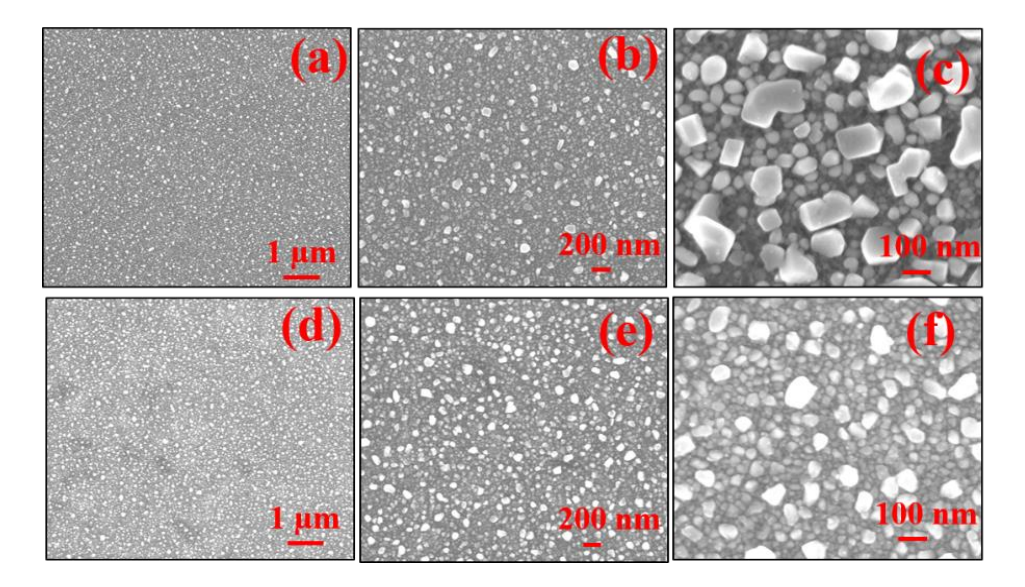


Figure 3.9: FE-SEM images of the top surface of the 10 nm SnA film (a-c), SnO film (d-f) at different magnifications.

Annealing of the Sn seed layers (SnO) at 300°C for 2hrs resulted in breaking up of these particles into spherical agglomerates of the order of 30-50 nm (figure 3.11(d-f)).

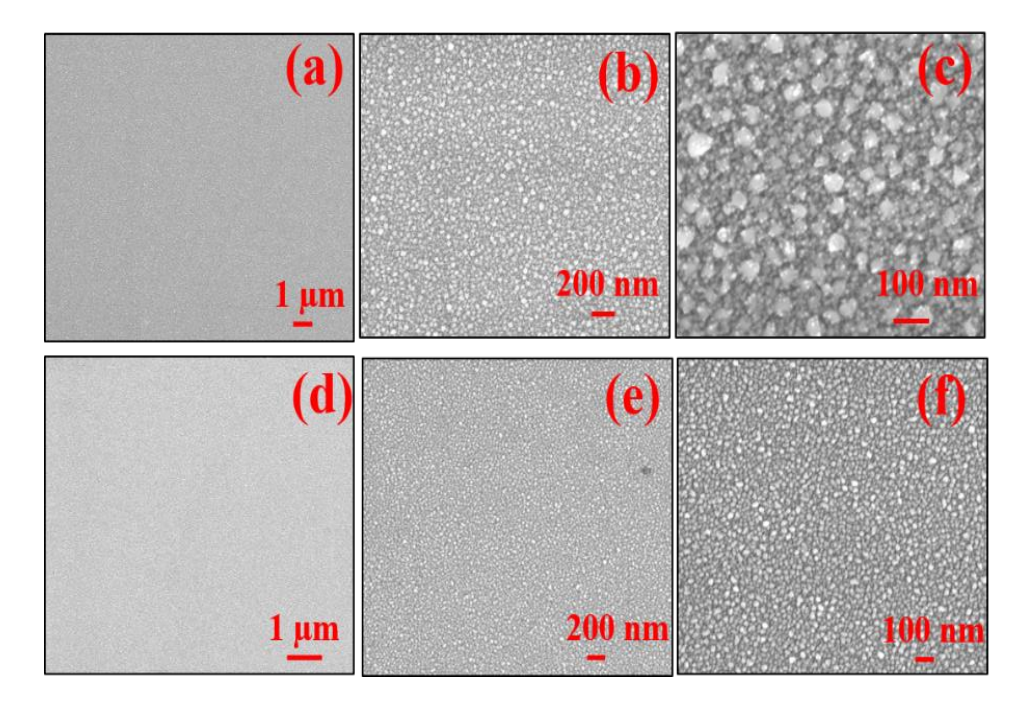


Figure 3.10: FE-SEM images of the top surface of the 20 nm InA film (a-c), InO film (d-f) at different magnifications.

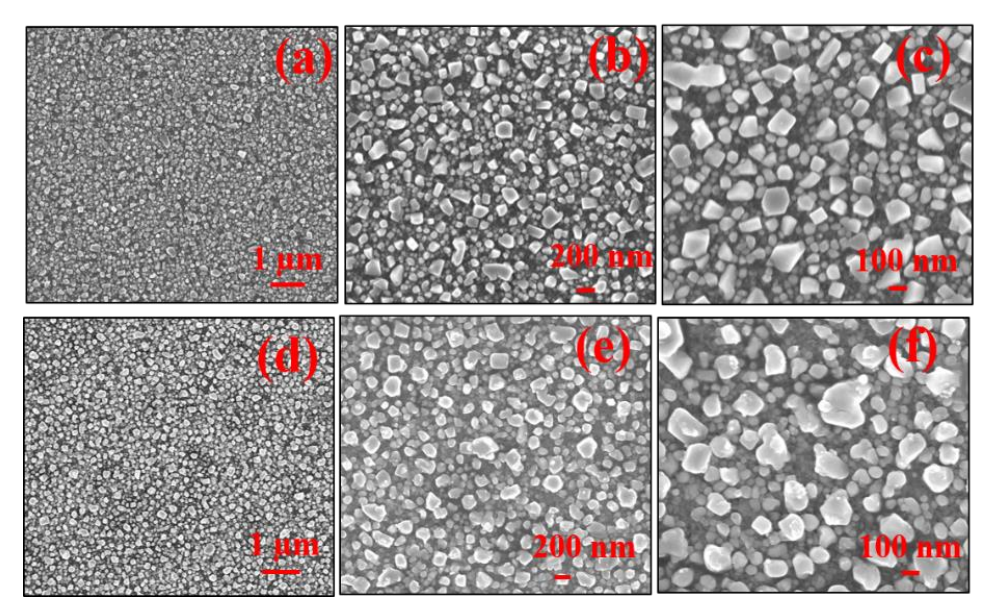


Figure 3.11: FE-SEM images of the top surface of the 20 nmSnA film (a-c), SnO film (d-f) at different magnifications.

The surface of the 30 nm thickness as deposited In (InA) seed layers shows large agglomerates of 80-100 nm diameter superposed on which are smaller particles of 10-20 nm diameter (figure 3.12(a-c)). The annealing of the In seed layers (InO) at 200°C for 2hrs (Figure 3.12(d-f)) results in a more uniform morphology, consisting of 10-20 nm particles.

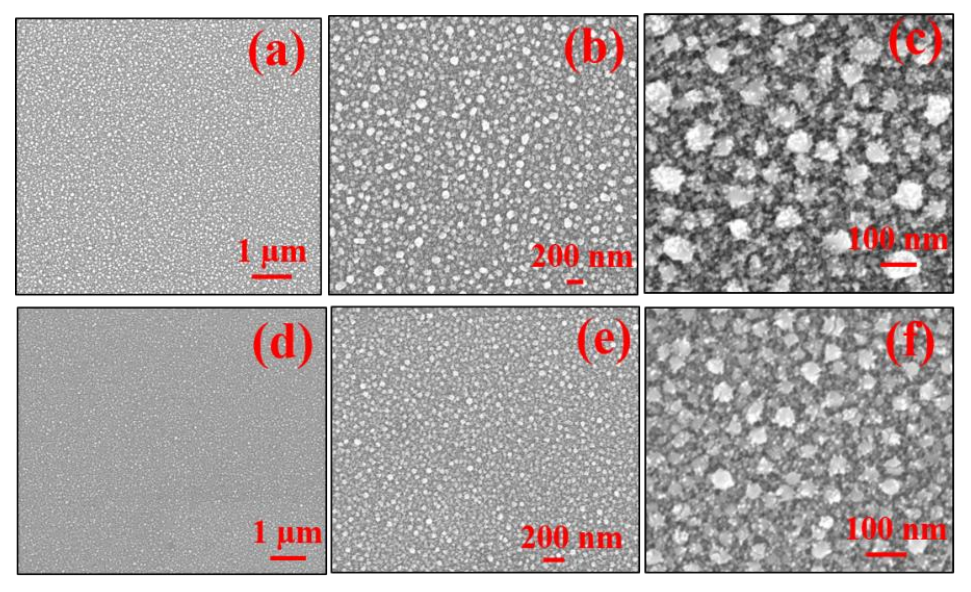


Figure 3.12: FE-SEM images of the top surface of the 30 nm InA film (a-c), InO film (d-f) at different magnifications.

In the case of Sn seed layers the as deposited films (SnA) display large cuboidal particles with 100 nm size (figure 3.13(a-c)) and superposed on which are smaller particles of 30-50 nm diameter. Annealing of the Sn seed layers (SnO) at 300°C for 2hrs resulted in breaking up of these particles into spherical agglomerates of the order of 20-30 nm (figure 3.13(d-f)).

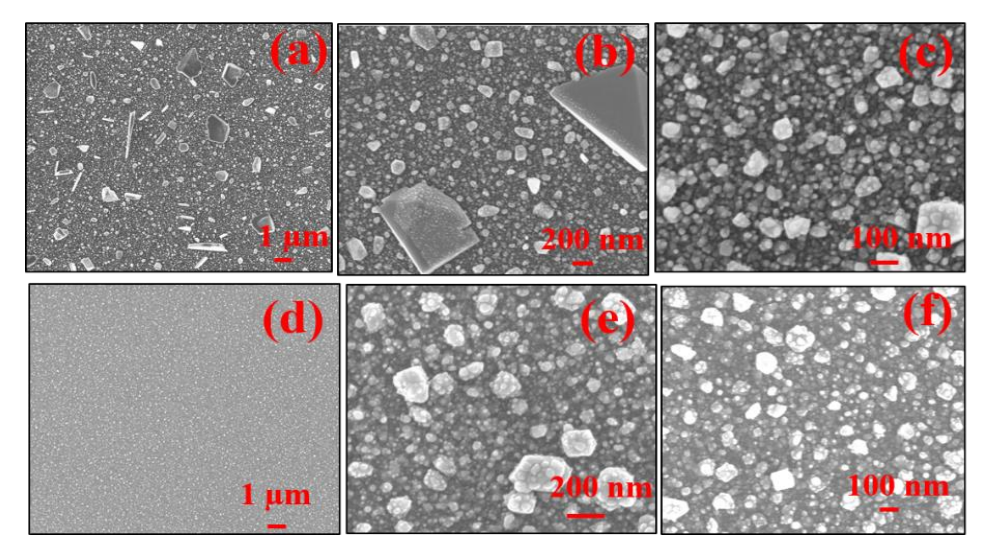


Figure 3.13: FE-SEM images of the top surface of the 30 nm SnA film (a-c), SnO film (d-f) at different magnifications.

The surface of the 40 nm thickness as deposited In (InA) seed layers shows large agglomerates of 100-120 nm diameter superposed on which are smaller particles of 20-30 nm diameter (figure 3.14(a-c)). The annealing of the In seed layers (InO) at 200°C for 2hrs (figure 3.14(d-f)) results in a more uniform morphology, consisting of 80-100 nm particles.

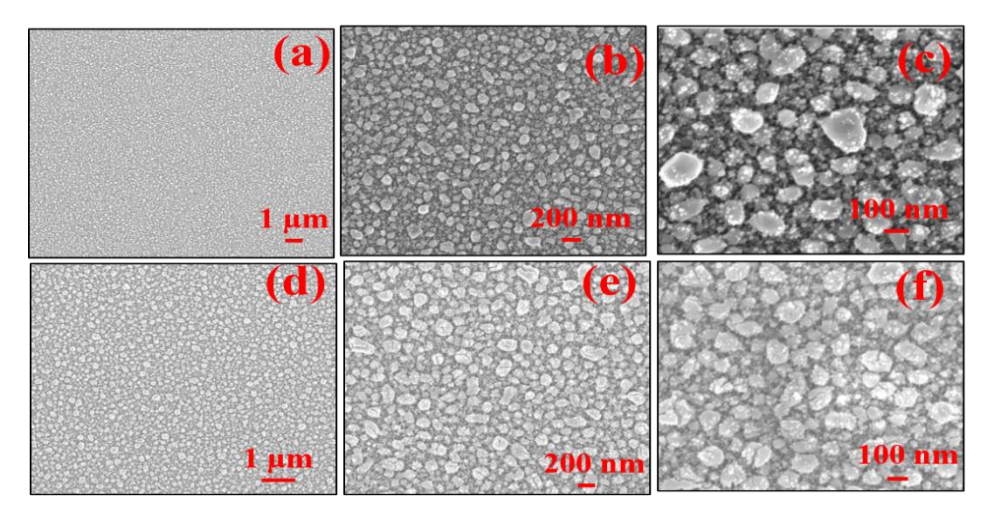


Figure 3.14: FE-SEM images of the top surface of the 40 nm InA film (a-c), InO film(d-f) at different magnifications.

In the case of Sn seed layers the as deposited films (SnA) display large cuboidal particles with 100-150 nm size (figure 3.15(a-c)) and superposed on which are smaller particles of 30-50 nm diameter. Annealing of the Sn seed layers (SnO) at 300°C for 2hrs resulted in breaking up of these particles diameter 100 nm and superposed spherical agglomerates of the order of 20-30 nm (figure 3.15(d-f)).

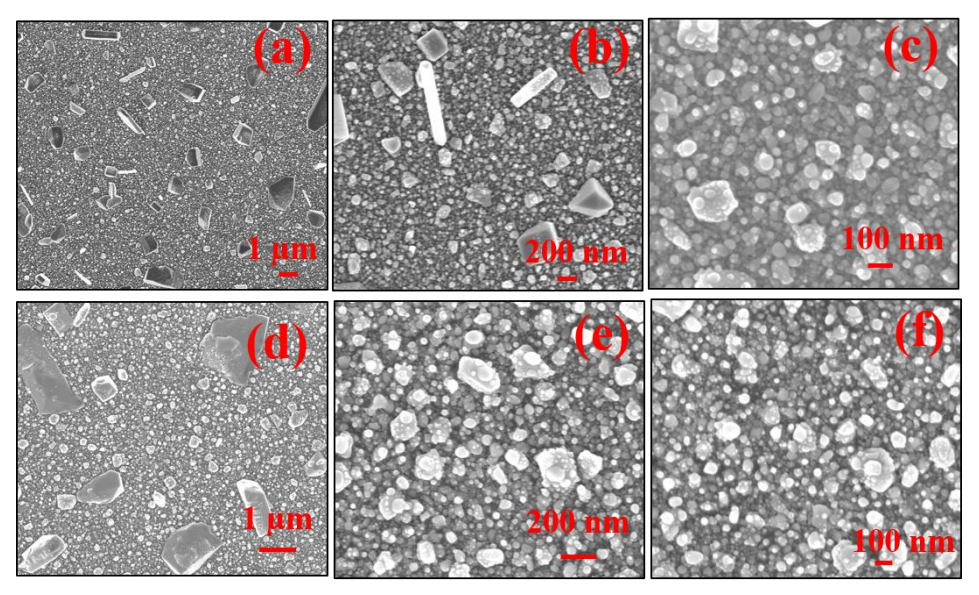


Figure 3.15: FE-SEM images of the top surface of the 40 nm SnA film (a-c), SnO film (d-f) at different magnifications.

Similarly, in the case of 50 nm thickness as deposited In (InA) seed layers shows large agglomerates of 120-150 nm diameter superposed on which are smaller particles of 20-30 nm diameter (figure3.16(a-c)). The annealing of the in seed layers (InO) at 200°C for 2hrs (figure 3.16(d-f)) results in a more uniform morphology, consisting of 80-100 nm particle diameter superposed on which are smaller particles of 20-30 nm.

In the case of Sn seed layers the as deposited films (SnA) display large cuboidal particles with 200-300 nm size (figure 3.17(a-c)) and superposed on which are smaller particles of 60-80 nm diameter. Annealing of the Sn seed layers (SnO) at 300°C for 2hrs resulted in breaking up of these particles into spherical agglomerates of the order of 30-50 nm (figure 3.17(d-f)). The phase formation and crystallographic information of the In and Sn seed layers investigated using XRD are displayed in figure 3.18 ((a)-(b)). The crystallite size 40 nm in InA and 32 nm in InO seed layers.

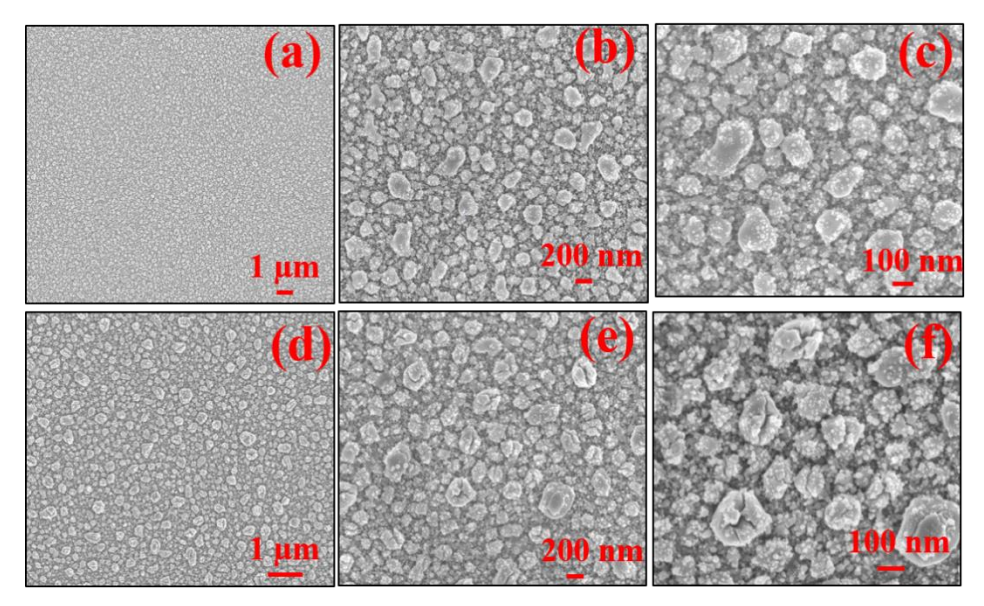


Figure 3.16: FE-SEM images of the top surface of the 50 nm InA film (a-c), InO film (d-f) at different magnifications.

Similarly, in the case of SnA and SnO the crystallite size order of 60 nm and 41 nm. The more interesting observation was that the strain was tensile in nature, on all the seed layers.

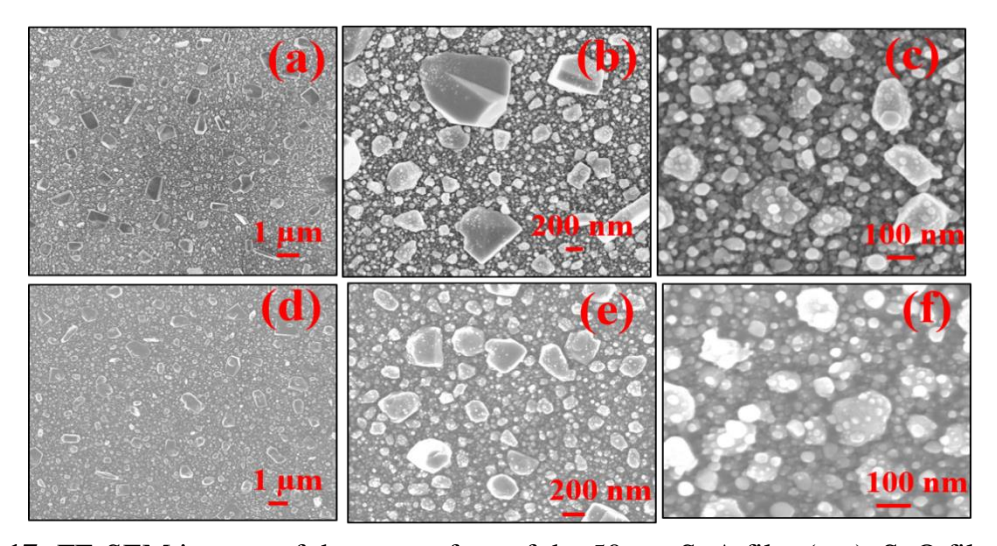


Figure 3.17: FE-SEM images of the top surface of the 50 nm SnA film (a-c), SnO film (d-f) at different magnifications.

Both In and Sn crystallize in the body centred tetragonal structure with lattice parameters of a=b= 3.25Å, c= 4.94 Å and a=b= 5.83Å c= 3.18 Å respectively.

The rhombohedral form of Indium oxide has a lattice parameter of a=b=c=5.48Å while tin oxide crystallizes in the rutile structure with lattice parameters of a=b=4.75 and c=3.18 Å respectively. Clearly the origin of strain in the ZnO structures is the large lattice mismatch between the seed layers and ZnO.

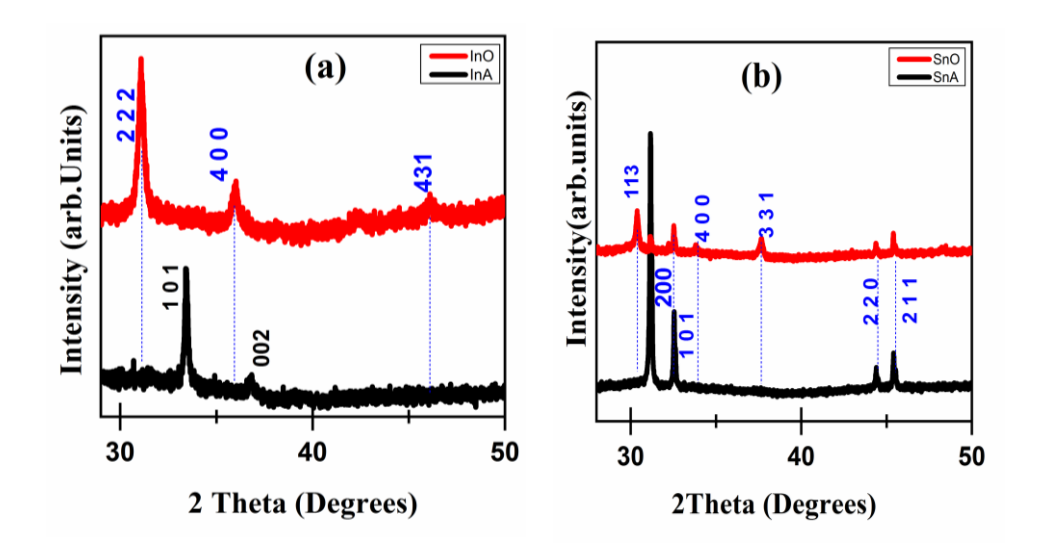


Figure 3.18: X-ray diffraction patterns of (a) InA and InO, (b) SnA and SnO seed layers.

3.2.1. Optical properties of InO and SnO seed layers

The optical transmission spectra, in figure 3.19 (a), revealed that the increase in thickness of InO seed layers has almost 40% - 80% transmission in a wavelength range of 300–1000 nm. The transmission of InO increase as the thickness of seed layers decrease. The band gap, as a consequence of increased thickness, decreases from 3.8 eV to 3.6 eV. In the case of SnO seed layers in figure 3.19 (b), these seed layers has almost 30% - 80% transmission in a wavelength range of 300-1000 nm. The transmission of SnO increases as the thickness of seed layers decreases. The band gap, as a consequence of increased thickness, decreases from 3.9 eV to 3.7 eV.

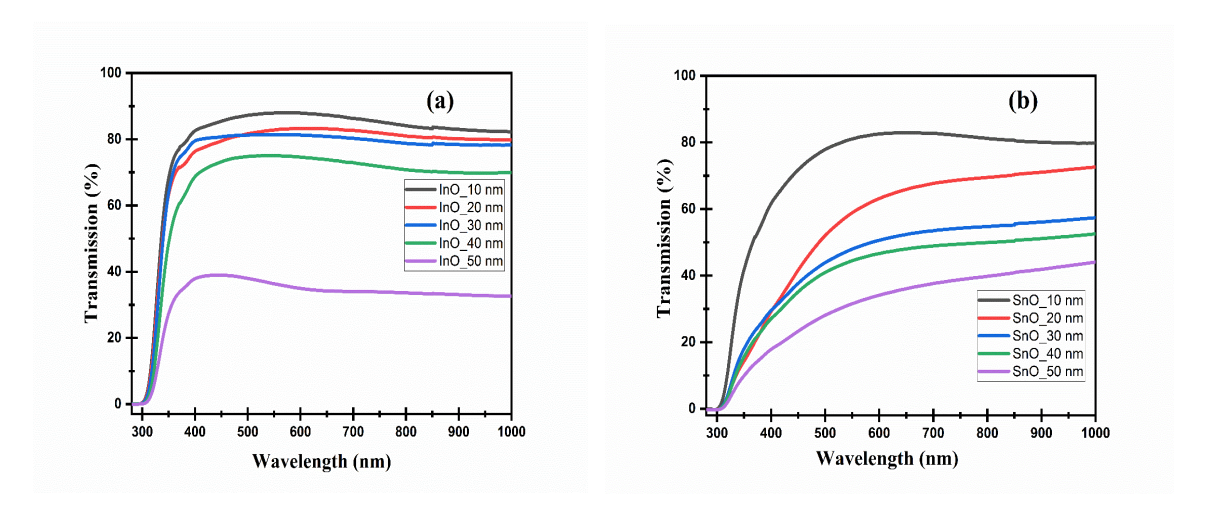


Figure 3.19: Effect of seed layers thickness on transmission spectra of (a) InO and (b) SnO films. It is to be noted that the as-deposited InA and SnA films are metallic and, hence, do not show any transmission.

3.3. Microstructure and structure of gold (Au) seed layer

The final seed layer used in this study are Au thin films of 100 nm thickness deposited by thermal evaporation. The surface microstructure displayed in Figure 3.20 (a-b) consists of densely packed spherical particles of diameter 10-20 nm.

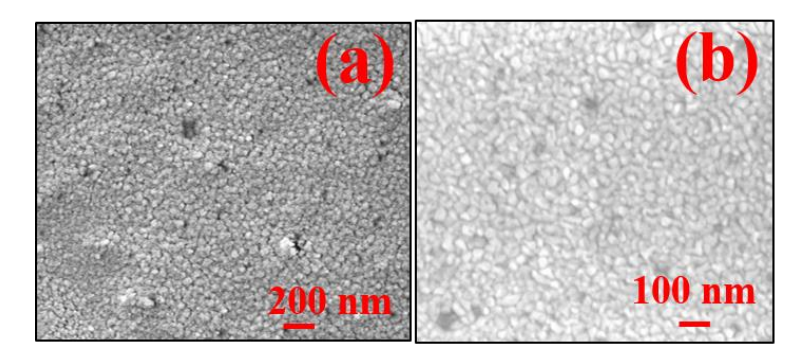


Figure 3.20 (a-b): FE-SEM image of the top surface of the 100 nm Au seed layer at different magnification.

The crystallographic information of the Au seed layer investigated using XRD are displayed in figure 3.21. All the diffraction peaks can be attributed to the face-centered cubic (FCC) structure of Au with peaks at 38.40, 44.59, 64.72, and 77.83°, which could be indexed well to the (111), (200), (220), and (311) planes using JCPDS file no: 04-0784 [270]. In addition, there is a shift in

the peak positions to lower 2-theta values, which indicates the presence of tensile residual stresses owing to mismatch in the thermal expansion coefficient of film and substrate. The crystallite size of the Au film is 40 nm.

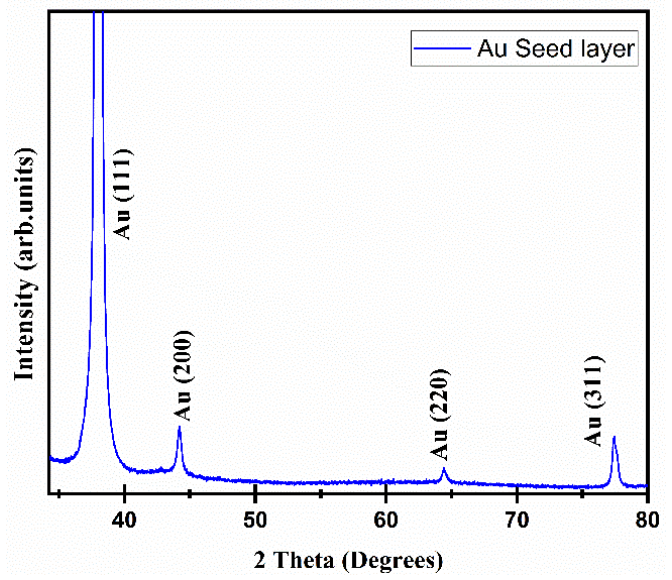


Figure 3.21: X-ray diffraction pattern of the Au seed layer.

3.3.1. Optical properties of gold (Au) seed layer

The optical transmission spectra, in Figure 3.22, reveal an absorption peak at 520 nm due to Localized Surface Plasmon Resonance (LSPR). The presence of LSPR peak indicates the nanocrystalline nature of the Au films.

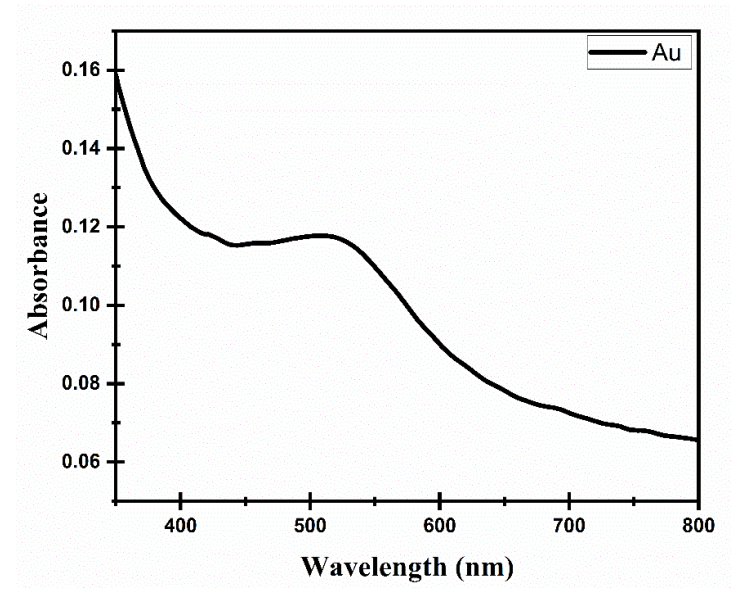


Figure 3.22: Optical absorption spectrum of the Au seed layer.

3.4 Conclusion

In summary, In, Sn and Au metal films and In₂O₃, SnO and ZnO thin films have been prepared on glass substrates by thermal evaporation in vacuum to determine their efficacy as seed layers for the growth of ZnO nanostructures. A thermal oxidation protocol was optimized for the formation of the oxides. Based on the surface microstructure, nature of defects and vacancies as well as nanocrystalline nature, ZnO seed layer thin films of 100 nm thickness is determined to be the optimum for growth of nanostructures. In the case of In and Sn metal films the 10 nm thickness films appear to possess the microstructure and structure required for the growth of ZnO nanostructures. Hence, the corresponding oxides are also optimized as seed layer thin films for the growth of ZnO nanostructures. Finally, the Au thin film of 100 nm thickness is optimized for application as seed layer.

Chapter

4

Comparison of growth of ZnO nanowires/nanorods by conventional and microwave hydrothermal synthesis

Part A of this chapter was published in the paper: Y.Rajesh, S.K.Padhi and M. Ghanashyam Krishna, *ZnO thin film-nanowire array homo-structures, with tunable photoluminescence and optical band gap*, RSC Advances, 10, 25721 (2020).

PART B of this chapter was published in the paper: Y. Rajesh, M.A. Mohiddon, and M.G.Krishna, Shape evolution and optical response of ZnO nanostructures grown on thermally evaporated ZnO and Au thin films. Materials Chemistry and Physics, p.125448 (2021).

Abstract

In this chapter, the growth of ZnO nanowires on ZnO seed layers described in the previous chapter are discussed. There are three objectives of this study: (1) To establish the effect of temperature and duration of the hydrothermal process on the growth patterns of the ZnO nanostructures, (2) examine the role of ZnO seed layers on the growth and optical behavior of ZnO thin film-nanowire arrays and (3) compare the efficiency of the conventional and microwave assisted hydrothermal processes in controlling the growth patterns of the ZnO nanostructures.

The chapter is divided into two parts: Part A deals with conventional hydrothermal processing and in Part B the microwave hydrothermal processing of ZnO nanostructures is described. Since, the nanostructures are grown on ZnO seed layers they are called homo-structures.

In the conventional hydrothermal process, Zinc Acetate and HMTA are used as the precursor media to obtain nanostructures. The study on effect of duration (10 min-10 hrs.) and temperature (90 °C -180 °C) shows that processing at 120 °C for 3hrs is a threshold value realize nanowire arrays with suitable aspect ratios, packing density and uniform distribution across the surface. It is demonstrated that low temperature and short duration are ideal for producing nanowires with diameter < 100 nm, while longer durations and higher temperatures lead to large diameter and long length nanowires. Interestingly, all wires converge to a hexagonal shape with increase in duration or temperature. Optical band gap of the homo-structures is of the order of 3.4 -3.5 eV. Raman and photoluminescence spectra indicate the presence of defects in the films. The thin films exhibit a strong defect related photoluminescence peak centred around 550 nm. The nanowires grown on the films display both the UV-Near band edge peak as well as the defect related peak.

It is also demonstrated that nanowires or nanorods can be obtained on Au seed layers and directly on glass substrates. However, aspect ratios, packing density and distribution across the surface are very poor. Hence, these are not suitable for applications. The reasons for differences in observed growth patterns on different seed layers are discussed.

Part-4A (Conventional Hydrothermal synthesis)

4.1 Background

In this chapter, the growth of ZnO nanowires on ZnO seed layers described in the previous chapter are discussed. There are three objectives of this study: (1) To establish the effect of temperature and duration of the hydrothermal process on the growth patterns of the ZnO nanostructures, (2) examine the role of ZnO seed layers on the growth and optical behavior of ZnO thin film-nanowire arrays and (3) compare the efficiency of the conventional and microwave assisted hydrothermal processes on the growth patterns of the ZnO nanostructures.

The chapter is divided into two parts: Part A deals with conventional hydrothermal processing and in Part B the microwave hydrothermal processing of ZnO nanostructures is described. Since, the nanostructures are grown on ZnO seed layers they are called homo-structures.

In Part A, ZnO thin films of thickness 100-400 nm are deposited by thermal evaporation on glass substrates from a ZnO source. The source to substrate separation and duration of ZnO evaporation are varied and four different thickness ZnO films are achieved. All the films are deposited at RT and subjected to post-deposition heat-treatment in air at 400 °C for 2 hrs.

These ZnO thin film deposited substrates are then introduced into a hydrothermal reactor for growing different ZnO nanostructures. In a typical process run, these films are placed in a 100 mL Teflon-liner stainless steel autoclave containing aqueous solution of 25 mM each of Zinc acetate dehydrate [Zn(O2CCH3)2(H2O)2, 99.0%- ZnAcD] and 25 mM hexamethylenetetramine (HMTA) [(CH2)6N4, 99.0 %]. Experiments are also carried out at 15 mM (ZnAcD, precursor deficient) and 35 mM (ZnAcD, precursor rich) concentrations, maintaining the HMTA concentration at 25 mM. The duration of hydrothermal processing of ZnO (HP) is varied between 10 min to 10 hrs and temperatures are varied from 90 °C to 180 °C.

4.1.1. Effect of precursor concentration on microstructural evolution of ZnO homostructures

The first set of experiments carried out on the ZnO films investigates the role of Zinc Acetate (ZnAcD) precursor at 15, 25, and 35mM concentration maintained at 120 °C for 3 hrs on the microstructure evolution. It is observed that the microstructure consists of nanorods with different densities of packing in each case (figure 4.1(a)-(c)). In the 15 mM case, there is low density of

rods which are hexagonally shaped with a tapered end. As shown in figure 4.1(a), in blue color, the rods have a lateral dimension of 800-1000 nm and axial length up to 10 microns. The diameter of the rods decreases to 50-100 nm and lengths to 2 microns when 25 mM of ZnAcD is used. This is accompanied by a significant increase in the packing density of the rods, which favors increased aspect ratio (AR) and observed flexibility (like a cantilever, nanowires are observed to move back and forth under FE-SEM beam, see figure 4.1(d)), which can be ascribed to the formation of nanowires. When the concentration of (ZnAcD) is further increased to 35 mM, there is again decrease in density of the rods followed by decrease in AR to 7. Thus, it appears that an optimal concentration of 25 mM of both ZnAcD and HMTA is required to realize nanowires that are densely packed.

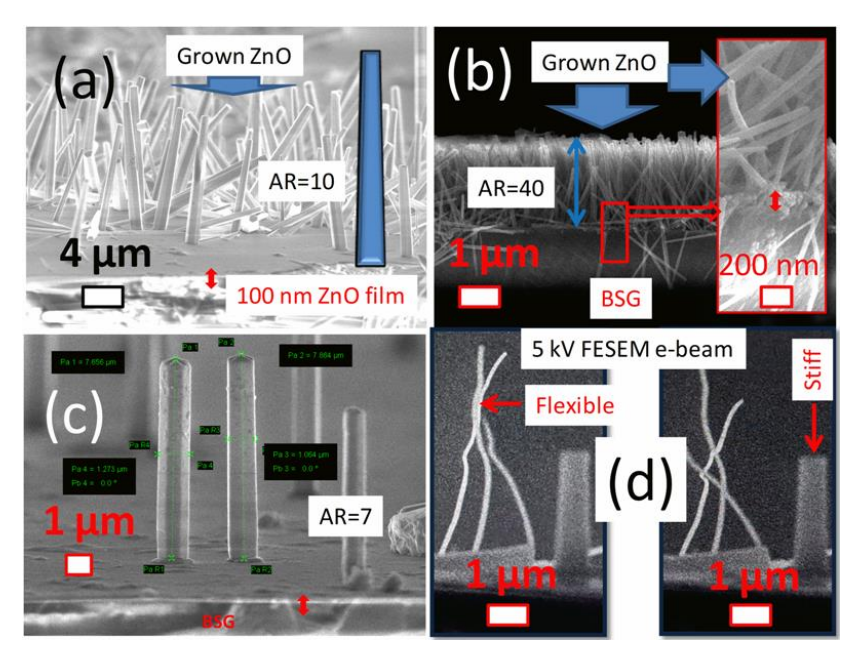


Figure 4.1: Scanning electron microscope images of the hydrothermally processed ZnO on thin film of 100 nm thickness showing the effect of ZnAcD precursor in (a) 15, (b) 25 and (c) 35mM concentration; (d) shows the movement of nanowires under the SEM electron beam. The tapering of the rods is schematically shown in figure 4.1(a) by highlighting one of them in blue.

The next experiment is carried out by replacing HMTA with NaOH and NH₃ solution at the optimal concentration of 25 mM and 120 °C for 3 hrs. Surprisingly, there is no growth of ZnO nanostructures in these two cases. In the case of NaOH (figure 4.2(a-b)), horizontal hexagonal rods that are sparsely distributed are observed over the surface of the ZnO film. In contrast, spherical particles over the ZnO thin film surface are formed when NH₃ solution is used (figure

4.2(c-d)). Clearly, the use of HMTA is more favourable to the formation of vertically oriented ZnO nanorods under these conditions of hydrothermal processing, and 25 mM is the optimal concentration. Although NaOH and NH₃ have been successfully used earlier to synthesize vertically aligned nanowires [271], in the present study, they are not observed.

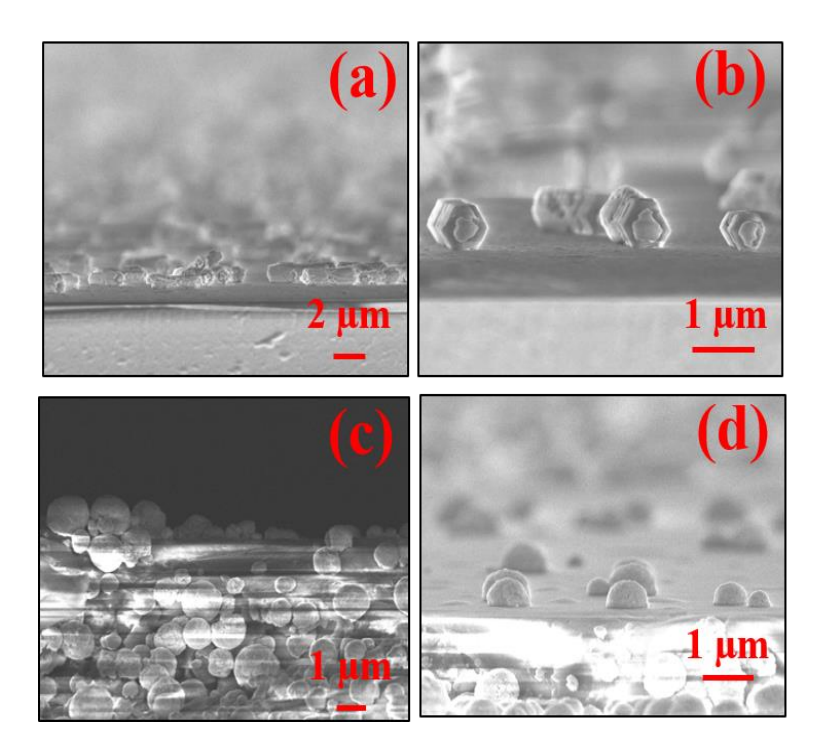


Figure 4.2: Scanning electron microscope images at different magnification showing the effect of (a) NaOH and (b) NH₃ precursor on the growth of hydrothermally processed ZnO clearly demonstrating the lack of nanowire formation.

The difference can be attributed to differences in chemical conditions such as pH, concentrations, temperature, and time of synthesis, all of which play an important role. The results pertaining to HMTA are consistent with the literature, which indicates that the supply of HMTA provides the hydroxyl ions needed for the precipitation reaction. In addition, it acts as a pH buffer. HMTA also attaches to the non-polar facets of ZnO, exposing the polar (001) plane, leading to axial or 1D crystal growth. Until supersaturation is reached, this process leads to suppression in lateral but enhanced axial growth leading to vertical nanowires growth and development [272-274].

4.2. Effect of thickness of ZnO seed layers and duration of synthesis on the growth of nanorods

In this section, the effects of thickness of ZnO seed layers and duration of hydrothermal process on the growth patterns of ZnO nanostructures is presented. In the first part the thickness of the seed layer is fixed at 100 nm (because comparatively smooth surface has good densely packed spherical shape of particles as mentioned in chapter 3) and the process temperature is fixed at 120 °C while the durations are 10, 30, 60, 180, 360, and 600 mins. The FE-SEM images of the nanostructures are shown in figure (4.3 (a)-(f)). For the purpose of this discussion low aspect ratio structures are called nanorods while larger aspect ratio structures are termed as nanowires. Based on this definition, in the case of 10 mins duration, nanorods of length 500-700 nm and diameter 90-100 nm are formed. At 30 mins and 60 mins the length of nanorods is 600-700 nm and 1.3 μ m, respectively, and the diameter of the nanorod is 40-70 nm and 50-60 nm. In the case of 180 mins duration, densely packed nanowires were formed; the average length of nanowires is 2 μ m with a diameter of 50-100 nm, while these values are 2-3 μ m and 100-120 nm nm at 120 °C for 360 mins. When the duration is increased to 600 mins the nanowires transform into hexagonal shaped nanorods with length of 6-8 μ m and diameter of nanowire 900 nm-1 μ m.

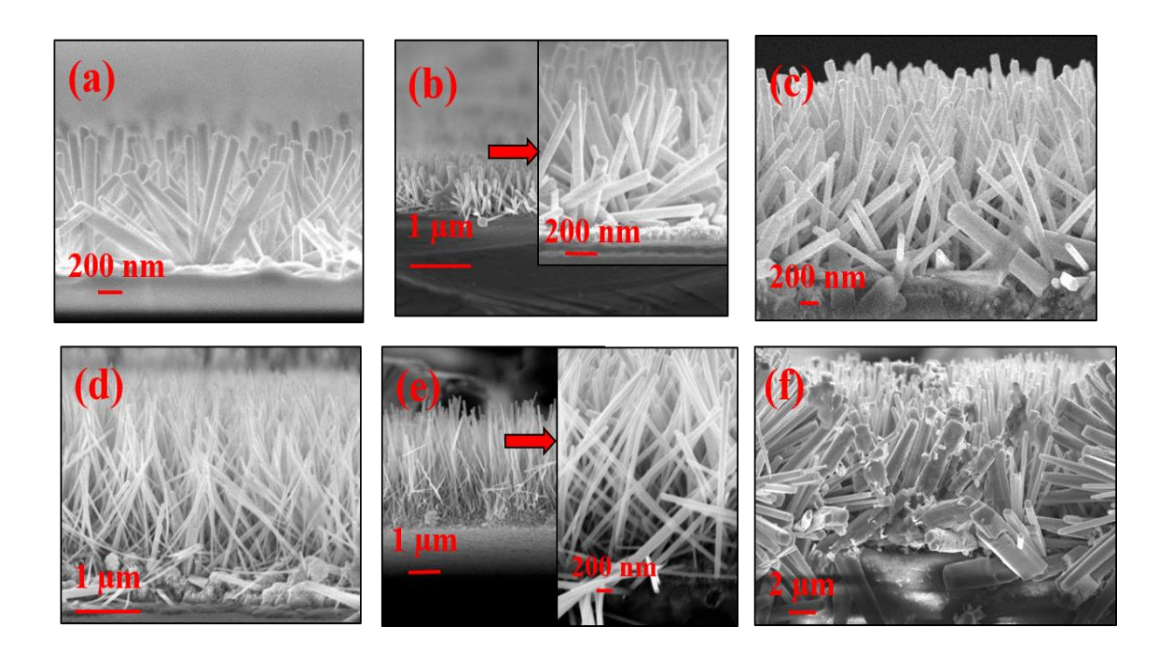


Figure 4.3: Scanning electron microscope cross-section images of hydrothermally processed ZnO on 100 nm thickness ZnO seed layer at 120 °C for (a) 10 mins, (b) 30 mins, (c) 60mins, (d) 180 mins, (e) 360 mins and (f) 600 mins.

The FE-SEM images of the ZnO nanostructures grown on ZnO seed layer thin films thickness of 150, 200 and 400 nm are shown in figure (4.4 (a)-(c)),(4.5(a)-(c)), and (4.6(a)-(c)) respectively. In all cases the temperature is constant at 120 °C while the process durations are 10, 30, and 60 mins.

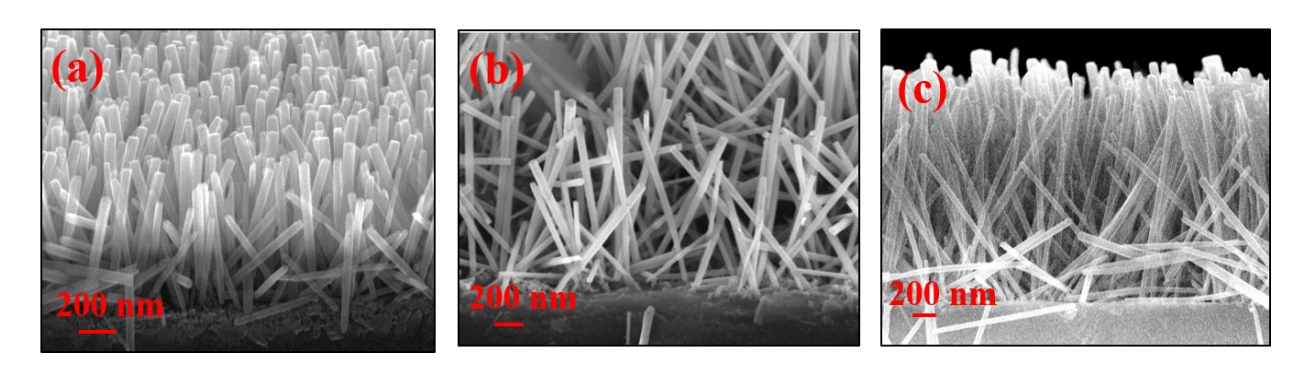


Figure 4.4: Cross-section scanning electron microscope images of ZnO nanostructures at 150 nm thickness of seed layer at 120 °C for (a) 10 mins, (b) 30 mins, (c) 60 mins process duration.

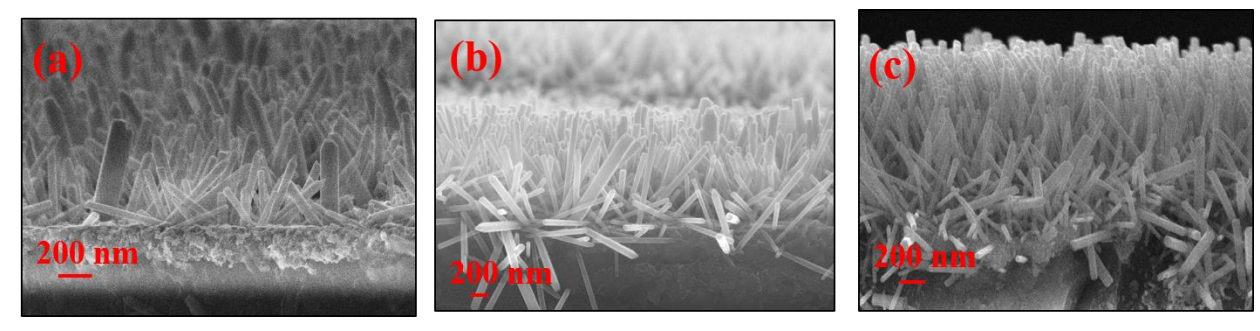


Figure 4.5: Cross-section scanning electron microscope images of ZnO nanostructures at 200 nm thickness of seed layer at 120 °C for (a) 10 mins, (b) 30 mins, (c) 60 mins process duration.

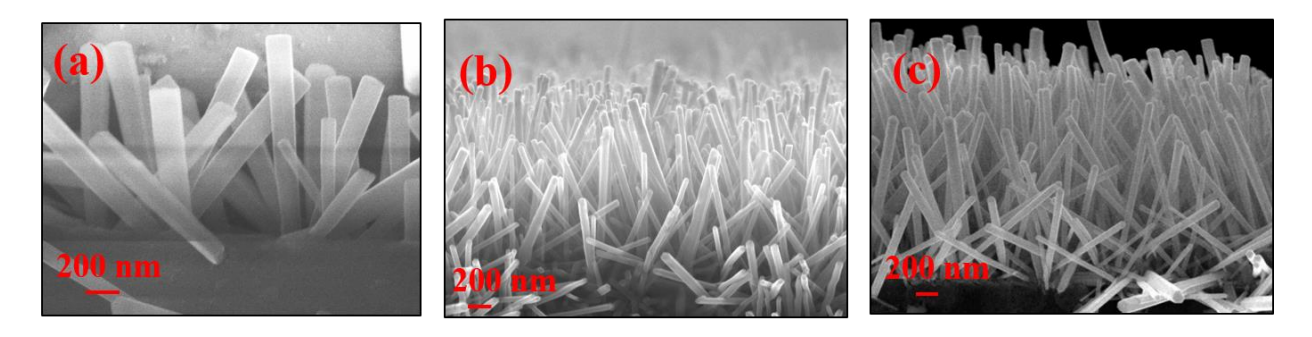


Figure 4.6: Cross-section scanning electron microscope images of ZnO nanostructures at 400 nm thickness of seed layer at 120 °C for (a) 10 mins, (b) 30 mins, (c) 60 mins process duration.

The observations made from the cross-section scanning electron microscope images are summarized in figure 4.7 (a) and (b). It is seen that there is an increase in length and diameter of the rods with the increase in the duration of synthesis on 100 nm thickness films. The insets show the results for the other thicknesses. Significantly, ZnO is nanowires of diameter < 50 nm are observed for 10 min duration of synthesis. Most significantly, aspect ratios (AR) of the order of 10 are achieved for long durations of processing. In summary, a short duration of synthesis is essential for short-length and low-diameter nanowires/rods. An increase in length and diameter can be achieved by increasing the duration of hydrothermal processing.

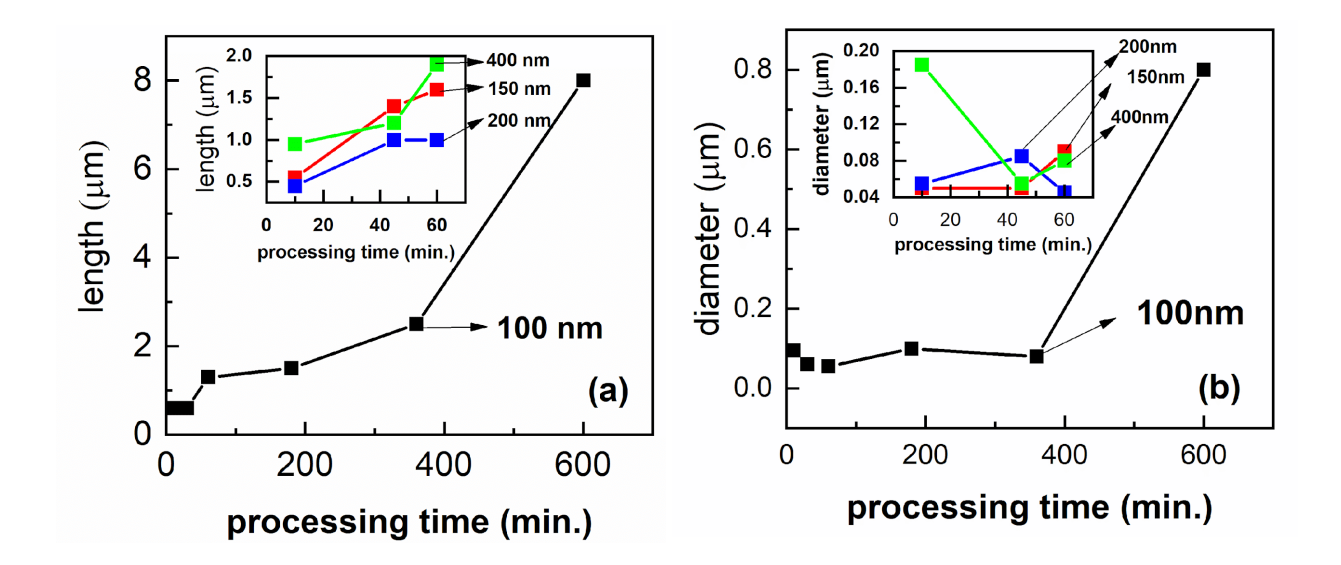


Figure 4.7: Effect of hydrothermal processing time on the (a) length and (b) diameter of the ZnO nanostructures grown on 100 nm thickness ZnO thin films. The insets display the effect of varying ZnO thin film thickness on the length and diameter.

The effect of these conditions on the crystallographic texture is shown in figures 4.8 (a-b). It is evident that crystallization occurs within 10 min of hydrothermal synthesis. At this point the ZnO structures are polycrystalline with crystallite sizes in the range of 20-30 nm. After 60 min of hydrothermal synthesis, the ZnO nanorods on the 100, 150 and 200 nm thin films show preferred c-axis orientation. However, the ZnO nanorods on the 400 nm film do not exhibit any preferred orientation. These microstructural and structural evolutions of the ZnO nanorods indicate that there is a "memory" effect *i.e.* the growth patterns are sensitive to the surface morphology of the ZnO films on which they are grown.

The surface of the 100 nm thin films comprises 50-60 nm sized spherical particles and there is increase in size of particles accompanied by a change in shape (from figure 4.1 (a)-(d)) as the thickness is increased. The porosity also appears to increase with increase in thickness. As stated earlier, surface roughness as a contributing factor cannot be neglected. It would, thus, indicate that the surface of the 100 nm film provides more nucleation sites for the growth of nanorods/wires leading to the higher density and their lower diameter. The number of nucleation sites available for growth decrease with increase in thickness as a result of increase in grain size [255]. It can, thus, be hypothesized that the interfacial free energy (i.e. at the interface between ZnO film and rods) is an important energy barrier that needs to be overcome for the growth of nanowires/rods. This can also be explained within the framework of the Volmer-Weber mechanism, wherein the growth of nanowires on thin films is determined by strain energy minimization at the interface [275].

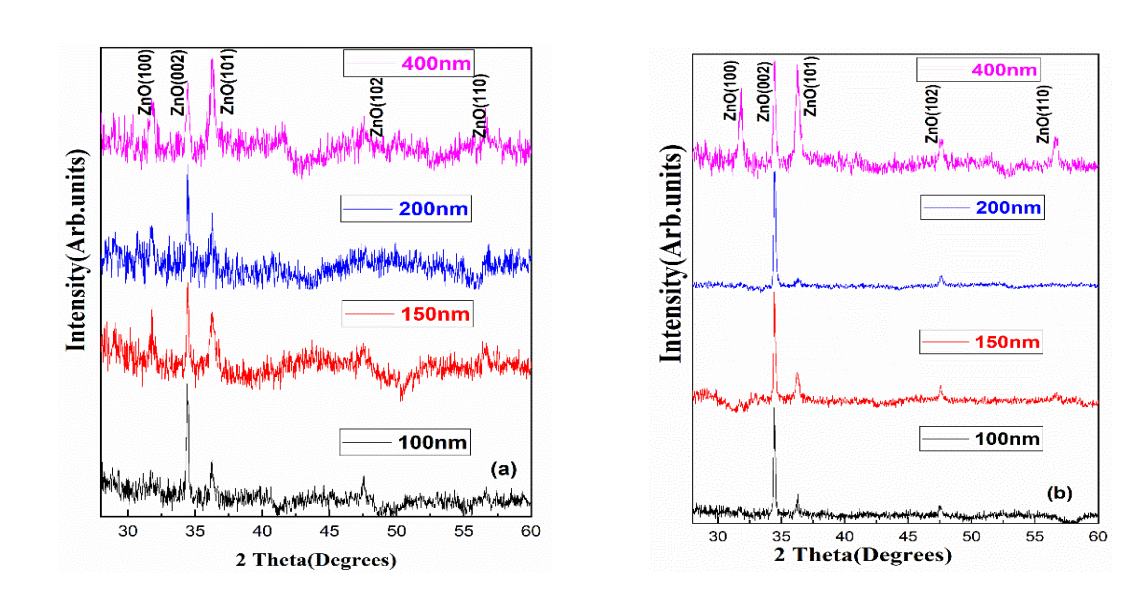


Figure 4.8: X-ray diffraction patterns of hydrothermally processed ZnO at 120 °C for (a) 10 min and (b) 60 min on ZnO thin films of different thickness as indicated.

4.3. Effect of hydrothermal synthesis temperature on the growth of nanorods and wires

The next set of growth experiments are carried out on the 100 nm thickness ZnO films to understand the effect of increasing temperature (between 90 °C to 180 °C) at a constant duration of 3 hrs (figure 4.9 (a)-(d)). Interestingly at 90 °C the growth of nanotubular structures which transform into nanowire-like structures of diameter 50-60 nm, at a temperature of 120 °C (as

discussed in the previous section)is observed. Further increase in temperature to 150 and 180 $^{\circ}$ C, results in slight increase in diameter to 100 nm with lengths up to 2µm, indicating AR of the order of 20. The shape of the rods is more hexagonal than cylindrical at these temperatures. The edges of the rods are very rough, but they are flexible as in the case of the samples synthesized at 120 $^{\circ}$ C. The XRD patterns in all the cases shown in figure (4.10 (a) and (b)) indicate that the ZnO nanorod/wire arrays are polycrystalline in nature with no obvious preferred orientation.

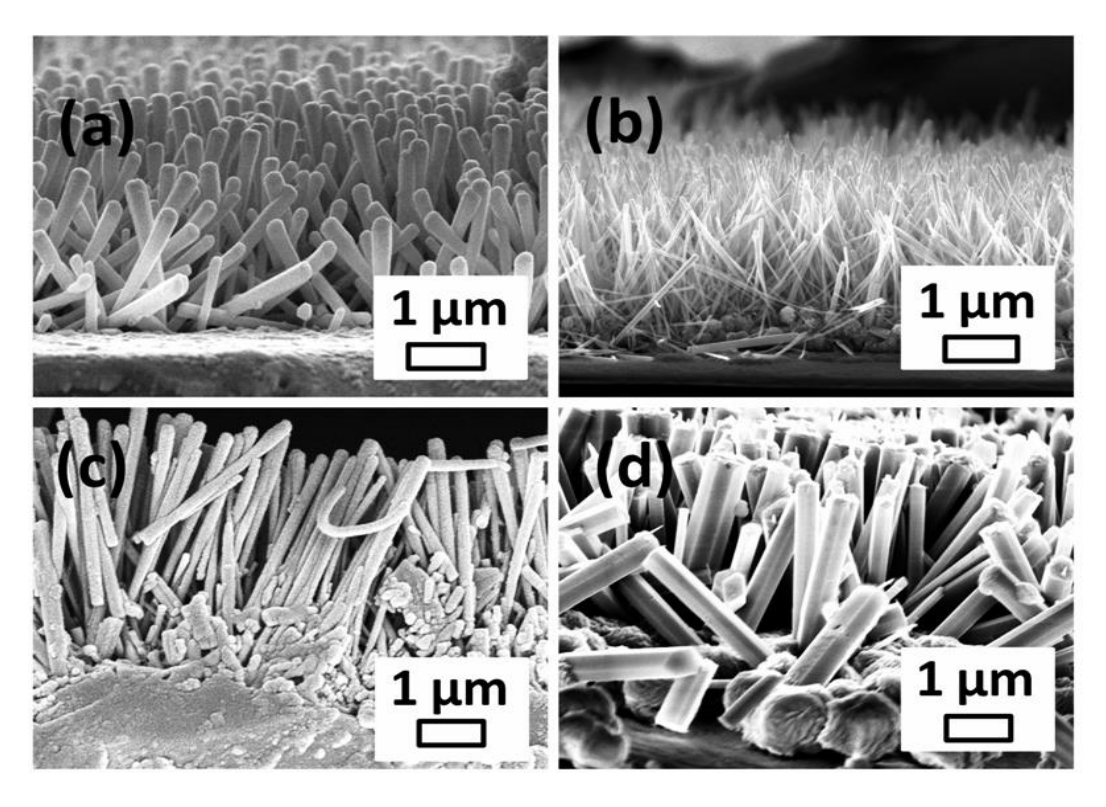


Figure 4.9: Scanning electron microscope images of hydrothermally processed ZnO for a duration of 3 hrs on 100 nm thickness ZnO films at (a) 90 °C, (b) 120 °C, (c) 150 °C and (d) 180 °C.

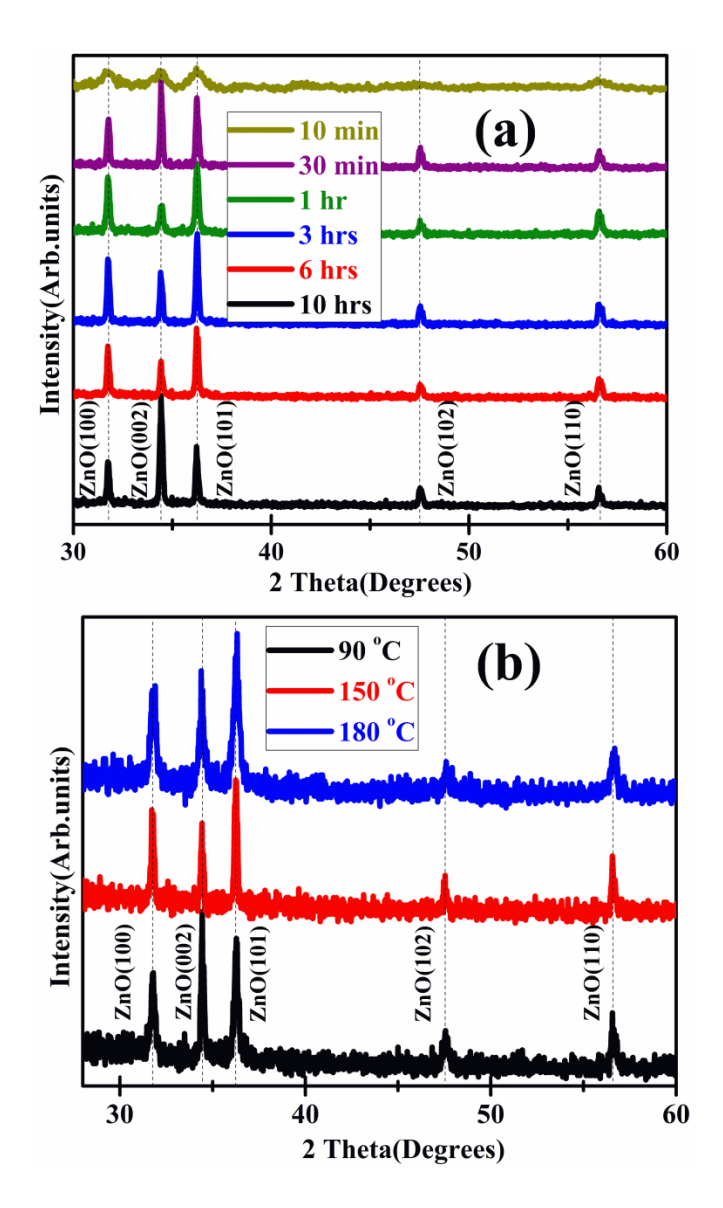


Figure 4.10: X-ray diffraction patterns of hydrothermally processed ZnO on 100nm thickness ZnO film showing the effect of (a) increasing duration of processing at 120°C and (b) increasing temperature at a fixed processing duration of 3hrs.

4.4. Transmission electron microscopy of ZnO nanowires

Transmission electron microscope (TEM) imaging was carried out in a FEI G2-STwin microscope to confirm the formation of nanowires. A typical result in Figure 4.11(a), for the sample processed at 120 °C for 10 mins, shows a lump of ZnO-nanowires in the bright field (BF) micrograph. The selected area diffraction pattern (SAED) aperture of a single nanowire in figure 4.11(b), the High resolution TEM (HR-TEM) in figure 4.11(c) and the spot pattern in the SAED pattern in figure

4.11(d) demonstrate the highly crystalline nature of the nanowires. The theoretically simulated SAED pattern of ZnO using WebEMAPS online software and crystal structure database (ICCD PDF: 36-1451) is shown in Figure 4.11 (d) for comparison and indexing. Incidentally, both patterns show an exact match revealing the ZnO nanowire growth and crystallization in the hexagonal wurtzite structure.

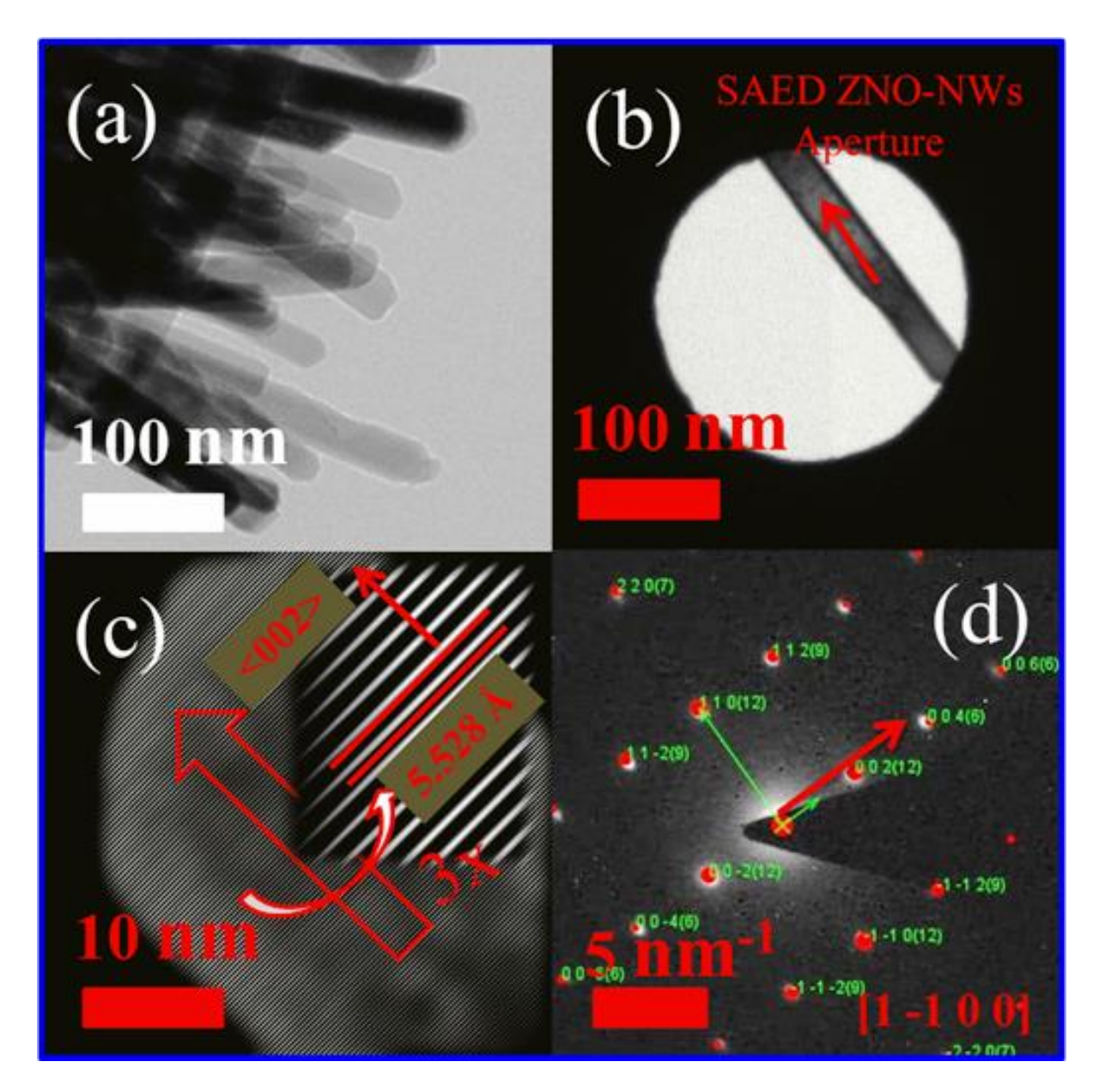


Figure 4.11: (a) TEM Bright field image of the nanowires (b) focus on a single nanowire inside SAED aperture, (c) HRTEM and (d) SAED pattern of the single nanowire.

The HRTEM (see figure 4.11 (c)) images and SAED patterns taken over several such nanowires are in conformity with the bulk XRD result presented earlier.

4.5. Photoluminescence, Raman spectroscopy, and Optical properties of ZnO homostructures

It is pointed out that, since the ZnO nanostructures are grown on ZnO seed layer thin films they are called homo-structures. In this section, the effect of process parameters on the PL, Raman and optical spectra of the nanostructures grown on the 100 nm thickness ZnO film are examined.

ZnO is known to exhibit three PL peaks at wavelengths of 380 nm, 550 nm and 650 nm corresponding to the UV near band-edge emission, green emission and red emission respectively [276-278]. The UV band edge emission is attributed to the exciton–exciton scattering process from the n=1state to the exciton continuum state (P-line). In contrast, the emission near 550 nm is generally assigned to oxygen vacancies (Vo) [260].

The effect of increasing duration of hydrothermal processing at 120 °C on the PL spectra is shown in figure 4.12 (a). As in the case of the thin film (chapter 3), the visible region peak centred around 550 nm is significantly more intense than the ultraviolet-near band edge (UV-NBE) peak at 378(±2) nm after 10 min of hydrothermal process (HP). As the duration of processing increases there is a very strong increase in the intensity of UV-NBE peak, while the intensity of the visible region peak (at 560±2 nm) does not increase that significantly. After 10 hrs of HP, in addition to the peak at 378 nm, there are also two other peaks at 418 and 450 nm signifying the improved crystallinity of the nanowires as well as their hexagonal nature. This is also inferred from the large blue-shift of the defect related peak from 550 nm to 508 nm. Interestingly, when the temperature is increased from 90 °C to 180 °C at a fixed duration of 3 hrs (figure 4.12 (b)), the intensity of the PL peak at 562(±2nm) does not change very significantly upto 150 °C, but shows a decrease thereafter at 180 °C (figure 4.12 (b)). The UV-NBE emission does not dominate over the visible PL, in this case implying that defects are still present and contributing to the PL spectra. This is also evident from the very intense peak at 650 nm in the case of the 90 °C HP sample.

Wurtzite ZnO belongs to C6V (P63mc) space group for which the possible vibrational modes [279-286] are

$$Uopt = A1 + 2B1 + E1 + 2E2$$

where A1, E1, and E2 are Raman active and B1 is Raman forbidden.

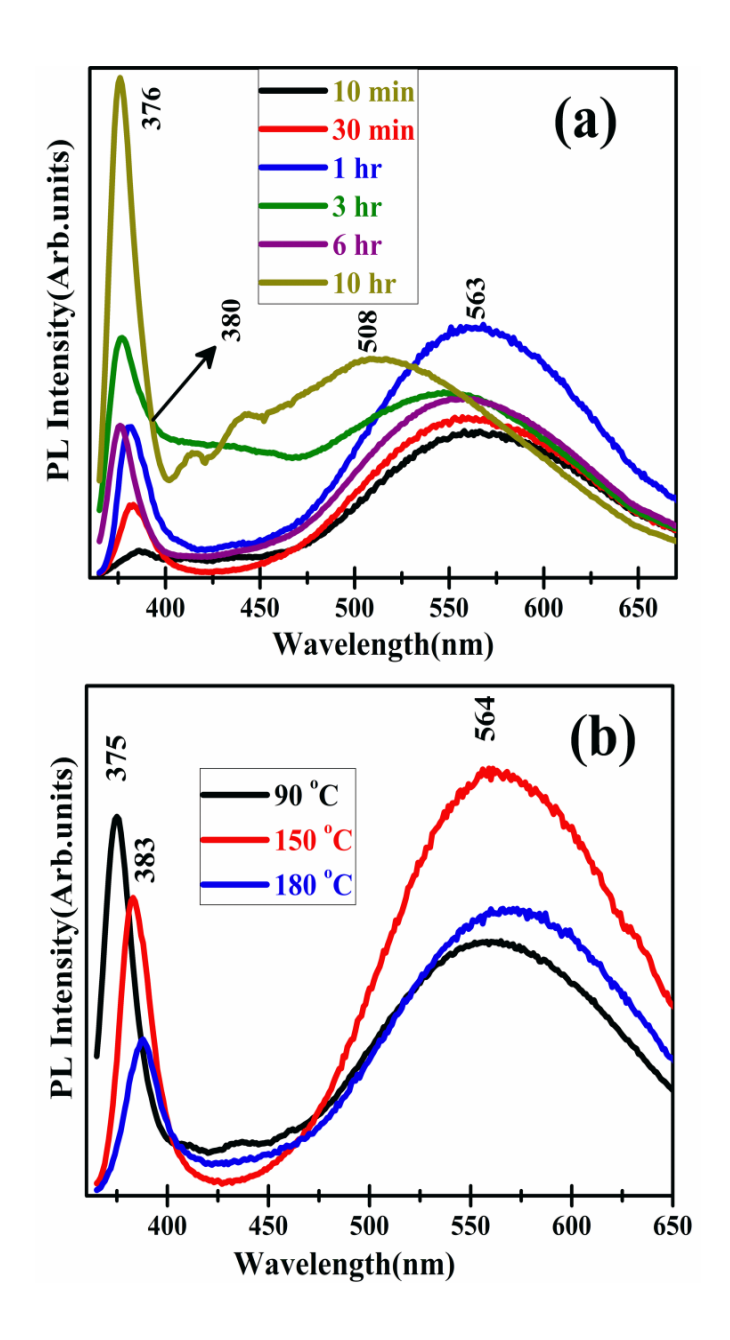


Figure 4.12: Photoluminescence spectra of hydrothermally processed ZnO nanostructures on 100 nm thickness ZnO films showing the effect of (a) varying duration of processing at 120 °C and (b) increasing temperature at a fixed processing duration of 3 hrs.

In bulk samples and single crystals these appear approximately at 380 cm⁻¹(A₁TO), 574 cm⁻¹ (A₁LO), 405 cm⁻¹ (E₁TO), 592 cm⁻¹ (E₁LO), and 430 cm⁻¹ (E₂ high). There can be shifts in the peak position, shape and width depending on the sample conditions (crystallinity, strain, defects, vacancies etc). Raman spectra displayed in figure 4.13 (a) for the homo-structures as a function of increasing HP duration are very interesting due to their difference from the spectra of the thin

films. In contrast to the thin films, there is complete absence of the second order Raman scattering peaks (at low wavenumbers) in the case of nanowires. The most intense peak is centred around 437 cm⁻¹ characteristic of wurtzite ZnO, as stated earlier. This is also consistent with PL spectra discussed in figure 4.12, wherein the defect related peak decreases in intensity with increase in duration of HP. The appearance of very low intensity peaks at 569 and 579 cm⁻¹ indicates the presence of a very small fraction of oxygen vacancies and other defects.

Interestingly, at a fixed duration of HP with increasing temperature (figure 4.13 (b)), the second order Raman peak at 330 cm⁻¹ is very visible. In addition, the peak at 379 cm⁻¹ assigned to the A1 (TO) mode as a result of the displacement of Zn²⁺ and O²⁺ ions parallel to the c-axis is also observed. Both these modes indicate that an increase in temperature for a fixed duration is not very conducive to remove the defects. However, this result is consistent with the PL data.

The optical transmission spectra, in figure 4.14 (a), reveal that increase in duration of HP at a fixed temperature of 120 °C results in decrease in transmission as well as optical band gap. The 10 min HP sample has almost 60% transmission, which decreases to approximately 20% after 10 hrs of HP. The band gap, as a consequence of increased duration of HP, decreases from 3.4 eV to 2.6 eV. However, at a fixed HP duration of 3 hrs (figure 4.14 (b), the red-shift in band gap is much less (from 3.4 eV to 3.1 eV) in comparison to the change observed with increase in HP duration at a fixed temperature. Furthermore, the impact of increased temperature on optical transmission is very limited. All these homo-structures exhibit about 40% transmission in the visible and NIR regions. As discussed in chapter 3, there is a large density of defects in the seed layer thin films independent of thickness (figure 3.7 (a) and (b)). It is pertinent to recall that the emission at 380 nm is attributed to the recombination of free-excitons. The broad band emission from 450 nm to 650 nm (in figure 4.12(a) and (b)) revealed the occurrence of radiative recombination of the photogenerated hole with the electrons that belonged to the singly ionized oxygen vacancies [260]. The broad peak (peak position and peak intensity) in the PL spectra also gives the information of defect level distribution and its density. The peak position relates to defect level depth or nature of the defect while the width and intensity of the emission peak reveal information on distribution of defect types and defect density, respectively. It is, thus, evident from the intensities and position of the PL spectra of the HP ZnO samples grown over the different thin films that the defects in the nanowires and, as a consequence, the emission (wavelength and intensity) from them is strongly

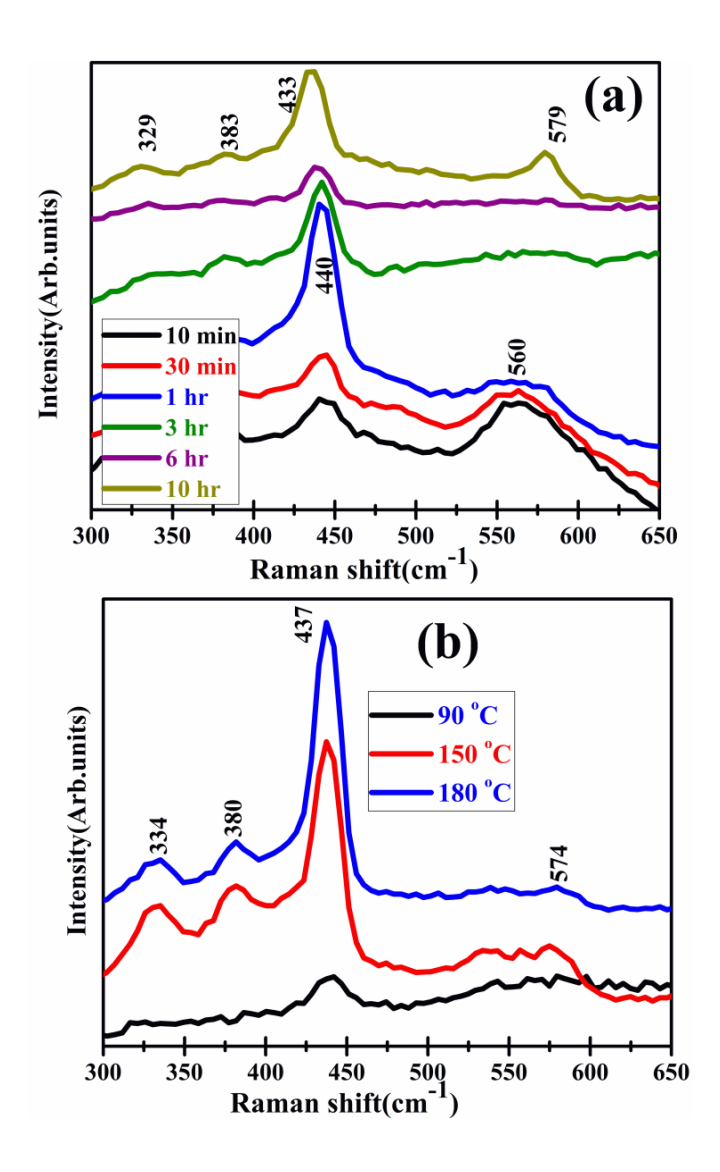


Figure 4.13: Raman spectra of hydrothermally processed ZnO nanostructures on 100 nm thickness ZnO films showing the effect of (a) varying duration of processing at 120 °C and (b) increasing temperature at a fixed processing duration of 3hrs.

dependent on the defects in the underlying thin films. It could be inferred that the defects propagate into the nanowires upto a length of 1-2 microns. As the length of the nanowires increase beyond this value, the effect of the defects on photoluminescence decreases leading to a decrease in the defect related peak intensity and increase in the intensity of the UV-NBE peak.

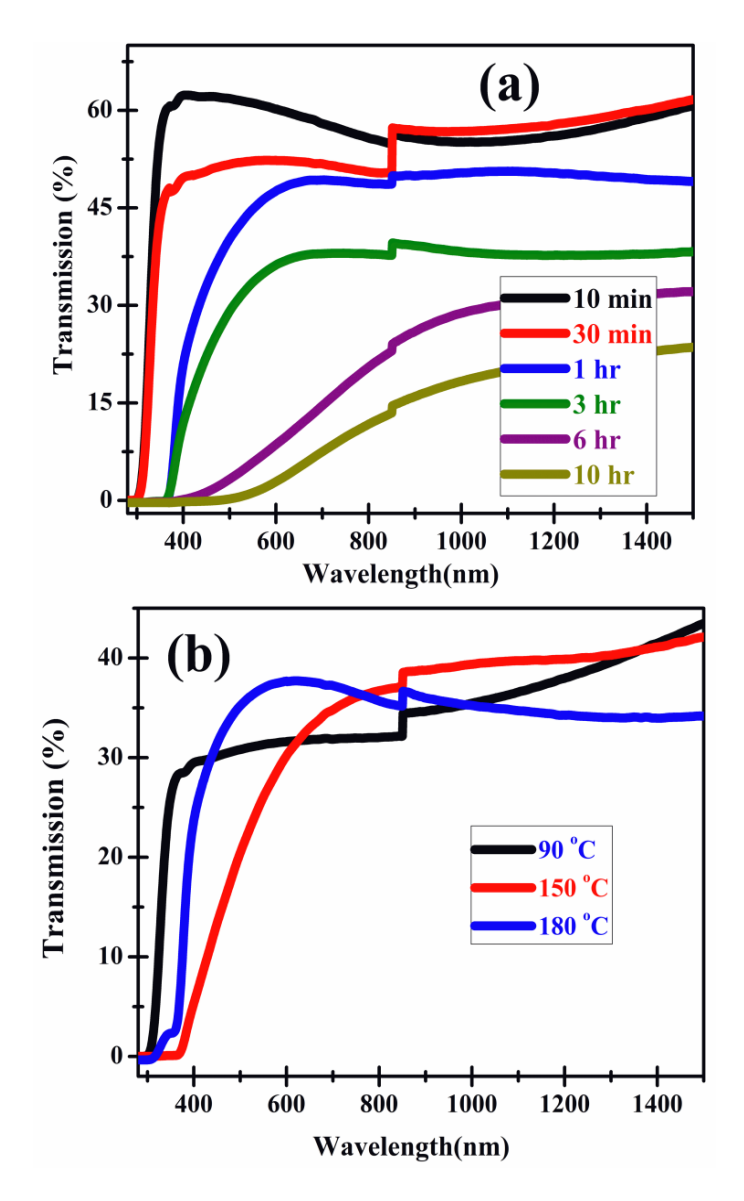


Figure 4.14: Optical transmission spectra of hydrothermally processed ZnO nanostructures on 100 nm thickness ZnO films showing the effect of (a) varying duration of processing at 120 °C and (b) increasing temperature at a fixed processing duration of 3 hrs.

This is very interesting for LED applications based on such homo-junctions as it provides the possibility of defect-controlled emission [271, 287-292, 293].

4.6. Microstructure and structure of ZnO nanostructures on Gold (Au) seed layers

The next set of growth experiments were carried out on hydrothermally processed ZnO nanostructures, at 120° C for 3,6 and 10 hrs and 150 and 180°C for 3 hrs, on the 100 nm thickness Au seed layers. The growth patterns of the ZnO nanostructures at 120° C for 3,6 and 10 hrs are shown in figure 4.15 (a-c), 4.16(a-c) and 4.17(a-c) respectively. After a HP duration of 3 hrs, the formation of hexagonal ZnO nanorods with very low density of packing is observed. The dimension of the hexagons is of the order of 800-1000 nm and length 4-5 μ m (figure 4.15 (a-c)). When the processing duration is increased to 6hrs, interestingly, the formation of hexagonal nanotubes with sides of 800 nm and length of 4-5 μ m is observed (figure 4.16 (a-c)). Further increase in HP duration to 10 hrs shows that the tubular structure is retained and there is not much change in the dimensions in comparison to the 6hrs case. The packing density also remains low (figure 4.17 (a-c)). It is not clear why the tubes are forming.

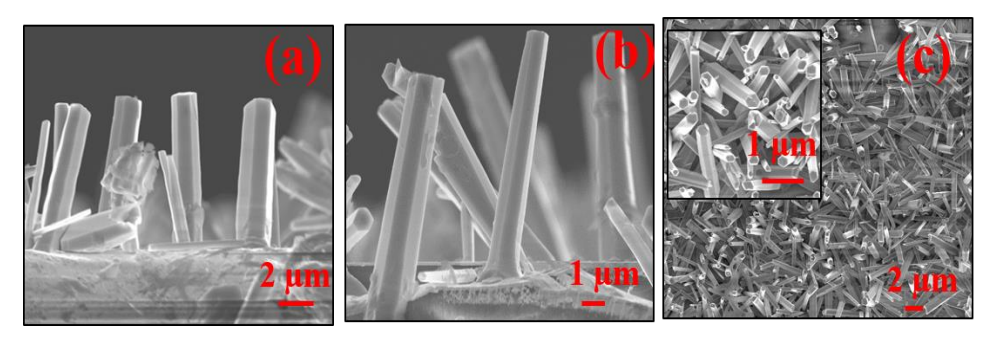


Figure 4.15: FESEM images of hydrothermally processed ZnO nanostructures on Au seed layer at 120 °C for 3 hours (a-b) Cross-sectional images at different magnification and different locations, (c) Top view.

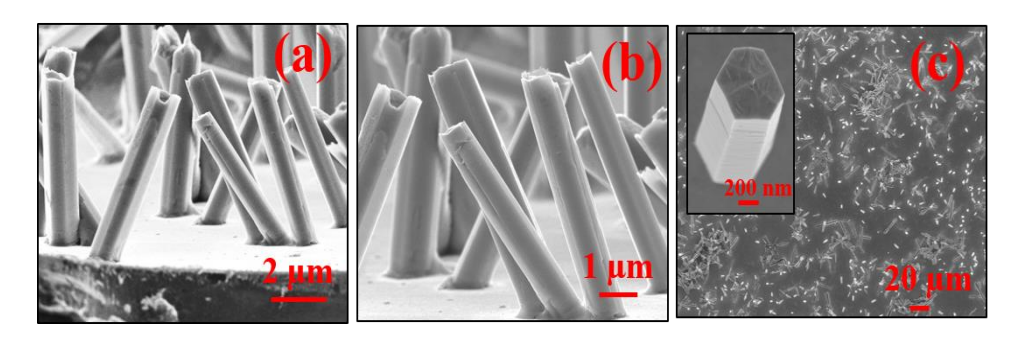


Figure 4.16: FESEM images of hydrothermally processed ZnO nanostructures on Au seed layer at 120 °C for 6 hours (a-b) Cross-sectional images at different magnification and different locations, (c) Top view.

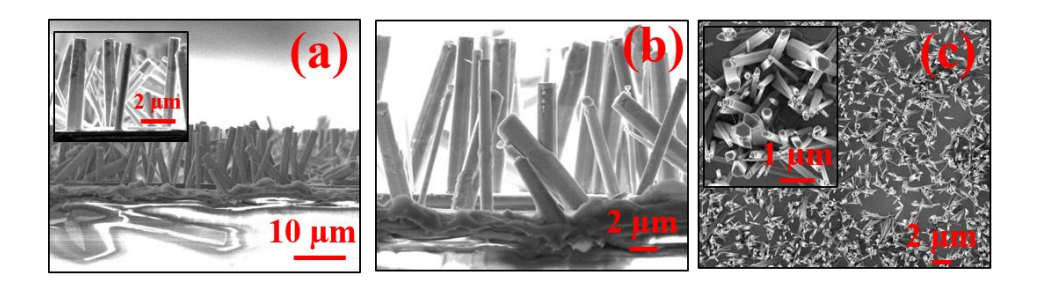


Figure 4.17: FESEM images of hydrothermally processed ZnO nanostructures on Au seed layer at 120 °C for 10 hours (a-b) Cross-sectional images at different magnification and different locations, (c) Top view.

The effect of increasing temperature ($150\,^{\circ}\text{C}$ - $180\,^{\circ}\text{C}$) at a constant duration of 3 hours is shown figure 4.18 (a-b) and 4.19 (a-b) respectively. There is a very significant change in the shape as well as the packing density of the nanostructures. They now grow in the form cylindrical nanowires that are flexible and densely packed with diameter in the order of 200-300 nm and length 6-7 μ m. As the temperature is increased to $180\,^{\circ}\text{C}$ the diameter increases to 500-600 nm without much change in the length, thereby decreasing the aspect ratio, or packing density.

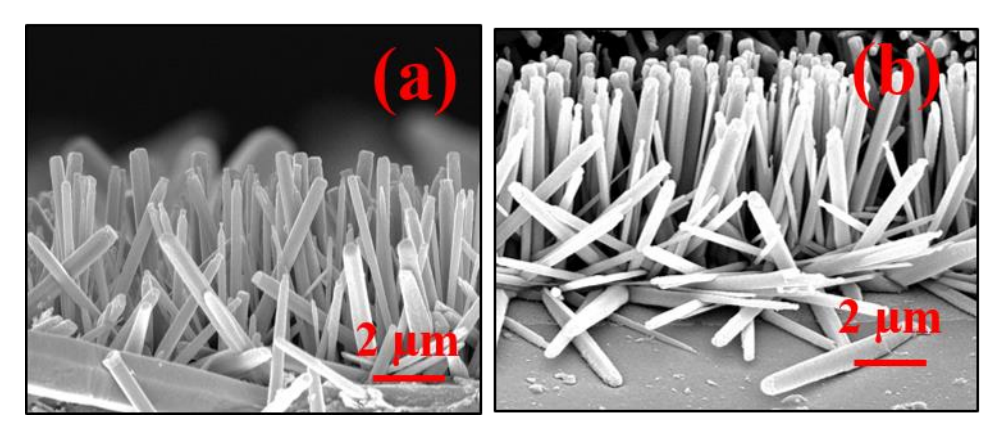


Figure 4.18: (a-b) Cross-sectional FE-SEM images of hydrothermally processed ZnO nanostructures on Au seed layer at 150°C for 3 hours at different magnification and different locations.

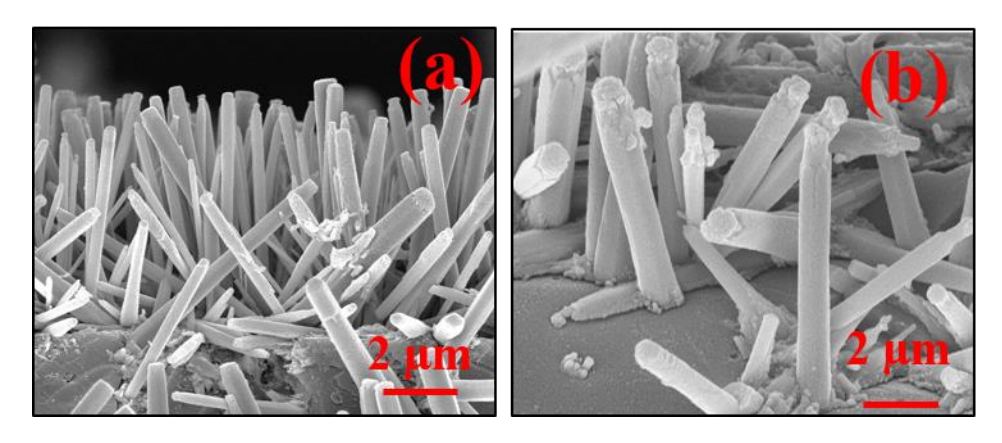


Figure 4.19: (a-b) Cross-sectional FE-SEM images of hydrothermally processed ZnO nanostructures on Au seed layer at 180°C for 3 hours at different magnification and different locations.

XRD patterns of the ZnO nanostructures discussed above are displayed in figure 4.20(a) over the full range and in 4.20(b) for the range 30-37°. The diffraction peaks of Au occur at 2θ values of 38.40 and 44.59°, which are indexed to the (111) and (200) planes of the FCC phase of Au (JCPDS file no: 04-0784). All other peaks could be assigned to the wurtzite phase of ZnO with no evidence for unreacted Zn. At durations of HP less than 10 hrs, the diffraction peaks relating to wurtzite ZnO are dominated by the Au diffraction peaks. The XRD pattern for the 10hrs samples shows a preferred c-axis orientation for the ZnO nanowires.

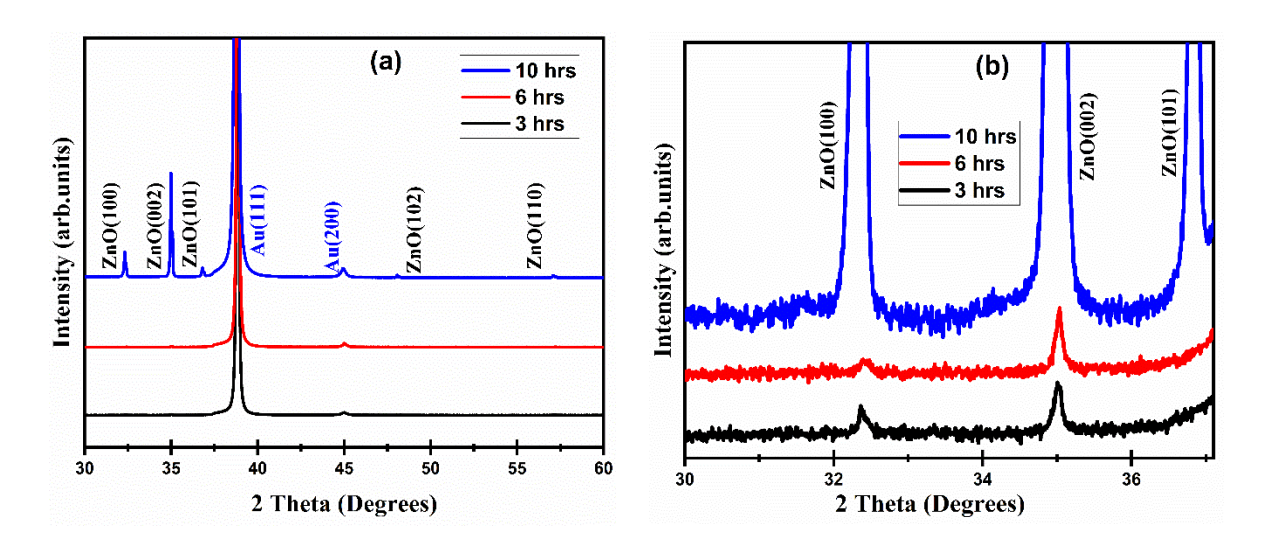


Figure 4.20: X-ray diffraction patterns of hydrothermally processed ZnO nanostructures on Au seed layer at 120°C with increasing duration of processing (a) for the full range of 2theta values recorded and (b) in the range of 30-37°.

4.7. Raman spectroscopy of ZnO nanostructures on Au seed layer

Raman spectra displayed in figure 4.21 (a) for the ZnO nanostructures on Au thin-film as a function of increasing HP duration are very interesting due to their difference from the spectra of the thin films. In contrast to the thin films, there is complete absence of the second order Raman scattering peaks (at low wavenumbers) in the case of nanowires. The most intense peak is centred around 437 cm⁻¹ and 441 cm⁻¹ which is characteristic of wurtzite ZnO, as stated earlier.

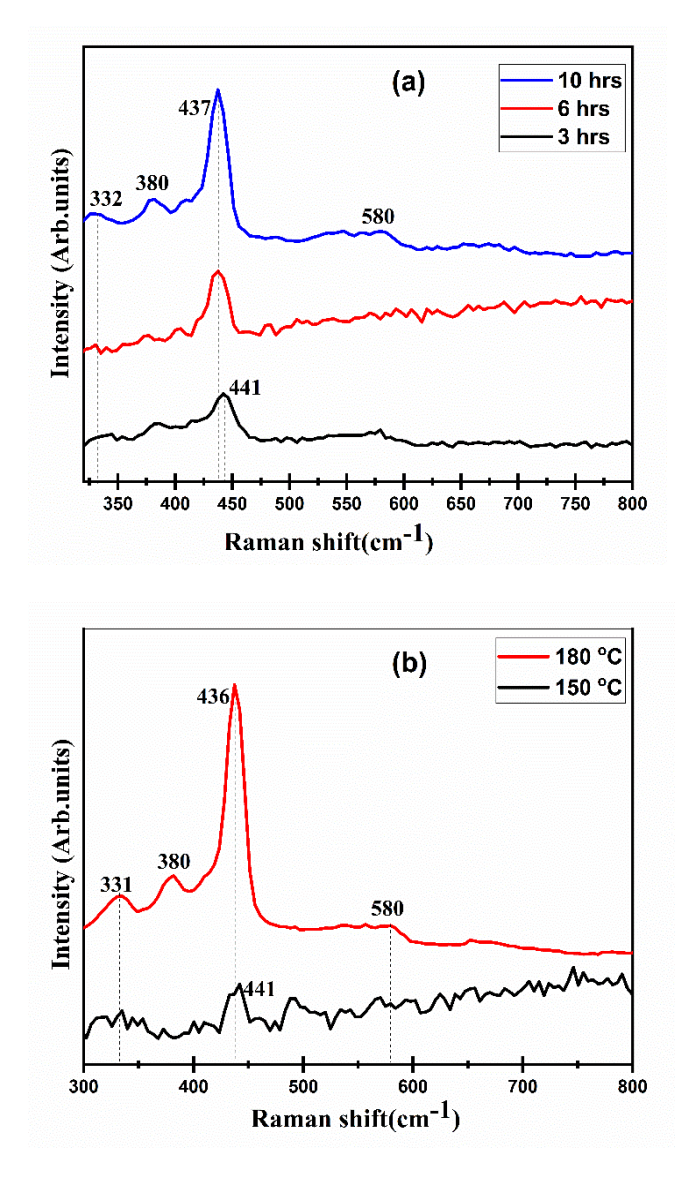


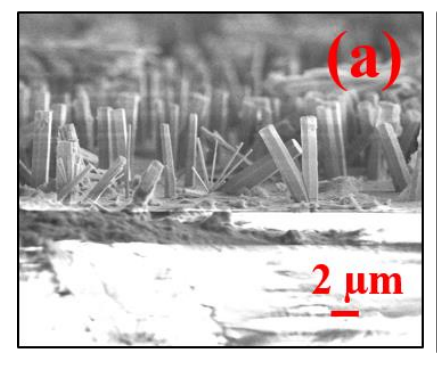
Figure 4.21: Raman spectra of hydrothermally processed ZnO nanowires on Au seed layer (a) increasing duration of processing at 120°C (b) increasing temperature at a fixed processing duration of 3hrs.

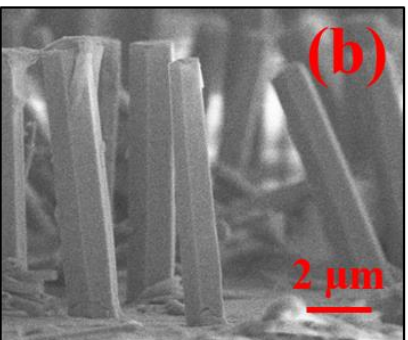
The appearance of a very low intensity peak 580 cm⁻¹ indicates the presence of a very small fraction of oxygen vacancies and other defects. Interestingly, at a fixed duration of HP with increasing temperature (figure 4.21 (b)), the second order Raman peak at 331 cm⁻¹ is very visible. In addition, the peak at 380 cm⁻¹ assigned to the A1 (TO) mode as a result of the displacement of Zn²⁺ and O²⁺ ions parallel to the c-axis is also observed. Both these modes indicate that an increase in temperature for a fixed duration is not very conducive to remove the defects.

Optical transmission measurements showed that the ZnO nanostructures had <1% transmission in the wavelength range of 200-2500 nm. This is attributed to the presence of the Au seed layer.

4.8. Microstructure and structure of ZnO nanostructures on glass substrate (Seedless growth)

The need for a seed layer and its impact on the growth of ZnO nanostructures by hydrothermal processing is examined in this section. The ZnO nanostructures are grown directly on the glass substrate, termed as seedless growth, at 120° C for 3, 6 and 10 hrs and 150 and 180° C for 3hrs. These experiments provide insight into the role of the seed layer. The cross-sectional FE-SEM images displayed in figure 4.22 (a-c), figure 4.23 (a-c) and figure 4.24 (a-c) for the samples grown at 120° C for 3, 6 and 10 hrs, respectively, indicate the formation of hexagonal micro-rods with side dimensions of 1-1.5 μ m and length 8-10 μ m. The packing density of the rods is quite low. It is also observed that several rods emerge from a single nucleating site forming microflower like objects (see for example inset of figure 4.22(c)). Longer duration of processing leads to the formation of tetrapods (figure 4.23 and 4.24).





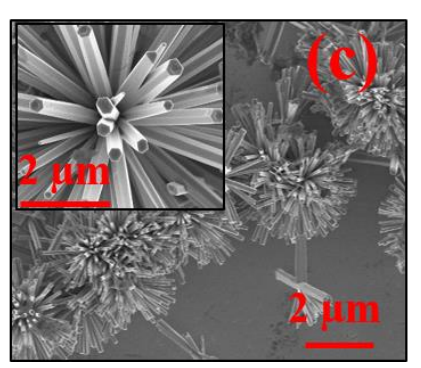


Figure 4.22: FE-SEM images of hydrothermally processed ZnO micro/nanostructures at 120 °C for 3 hours on glass substrate, (a-b) Cross-sectional images at different magnification and different locations, (c) Top view.

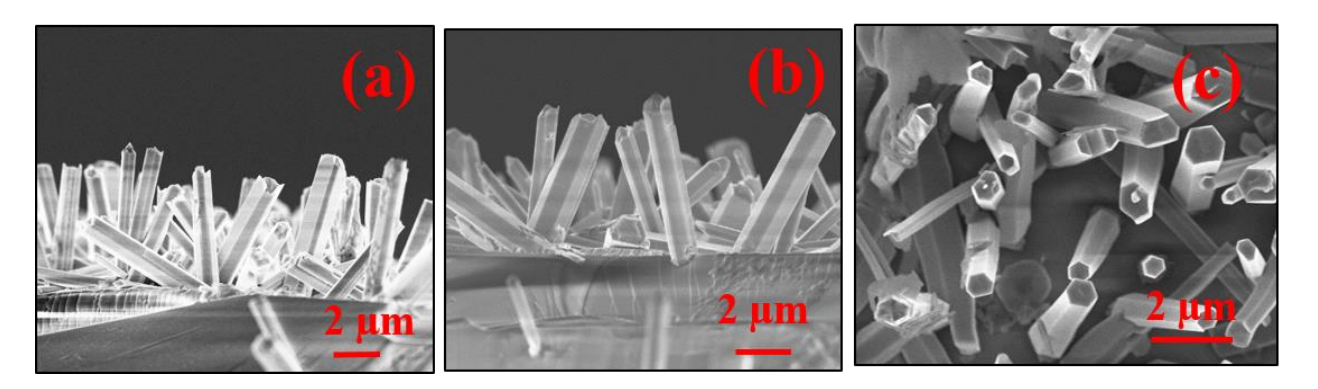


Figure 4.23: FE-SEM images of hydrothermally processed ZnO micro/nanostructures at 120 °C for 6 hours on glass substrate, (a-b) Cross-sectional images at different magnification and different locations, (c) Top view.

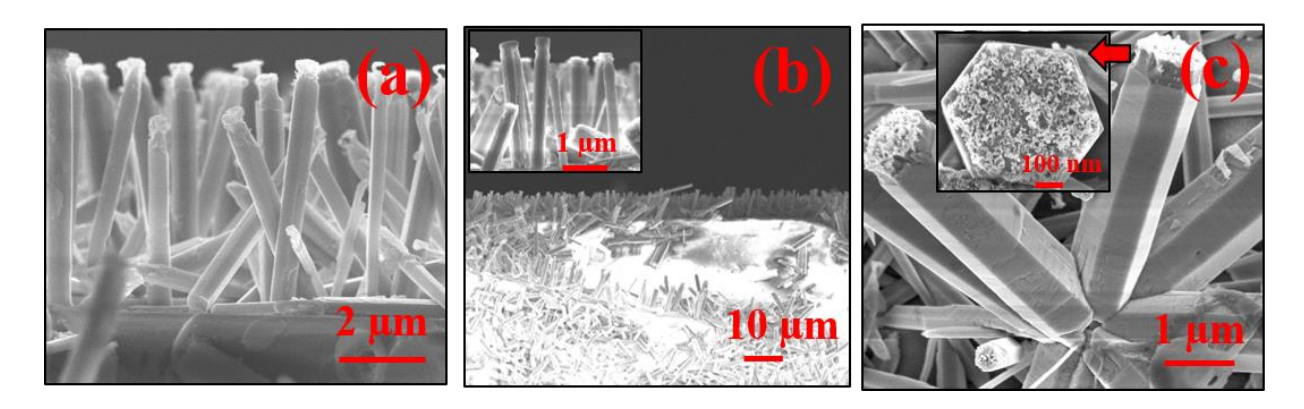


Figure 4.24: FE-SEM images of hydrothermally processed ZnO micro/nanostructures at 120 °C for 3 hours on glass substrate, (a-b) Cross-sectional images at different magnification and different locations, (c) Top view.

XRD patterns of the hexagonal microrod arrays synthesized at 120 $^{\circ}$ C for 3, 6 and 10 hrs are shown in figure 4.25. For HP durations upto 6 hrs, the microrods are weakly crystalline showing only peak in each case corresponding to the (110) and (100) planes of wurtzite ZnO at 3 and 6hrs, respectively. However, when the HP duration is increased to 10 hrs, the microrods become completely crystalline with prominent diffraction peaks at 20=31.64, 34.12, 36.2 and 56.6 $^{\circ}$ which are indexed to (100), (002), (101) and (110) planes of hexagonal wurtzite phase (JCPDS file no: 80-0074) of ZnO respectively.

4.9. Raman spectroscopy and Optical properties of ZnO micro/nanostructures on BSG substrate

Raman spectra are displayed in figure 4.26 (a) for the ZnO microrod structures as a function of increasing HP duration. The second order Raman scattering peaks (at low wavenumbers) in the of case microrods which were not visible on the Au seed layers is now evident at 332 and 385 cm⁻¹.

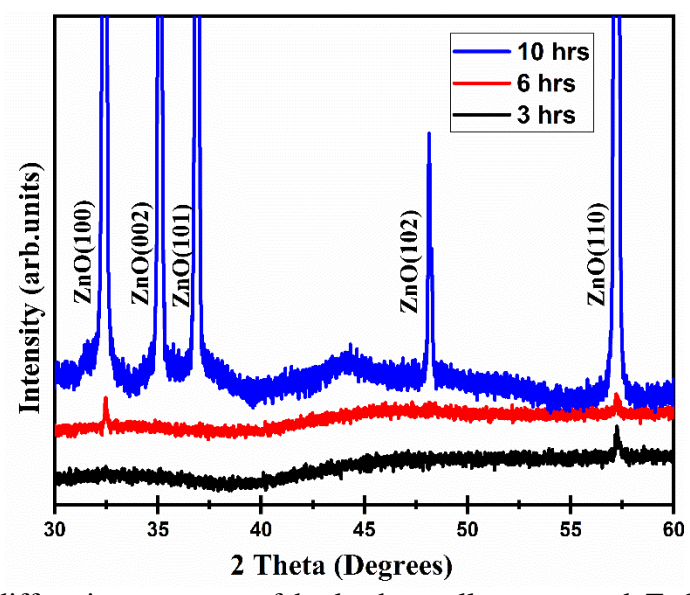


Figure 4.25: X-ray diffraction patterns of hydrothermally processed ZnO microrods on glass substrate with increasing duration of processing at 120°C.

The most intense peak is centred around 437 cm⁻¹ and 441 cm⁻¹ characteristic of wurtzite ZnO, as stated earlier, while the peak at 580 cm⁻¹ continues to show very low intensity. Interestingly, at a fixed duration of HP with increasing temperature (figure 4.26 (b)), the second order Raman peak at 331 cm⁻¹ and the peak at 382 cm⁻¹ assigned to the A1 (TO) mode as a result of the displacement of Zn²⁺ and O²⁺ ions parallel to the c-axis are also observed. Both these modes indicate that an increase in temperature for a fixed duration is not very conducive to remove the defects.

The optical transmission spectra, in figure 4.27 (a), reveal that increase in duration of HP at a fixed temperature of 120 °C results in decrease in transmission as well as optical band gap. The 3 hours HP sample has almost 75% transmission, which decreases to approximately 20% after 10 hrs of HP. The band gap, as a consequence of increased duration of HP, decreases from 3.8 eV to 3.4 eV.

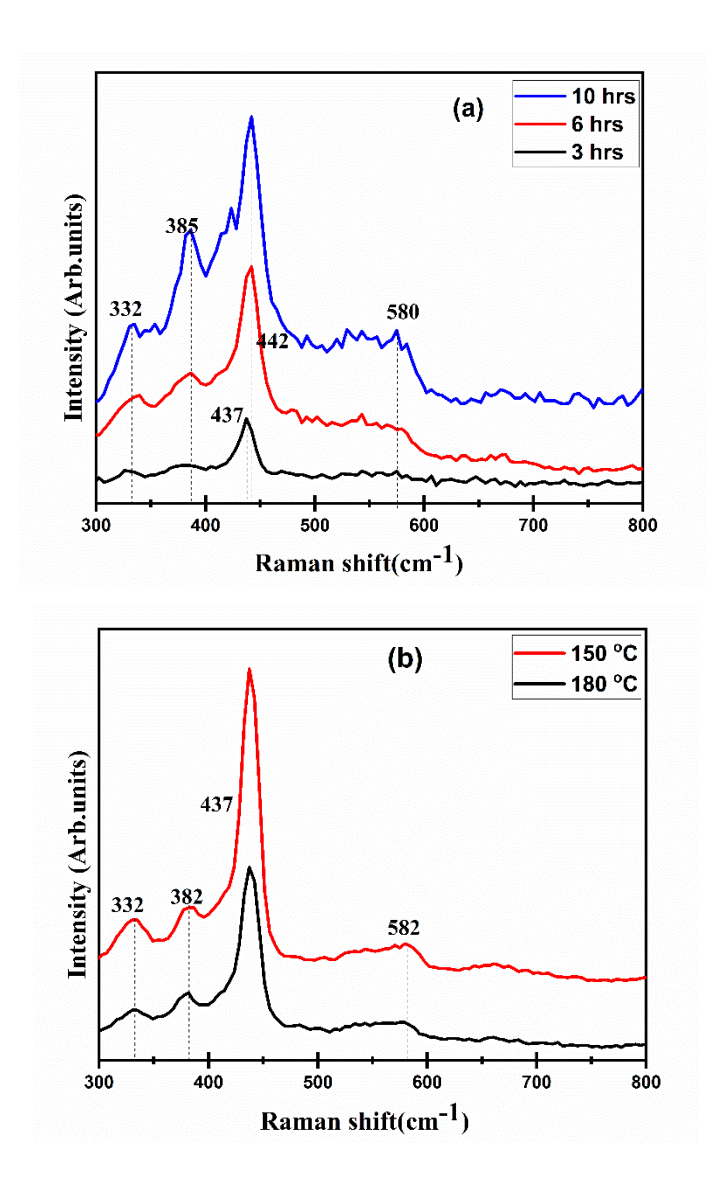


Figure 4.26: Raman spectra of hydrothermally processed ZnO micro/nanorods on Au seed layer (a) increasing duration of processing at 120°C (b) increasing temperature at a fixed processing duration of 3hrs.

However, at a fixed HP duration of 3 hrs (figure 4.27 (b), the red-shift in band gap is much less (from 3.6 eV to 3.4 eV) in comparison to the change observed with increase in HP duration at a fixed temperature. Furthermore, the impact of increased temperature on optical transmission is very limited. All these homo-structures exhibit about 10% - 20 % transmission in the visible and NIR regions.

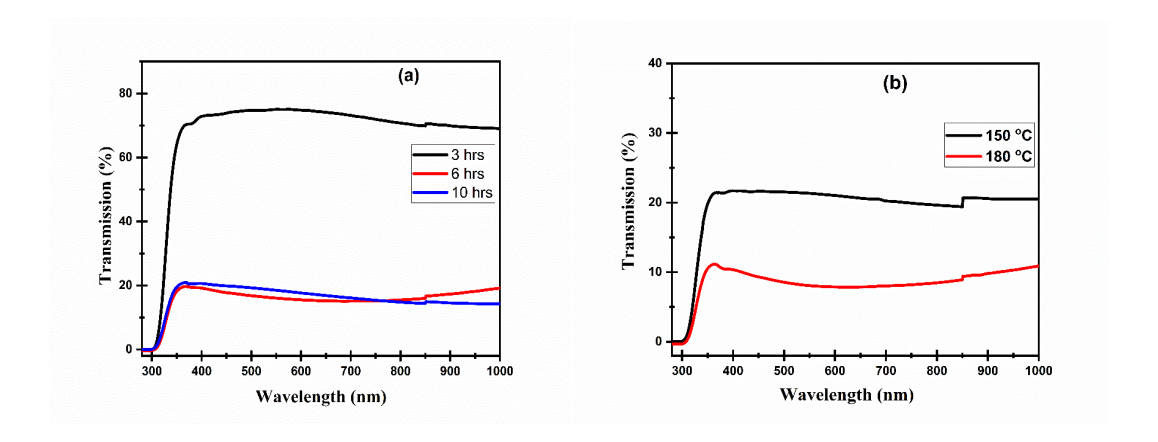


Figure 4.27: Optical spectra of hydrothermally processed ZnO micro/nanorods on BSG substrate (a) increasing duration of processing at 120°C (b) increasing temperature at a fixed processing duration of 3hrs.

4.10. Discussion on the mechanisms of the growth of ZnO nanostructures

At this point it is relevant to summarize the different conditions under which the ZnO nanostructures are grown and understand the possible mechanisms for the observed growth. The ZnO structures are grown directly on glass substrates, Au seed layers and ZnO seed layer thin films of thickness 100-400 nm. The hydrothermal processing is carried out at different temperatures for a fixed duration and at a fixed temperature for different durations (all other conditions being the same). The major observations that can be made are (1) all the nanostructures are vertically oriented, independent of the conditions of processing and nature of underlying thin film surface; (2) the structures are hexagonally shaped on the Au seed layer and also on glass substrates; (3) the dimensions and shapes are significantly dependent on the nature of the underlying surface of the seed layers and (4) the nanowires are cylindrical in nature for hydrothermal durations of <3 h. Longer synthesis durations lead to the hexagonality of rods. However, on Au and glass substrates the rods are hexagonal shaped independent of duration and temperature of processing. It is inferred, from these observations, that the hexagonal shape is the equilibrium shape for the rods, i.e. given favourable conditions it is most likely that the nanostructures will only grow in the form of hexagonal rods, probably due to the wurtzite structure of ZnO. This is consistent with earlier observations in literature [255]. The reasons for the formation of vertical micro/nano structures are now discussed. It is known that the chemical reactions driving the growth of ZnO using

hexamethylenetetramine ($(CH_2)_6N_4$ or HMTA) and zinc acetate dihydrate as precursors follow the sequence below. [272-274]

Step 1

$$(CH_2)_6N_4 + 6H_2O \longrightarrow 6HCHO + 4NH_3$$

Step 2

$$NH_3 + H_2O \longleftrightarrow NH_4^+ + OH^-$$

Step 3

$$2OH^-+Zn^{2+} \longrightarrow Zn(OH)_2$$

Step 4

$$Zn(OH)^2 \longrightarrow ZnO + H_2O$$

It is reported that HMTA has several functions in hydrothermal synthesis of ZnO.

HMTA

- 1. provides OH- ions required for the precipitation reaction
- 2. acts as a pH buffer.
- 3. generally attaches itself to the non-polar facets of ZnO exposing only the polar (001) plane for crystal growth.

In this sequence, the growth relies on controlling the supersaturation of the reactants and depending on the magnitude, high or low, nucleation or crystal growth occurs. An important point is the rate of production of OH^- ions. If a large number is produced in a very short duration, the Zn^{2+} ions will precipitate rapidly due to the high pH of the solution. As a consequence, these ions make a negligible contribution to the nano/micro structure growth and will result in the complete consumption of the nutrients inhibiting any further growth. Sugunan et al [274] have also demonstrated in a controlled experiment that HMTA plays the role of a surfactant which induces hexagonal shapes. The formation of hexagonal prism and pyramid like ZnO crystals is attributed to the difference in the growth velocities of various crystal facets. The growth velocities under hydrothermal conditions along the different directions are known to follow the pattern V(0001) > V(1011) > V(1010) [294]. The relative growth rate of these crystal faces will determine the final shape and aspect ratio of the ZnO nanostructures. It is, thus, inferred in the present study that HMTA plays an important role in the alignment, shape and crystallographic

texture of the observed structures. It may be recalled that in the conditions used in the present study, NaoH and KOH do not support the formation of nanowires/rods.

Comparison between ZnO and Au seeded HP of ZnO at 120°C for 30 and 180 min in figure 4.28 (a)-(d) shows that flexible nanowires form on the ZnO seed layer while the structures are more rod-like on the Au seed layer. The nanostructures are more densely packed on ZnO than on the metal seed layers.

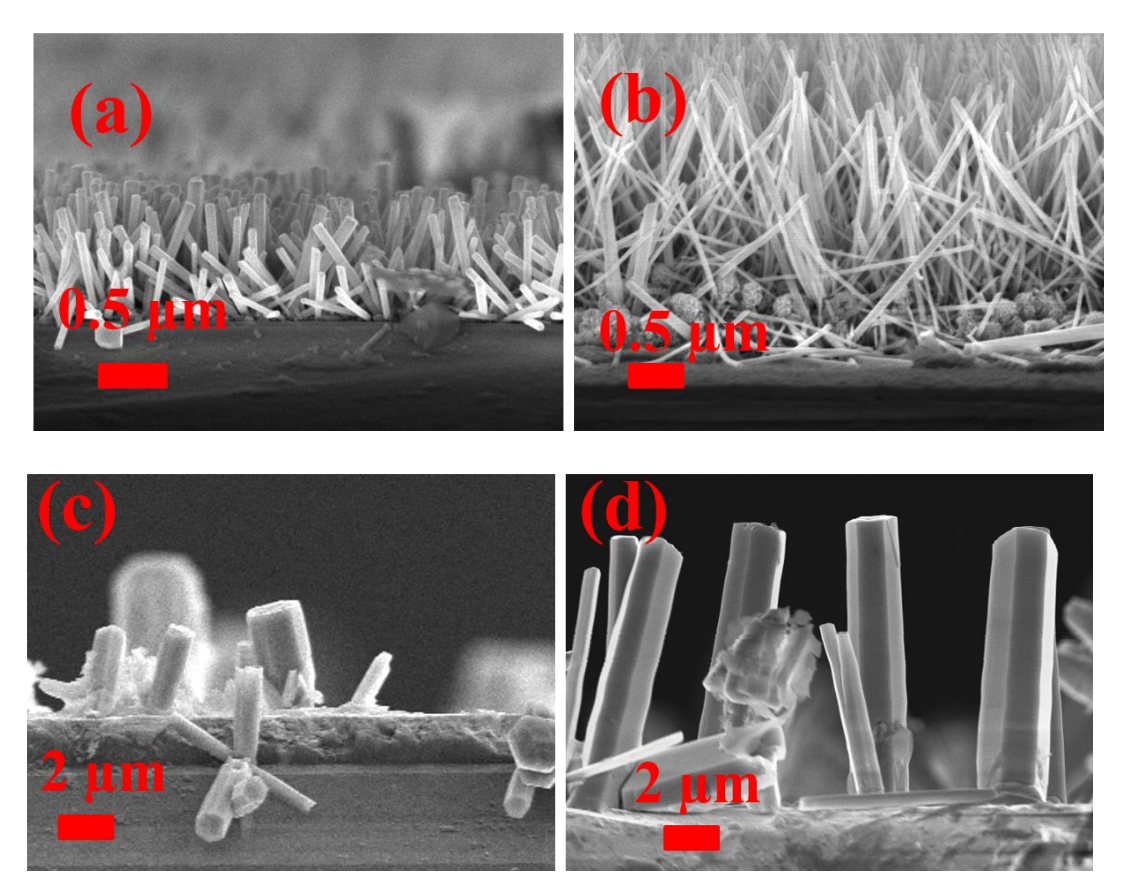


Figure 4.28: Cross-sectional FE-SEM images of ZnO structures on ZnO seed layers after (a) 30 min, (b) 3 hours and Au seed layers after (c) 30 min (d) 3 hrs.

The comparison with ZnO and Au seed layers is presented in figure 4.29 (a)-(b). The arrays are polycrystalline in nature with marginal preference towards the (100) orientation. The preferred orientation becomes stronger with an increase in duration of HP from 30 to 180 min. It appears from the microstructural observations that an increase in the duration of HP causes mass transport both in-plane and out-of-plane of the substrate. However, ZnO's mass transport in the direction

normal to the seed layer is greater, leading to a large increase in the rods and wires' length. It is observed, in the present case, that the interface between the seed layer and ZnO is quite important. The activation barrier for growth is much higher on the metal seed layers as evidenced by the absence of nano/micro rods after 30 min of processing.

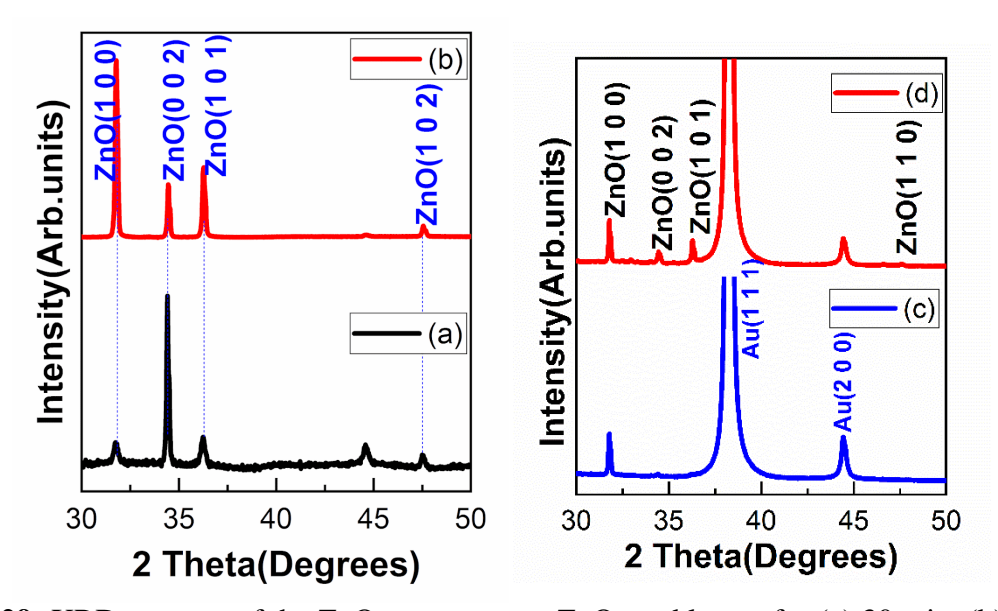


Figure 4.29: XRD patterns of the ZnO structures on ZnO seed layers for (a) 30 min, (b) 3 hrs and Au seed layers for (c) 30 min, (d) 3 hrs.

On Au seed layers no growth is observed at 30 min whereas on ZnO there is clear evidence for the formation of nanowires. Thus, oxide seed layers are more amenable for the growth of nanorod arrays than metal seed layers. This point is confirmed in chapter 5 where comparison of growth patterns on In and Sn metal and In and Sn oxides is presented.

A significant observation is that even seedless growth, directly on a glass substrate, yields hexagonal microrods. But nanostructures are only observed on ZnO seed layers.

4.11. Summary

In summary conventional hydrothermal synthesis has been used to grow ZnO nanostructures over Au seed layers, ZnO seed layers and directly on glass substrates. The growth patterns are strongly dependent on the temperature (90 °C to 180 °C) and duration of synthesis (10 min to 10 hrs) apart from the morphology of the seed layer films. It appears that a temperature of 120 °C and duration of 3hrs are the threshold values to obtain good quality nanostructures. At these values, ZnO grows in the form of vertically aligned densely packed nanowire arrays on ZnO seed layers, low packing density hexagonal nanorod arrays on Au seed layers and hexagonal microrods on the glass substrates. XRD studies show that the nano/micro rods are polycrystalline in nature. Photoluminescence and Raman spectroscopy studies reveal the presence of defects in the nano/microstructures. Interestingly, the defect-related emission can be controlled by controlling dimensions and defects in the nanowires. This is an extremely important observation for applications. The mechanisms by which HMTA and seed layers control the growth are discussed.

Part-4B (Microwave Hydrothermal synthesis)

Abstract (Part B)

The aim of Part 4B is to investigate if the temperature and duration at which ZnO nanowires can be changed by using microwave assisted hydrothermal synthesis. As in the previous section, ZnO thin films of 100-400 nm thickness and Au thin films of 100 nm thickness were deposited on glass substrates by thermal evaporation. Due to experimental limitations, the study is restricted to 90°C for 30 min using zinc nitrate and zinc acetate as the precursors. In contrast to the conventional process described in Part 4A, there is a hierarchy of shapes comprising star shaped tetrapods and ball-shapes at the microscale made up of rice grains at the nanoscale on the ZnO and Au thin films respectively, when the precursor is zinc nitrate. The typical dimensions of the nano rice grains are 1µm length, 100nm width and tips of the order of 10 nm. However, when the precursor is zinc acetate the nanostructures grow as hexagonal rods on the ZnO films and hexagonal tetrapods on the Au films with dimensions of 1-3 µm length and hexagon side of the order of 100-150 nm. Raman spectroscopy studies indicate the presence of defect related peaks in the nanostructures that are suppressed with increase in thickness of the ZnO films. The intensity of the defect peaks is much higher in the nanostructures grown on the Au films and is dependent on the precursor used to produce the nanostructures. Photoluminescence studies indicate that the ultraviolet-near band edge emission is the strongest on ZnO while defect related emission is prominent on the Au films. Shape control by microwave assisted hydrothermal synthesis is, thus, a facile low temperature method to produce nanostructures with different properties by simply changing the precursor and substrate on which they are grown. Most significantly, even with microwave hydrothermal synthesis, the temperature at which vertically aligned ZnO nanostructures grow, could not be decreased.

4.12 Background

In this part of the chapter, microwave assisted hydrothermal synthesis of ZnO nanostructures on ZnO and Au seed layers is described. The microwave assisted hydrothermal process is carried out at only one condition ie. 90°C for 30 min, due to experimental limitations and compared with the conventional process at the same temperature and time. It is demonstrated even under these limited conditions that there is a profound difference between the nano/microstructures obtained from the two processes.

ZnO nanostructures were then synthesized on these films by the microwave assisted hydrothermal process (MAHP). The typical sequence of steps followed in the MAHP were

- 1. 25mM of Zinc acetate dihydrate [Zn $(O_2CCH_3)_2(H_2O)_2$, 99.0%] or 25mM of zinc nitrate hexahydrate [Zn(NO_3)₂(H_2O)₆, 98.0%] were mixed with 25 mM of hexamethylenetetramine (HMTA) [(CH_2)₆ N_4 , 99.0 %] to obtain an aqueous solution. The mentioned chemicals (of Sigma-Aldrich) were used as received without any more purification. In the rest of the paper zinc acetate di-hydrate is referred as ZnAcD and zinc nitrate hexahydrate as ZnNH
- 2. The substrates coated with the ZnO or Au thin films were then dipped into the aqueous solutions
- 3. The process is carried out in a microwave oven (2.45 GHz) operated at 700 W at a fixed temperature of 90 °C and duration of 30 minutes for all the cases.
- 4. For comparison samples were also prepared by conventional hydrothermal synthesis under the same conditions

After processing it is ensured that no precursor residue is present using standard protocols

4.12.1 Microstructural shape evolution and crystal structure

The FE-SEM microstructural images of MAHP ZnO nanostructures synthesized using ZnNH as the precursor on ZnO thin films of 100,150, 200, and 400 nm thickness are displayed in figure 4.30 (a)-(d). Detailed characterization of the structure and microstructure of the films was reported earlier. It is evident from the images that the ZnO nanostructures present a hierarchy of shapes with the appearance of star-shaped tetrapods at the micro-scale, which appear from the attachment

of rice grain shapes at the nanoscale. The tetrapod length is 3-5 μ m, while each nano-rice grain is 1 μ m in length, about 100 nm in width, and tip size of 5-10 nm. The hierarchy in the case of nanostructures on Au films, in figure 4.30 (e) comprises a ball at the microscale, which emerges from the attachment of rice grain-shaped structures at the nanoscale. The diameter of the ball is 2-3 μ m, while the nano-rice grains are again 1-2 μ m in length, about 100 nm in width, with a tip size of 5-10 nm.

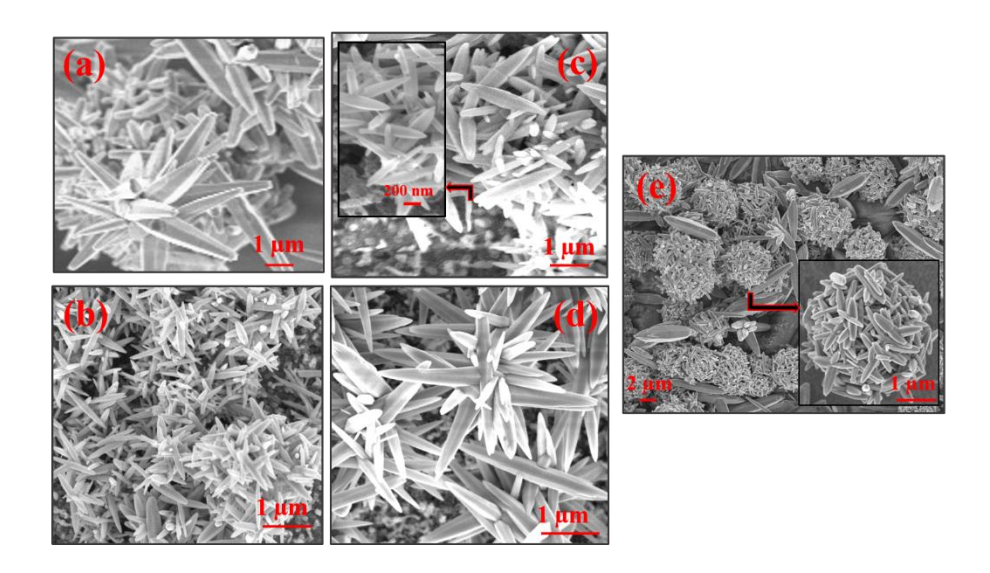


Figure 4.30: FE-SEM images of ZnO nanostructures showing the hierarchy of star shaped tetrapods at the microscale and rice grains at the nanoscale on ZnO thin films of thickness (a) 100 nm, (b) 150 nm, (c) 200 nm and (d) 400 nm. The FE-SEM image in (e) corresponds to the nanostructures on Au thin films of 100 nm thickness displaying the hierarchy of ball shape at the microscale and rice grain shaped particles at the nanoscale. The precursor used in the MAHP in these cases was zinc nitrate.

Evidently, the thin films on which the nanostructures appear to have an influence on the microscale shape of the hierarchy but no impact on the shapes at the nanoscales. This is inferred from the fact that the individual nanostructures are rice grain shaped but aggregate into tetrapods on the ZnO films and ball shape on Au films. The increase in thickness of the ZnO film from 100-400 nm has a very negligible effect on the shape evolution. To understand whether the precursor hydrate level and electric dipole moments of chemical constituents have any role in determining the initial shape of the nanostructures, the MAHP was carried out using ZnAcD as the precursor. The FE-SEM images of the obtained nanostructures on the 100 nm thickness ZnO and Au films are shown in figure 4.31 (a) and (b) respectively. It is clear that the hexagonal nanorods are formed on the ZnO

thin films in contrast to hexagonal nanorod based tetrapods on the Au film. Thus, the hierarchy of structures are seen in the case of the Au film while they are absent on the ZnO film. The most important inference drawn from these images is that the precursor does, indeed, have a profound influence on the shape of the nanostructures. In the case of ZnO films the nanorods are 500-700 nm in length with a side of 100 nm.

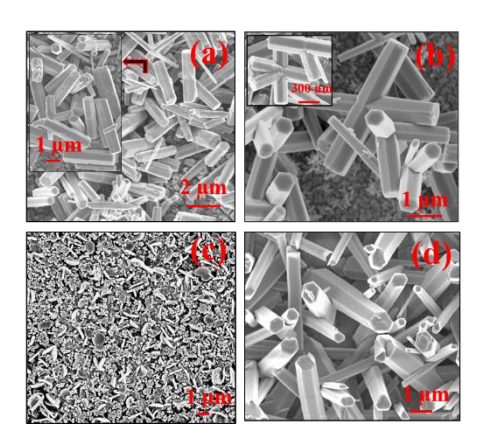


Figure 4.31: FE-SEM images of the nanostructures showing the effect of the use of zinc acetate as the precursor on (a) ZnO and (b) Au film of 100 nm thickness in both cases. Only hexagonal nanorods are formed on ZnO while tetrapods are formed on the Au film. (c) The FE-SEM image of the conventional hydrothermal processed ZnO using zinc acetate precursor on a ZnO thin film of 100 nm thickness at the same temperature and duration as (a) and (b) clearly showing the absence of any nanostructuring. In the case of (d) ZnO nanostructures on Au films a temperature of 120°C and 3hrs duration was required

Interestingly, under the same processing conditions without microwave assistance there is no evidence of nanostructuring of the ZnO on the 100 nm thick ZnO film as seen from figure 4.31 (c). In Part A it is already demonstrated that a temperature of 120°C and duration of at least 3hrs is required on ZnO films as well as in the case of Au films by conventional hydrothermal synthesis. Thus, microwave assistance indeed accelerates the process of nanostructuring and enables it at lower temperature.

X-ray diffraction patterns of the ZnO star-shaped tetrapods on the ZnO films using the ZnNH precursor are shown in figure 4.32 (a). The effect of using ZnAcD as the precursor is also shown in the same figure. All diffraction peaks are indexed to ZnO with a hexagonal wurtzite crystal structure using JCPDS file no – 80-0074. All XRD peaks are diffuse and broad, which indicates the nanocrystallinity of the samples. The crystallite size increases as the ZnO film thickness increases, with values of 12.6, 20.8, 32.2 and 32.4 nm obtained for the nanostructures grown on

the 100, 150, 200 and 400 nm thickness films respectively, as estimated from Scherrer's formula. The XRD pattern of the hexagonal ZnO nanorods synthesized using ZnAcD precursor does not display any major differences from the ZnNH based nanostructures with the crystallite size being of the order of 20 nm.

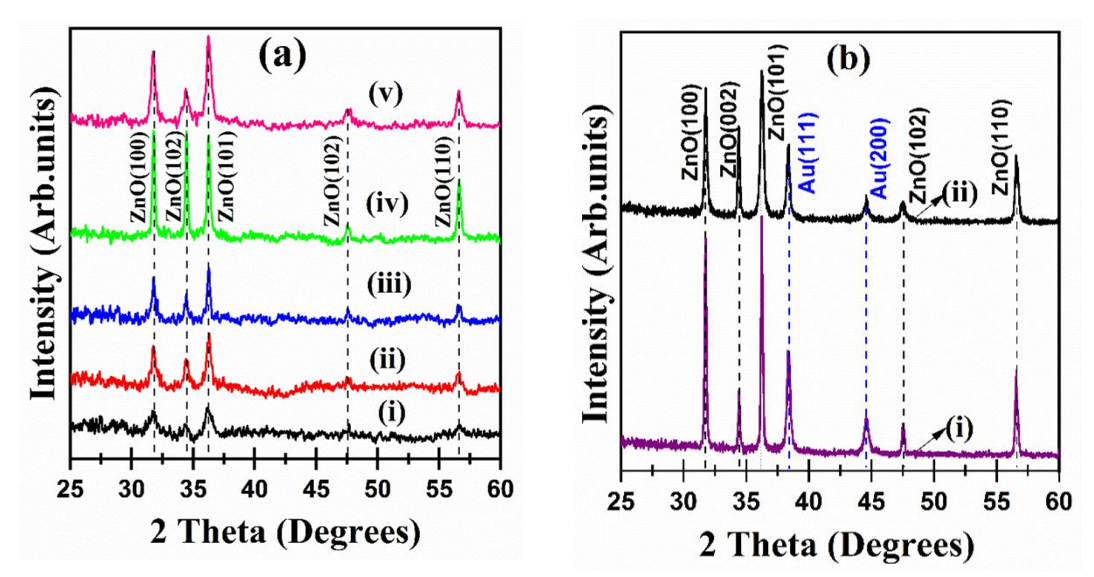


Figure 4.32: (a) XRD patterns of the ZnO nanostructures on ZnO films obtained using zinc nitrate as the precursor on ZnO thin films of (i) 100, (ii) 150, (iii) 200 and (iv) 400 nm thickness leading to the formation of rice-grain shape based tetrapods; (v) on 100 nm ZnO thin film using zinc acetate as the precursor leading to the formation of hexagonal nanorods. (b) XRD patterns of the (i) hexagonal tetrapods using zinc acetate precursor and (ii) ball shaped nanostructures using zinc nitrate precursor synthesized on Au thin films of 100 nm thickness.

XRD patterns of the hexagonal tetrapods achieved using ZnAcD as the precursor in figure 4.32 (b)-(i) is shown along with the diffraction patterns of ball shaped ZnO nanostructures on the Au thin films in figure 4.32 (b)-(ii). The diffraction peaks of Au occur at 2θ values of 38.40, 44.59, 64.72, and 77.83°, which could be indexed well to the (111), (200), (220), and (311) planes of the typical FCC phase of Au (JCPDS file no: 04-0784). All other peaks could be assigned to the wurtzite phase of ZnO with no evidence for unreacted Zn, in both cases. The crystallite size of the nanostructures in the case of Zinc acetate and Zinc nitrate are 47.2 and 27.1 nm respectively, as estimated from Scherrer's formula.

4.12.2 Raman spectra, photoluminescence and optical transmission

The Raman spectra of ZnO tetrapods synthesized from the zinc nitrate precursor on ZnO thin films of different thickness and the hexagonal nanorods using the zinc acetate precursor are displayed

in figure 4.33 (a). All the nanostructures exhibit the characteristic Raman peak of wurtzite ZnO at 437 cm⁻¹. In addition there are weak peaks observed at 330 cm⁻¹, 391 cm⁻¹ and 584 cm⁻¹ which can be attributed to the presence of different types of defects such as vacancies and interstitials, as described in detail earlier.

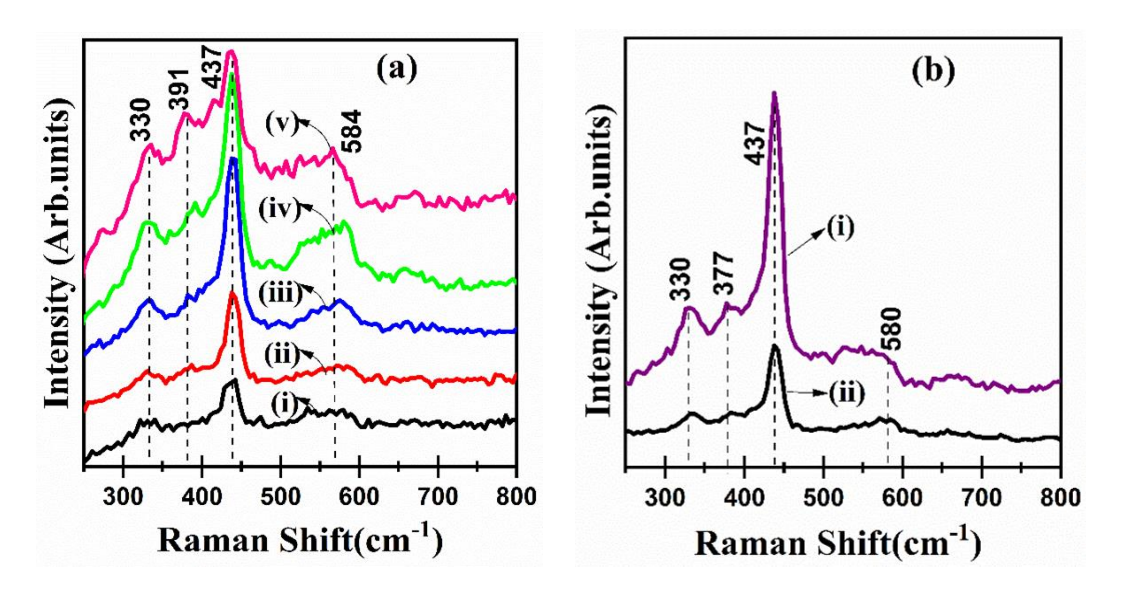


Figure 4.33: Raman spectra of (a) star shaped ZnO tetrapods synthesized using zinc nitrate precursor on ZnO thin films of different thickness (i)100,(ii)150, (iii) 200, (iv) 400 nm and (v) hexagonal nanorods on ZnO thin film of 100 nm thickness using the zinc acetate precursor. (b)-(i) hexagonal tetrapods produced using zinc acetate precursor and (ii) ball shaped ZnO nanostructures synthesized using zinc nitrate on Au thin film of 100 nm thickness.

The Raman spectra of ZnO hierarchical structures on Au synthesized by ZnAcD and ZnNH displayed in Figure 4.33 (b)-(i) and (ii) respectively also display a strong Raman peak at 437cm⁻¹, mentioned earlier. However, there is considerable weakening of the defect related peaks at 330, 377 and 580 cm⁻¹ in the case of the ZnNH precursor. In contrast, the peak at 580 cm⁻¹ is fairly intense in the case of the ZnacD precursor; there is a slight shift in the wavenumbers at which the peaks occur on ZnO and Au thin films indicating the presence of stress between the film and nanostructures.

The photoluminescence (PL) spectra of the nanostructures on ZnO thin films are shown in figure 4.34 (a). The spectra are characterized by a strong UV- near band-edge emission of ZnO centered around 376-380 nm. In addition, there are peaks at 419, 442, 505 and 543 nm which can be

attributed to the presence of defects. The defect related peaks decrease in intensity with increase in thickness of the ZnO films and change in precursor from ZnNH to ZnAcD.

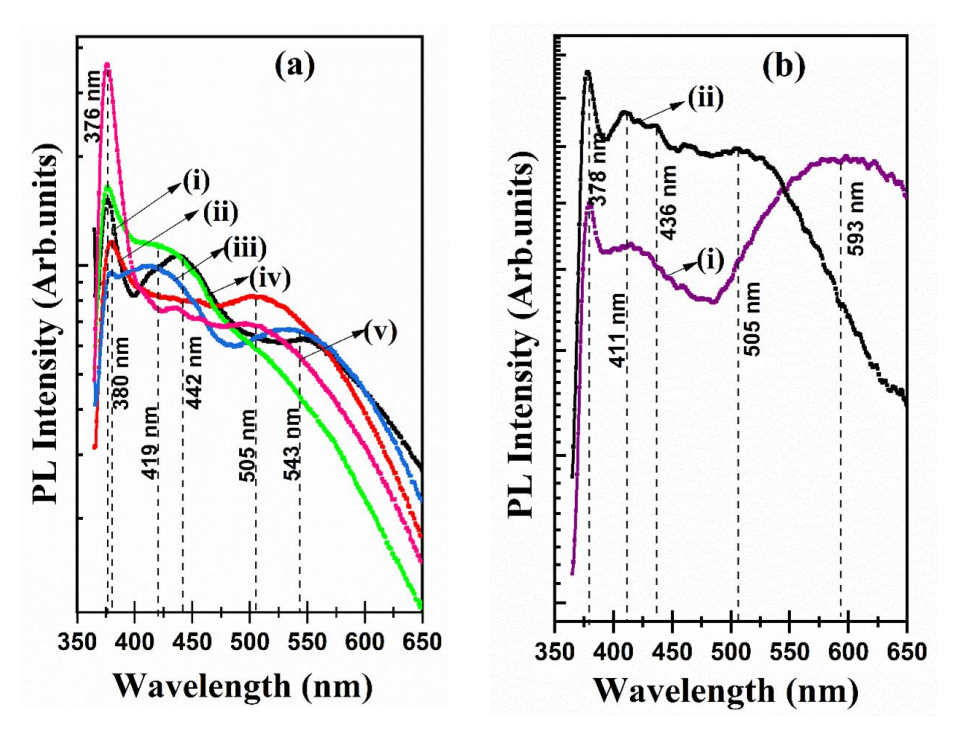
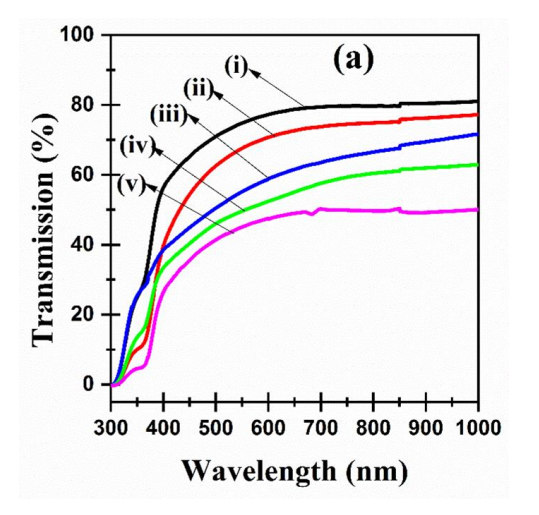


Figure 4.34: Photoluminescence spectra of (a) star shaped ZnO tetrapods synthesized using zinc nitrate precursor on ZnO thin films of different thickness (i)100, (ii)150, (iii) 200, (iv) 400 nm and (v) hexagonal nanorods on ZnO thin film of 100 nm thickness using the zinc acetate precursor. (b)-(i) hexagonal tetrapods produced using zinc acetate precursor and (ii) ball shaped ZnO nanostructures synthesized using zinc nitrate on Au thin film of 100 nm thickness.

In the case of the nanostructures grown on the Au films (figure 4.34 (b)), similar to ZnO films, the most intense peak occurs at a wavelength of 378 nm and is attributed to the UV-NBE. Additional weak intensity peaks appear at 411, 436 and 505 nm. However, in contrast to the previous case, the hexagonal tetrapods display a fairly intense and broad emission centered around 593 nm which is absent for the ball shaped nanostructures. This indicates that the hexagonal tetrapods have a large number of defects which is consistent with the observations of the Raman spectra discussed earlier. The Raman and PL spectra indicate that the nanostructures, derived from zinc nitrate precursor, are relatively defect free while those synthesized using the zinc acetate precursor contain a large number of defects most likely due to oxygen vacancies.

The optical transmission spectra of the nanostructures on ZnO thin films of different thickness and nanostructures on ZnO thin film of 100 nm thickness synthesized using ZnAcD precursor are

shown in figure 4.35 (a). At a wavelength of 600 nm, the transmission on the of the star shaped tetrapod nanostructures produced with the ZnNH is of the order of 80% on the 100 nm thickness film which decreases to 55% for the 400 nm film. The hexagonal nanorods synthesized using ZnAcD show a much lower transparency of 48% at 600 nm. All the films display a sharp fall in transmission at a wavelength of ~330 nm corresponding to the optical band gap of ZnO. The ball-shaped and hexagonal tetrapod structures, in figure 4.35 (b), in contrast show a very low transmittance probably due to the very low transmission of the Au thin films on which they are grown.



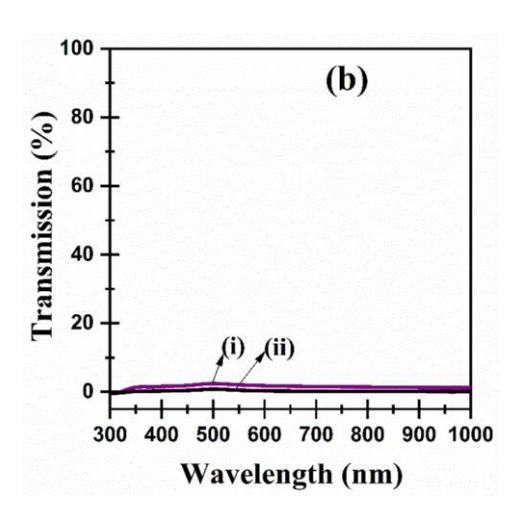


Figure 4.35: Optical transmission spectra of (a) star shaped ZnO tetrapods synthesized using zinc nitrate precursor on ZnO thin films of different thickness (i)100, (ii)150, (iii) 200, (iv) 400 nm and (v) hexagonal nanorods on ZnO thin film of 100 nm thickness using the zinc acetate precursor. (b)-(i) hexagonal tetrapods produced using zinc acetate precursor and (ii) ball shaped ZnO nanostructures synthesized using zinc nitrate on Au thin film of 100 nm thickness.

4.13 Role of different parameters on shape evolution

It is pertinent to note at this point that the microwave power, temperature of processing and duration are fixed for the synthesis of all the nanostructures. The only parameters that are varied are the precursor type (i.e. zinc nitrate or zinc acetate) and the films on which they are grown (ZnO or Au). In the case of ZnO films, the thickness is also varied. However, the FE-SEM images presented in figure 4.28 indicate that, there is not much effect of the thickness on the basic shape of the nanostructures. It is also evident that, independent of their shape and thickness of films on which they are grown, the nanostructures are polycrystalline with no preferred crystalline orientation. Significantly, independent of the shape, all the nanostructures are nanocrystalline in

nature. There are previous reports in literature that suggest that the shapes of the formed nanostructures are nucleated in solution. The role of microwave assistance is primarily to accelerate the process of nanostructuring. Both zinc nitrate and zinc acetate are known to yield shapes such as rice grain shapes, hexagonal rods, needles, balls and tetrapods in microwave hydrothermal synthesis [295-306, 272]. To understand this, the shape evolution can be traced to the chemical reactions that lead to the formation of ZnO, as stated in Part A. The first step is the decomposition of HMTA ((CH₂)₆N₄) to yield 4NH₃ which then reacts with water to form NH⁴⁺ and OH⁻ ions. The zinc precursors then react with the OH⁻ ions to form Zn(OH)₄²⁻ which then leads to the formation of ZnO. The role of HMTA is crucial in shape forming as it attaches to the non-polar facets of ZnO exposing only the polar (001) plane for crystal growth. Furthermore, in microwave assisted processes a large number of OH⁻ ions will be produced in a short time resulting in fast precipitation of Zn²⁺ ions. Due to this, they do not contribute significantly to the shape forming process.

Different shapes of nanostructures in ZnO produced by microwave hydrothermal synthesis have been reported using zinc nitrate and zinc acetate as the precursors and NaOH, KOH, CTAB and HMTA to aid the nanostructuring process. There are only limited studies that compare the shape evolution of ZnO nanostructures, as done in the present study, using two different precursors keeping all other growth parameters fixed. Cho et al [300] showed that Zinc nitrate precursor based nanostructures evolve in the form of rods because of the higher growth rate along the [0001] direction whereas. In the ZnO structure, the polar zinc and oxygen centres are tetrahedral in nature and there are six symmetric non-polar [1010] planes which are parallel to the [0001] direction and, if growth along these planes is reduced with respect to the [0001] direction, then needles or ricegrain shaped nanostructures form. Furthermore, the star shaped tetrapods could be the result of a large number of Zn(OH)₄²⁻ being generated in a short time. This is the probable explanation for the growth of star shaped tetrapods using the ZnNH. It has also been shown that the formation of hexagonal discs is promoted when growth along the six symmetric planes occurs at the expense of the growth in the [0001] direction, hexagonal discs form which possibly leads to the formation of nano-hexagonal rods using ZnAcD precursor on the ZnO film. The nucleation of the shape, thus, occurs in solution due to contributions from the chemical reactions and microwave radiation.

structures while zinc acetate precursors results in the formation of hexagonal rod based tetrapods as against the rice grain shaped tetrapods and hexagonal rods on the ZnO film. This points to the role of the thin film surface in determining the final shape. Oriented attachment and coarsening are two process that are commonly cited as driving nanoparticle growth [307-310]. It is hypothesized that subsequent to nucleation of the basic shape, oriented attachment enables the nanostructures to retain the shape as the dimension increases. The increase in dimension itself is facilitated by the process of coarsening. Thus, it is possible that the film provides a low free energy surface that aids in retaining the shapes that are first nucleated and subsequent oriented attachment and coarsening processes. A schematic view of the process of nanostructuring is shown in figure 4.36.

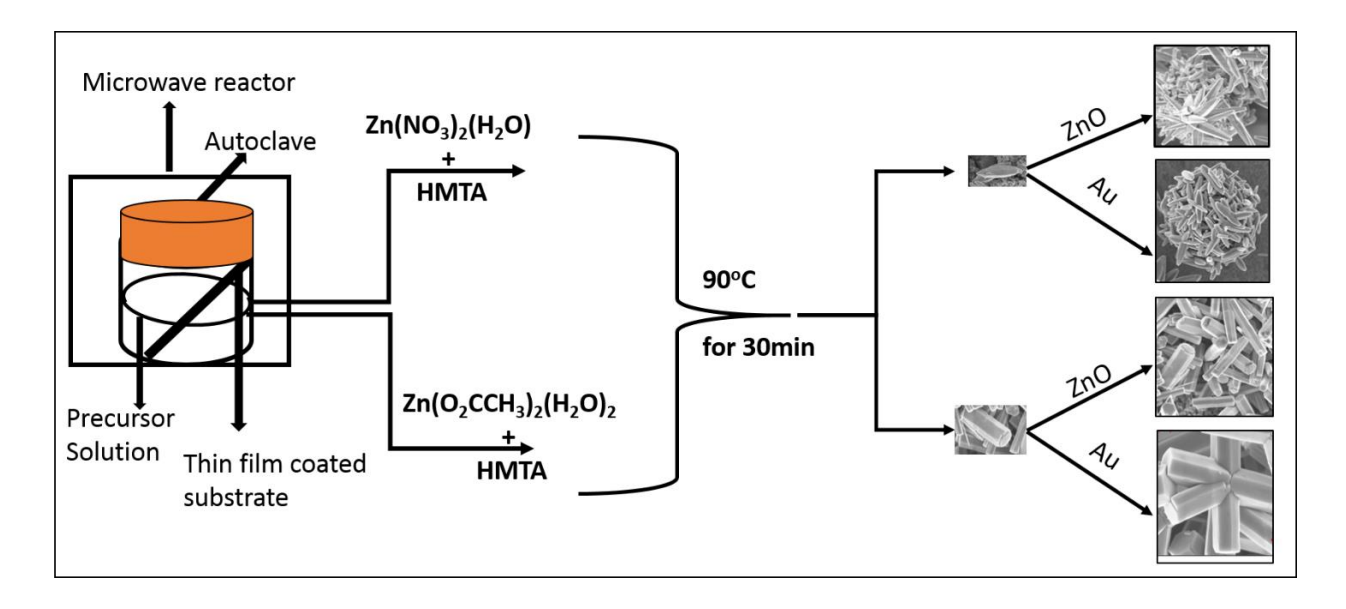


Figure 4.36: A schematic view of the process of nanostructuring.

The Raman and PL spectroscopy studies also indicate that the nanostructures on ZnO films have higher level of defects than the nanostructures on Au films. In addition, the PL spectra of nanostructures on ZnO are dominated by the UV-near band edge emission while those on Au films comprise both the UV peak and the defect related peak in the visible region. This is an important result from the applications perspective since the emission spectrum can be controlled by simply changing the substrate on which the nanostructures are given without changing any processing parameter. It would, thus, appear that the microwave assisted hydrothermal process lowers the

temperature and duration required for forming ZnO nanostructures, in comparison to the conventional process. It also leads to the formation of a hierarchy of structures which was not observed in the conventional process. However, given the limitations on experimentation, it was not possible to establish the temperature and duration of processing at which vertical alignment occurs.

4.14 Summary

In summary, the shape evolution of ZnO nanostructures produced on ZnO and Au thin films by microwave assisted hydrothermal processing is reported. A hierarchy of shapes that include ricegrain shaped particles at the nanoscale which assemble to form star shaped tetrapods, hexagonal rods that form hexagonal rod shaped tetrapods and micro-balls that emerge from clustering ricegrain shaped particles is obtained. The nanostructuring is controlled by a combination of microwave assistance, precursor used (zinc nitrate hexahydrate or zinc acetate dihydrate) and the thin films on which they are grown. The role of each of these parameters is elaborated. Raman and photoluminescence studies indicate the presence of defects which are both shape and thin film surface dependent. The photoluminescence spectra are dominated by the UV-near band edge emission and defect peaks that are shape dependent. The present study thus, provides, a simple technique to synthesize device quality nanostructures with controllable optical properties without the need to change many processing parameters. As a first approximation, it can also be inferred that the microwave assistance accelerates the process of nanostructuring and may be more suitable for applications involving flexible substrates.

Chapter

5

Effect of different metal and metal oxides seed layers on the growth and wettability of ZnO nano/ micro structures

Parts of this chapter were published in the paper: Y. Rajesh, D. D. Purkayastha, M. Ghanashyam Krishna, *Seed layer mediated wettability and wettability transition of ZnO nano/micro-rod arrays*, Journal of Alloys and Compounds, 857, 157617 (2021).

Abstract

In this chapter, an overall comparison of the growth of ZnO nano/micro rod arrays (NMRA) on different metals (In, Sn and Au) and different metal oxides (In₂O₃, SnO₂-x and ZnO) is presented. The objective is to establish whether a metal seed layer or metal oxide layer is better suited for the growth of ZnO NMRAs. These studies indicate that metal oxide seed layer thin films are more suited for the growth of nanowire arrays and even among the metal oxides, ZnO is the most favourable oxide. In the case of metals, the structures grow in the form of hexagonally shaped micro-rod arrays with low packing density. All the rod arrays grow preferentially along the (100) direction. Photoluminescence and Raman spectroscopy of the structures on oxidized In and Sn exhibit fewer oxygen vacancies and defects in comparison to Au and ZnO seeded structures. Wettability studies indicate that all the arrays are hydrophobic in nature, the arrays are superhydrophobic on ZnO with a contact angle of 150.4°. There is a rapid transition to the hydrophilic/superhydrophilic state under the influence of UV irradiation. The transition is fastest on ZnO seed layers followed by oxidized indicate that all the arrays are hydrophobic in nature, the arrays are superhydrophobic on ZnO with a contact angle of 150.4°. There is a rapid transition to the hydrophilic/superhydrophilic state under the influence of layers, suggesting promise for selfcleaning applications.

5.1. Background

4.

In this chapter the main objectives are to grow ZnO nano/micro rod arrays (NMRAs) by hydrothermal process (HP) on different metal and metal oxide thin film seed layers and investigate their effect on the wettability. The metal layers are Au, In and Sn while the oxide layers are In, Sn and Zn oxides. The In and Sn oxides are prepared by post-deposition annealing of the corresponding metal layers. In contrast, the ZnO films are prepared directly by vacuum thermal evaporation of a ZnO source, followed by annealing. A study of (1) the hydrothermal growth of ZnO nanostructures on non-patterned as-deposited and annealed In and Sn seed layers and (2) their wettability and wettability transitions under UV irradiation has not been reported in literature, earlier. The NMRAs are characterized using scanning electron microscopy, x-ray diffractometry, photoluminescence Raman spectroscopy and water contact angle measurements.

Indium (In, 10 -50 nm thickness), Tin (Sn, 10 -50 nm thickness), and ZnO (100 nm thickness) thin film seed layers were deposited using thermal evaporation on glass substrates. The as-deposited metal seed layers are heat treated as follows: (1) Indium layer is annealed at 200°C for 2hours (2) Tin layer is annealed at 300°C for 2hours and (3) ZnO layer is annealed at 400°C for 2 hours in air. In the rest of the chapter the as-deposited In layer is identified as InA, the heat-treated layer as InO. Similarly, the as-deposited tin layer is identified as SnA and the heat-treated layer as SnO. The hydrothermal process of ZnO structures grown on these seed layers involves the following steps: An aqueous solution containing each of 25 mM Zinc acetate dehydrate [Zn(O₂CCH₃)₂(H₂O)₂, 99.0%] is mixed with 25 mM hexamethylenetetramine (HMTA) [(CH₂)₆N₄, 99.0%]. The seeded substrates are dipped into above said aqueous solutions at growth temperature

of 120 °C for 30 and 180 minutes. The durations are fixed based on the results described in chapter

5.1.1. Growth patterns and crystallographic texture of ZnO structures

The cross-sectional SEM images of the hydrothermal processed (HP) ZnO on 10 nm thickness InA and InO thin films and grown at 120°C for 30 min and 180 min is shown in figure 5.1 (a)-(d). It is evident from these figures that after 30 min of HP, the ZnO grows only in the form of a layer on InA. However, after 180 min. there is clear growth of vertically aligned rod arrays. The rods are cylindrical in nature and vertically aligned at different angles. The diameter of the

rods is of the order of 500-1000nm with lengths between 10-15 μm indicating a very high aspect ratio (ranging from 10 to 30).

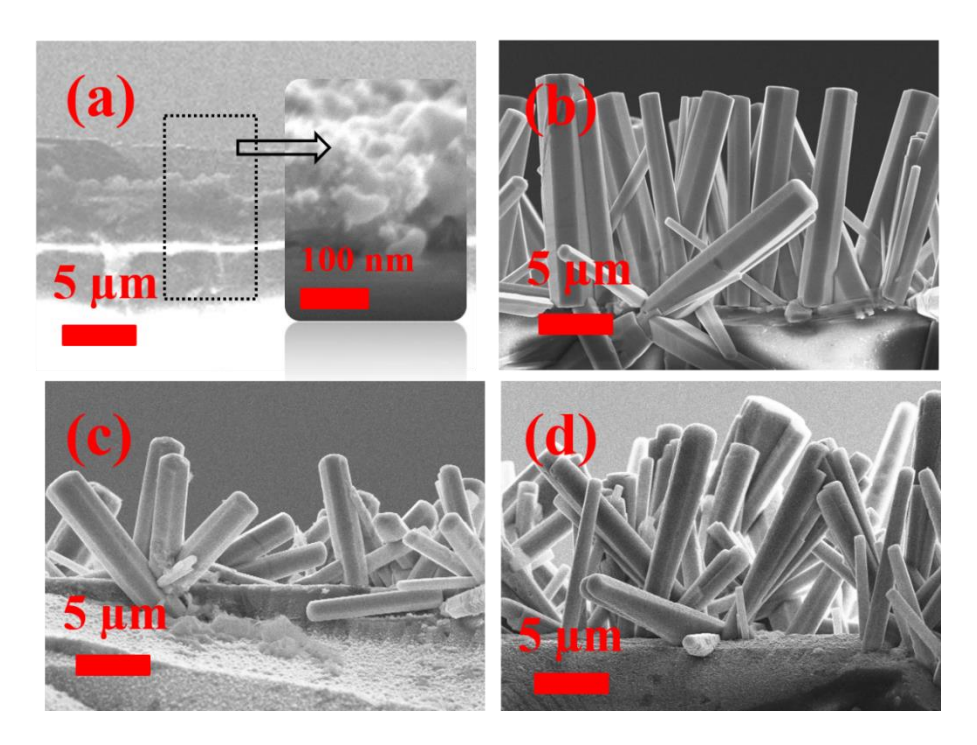


Figure 5.1: Cross-sectional SEM images of ZnO hydrothermally synthesized on 10 nm thickness as-deposited In metal thin film at 120 °C for (a) 30 min, (b) 3 hrs. and annealed In metal thin film at 120 °C for (c) 30 min, (d) 3 hrs.

Similar to the InA thin film, even on the InO thin film the growth of ZnO nanorods is inhibited for 30 min as observed in figure 5.1(c) from which it is evident that the diameter is of the order of 1 μ m but the length is only 5-7 μ m. However, after 180 min there is an increase in length of the rods to 10-15 μ m without significantly affecting the diameter (figure 5.1(d)).

The cross-sectional SEM images of the HP ZnO on 20 nm thickness InA and InO thin films and grown at 120°C for 30 min and 180 min is shown in figure 5.2 (a)-(d). It is evident from these figures that after 30 min of HP the ZnO grows only in the form of a layer on InA. However, after 180 min. there is clear growth of vertically aligned rod arrays. The rods are hexagonal and cylindrical in nature and vertically aligned at different angles. The diameter of the rods is of the order of 500-1000nm with lengths between 10-15 µm. Similar to the InA thin film, even on the InO thin film the growth of ZnO nanorods is inhibited for 30 min as observed in figure 5.2(c) from which it is evident that the diameter is of the order of 1 µm but the length is only 5-6 µm. However,

after 180 min there is an increase in length of the rods to 15-20 μ m without significantly affecting the diameter (figure 5.2(d)).

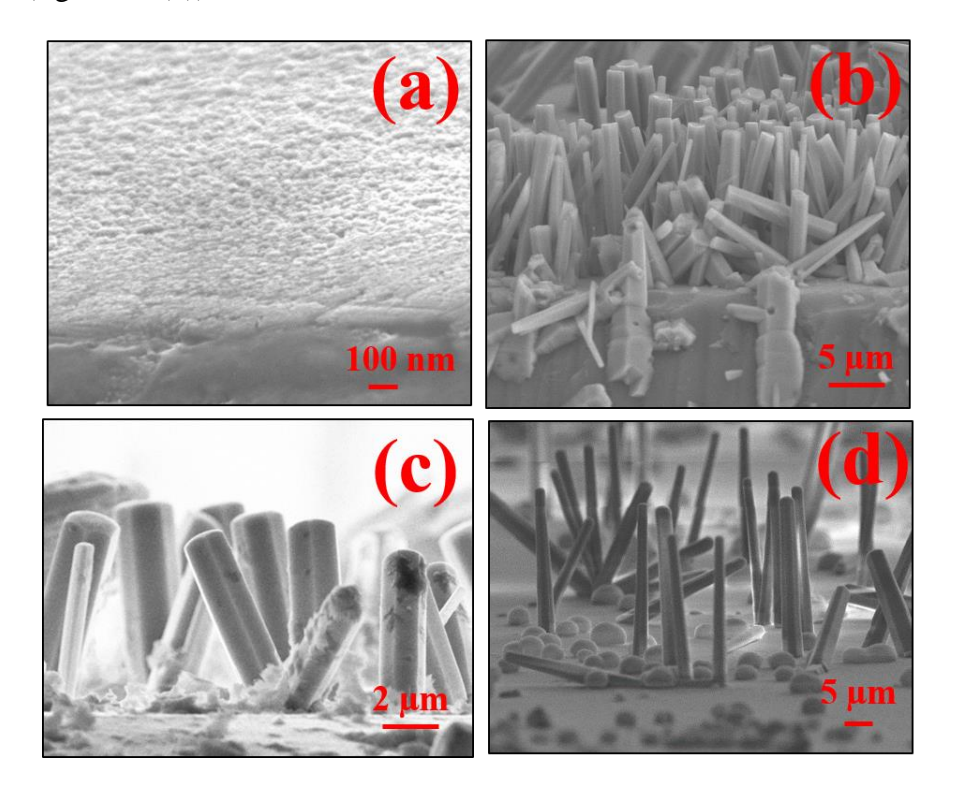


Figure 5.2: Cross-sectional SEM images of ZnO hydrothermally synthesized on 20 nm thickness as-deposited In metal thin film at 120 °C for (a) 30 min, (b) 3 hrs, and annealed In metal thin film at 120 °C for (c) 30 min, (d) 3 hrs.

The cross-sectional images of the ZnO structures on 30 nm, 40 nm and 50 nm thickness InA and InO films are displayed in figure 5.3 (a)-(d), 5.4 (a)-(d) and 5.5 (a)-(d) respectively. It is evident from figures 5.3, 5.4 and 5.5 that increase in thickness of the InA and InO films leads to increased packing density of the rods. The rods appear to be more hexagonal than those on the 10 nm thickness films, indicating initiation of faceting and in the case of InO 3hrs the rods shows cylindrical shapes. The cross-sectional images of the ZnO structures on 10 nm and 20 nm thickness SnA and SnO thin films are shown in figure 5.6 (a)-(d) and 5.7 (a)-(d). It is evident that ZnO nanorods do not form after 30 min of synthesis on as-deposited and annealed Sn metal layers (figure 5.6 (a) and (c)-5.7 (a)). Synthesis duration of 3 hrs results in initiation of randomly aligned nanorods on Sn thin films (figure 5.6 (b) 5.7 (b)) whereas on SnO thin films, in figure 5.6 (d)-5.7

(d), there is clear evidence for the growth of cylindrical nanorods of 15-20 μm length and approximately 1-1.5 μm diameter.

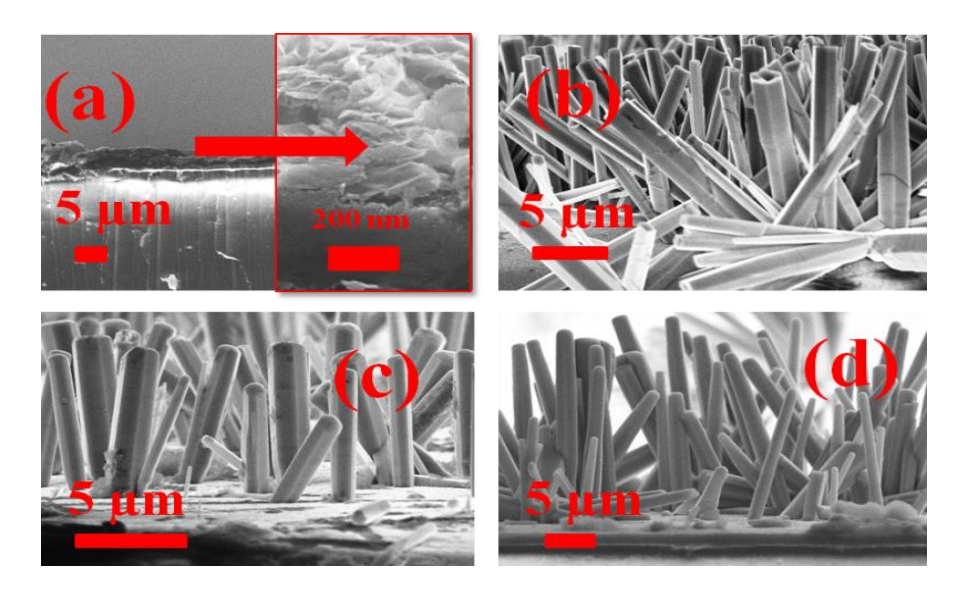


Figure 5.3: Cross-sectional SEM images of ZnO hydrothermally synthesized on 30 nm thickness as-deposited In metal thin film at 120 °C for (a) 30 min, (b) 3 hrs, and annealed In metal thin film at 120 °C for (c) 30 min, (d) 3 hrs.

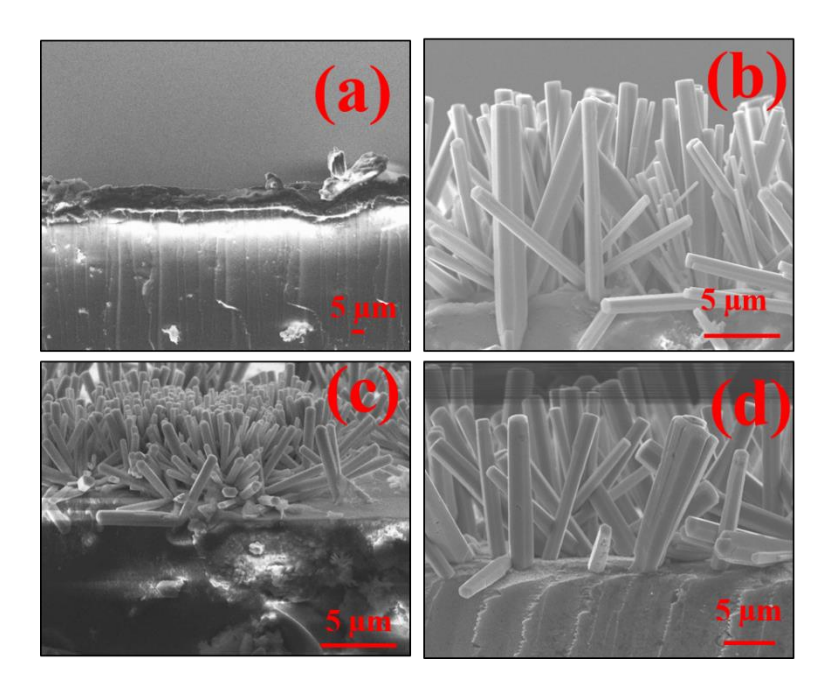


Figure 5.4: Cross-sectional SEM images of ZnO hydrothermally synthesized on 40 nm thickness as-deposited In metal thin film at 120 °C for (a) 30 min, (b) 3 hrs, and annealed In metal thin film at 120 °C for (c) 30 min, (d) 3 hrs.

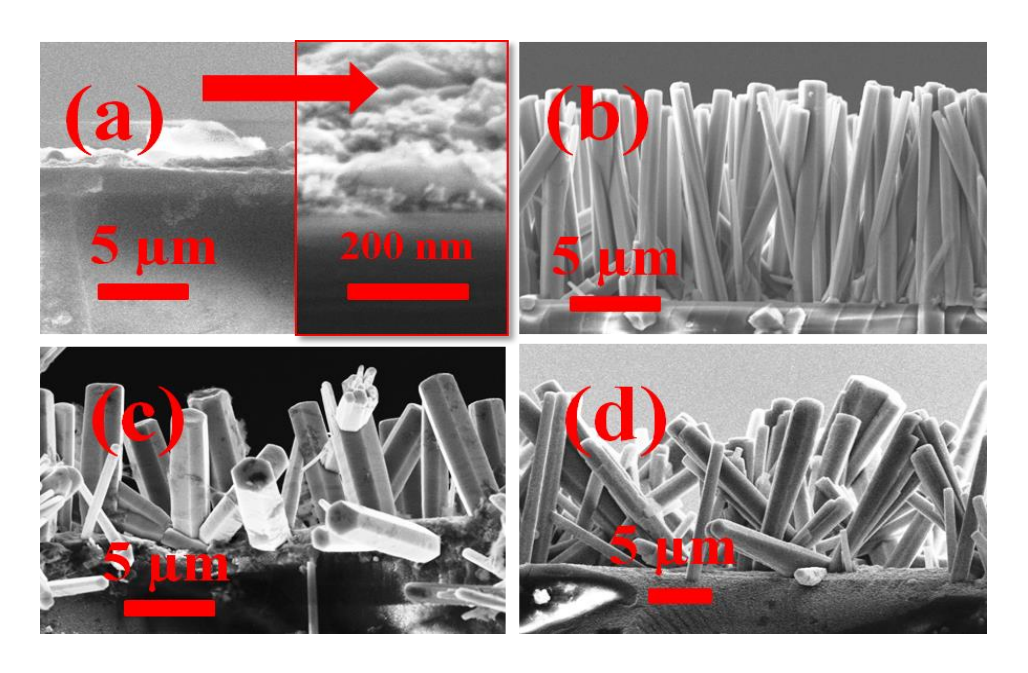


Figure 5.5: Cross-sectional SEM images of ZnO hydrothermally synthesized on 50 nm thickness as-deposited In metal thin film at 120 °C for (a) 30 min, (b) 3 hrs, and annealed In metal thin film at 120 °C for (c) 30 min, (d) 3 hrs.

It is clear that both diameter and length increase with duration but the increase in length with duration of HP is much greater than diameter. Further increase in thickness of the SnA and SnO films to 30, 40 and 50 nm has a profound effect on the nature of the ZnO rod arrays as observed from figures 5.8 (a)-(d),5.9 (a)-(d) and 5.10 (a)-(d). In contrast to the case of ZnO structures on InA and InO films, the rod density on SnA and SnO films decreases as the thickness is increased. However, in contrast to the InA and InO case, there is no hexagonalization of the rods at higher thickness of the underlying SnA and SnO films. It is clear that the activation barrier for growth on metal seed layers is grater than that on oxide layers. This inference is drawn from the fact that, on annealed In and Sn as well as ZnO seed layers, vertically aligned rods are observed after a much shorter processing duration. It also appears that a 10 nm thickness InA/ InO or SnA/ SnO film is sufficient to support the growth of good quality ZnO nano/micro rod arrays.

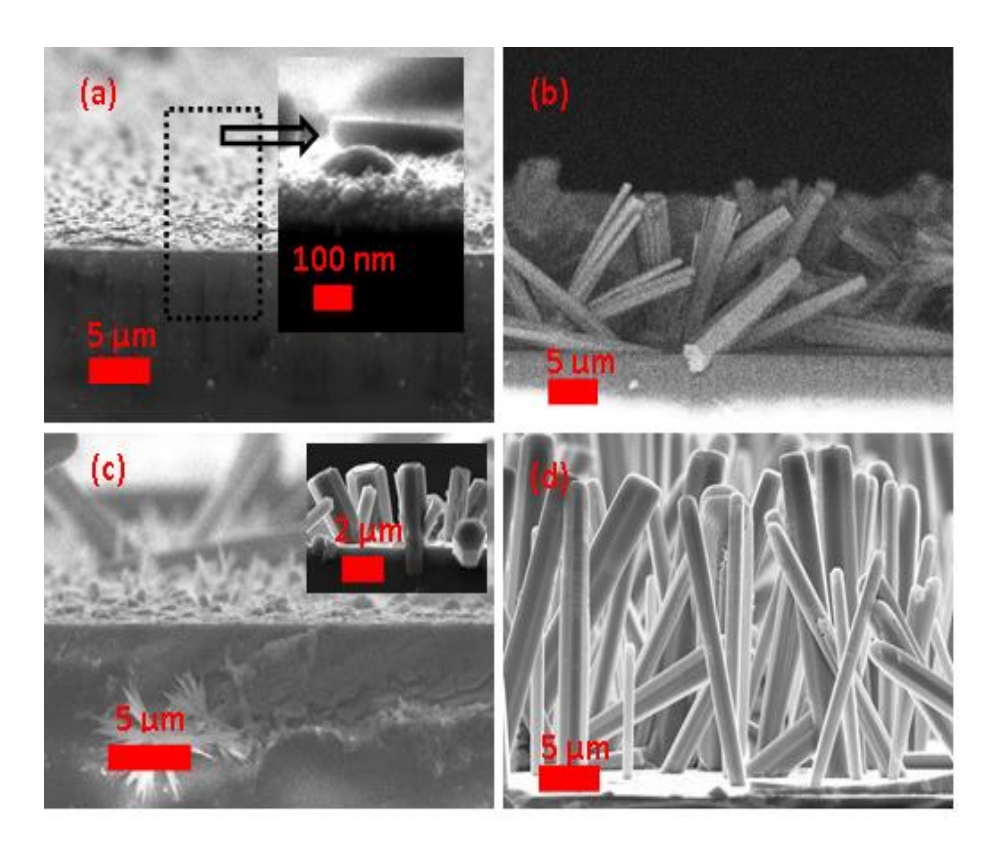


Figure 5.6: Cross-sectional SEM images of hydrothermally synthesized ZnO on 10 nm thickness as-deposited Sn metal thin film at 120 °C for (a) 30 min, (b) 3 hrs, and annealed Sn metal thin film at 120 °C for (c) 30 min, (d) 3 hrs.

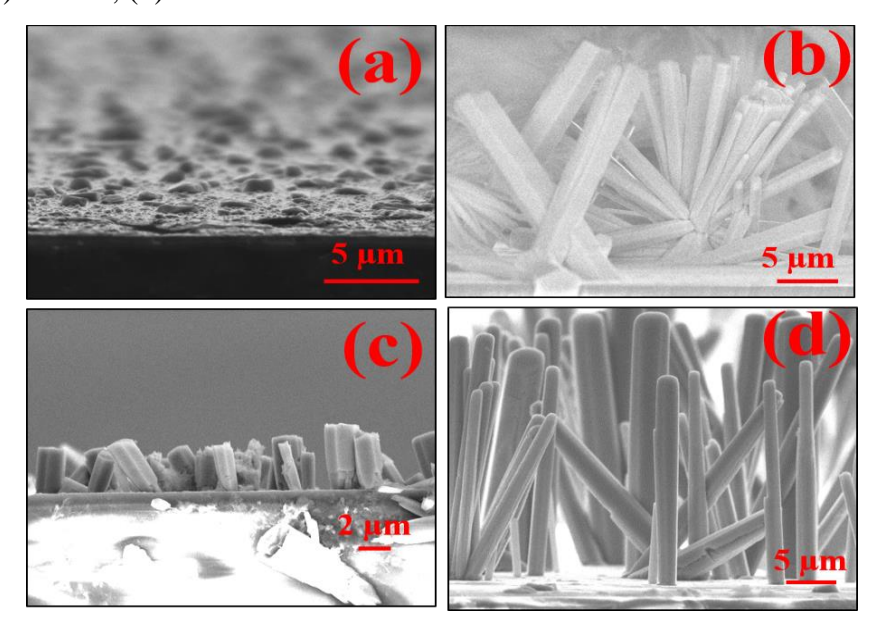


Figure 5.7: Cross-sectional SEM images of hydrothermally synthesized ZnO on 20 nm thickness as-deposited Sn metal thin film at 120 °C for (a) 30 min, (b) 3 hrs and annealed Sn metal thin film at 120 °C for (c) 30 min, (d) 3 hrs.

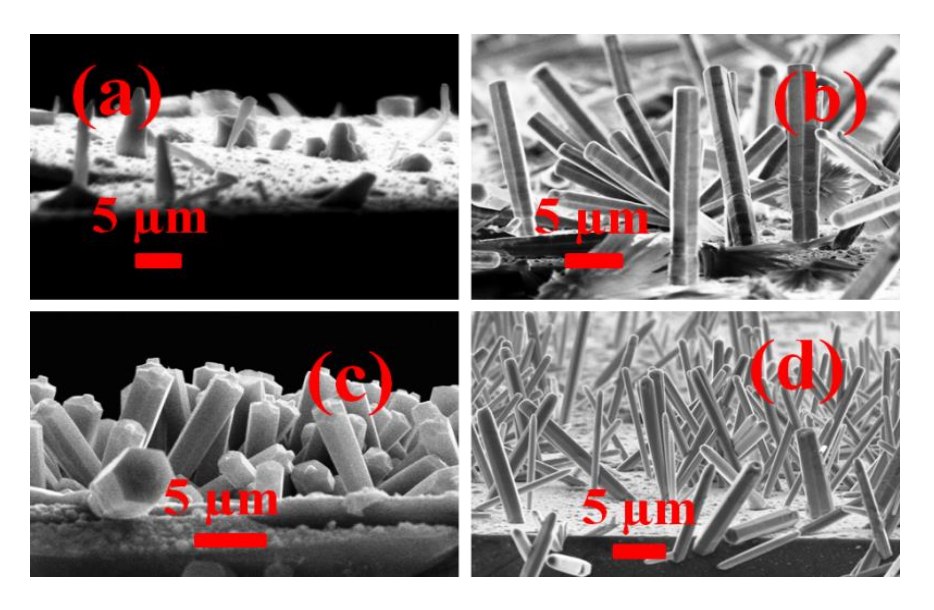


Figure 5.8: Cross-sectional SEM images of hydrothermally synthesized ZnO on 30 nm thickness as-deposited Sn metal thin film at 120 °C for (a) 30 min, (b) 3 hrs, and annealed Sn metal thin film at 120 °C for (c) 30 min, (d) 3 hrs.

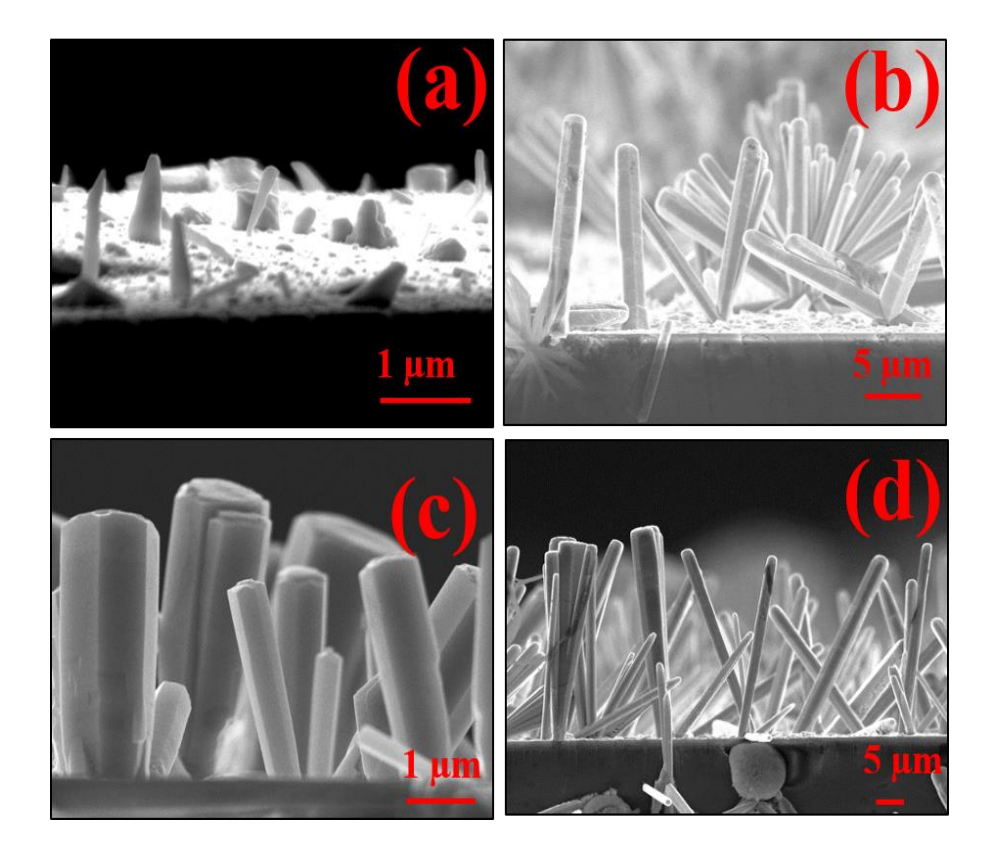


Figure 5.9: Cross-sectional SEM images of hydrothermally synthesized ZnO on 40 nm thickness as-deposited Sn metal thin film at $120\,^{\circ}$ C for (a) 30 min, (b) 3 hrs, and annealed Sn metal thin film at $120\,^{\circ}$ C for (c) 30 min, (d) 3 hrs.

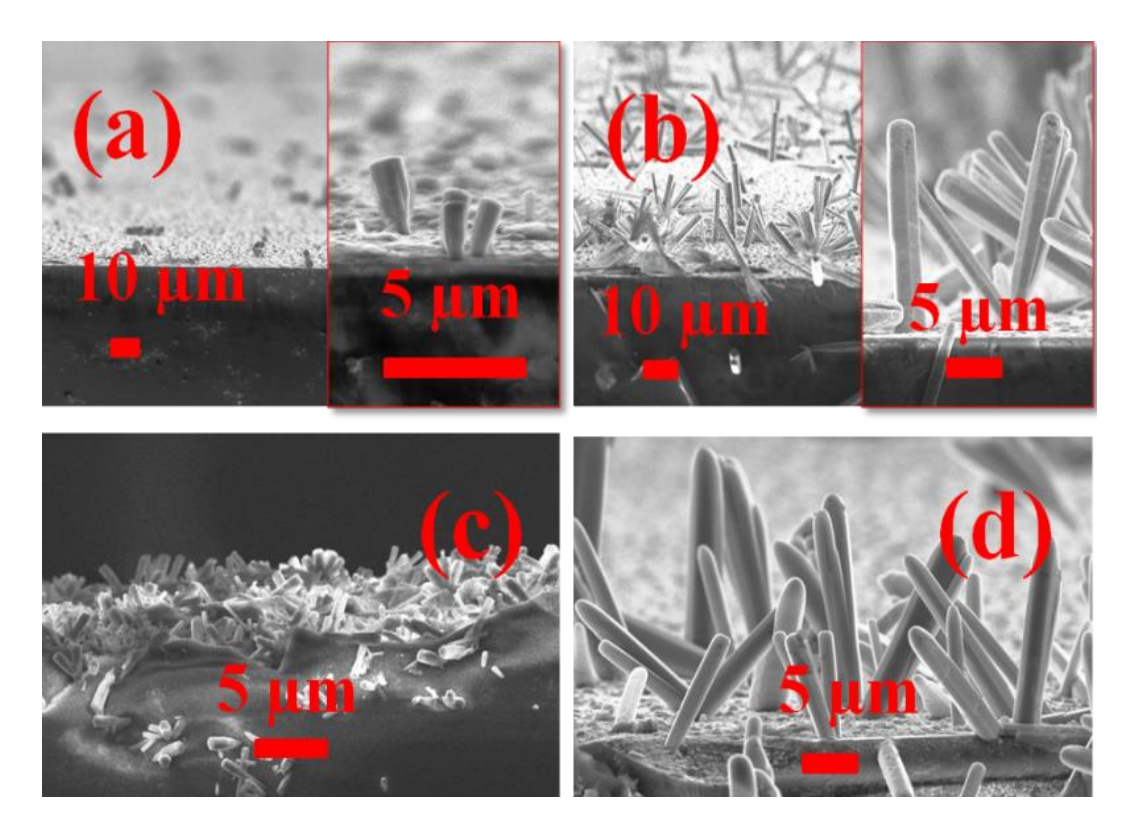


Figure 5.10: Cross-sectional SEM images of hydrothermally synthesized ZnO on 50 nm thickness as-deposited Sn metal thin film at 120 °C for (a) 30 min, (b) 3 hrs, and annealed Sn metal thin film at 120 °C for (c) 30 min, (d) 3 hrs.

X-ray diffraction patterns of the HP ZnO on 10 nm, 20 nm 30 nm, 40 and 50 nm thickness InA, InO, SnA and SnO thin films are displayed in figures 5.11 (a)-(d), 5.12 (a)-(d), 5.13 (a)-(d), 5.14 (a)-(d), and 5.15 (a)-(d). Similarly, the crystallographic texture of each thickness seed layers of the HP ZnO on the SnA and SnO seed layers is presented in figures 5.16 (a)-(d), 5.17 (a)-(d), 5.18 (a)-(d), 5.19 (a)-(d) and 5.20 (a)-(d).

The texture coefficient of the (100) peak on InA is of the order of 0.55 while it is 0.38 on the InO seed layer at thickness of 10 nm. The corresponding texture coefficient values are 0.44 and 0.23 on the 10 nm SnA and SnO seed layers. In the case of the ZnO seed layers the values are 0.53 and 0.20 respectively for 3hrs and 30 min synthesis. The crystallite size is of the order of 60-70 nm in all cases. The more interesting observation was that the strain was tensile in nature, on all the seed layers. Both In and Sn crystallize in the body centred tetragonal structure with lattice parameters of $a=b=3.25\text{\AA}$, c=4.94 Å and $a=b=5.83\text{\AA}$ c=3.18 Å respectively. The rhombohedral form of Indium oxide has a lattice parameter of a=b=c=5.48Å while tin oxide crystallizes in the rutile

structure with lattice parameters of a=b=4.75 and c=3.18 Å respectively. The lattice parameters of wurtzite ZnO are a=3.290, c=5.241Å. Clearly the origin of strain in the ZnO structures is the

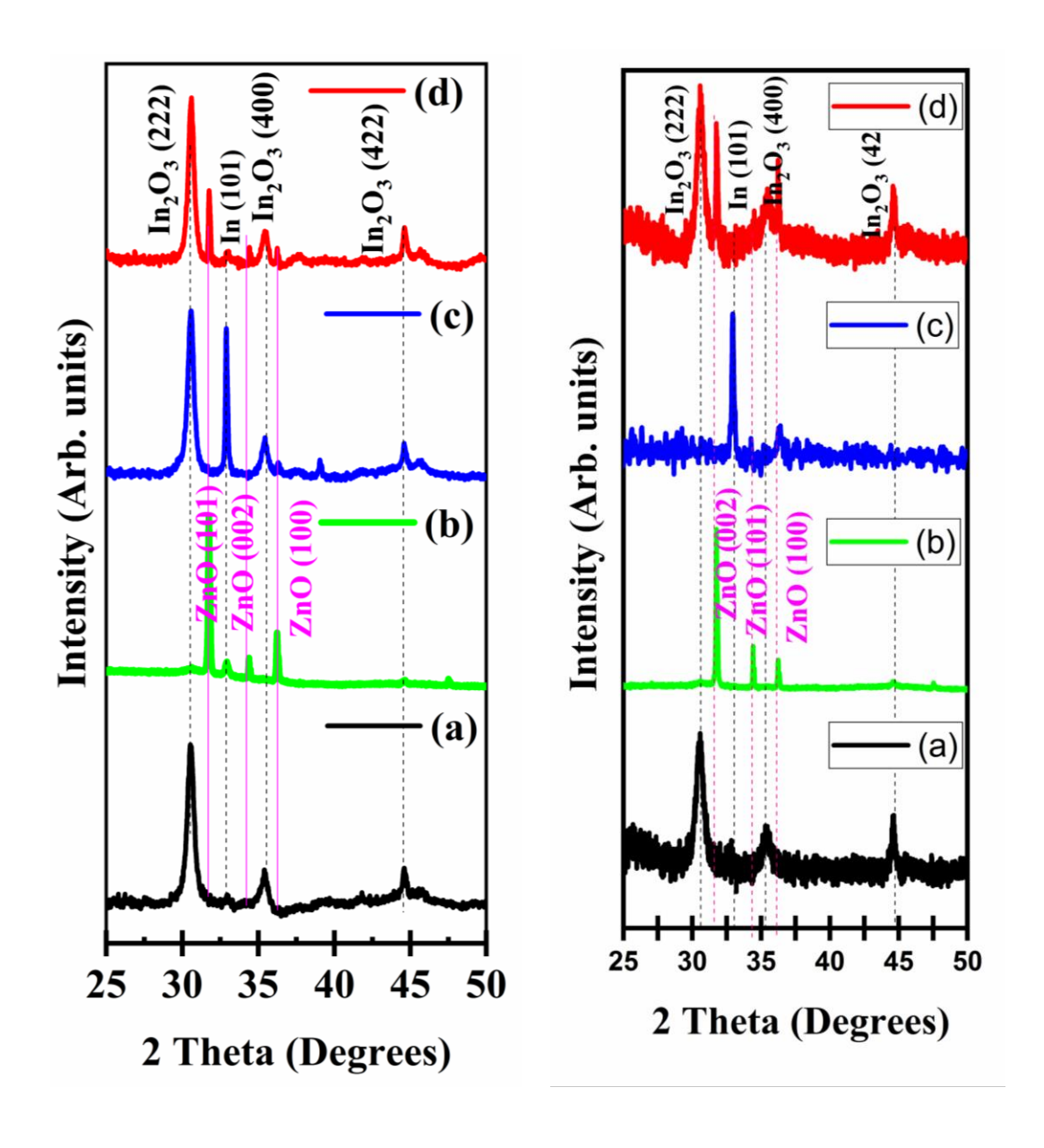


Fig: 5.11 (left panel): XRD patterns of the ZnO structures on 10nm of InA seed layers for (a) 30mins (b) 3hrs; InO seed layers for (c) 30 min (d) 3hrs.

Figure 5.12 (right panel): XRD patterns of the ZnO structures on 20nm of InA seed layers for (a) 30mins (b) 3hrs; InO seed layers for (c) 30 min (d) 3hrs.

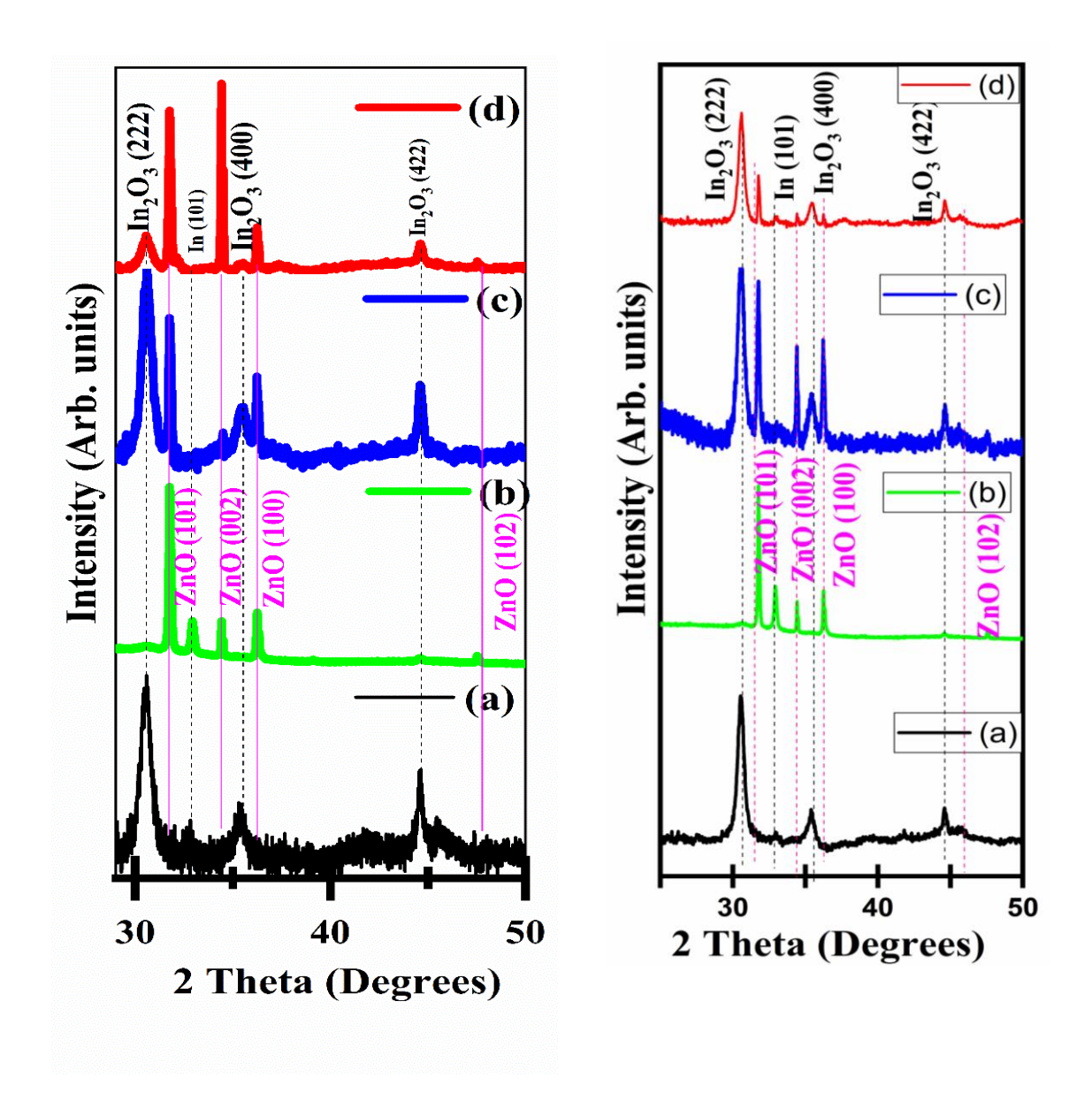


Figure 5.13 (Left panel): XRD patterns of the ZnO structures on 30 nm of InA seed layers for (a) 30mins (b) 3hrs; InO seed layers for (c) 30 min (d) 3hrs.

Figure 5.14 (right panel): XRD patterns of the ZnO structures on 40nm of InA seed layers for (a) 30mins (b) 3hrs; InO seed layers for (c) 30 min (d) 3hrs.

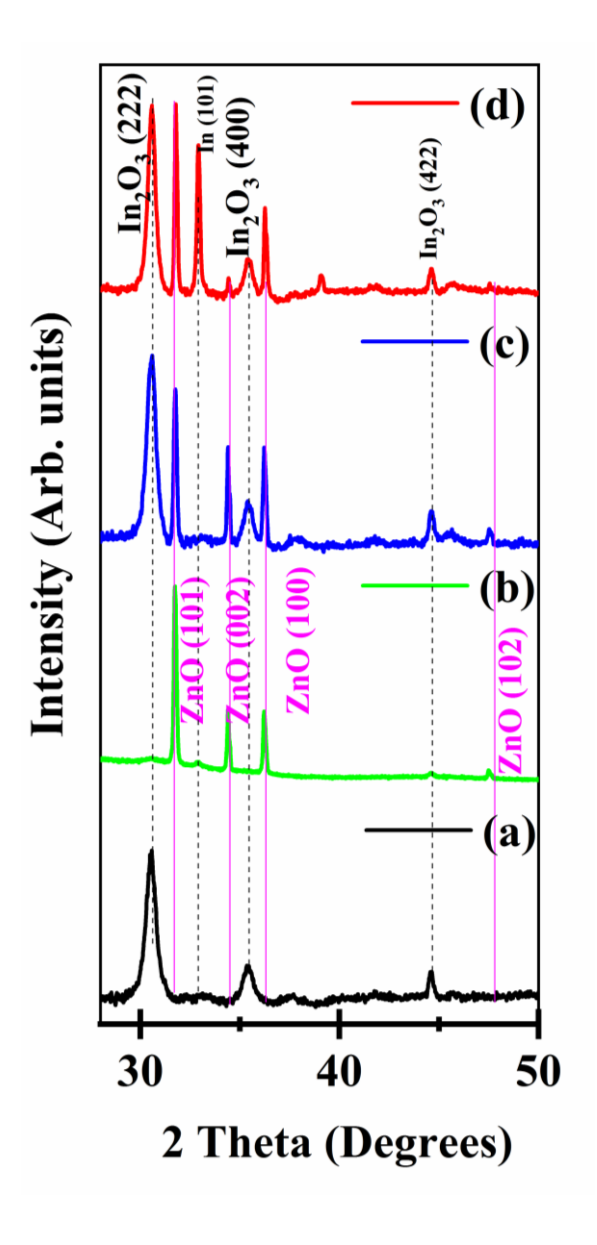


Fig: 5.15: XRD patterns of the ZnO structures on 50nm of InA seed layers for (a) 30mins (b) 3hrs; InO seed layers for (c) 30 min (d) 3hrs.

large lattice mismatch between the seed layers and ZnO. It is probable that the strain induces polycrystallinity as well the randomly aligned nanorods in many of the cases. The alignment on ZnO seed layers is more uniform possibly because of the lattice matching.

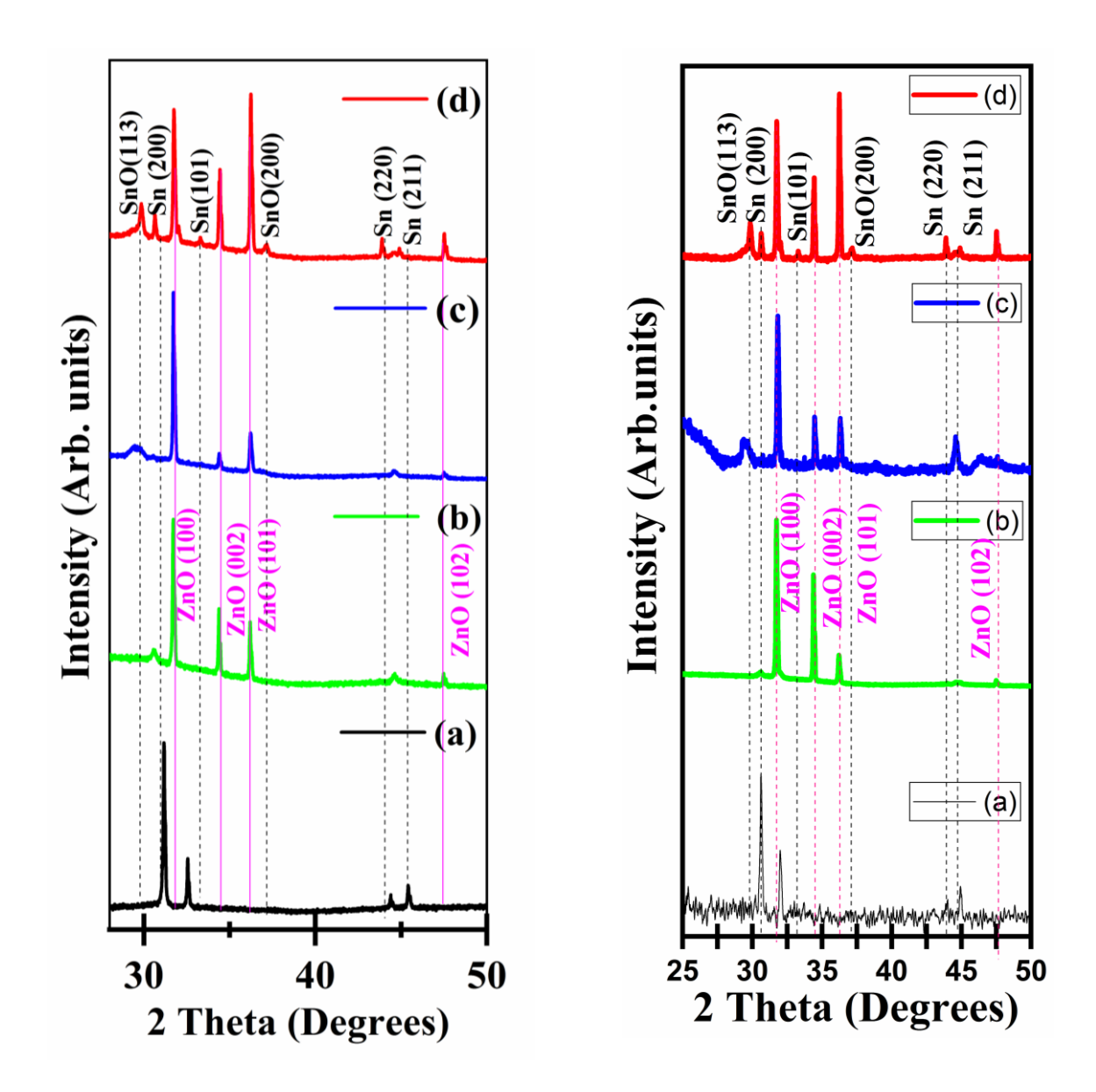


Figure 5.16 (Left panel): XRD patterns of the ZnO structures on 10 nm of SnA seed layers for (a) 30mins (b) 3hrs; SnO seed layers for (c) 30 min (d) 3hrs.

Figure 5.17 (right panel): XRD patterns of the ZnO structures on 20 nm of SnA seed layers for (a) 30mins (b) 3hrs; SnO seed layers for (c) 30 min (d) 3hrs.

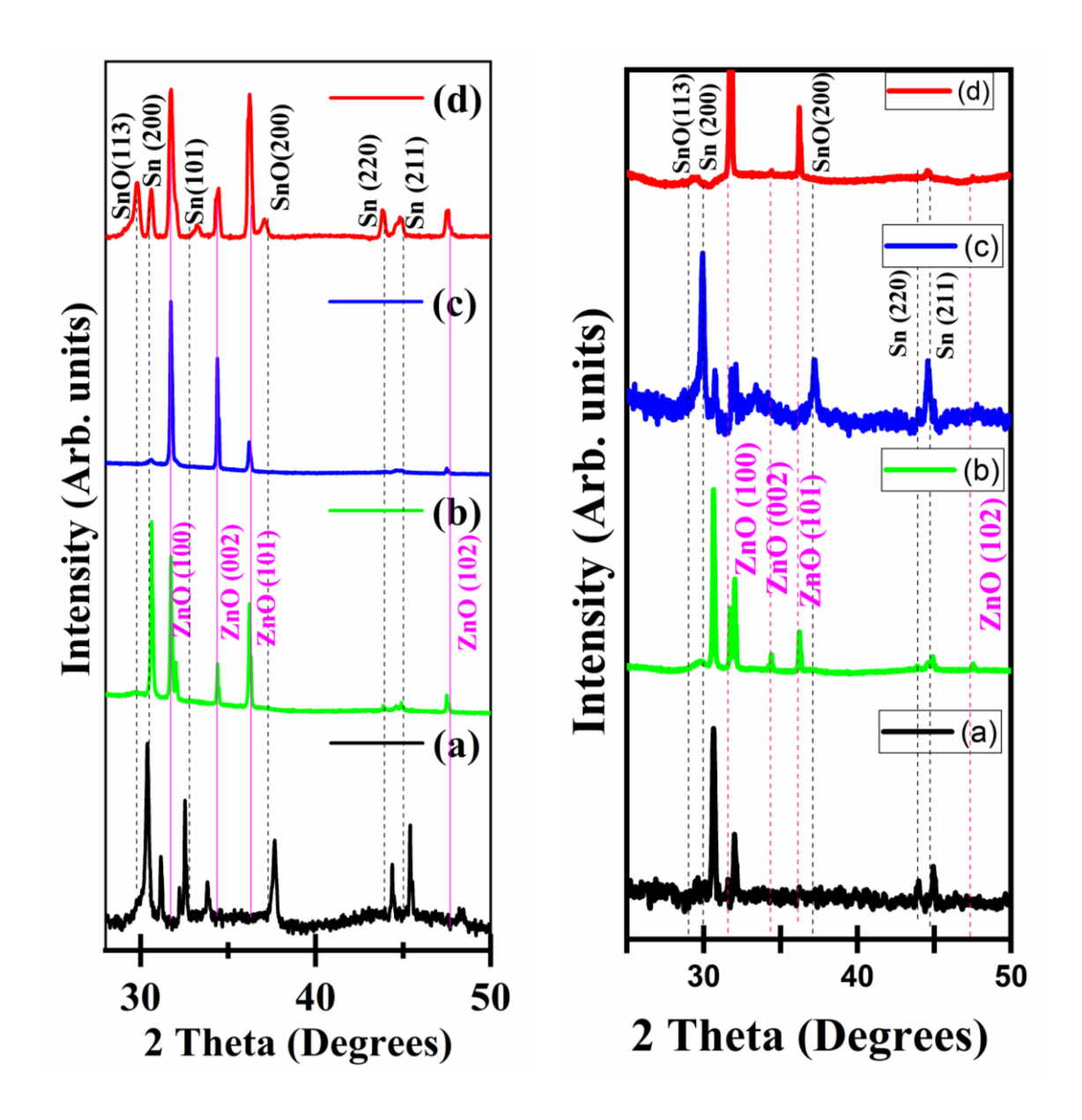


Figure 5.18 (Left panel): XRD patterns of the ZnO structures on 30 nm of SnA seed layers for (a) 30mins (b) 3hrs; SnO seed layers for (c) 30 min (d) 3hrs.

Figure 5.19 (right panel): XRD patterns of the ZnO structures on 40nm of SnA seed layers for (a) 30mins (b) 3hrs; SnO seed layers for (c) 30 min (d) 3hrs.

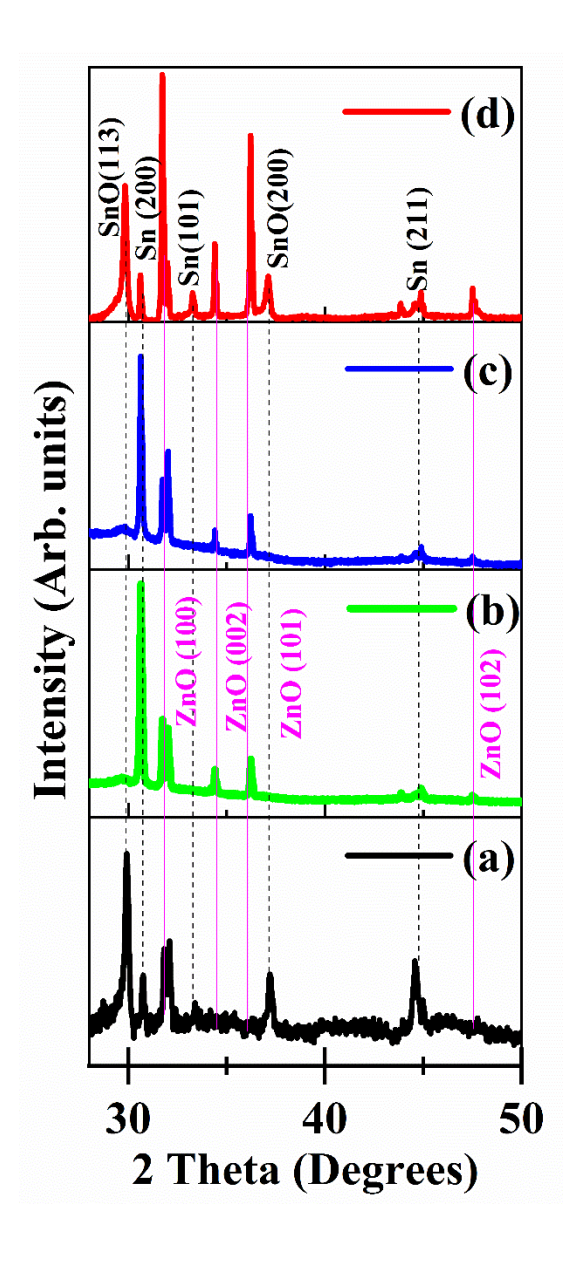


Figure: 5.20 XRD patterns of the ZnO structures on 50 nm of SnA seed layers for (a) 30mins (b) 3hrs; SnO seed layers for (c) 30 min (d) 3hrs.

As discussed in chapter 4, HMTA plays an important role in the alignment, shape and crystallographic texture of the observed structures. It is also observed that the interface between the seed layer and ZnO is quite important. This is particularly evident when the seed layers of In and Sn are pre-annealed to form oxides, prior to the HP process. The activation barrier for growth is much higher on the metal seed layers as evidenced by the absence of nano/micro rods after 30 min of processing. On the pre-annealed seed layers, in contrast, even at 30 min there is evidence

for the formation of nano/micro rod arrays. The growth patterns on Au and ZnO confirm this observation. On Au seed layers no growth is observed at 30 min whereas on ZnO there is clear evidence for the formation of nanowires. Thus, oxide seed layers are more amenable for the growth of nanorod arrays than metal seed layers.

5.2 Raman spectroscopy

The Raman spectra of ZnO at different thickness on InA, InO seed layers are shown in figures 5.21 (a)-(c). In the present case, on the In metal seed layer for 3hrs, the most intense peak appears at 437cm^{-1} and is assigned to the E_2 high mode. There can be shifts in the peak position, shape and width depending on the sample conditions (crystallinity, strain, defects, vacancies etc.).

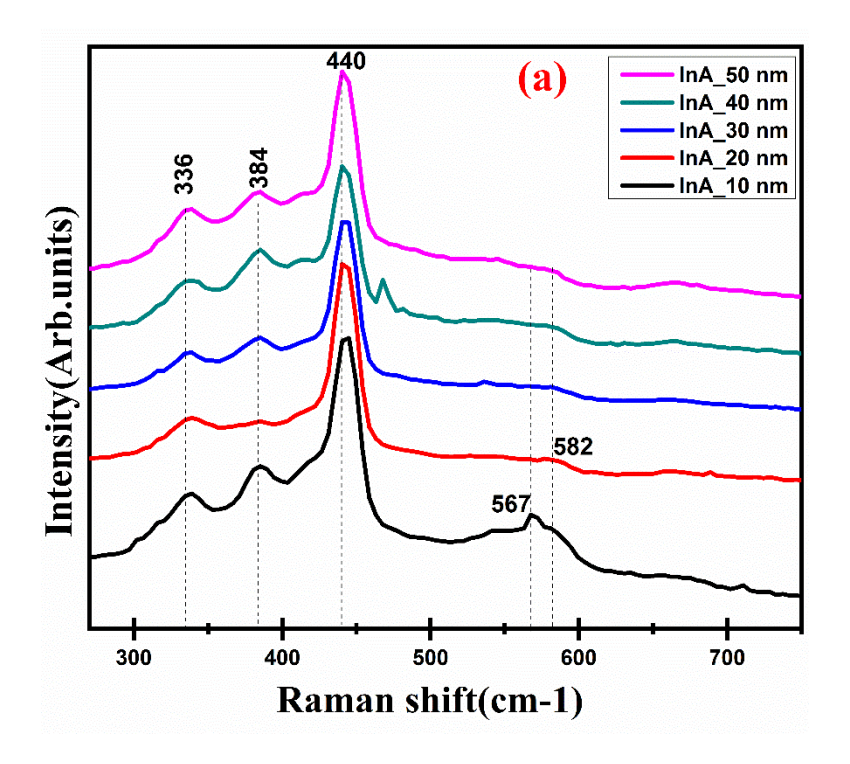


Figure 5.21: Raman spectra of ZnO NMRAs different thickness of InA seed layer for (a) 3hrs.

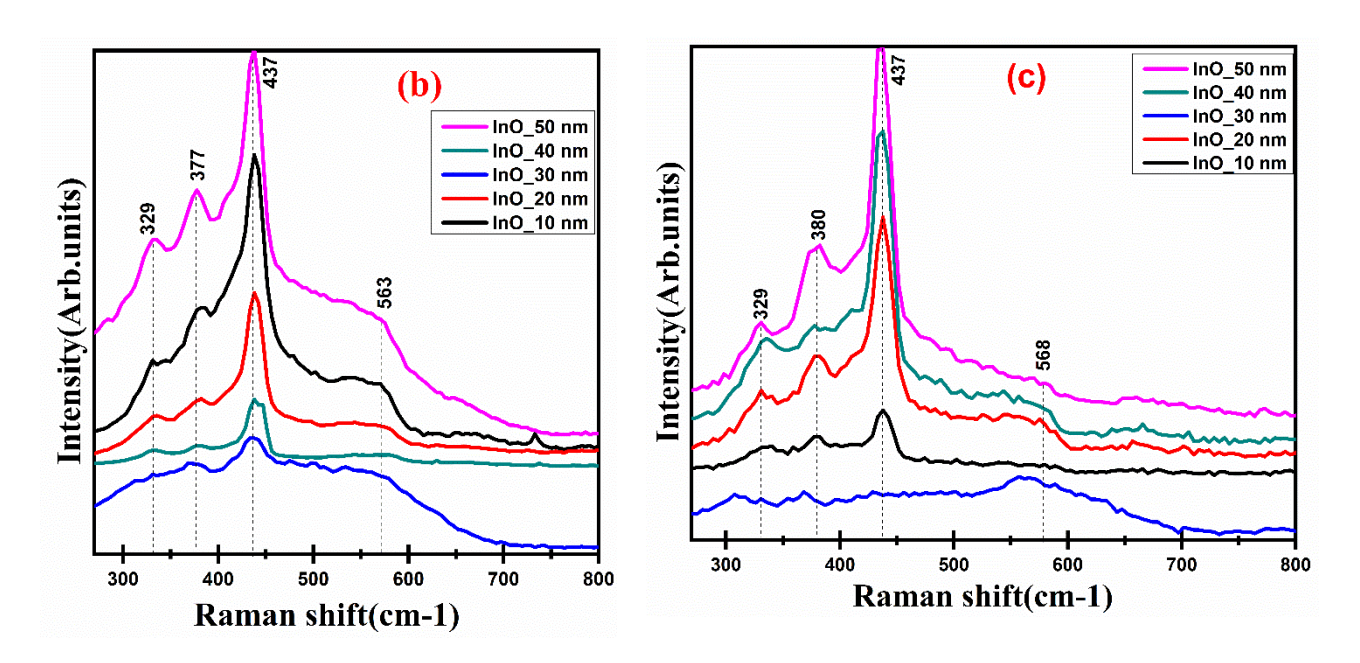


Figure 5.21 (b): Raman spectra of ZnO NMRAs different thickness of InO seed layer for (b) 30 mins, and (c) 3hrs.

Similarly, the Raman spectra of ZnO at different thickness of SnA, SnO seed layers are shown in figures 5.22 (a)-(c). It is observed on the Sn metal seed layer for 3hrs, the most intense peak appears at 437cm^{-1} and is assigned to the E_2 high mode.

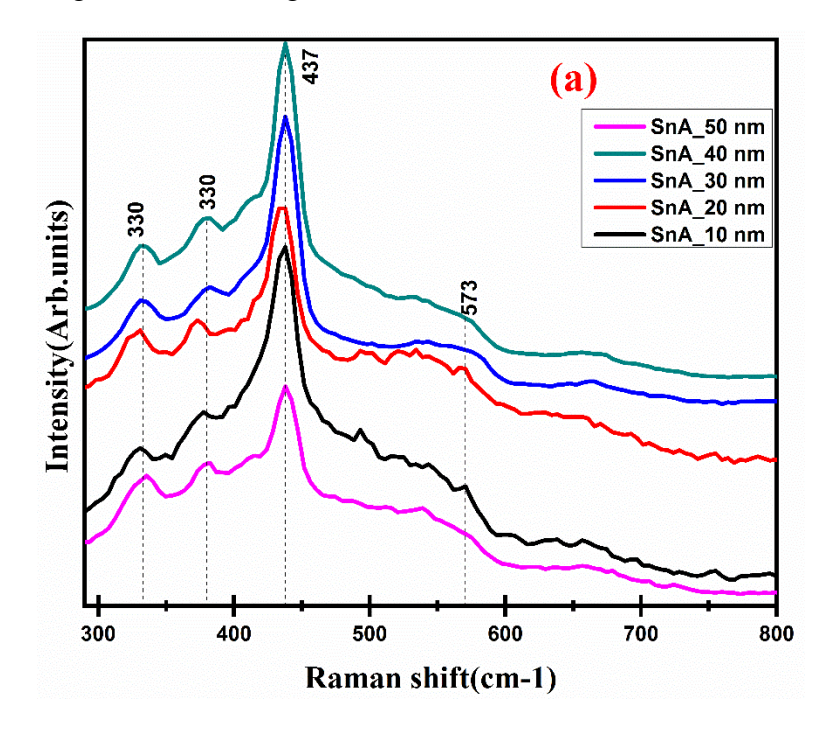


Figure 5.22: Raman spectra of ZnO NMRAs different thickness of SnA seed layer for (a) 3hrs.

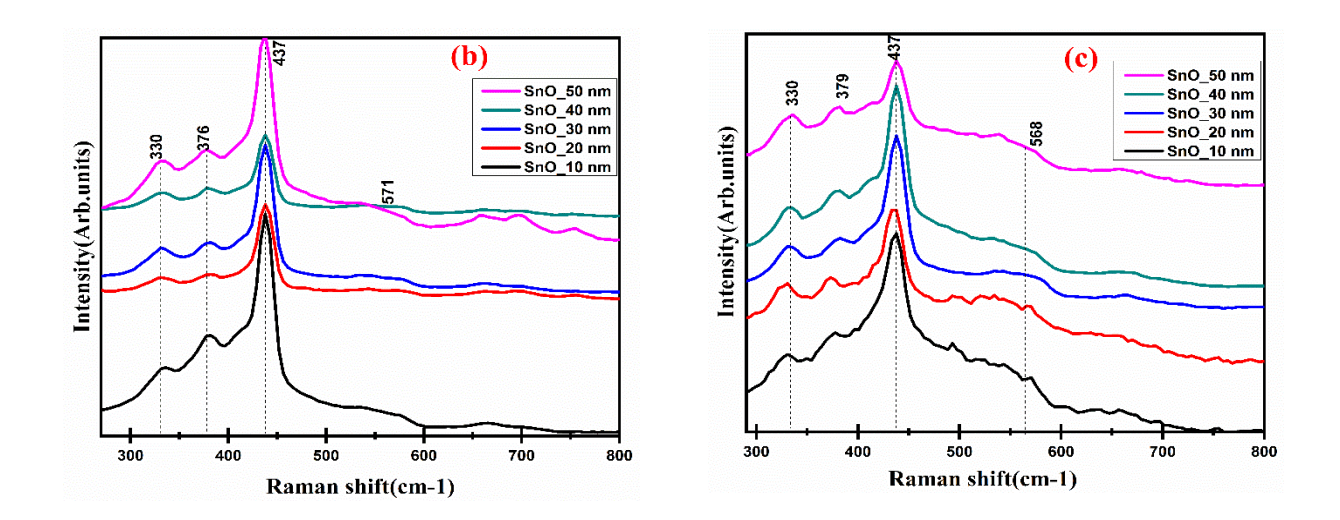


Figure 5.22: Raman spectra of ZnO NMRAs different thickness of SnO seed layer for (b) 30 mins. (c) 3hrs.

The Raman spectra of ZnO NMRAs on ZnO and Au seed layers are shown in figures 5.23 (a)-(c). The peaks at 329, 377 and 569 cm⁻¹ are assigned to the B1 low, E_{2H}-E_{2L} and E₁LO modes. The appearance of the mode at 569 cm⁻¹, although relatively low in intensity, signifies the presence of oxygen vacancies. These peaks appear even in the case of the ZnO structures grown on InO for 30 min with one exception. The peak at 569 cm⁻¹ is suppressed and there is a relatively low intensity peak at 563 cm⁻¹. As the duration of hydrothermal synthesis on InO is increased to 3hrs the same set of peaks appears but it is accompanied by decrease in the intensity of peak at 563 cm⁻¹ and suppression of the peak at 569 cm⁻¹. The Raman spectra of ZnO grown on SnA and SnO seeds at 120°C for 30 min and 3hrs are very similar to those on InA and InO seed layers. However, there is one major difference which is the complete absence of the peaks between 569-578 cm⁻¹. It would thus appear that oxygen vacancies are fewer in the ZnO structures grown on SnA and SnO seed layers.

In the case of the ZnO structures grown on the ZnO seed layer (figure 5.23(b) and (c)), the most intense peak appears at 439-441 cm⁻¹ for the nanostructures grown on top which is assigned to the E_2 high mode [279-286]. An interesting aspect is that the ZnO structures grown on the Au seed layer displayed a very intense peak at 437 cm⁻¹ assigned to the E_2 high mode at 3hrs of hydrothermal synthesis (figure 5.23(a)). In addition there are peaks at 331, 380, 546, 576 and 664 cm⁻¹ which are assigned to the B1 low, E_{2H} - E_{2L} , B1 high, E_1 LO and transverse acoustic (TA),

longitudinal acoustic (LA) modes, respectively. Evidently there is a significant fraction of oxygen vacancies and defects in these samples.

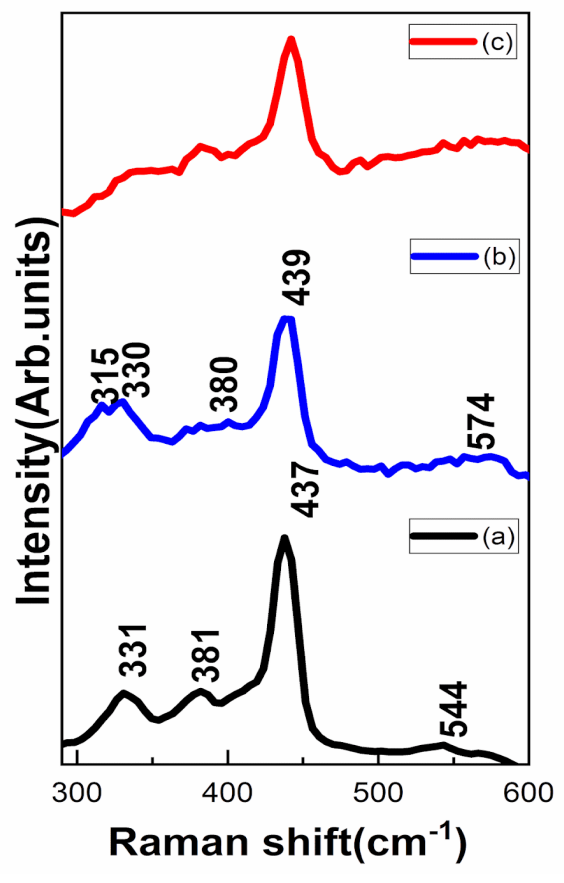


Figure 5.23: Raman spectra of ZnO structures on, Au seed layer for (a) 3hrs, and ZnO seed layer (b) 30 mins hrs, (c) 3hrs.

It is evident that the intensity of the E_2H mode is maximum independent of seed layer type. The $A_1(TO)$ mode that appears between 376–380 cm⁻¹ is known to be a result of the displacement of Zn^{2+} and O^{2-} ions, parallel to the c-axis. For example, A_1 (LO) mode seen at 571–577 cm⁻¹ corresponds to the presence of V_o , Zn_i and free carriers in the compounds. An irregular shift of the $A_1(LO)$ mode is mainly associated with the variation of the V_o defects. Finally, the weak hump appearing in the range of 638–668 cm⁻¹ is identified as an intrinsic mode for ZnO nanostructures originating due to the intrinsic defects such as V_o , Zn_i and oxygen antisites (OZn) [260, 311]. It is also expected that phonon confinement and non-stoichiometry related effects would be present in the Raman spectra of nanostructures. In addition, defects, such as vacancies [312] and stacking faults are very common in ZnO and they can affect the Raman peak positions and widths at the

nanoscale [313-314, 54)]. It is also reported that surface stresses at large surface-to-volume ratio can affect Raman peak positions and widths. Evidently the Raman spectra demonstrate the presence of oxygen related defects/vacancies. However, it appears that the defect related peaks are weaker in intensity on the In and Sn seeded layers (as-deposited and annealed) in comparison to the ZnO and Au seed layers. This has a profound effect on photoluminescence as discussed in the next section.

5.3. Photoluminescence

The PL spectra of the ZnO nanostructures at different thickness on the InA and InO seed layers (figure 5.24 (a)-(c)), (figure 5.25(a)-(c)), (figure 5.26 (a)-(c)), (figure 5.27 (a)-(c)) and (figure 5.28 (a)-(c)) exhibit only a very high intensity near band edge emission peak at a wavelength of 380-383 nm with less defects related emission.

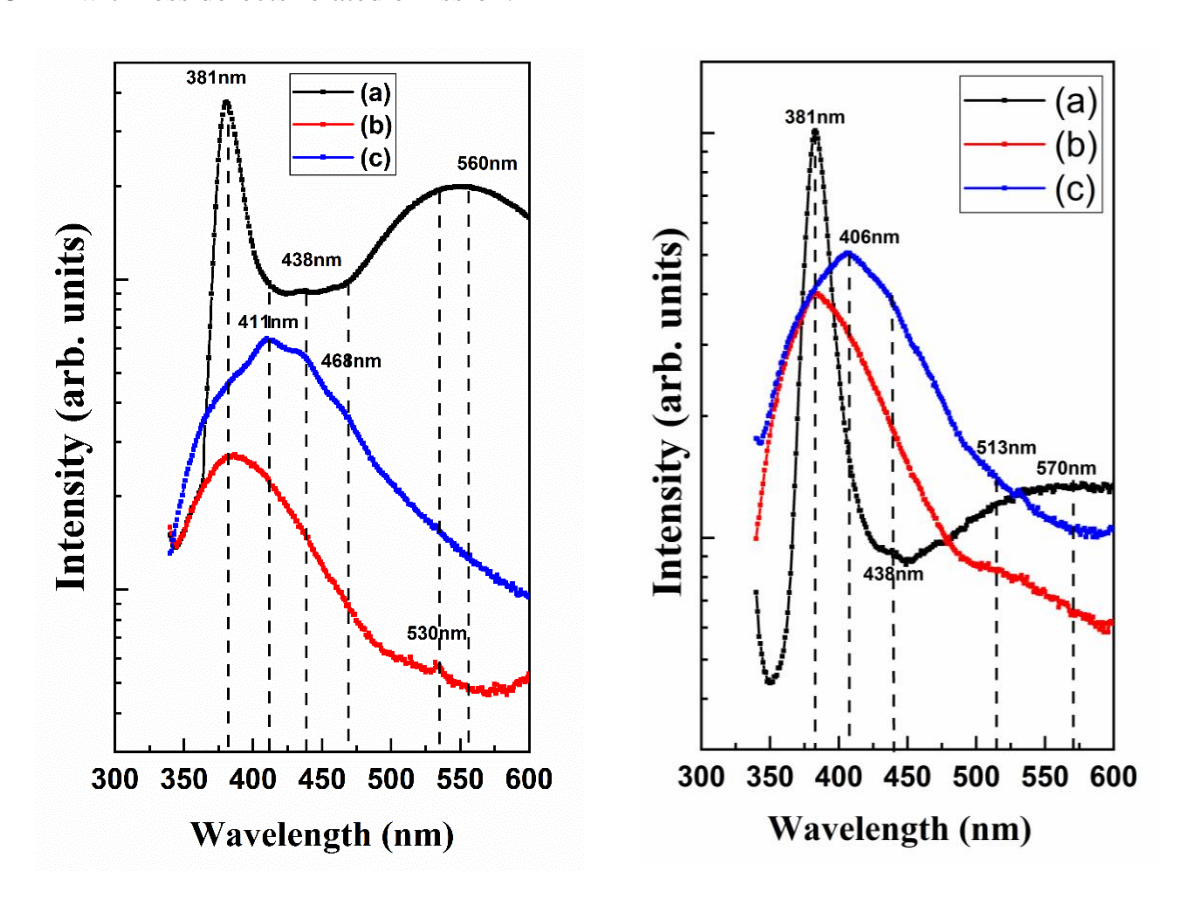


Figure 5.24 (left panel): Photoluminescence spectra of ZnO structures on 10 nm, InA seed layer for (a) 3hrs, InO seed layer for (b) 30 min, (c) 3 hrs.

Figure 5.25 (**right panel**): Photoluminescence spectra of ZnO structures on 20 nm, InA seed layer for (a) 3hrs, InO seed layer for (b) 30 min, (c) 3 hrs.

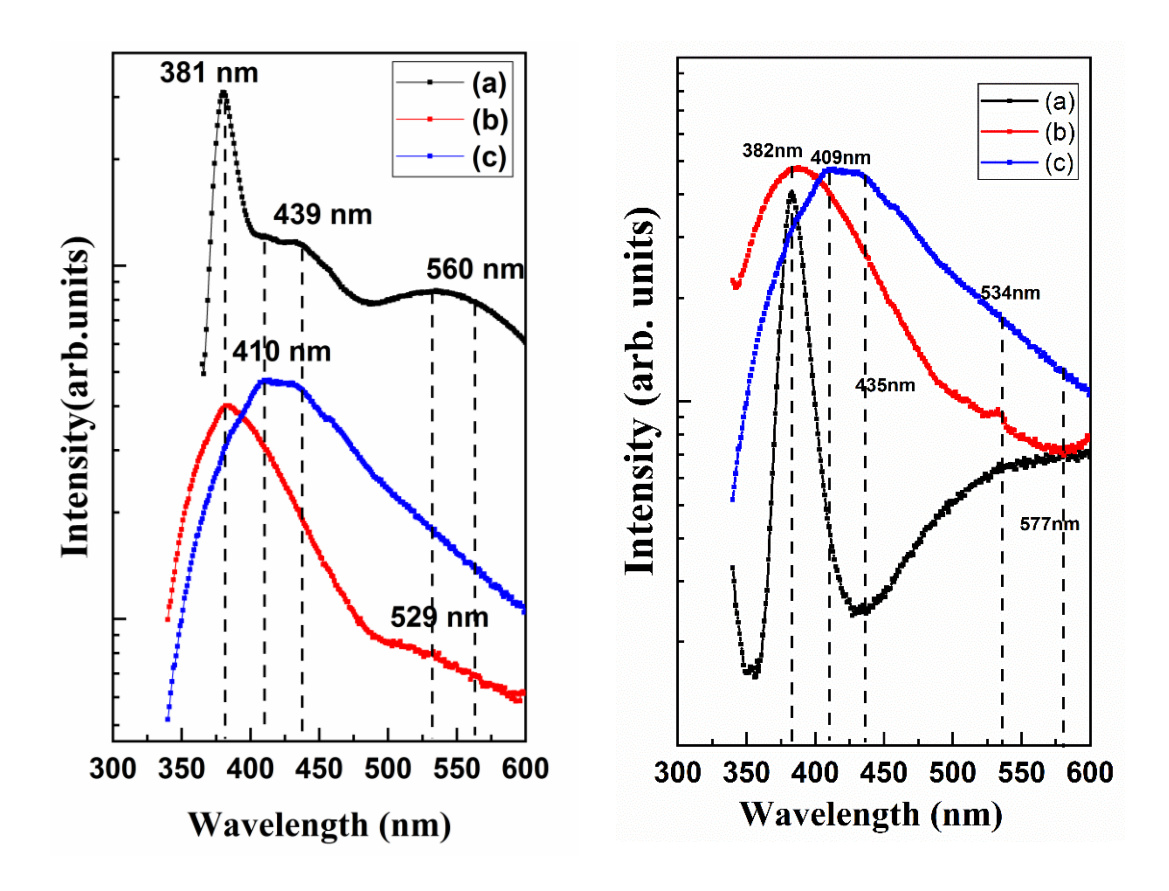


Figure 5.26 (left panel): PL spectra of ZnO structures on 30 nm thickness InA thin film for (a) 3hrs; InO thin film for (b) 30 min, (c) 3 hrs.

Figure 5.27 (right panel): PL spectra of ZnO structures on 40 nm thickness InA thin film for (a) 3hrs; InO thin film for (b) 30 min, (c) 3 hrs.

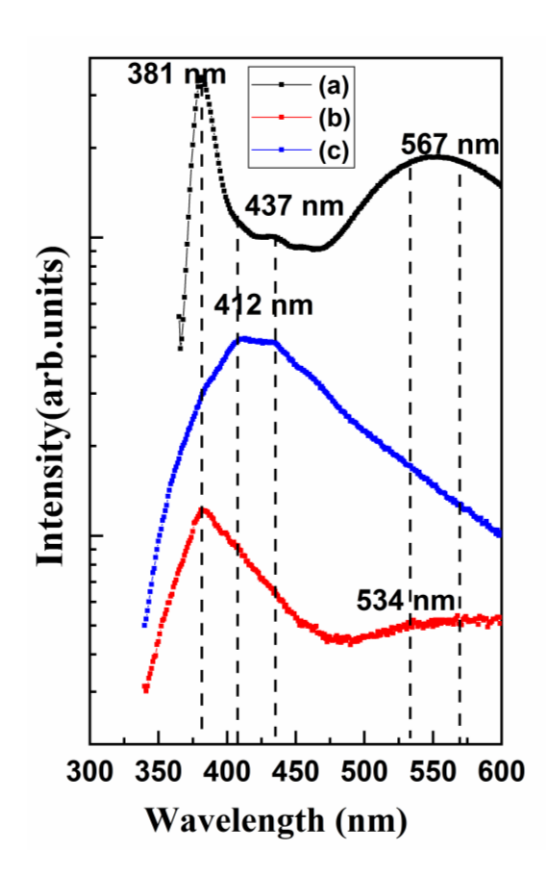


Figure 5.28: Photoluminescence spectra of ZnO structures on 50 nm, InA seed layer for (a) 3hrs, InO seed layer for (b) 30 min, (c) 3 hrs.

Similarly, in the case of SnA and SnO seed layers study it is observed that the ZnO nanostructures at different thickness on the SnA and SnO seed layers (figure 5.29 (a)-(c)), (figure 5.30(a)-(c)), (figure 5.31 (a)-(c)), (figure 5.32 (a)-(c)) and (figure 5.33 (a)-(c)) exhibit only a very high intensity near band edge emission peak at a wavelength of 380-386 nm with less defects related emission.

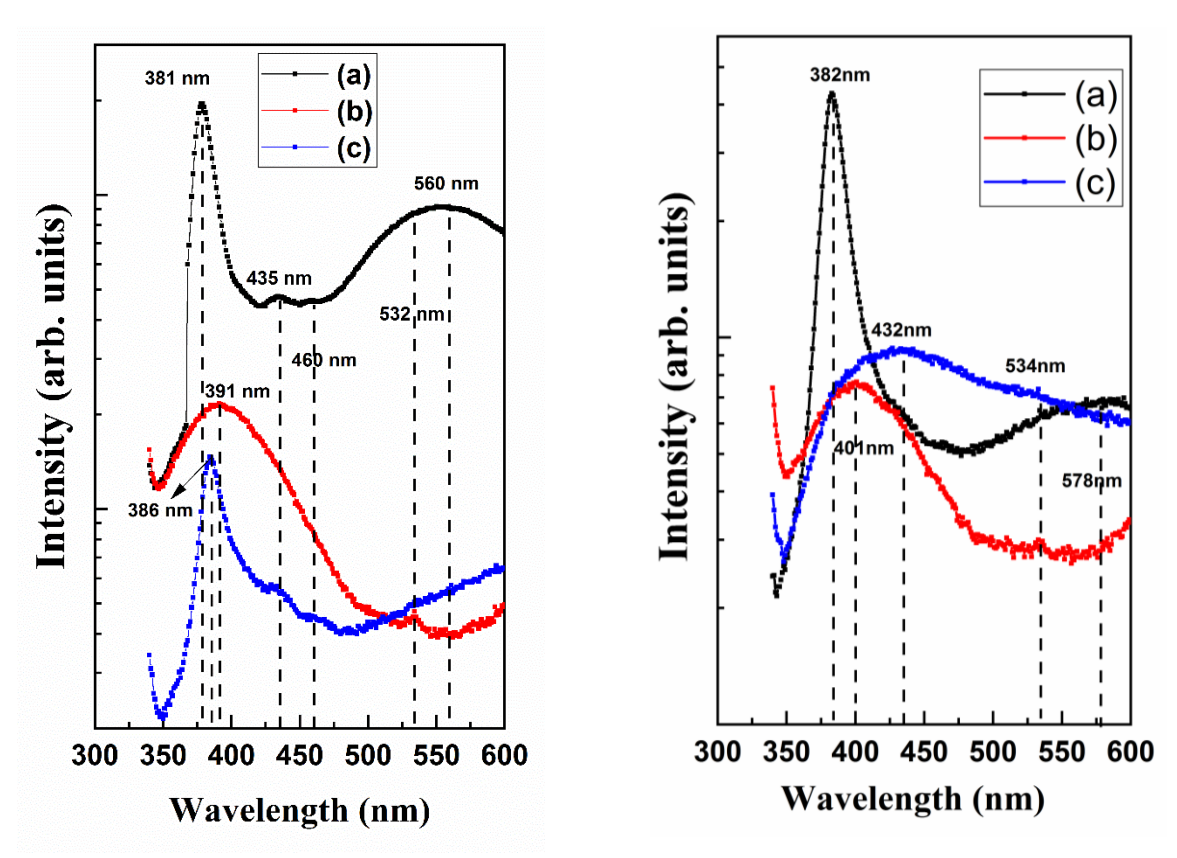


Figure 5.29: (left panel): Photoluminescence spectra of ZnO structures on 10 nm, SnA seed layer for (a) 3hrs, SnO seed layer for (b) 30 min, (c) 3 hrs.

Figure 5.30: (right panel): Photoluminescence spectra of ZnO structures on 20 nm, SnA seed layer for (a) 3hrs, SnO seed layer for (b) 30 min, (c) 3 hrs.

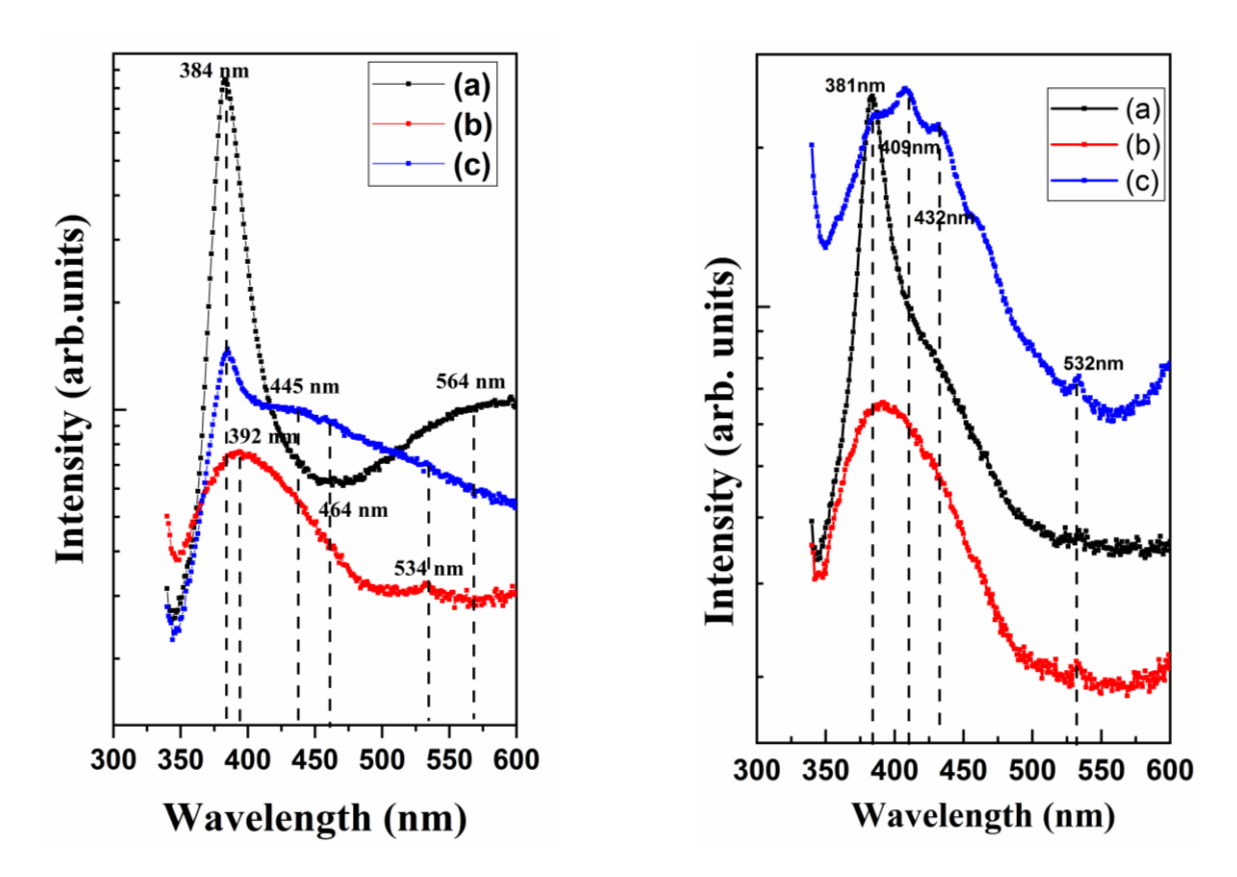


Figure 5.31: (left panel): Photoluminescence spectra of ZnO structures on 30 nm, SnA seed layer for (a) 3hrs, SnO seed layer for (b) 30 min, (c) 3 hrs.

Figure 5.32: (right panel): Photoluminescence spectra of ZnO structures on 40 nm, SnA seed layer for (a) 3hrs, SnO seed layer for (b) 30 min, (c) 3 hrs.

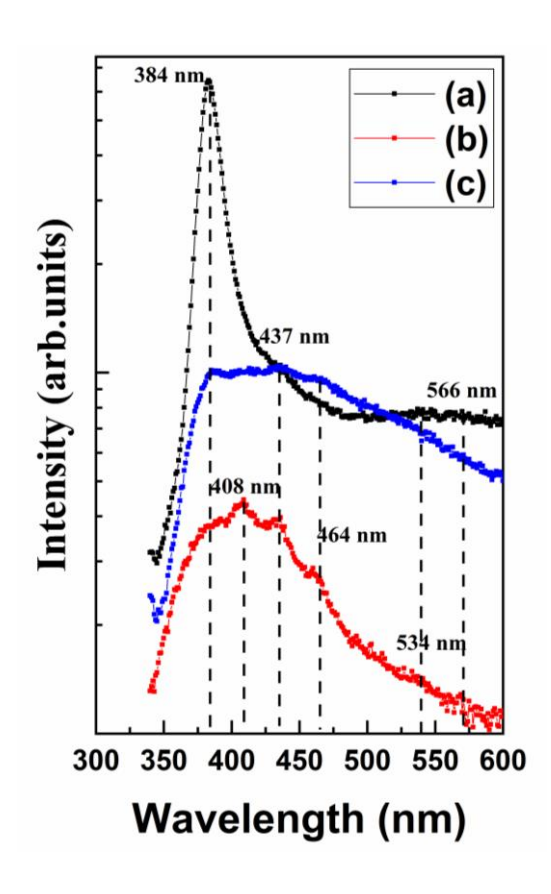


Figure 5.33: Photoluminescence spectra of ZnO structures on 50 nm, SnA seed layer for (a) 3hrs, SnO seed layer for (b) 30 min, (c) 3 hrs.

This is also true for the SnA seed layers all the case (a), on which the ZnO nanostructures exhibit strong near band edge emission. In the case of the SnO seed layers (b) and (c) this peak which is very broad after 30 min of HP increases in intensity and decreases in width after 3hrs of HP. In contrast, on the ZnO and Au seed layers, apart from the near band edge emission there is evidence for the presence of defect related emission(figure 5.34 (a)-(c)). It is only in the cases of ZnO nanostructures on the Au, and ZnO seed layers there is evidence for the appearance of weak shoulders at 383, 410, 438 and 461 nm, approximately.

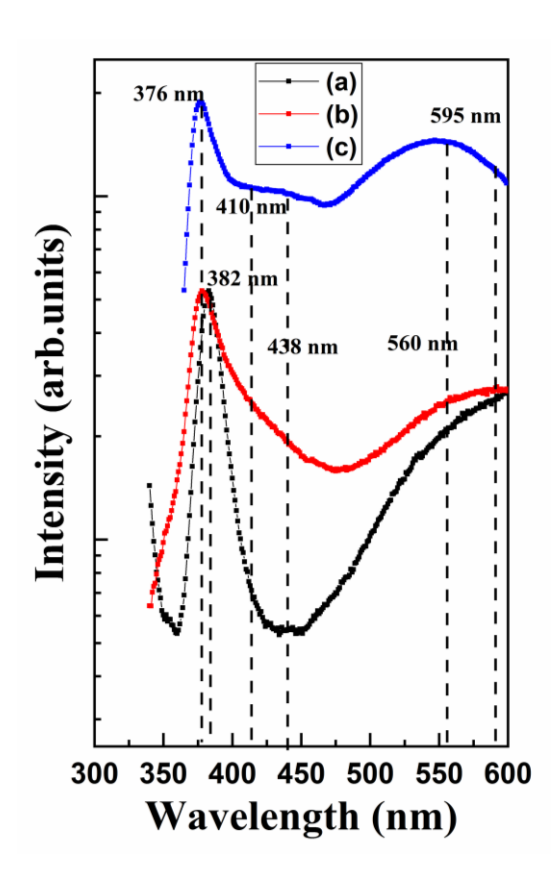


Figure 5.34: Photoluminescence spectra of ZnO structures on Au seed layer for, (a) 3 hrs; ZnO seed layer for (a) 30 min, (b) 3hrs.

Similar splitting in the UV band has been reported earlier [260, 315-317]. The broadening and splitting has been correlated with decrease in grain size leading to quantum confinement effects. It has also been reported that the violet emission originates due to the zinc interstitials (Zn_i) in the interface traps or Zn vacancy related defects [318-320].

In the case of 10 nm, it is observed that the ZnO NMRAs on the InA seed layers for 3hrs and InO seed layer for 30 min figure 5.24 exhibit a UV-NBE emission peak at a wavelength of 381nm. The ZnO NMRAs on InA seed layers display a weak hump at 438 nm and an additional defect related peak centred around 560 nm. Interestingly, this peak has very low intensity on the InO seed layers. The ZnO NMRAs grown on the InO seed layers for 30 min exhibit a weak peak at 530 nm and broadening of the UV-NBE peak. When the synthesis duration is increased to 3hrs, this broad UV-NBE peak appears as a shoulder at 381 nm and is accompanied by splitting with features at 411, 438 and 468 nm. The PL spectra for ZnO NMRAs on SnA and SnO seed layers are shown in

(figure 5.29). The ZnO NMRAs on SnA seed layers for 3hrs display a high intensity UV-NBE peak at 381 nm, a defect related peak centred around 560 nm and a weak hump at 435 nm. In the case of ZnO NMRAs on SnO seed layers, synthesized for 30 min., the UV-NBE peak is very broad and centred around 390 nm. A low intensity peak at 532 nm is also observed. As the synthesis duration is increased to 3hrs, the UV-NBE peak at 386 nm is narrow and there is also evidence for splitting of the peak with features at 435 and 460 nm. However, the peak in the visible region is not observed. In contrast, on the ZnO seed layers (figure 5.34 (b)-(c)) for a synthesis duration of 30 min, the UV-NBE peak appears at 378 nm and the peak in the visible region is broad, being centred around 595 nm. The ZnO NMRAs synthesized on ZnO seed layers for 3hrs show a peak at 376 nm corresponding to the UV-near band edge emission. And also, on the Au seed layers (figure 5.34 (a)) for a synthesis duration of 3hrs the UV-NBE peak appears at 382 nm and the peak in the visible region is broad being centred around 595 nm. There are additional features at 410 and 438 nm and a strong peak centred around 560 nm. Thus, in the case of InA and SnA seed layered ZnO NMRAs there are two strong features; one corresponding to the UV- near band edge emission and the other related to oxygen vacancies in the visible region. In the case of InO and SnO seed layers while the UV-NBE feature is observable, the peak in the visible region is suppressed. However, this is accompanied by splitting and broadening of the UV-NBE peak. The PL spectra on ZnO seed layers also exhibit strong UV-NBE related peak, independent of the synthesis duration. However, the peak in the visible region blue-shifts and becomes narrower. In addition, there is splitting of the UV-NBE peak after 3hrs of synthesis. It can, thus, be generalized that longer duration of synthesis leads to splitting of the UV-NBE peak. The origin of emission in the region between 400-470 nm is attributed to zinc interstitials (Zn_i) in the interface traps or Zn vacancy related defects [260, 315-320]. The inference from these observations is that while oxygen vacancies decrease in ZnO NMRAs on InO and SnO seed layers, defects such as Zn interstitials and vacancies are still present. In contrast, on the ZnO seed layer the oxygen vacancies are present, independent of the duration of synthesis.

It can also be inferred from the high intensity of the band edge PL relative to visible band in the emission spectra of ZnO that the ZnO nanostructures are of very high crystal quality on the InA, InO, SnA and SnO seed layers which is also consistent with Raman, FE-SEM and XRD results presented earlier. Thus, ZnO nanorod arrays grown on the In and Sn seed layers will be ideally suited for photoluminescence applications.

5.4. Optical transmission studies

The measured spectral transmission of the ZnO structures on different thickness InA and InO films is shown in (5.35 (a)-(d)), the corresponding spectra for SnA and SnO films is displayed in (5.36 (a)-(d) It is evident from these spectra that the ZnO/InA heterostructure has a high transmission (~80%) in the visible region wich decreases for the ZnO/InO heterostructures to about 40% for the samples synthesized for 3hrs. At 50 nm the ZnO/InA heterostructure has a high transmission (30-40%) in the visible region which decreases for the ZnO/InO heterostructures to about 20-30% for the samples synthesized for 3hrs.

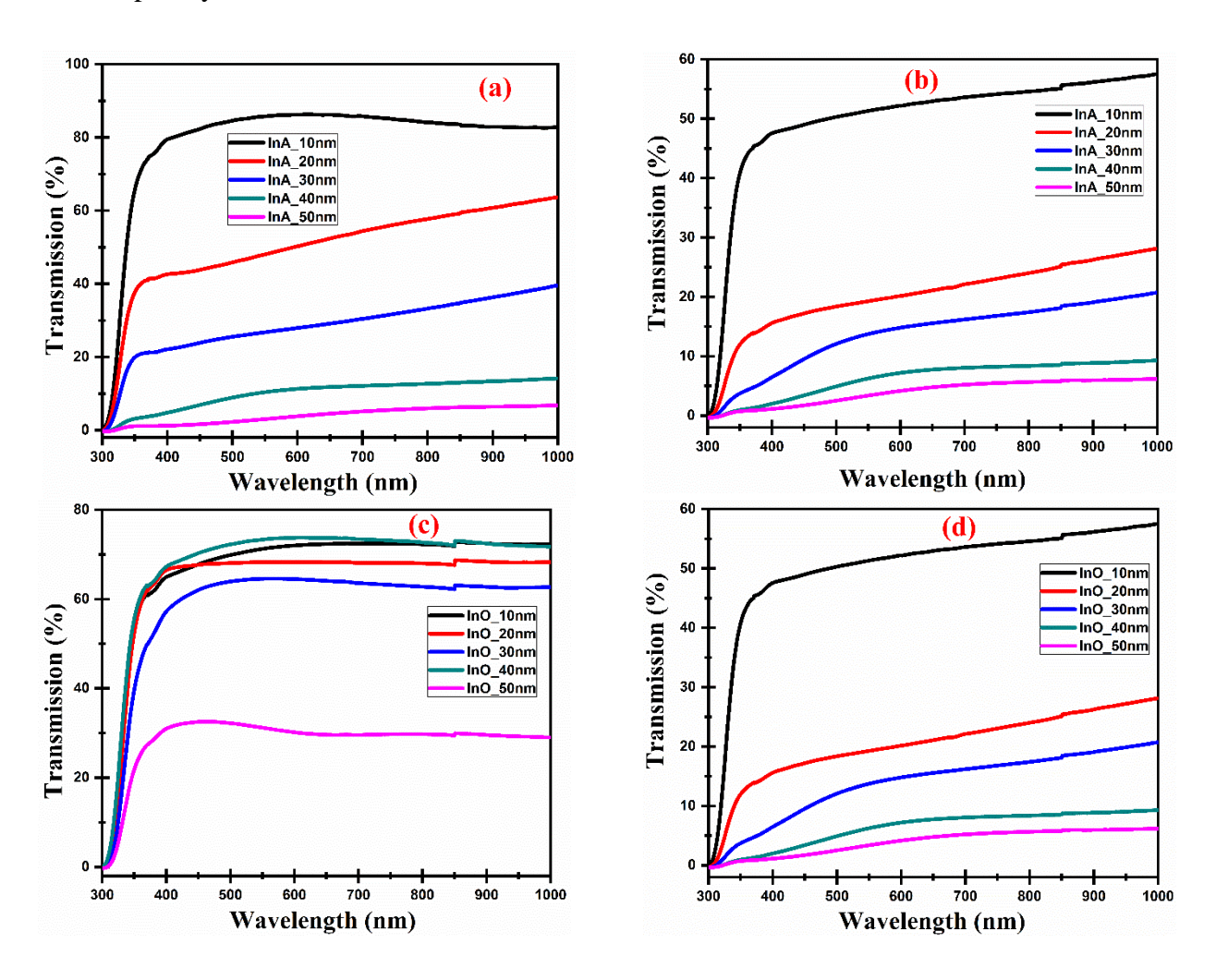


Figure 5.35: Optical transmission spectra of ZnO NMRAs different thickness for (a) InA duration process at 120°C, 30 mins, (b) InA duration process at 120°C, 3hrs; (c) InO duration process at 120°C, 30 mins, (d) InO duration process at 120°C, 3hrs.

he behaviour in the case of the ZnO/SnA and ZnO/SnO heterostructures is reverse. The transmission is low for the ZnO/SnA case but increases for the ZnO/SnO heterostructures to almost 50-60% for the samples synthesized for 3hrs.

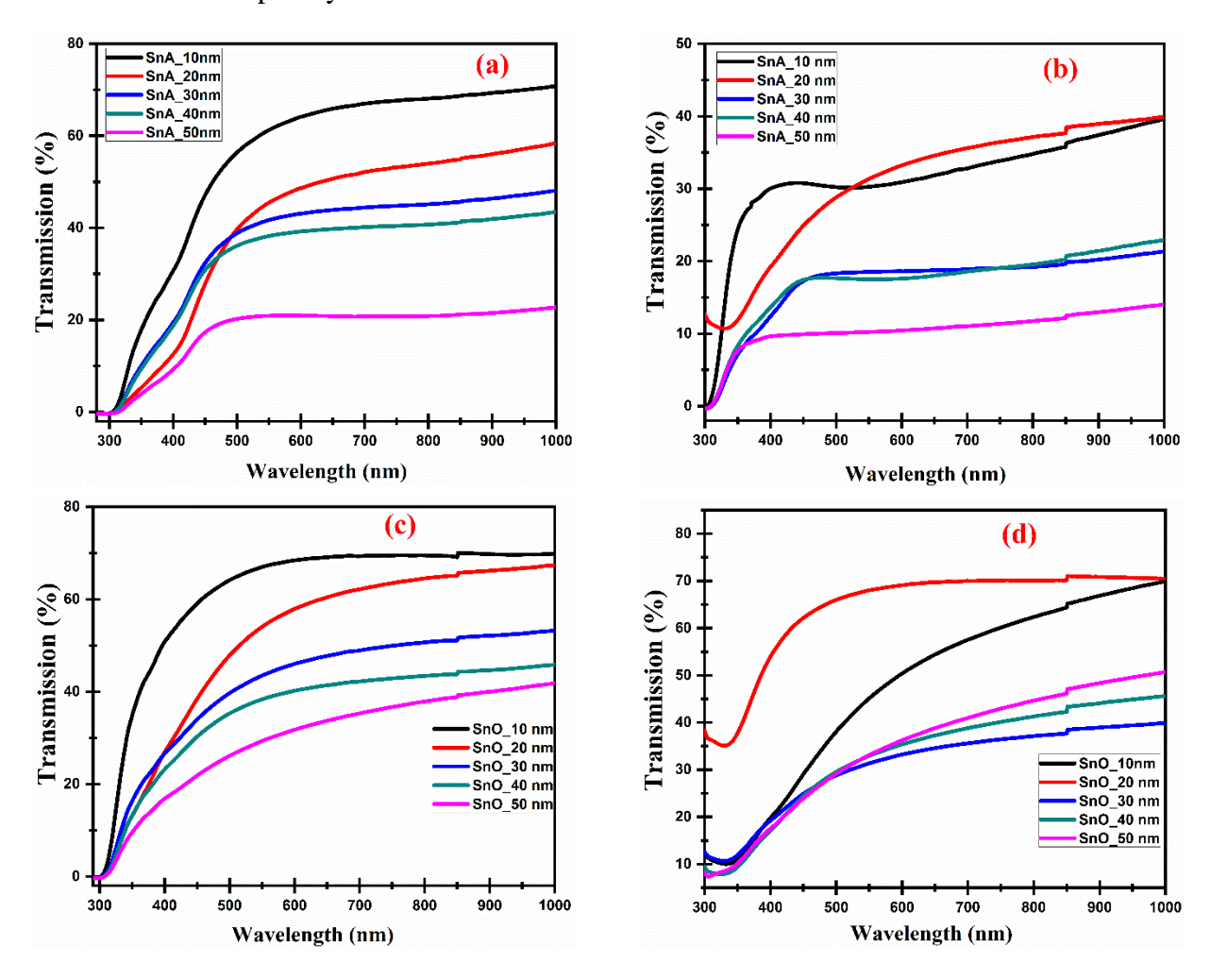


Figure 5.36: Optical transmission spectra of ZnO NMRAs different thickness for (a) SnA duration process at 120°C, 30 mins, (b) SnA duration process at 120°C, 3hrs; (c) SnO duration process at 120°C, 30 mins, (d) SnO duration process at 120°C, 3hrs.

The absolute value of transmission depends strongly on the thickness of the as deposited or annealed metal layers as shown. However, there is no change in the trend, i.e transmission of the ZnO/InA heterostructures > ZnO/InO heterostructures and reverse for the SnA and SnO based heterostructures. Another important point is that the band gap of the heterostructures shows a redshift with increase in the nature of the underlayer (i.e. as-deposited or annealed) as well as thickness. The obtained band gap values are of the order of 3.8-4.0 eV. These properties make the

studied heterostructures very suitable for many optical applications that require high band gap and high transmission.

5.5. Wettability studies

The most common method to quantify hydrophilicity and hydrophobicity of a surface is through measurement of contact angle. The wetting is characterized by the contact angle θ of liquids over the solid surfaces. The primary equation that quantified the contact angle of a liquid droplet on a flat surface was given by Young [321]. Contact angle can be related to the three interfacial tensions via Young's equation

$$\cos\theta = \frac{\gamma_{SV} - \gamma_{SL}}{\gamma_{LV}} \longrightarrow (5.01)$$

where γ_{SV} = solid-vapor interfacial tension,

 γ_{SL} = solid-liquid interfacial tension,

 γ_{LV} = liquid-vapor interfacial tension

Wettability is characterized by not only the chemical composition but also the roughness of the surface. Young's equation is developed for the case of an ideal solid surface, which is defined as a smooth, rigid, chemically homogeneous, insoluble and a non-reactive surface. Wetting on rough surfaces of solid cannot be described by Young's equation and wetting models that correlate surface roughness with the equilibrium contact angle are Wenzel [322] and Cassie-Baxter [323] models. The Wenzel apparent contact angle can be related to true contact angle by the relation:

$$cos\theta_W = r_W \left[\frac{[(\gamma_{SV} - \gamma_{SL})]}{\gamma_{LV}} \right] \rightarrow (5.02)$$

where r_W is the Wenzel's roughness factor and may be defined as the ratio of the actual area of a rough surface to the geometric projected area. The Cassie-Baxter's equation describes the wetting regime when air is trapped in the microstructures of the surface, and liquid sits on top of asperities.

The apparent-contact angle (θ_{CB}) in this case is given by the Cassie-Baxter's equation which is

$$cos\theta_{CB} = (r_{ff}cos\theta_Y + f - 1) \rightarrow (5.03)$$

where θY is the Young contact angle, f is the fraction of the projected area of the solid surface that is wetted by the liquid and rf is the roughness ratio of the wetted area. In general, Wenzel's model deals with homogeneous surfaces whereas Cassie-Baxter's model was found to be functional for heterogeneous surfaces.

The fundamental assumption is that wettability is independent of the roughness and chemical nature of the surface. However, both these assumptions have been proved to be incorrect. Wetting on rough surfaces of a solid cannot, therefore, be described by Young's equation. Subsequently models that correlate surface roughness with the equilibrium contact angle were developed by Wenzel [322] and Cassie-Baxter [323] models. In Wenzel's model, the liquid droplet is assumed to be in contact with the solid surface at all points, thus signifying a homogeneous surface. In contrast, the Cassie-Baxter model relates to liquid droplets sitting only on surface protrusions and, therefore, useful for the more realistic rough surfaces. A combination of these models is used to explain wettability in most cases. The values for water contact angles on ZnO structures grown on InA, InO, SnA and SnO seed layers are shown in Table1 and Table2. Table3 represents the water contact angle of ZnO structure on Au and ZnO seed layers.

Table 1: Water Contact angle of ZnO structures on different thickness InA, InO seed layers.

1	ZnO structure on 10nm InA seed layer for 3 hrs	A	102.5°
2	ZnO structure on 10nm InO seed layer for 30 mins		93.9°
3	ZnO structure on 10nm InO seed layer for 3 hrs		92.2°
4	ZnO structure on 20nm InA seed layer for 3 hrs		110.5°

5	ZnO structure on 20nm InO seed layer for 30 mins	98.2°
6	ZnO structure on 20nm InO seed layer for 3 hrs	98.1°
7	ZnO structure on 30nm InA seed layer for 3 hrs	114.8°
8	ZnO structure on 30nm InO seed layer for 30 mins	96.1°
9	ZnO structure on 30nm InO seed layer for 3 hrs	95.1°
10	ZnO structure on 40nm InA seed layer for 3 hrs	115.4°
11	ZnO structure on 40nm InO seed layer for 30 mins	100.4°
12	ZnO structure on 40nm InO seed layer for 3 hrs	99.8°
13	ZnO structure on 50nm InA seed layer for 3 hrs	110.3°
14	ZnO structure on 50nm InO seed layer for 30 mins	102.3°
15	ZnO structure on 50nm InO seed layer for 3 hrs	90.8°

Table 2: Water Contact angle of ZnO structures on SnA and SnO thin films.

- 1		10.5.50
1	ZnO structure on 10nm SnA seed layer for 3 hrs	106.6°
2	ZnO structure on 10nm SnO seed layer for 30 mins	95.5°
3	ZnO structure on 10nm SnO seed layer for 3 hrs	107.2°
4	ZnO structure on 20nm SnA seed layer for 3 hrs	98.5°
5	ZnO structure on 20nm SnO seed layer for 30 mins	94.9°
6	ZnO structure on 20nm SnO seed layer for 3 hrs	110.6°
7	ZnO structure on 30nm SnA seed layer for 3 hrs	107.3°
8	ZnO structure on 30nm SnO seed layer for 30 mins	91.5°
9	ZnO structure on 30nm SnO seed layer for 3 hrs	104.5°
10	ZnO structure on 40nm SnA seed layer for 3 hrs	96.2°
11	ZnO structure on 40nm SnO seed layer for 30 mins	94.8°

12	ZnO structure on 40nm SnO seed layer for 3 hrs	102.7°
13	ZnO structure on 50nm SnA seed layer for 3 hrs	95.5°
14	ZnO structure on 50nm SnO seed layer for 30 mins	93.8°
15	ZnO structure on 50nm SnO seed layer for 3 hrs	101.0°

In the present study, the ZnO nanorod arrays on InA and InO seed layers are hydrophobic in nature, with water contact angles between 92-102°. Similarly, in the case of the SnA and SnO seed layers the WCA is in the range of 95-107°. In comparison, on the Au seed layer the value is 92°. Interestingly on the ZnO seed layers the HP ZnO structures are superhydrophobic with a maximum WCA of 150°.

Table 3: Water Contact angle of ZnO structures on ZnO and Au seed layer.

A	ZnO structure on Au seed layer for 3hrs		92.3°
В	ZnO structure on ZnO seed layer for 30mins	þ	131.9°
С	ZnO structure on ZnO seed layer for 3hrs	0	150.4°

This is consistent with earlier observations, experimental and theoretical, that demonstrate a dependence of WCA on dimensions of the structures. It has been shown that [324-325] the apparent contact angles in the Wenzel (θ_W) and Cassie-Baxter states (θ_{CB}) of micropillar arrays are proportional to [1+ (4A/(a/H))] and A respectively. Here A = [1/((b/a)+1)^2], where b is the interpillar spacing, a is the width of the pillar and H is the height. Bormashenko while examining the

wettability of rough surfaces [326] has found a similar dependence. It was also found in this work that the Gibbs free energy for Cassie air trapping is the lowest followed by the Wenzel with the free energy for the Cassie water penetration state being the highest. In addition the energy of transition from the Cassie-Baxter to the Wenzel states is strongly dependent on the radius of the droplet with respect to the features of the arrays. There are a few other experimental observations on the dependence of WCA on the dimensions and spacing in arrayed micro/nanostructures of ZnO. Therefore, in the present work, it is inferred that increase in WCA can be directly correlated with change in dimensions of the micro/nano rods and inter-rod separation. This can, in turn, be correlated with the density of ZnO rods/wires per μm on the different seed layers. The number is of the order of 1-2 in the case of the In and Sn seed layers (as-deposited and annealed), <1 for Au. In contrast the number is between 5-8 for the ZnO seed layers.

The effect of UV irradiation on the WCA is presented in figure 5.37 (a). It is observed that in all cases there is a transition in the wetting state of all the structures. And also, we observed photoinduced hydrophilic conversion factor (K_f) on 10nm thickness of different seed layers which is obtained from slope of the plot of reciprocal of contact angle vs UV irradiation time (Figure 5.37(b)). Significantly, it is independent of initial contact angle [327]. The values of the K_f are estimated as (1) 6.81×10^{-4} (2) 2.44×10^{-4} (3) 1.21×10^{-3} (4) 6.75×10^{-4} (5) 1.87×10^{-3} (6) 2.46×10^{-3} degree⁻¹min⁻¹. The hydrophilic conversion rate is better in case of HP ZnO on oxide seed layer (InO, SnO) in contrast to their metal (In,Sn) counterpart. The hydrophilic conversion rate is best for HP ZnO (3hrs) grown on ZnO seeded substrate. In the case of ZnO on InA and InO seed layers the transition from the hydrophobic state starts within the first ten minutes and at the end of 120 mins the surfaces become hydrophilic. On the SnO seed layer that transition is much more rapid with the surface becoming superhydrophilic at the end of 120 mins. This is similar to the structures grown on ZnO seed layers which exhibit a superhydrophobic to superhydrophilic transition. induced hydrophilicity is generally attributed to the structural changes that occur at the surface due to UV irradiation of energy greater than bandgap of metal oxide. This leads to the generation of electron-hole pairs in the conduction and valence band. In photo-induced hydrophilicity some of the holes interact with lattice oxygen creating oxygen ion vacancies and the electrons interact with the metal producing surface trapped electron sites. As a consequence, the binding energy between metal and oxygen atom decreases. The creation of oxygen ion vacancies makes the surface suitable for hydroxyl adsorption and as a result these

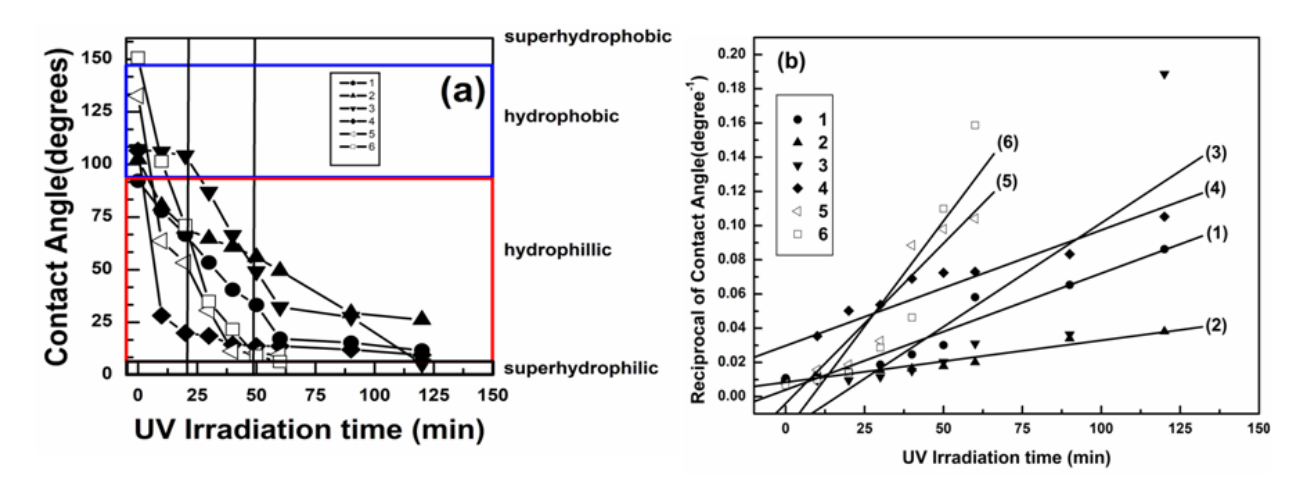


Figure 5.37: (a) Effect of UV irradiation on the change in contact angle of ZnO NMRAs grown on different seed layers.1=InO, 2=InA, 3=SnO, 4=SnA, 5 and 6 = ZnO seed layers. (b) Plot of reciprocal of contact angle against the UV irradiation time.

Substrates become hydrophilic after UV exposure. Indeed, oxygen vacancies play an important role in the hydrophilization of a surface, since reconstruction of surface hydroxyl groups occurs under UV illumination leading to an increase in their number. It may be recalled that both Raman spectroscopy and PL data, presented in the previous sections, indicated the presence of oxygen vacancies. The decrease in contact angle is, therefore, due to the formation of a metastable state which can absorb hydroxyl group [327]. Thus, the observed (super) hydrophobic—(super) hydrophilic transition is due to surface hydroxylation. The rate at which the transition occurs can be correlated with number of oxygen vacancies present initially on the surface

It is to be noted that, both Raman spectroscopy and PL data, discussed in the previous sections, indicate the presence of defects on the ZnO NMRAs. Mrabet et al. [328] reported that presence of oxygen vacancies improves the acidic character of a ZnO surface leading to increased hydrophilicity. However, in another study on Zn₂SnO₄ thin films annealed in air, Mrabet et al. have observed that multiple mechanisms are responsible for the variations in water contact angle [329]. They conclude that oxygen adatoms on the surface would also contribute to the observed wettability. In earlier work, Meng et al. while investigating ZnO nanowire arrays prepared under an Ar atmosphere confirmed the role of oxygen adatoms on the surface in determining the water contact angle [330]. Similarly, Zhang et al. show the presence of oxygen adatoms on the surface of ZnO and elimination of oxygen vacancies on surfaces annealed in air [331]. It would appear

that in the case of ZnO nanowires thermally annealed in air, oxygen adatoms adsorbed on the surface play a significant role in determining the wettability behaviour. Hence, in the present study, since all the NMRAs were prepared by annealing in air it is reasonable to infer that a combination of oxygen vacancies, Zn related defects and oxygen adatoms determine the wettability. Furthermore, the observed (super)hydrophobic – (super)hydrophilic transition can be attributed to surface hydroxylation [328, 320]. The rate at which the transition occurs can also be correlated with a combination of surface effects, as discussed above. Thus, it can be inferred that wettability and wettability transition can be controlled by an appropriate choice of the seed layer and manipulating the interface.

5.6. Conclusion

In summary, hydrothermal synthesis of ZnO nano/micro rod arrays on as-deposited and heat treated In and Sn seed layers as well as Au and ZnO, is described in this chapter. The dimensions of the arrays are profoundly dependent on the conditions of synthesis such as duration of reaction and nature of the seed layer. The arrays consist of rods that are oriented vertically at different angles and polycrystalline nature. The rods are either cylindrical or hexagonal in shape. They show excellent photoluminescence and wettability properties. A detailed comparison with arrays grown on ZnO and Au seed layers shows that the properties on as-deposited and heat treated In and Sn seed layers is comparable and, in some cases, superior.

Chapter

6

Application of Titanium nitride nanoparticle decorated ZnO nanowires as surface enhanced Raman scattering substrates

Parts of this chapter were published in the paper: Y. Rajesh, M.S.S. Bharati, S.V. Rao, and M.G. Krishna, ZnO nanowire arrays decorated with titanium nitride nanoparticles as surface-enhanced Raman scattering substrates. Applied Physics A, 127(4), pp.1-8 (2021).

Abstract

In this chapter, the potential of ZnO nanowire arrays decorated with titanium nitride (TiN) nanoparticles as surface enhanced Raman scattering (SERS) substrates is demonstrated. ZnO nanowires were grown by hydrothermal synthesis while commercially obtained TiN powders were subjected to several hours of mechanical grinding to achieve 30-100 nm diameter nanoparticles. The nanoparticles were then dispersed in acetone and drop cast on the ZnO nanowire arrays for decoration. Scanning electron microscopy confirmed the presence of TiN nanoparticles on the ZnO nanowires. TiN nanoparticles exhibited multiple absorption features at 430, 520 and 600 nm. SERS experiments using Nile blue and Methylene Blue as the analyte molecules exhibited enhancement in the Raman signals. It is shown that the origin of the SERS effect is chemical in nature, with contribution from different interactions between the analyte molecule and the TiN nanoparticles. It is, thus, a simple, cost-effective and facile method for the fabrication of TiN based SERS substrates.

6.1 Background

Recent literature has shown that titanium nitride (TiN) thin films display a strong absorption peak related to plasmonic resonance at approximately 530 nm, which is very close to that of Au nanostructures [332-333]. As a result, TiN thin films and nanostructures can be used as surface enhanced Raman scattering (SERS) substrates. This has been demonstrated by the ability to detect molecules such as R6G [238, 240, 241, 244, 334-337]. The aim of the current work is, therefore, to circumvent the problem of non-stoichiometry by producing nanoparticles from commercially available stoichiometric TiN powders and subjecting them to grinding for several hours. The produced nanoparticles are then dispersed in acetone and drop cast on hydrothermally synthesised ZnO nanowire arrays. Decoration of the ZnO nanowire arrays with TiN nanoparticles takes place at room temperature. The proof-of-concept for application as SERS substrates is demonstrated using two molecules, Nile blue (NB) and Methylene blue (MB). There are no other reports on TiN nanoparticle decorated ZnO nanowires for application as SERS substrates.

The ZnO nanowires are prepared on 100 nm thickness ZnO thin film coated glass substrates by hydrothermal synthesis, as described in the previous chapters. TiN nanoparticles (NPs) were prepared by hand-milling commercially purchased powders that contained particles of 3-5µm in diameter. After several hours of grinding, the particle size of the powders was reduced to 30-100 nm. The produced TiN nanoparticles are then dispersed in acetone and drop cast on the hydrothermally synthesised ZnO nanowire arrays to achieve decoration.

6.1.1. Microstructure

The surface microstructure shows the top view of a typical ZnO nanowire array surface shown in figure 6.1 (a) indicates that the nanowires are of diameter between 30-100 nm. The nanowires are relatively densely packed, and cross-sectional microscopy analysis reported earlier showed that they are reasonably vertically aligned as mentioned in chapter-4. The as-received TiN powders were subjected to grinding for several hours. As a result, many of the particles, which were initially 3-5µm sized, were reduced to ≤100 nm size after grinding, as demonstrated in figure 6.1 (b). A closer examination of the nanoparticles, in figure 6.1(c), indicates that the particles' agglomeration at some locations and the shapes are non-spherical. The ZnO nanowires underneath the nanoparticles are visible in these images. Thus, this method is a facile and straightforward technique to produce TiN nanoparticles and decorate them on ZnO nanowire surfaces.

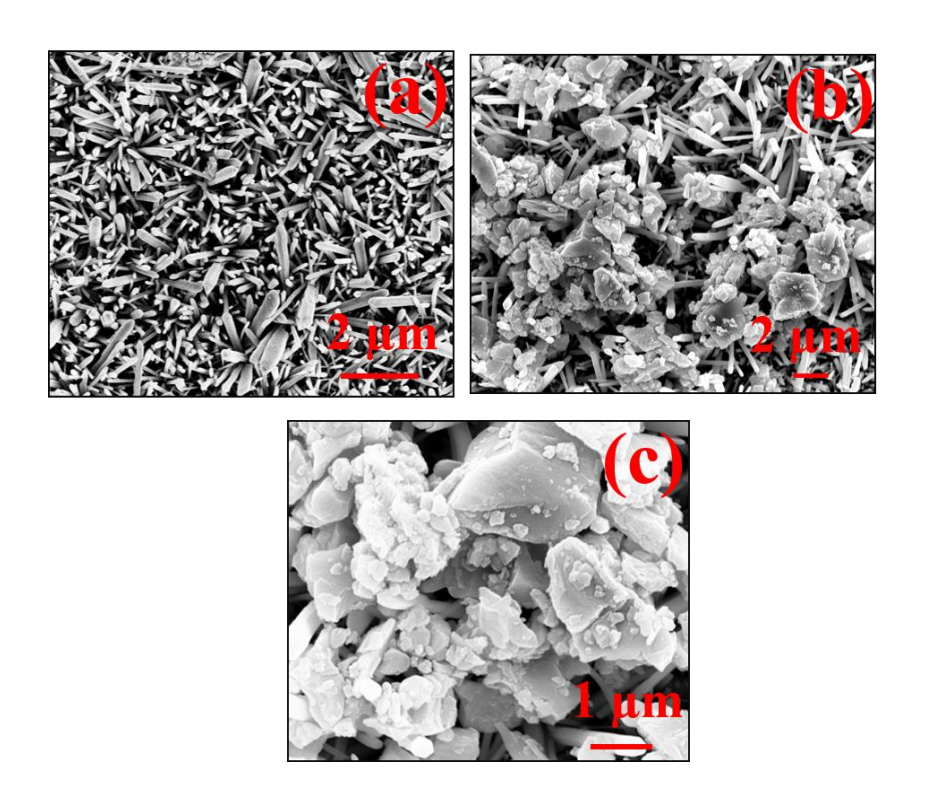


Figure 6.1: FE-SEM images of (a) ZnO nanowires and (b) and (c) TiN nanoparticles decorated ZnO nanowires at different magnifications.

6.1.2. Crystal structure

The X-ray diffraction pattern of fundamental TiN nanoparticles is shown in figure 6.2(a). The nanoparticles crystallize in the FCC structure with a crystallite size of 35 nm. The highest intensity diffraction peak is from the {200} plane, and the absence of XRD peaks from any substoichiometric phase indicates that the nanoparticles are indeed stoichiometric. The peaks from ZnO nanowires dominate the XRD pattern of the TiN nanoparticles decorated surfaces. However, a low-intensity peak from the {200} plane of FCC TiN is still visible.

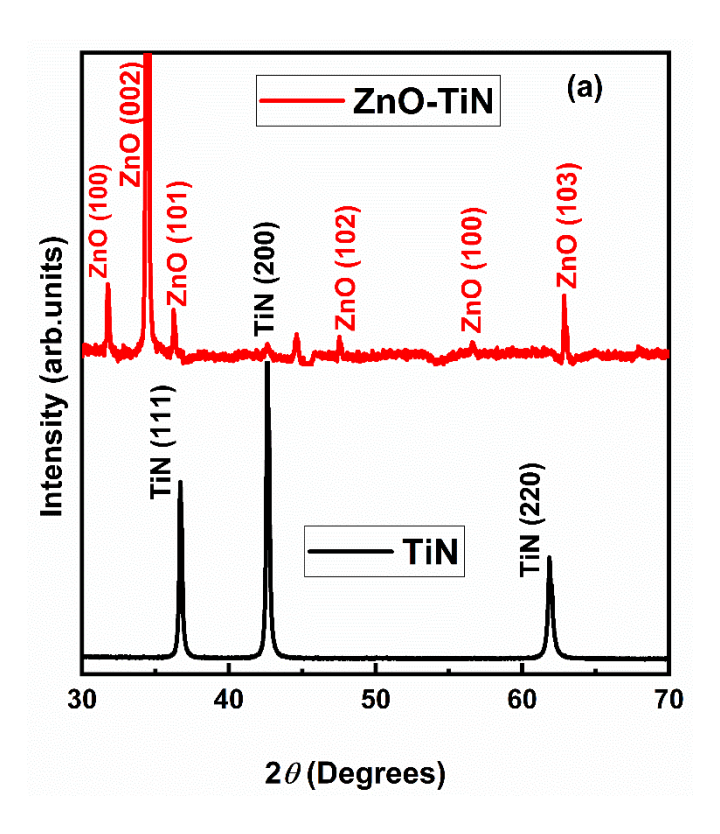


Figure 6.2: (a) XRD patterns of TiN nanoparticles and ZnO nanowires decorated with TiN nanoparticles.

6.1.3. Raman spectroscopy

The Raman spectrum for the TiN nanoparticle decorated ZnO nanowire surface is displayed in figure 6.2(b). Constable et al. [338] observed peaks at 215, 327, 566, and 609cm⁻¹ in the Raman spectra of TiN films, and these modes were assigned to the transverse acoustic(TA), longitudinal acoustic(LA), second-order acoustic (2A), and transverse optical (TO) modes, respectively. In a Subramanian and Jayachandran report [339], the Raman peaks were observed at 320, 440, and 570 cm⁻¹, respectively. Thus, in the present case, the peaks at 330, 559, and 662 cm⁻¹ are attributed to TiN nanoparticles, while the peaks 374, 436, and 478 cm⁻¹ are assigned to ZnO. The most intense peak observed at 436 cm⁻¹ is the E2 high mode of wurtzite ZnO. The peaks at higher wavenumbers may have contributions from both materials. It is evident from the data presented so far that TiN nanoparticles are formed on the ZnO nanowires' surface, and there is no chemical reaction between the two compounds.

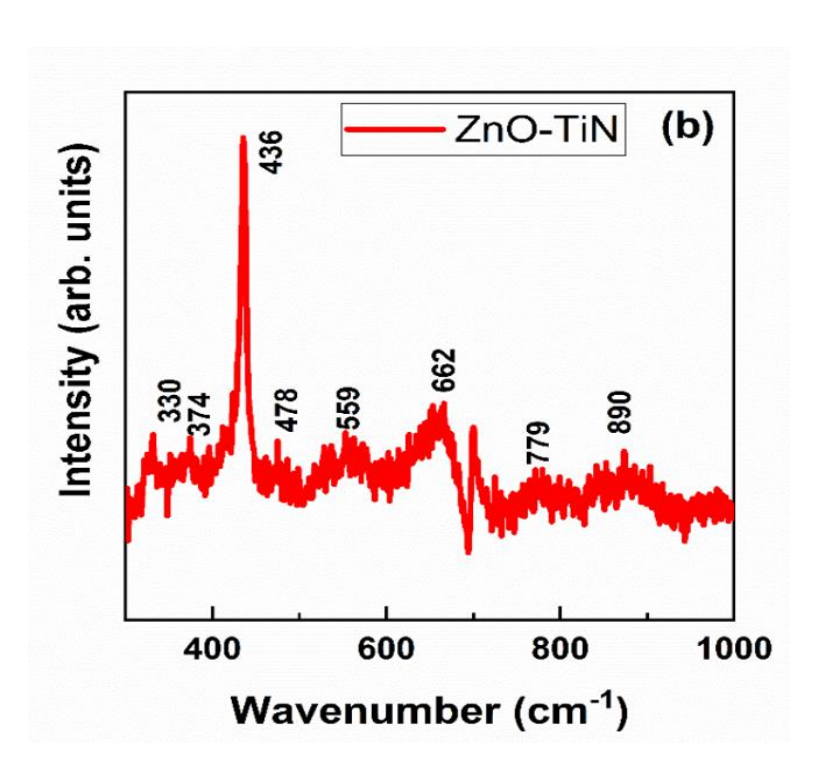
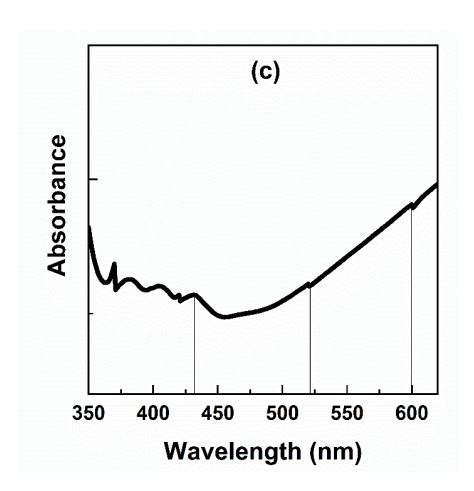


Figure 6.2: (b) Raman spectrum of TiN nanoparticles decorated with ZnO nanowires.

6.1.4. Optical properties

The optical absorption spectrum of TiN nanoparticles dispersed on a glass slide in the form of a thin film was recorded on a UV-Vis-Near IR spectrophotometer and shown in figure 6.2(c). The spectrum exhibits a strong absorption feature at 430 nm and low-intensity characteristics at 520 and 600 nm. In literature, this absorption peak has been attributed to plasmonic resonances [332-333]. However, it can be plasmonic only under doping by extra Ti, which is not the case in the present study. Hence, the prominent absorption peak in the transmission spectrum of TiN could be related to fundamental interband transitions.

In contrast, the other additional peaks could occur from Mie-resonances in nanoparticles as recognized in Si [340]. The EDX spectrum of the TiN particles in figure 6.2(d) indicates that they are nearly stoichiometric with no evidence for oxygen.



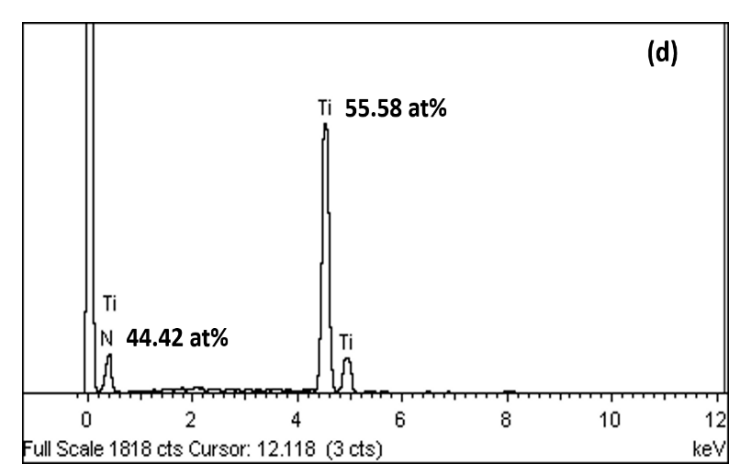


Figure 6.2: (c) optical absorption spectrum of TiN nanoparticles and (d) EDX spectrum of the TiN particles.

6.2. SERS studies

In this thesis two molecules are studied, (1) Nile blue (NB) and (2) Methylene blue (MB), were chosen as prototypes to investigate the efficacy of the TiN nanoparticles decorated ZnO nanowire arrays for SERS applications. The Raman spectrum of NB, recorded by dispersing it in the form of a film on a glass slide and displayed in figure 6.3(a) consisted of low-intensity modes at 382, 472, 553, and 653 cm⁻¹, and all of them matched with earlier reports. The most significant feature occurs at 592 cm⁻¹, assigned to C-C-C and C-N-C deformations [341]. In contrast, the Raman spectrum of MB in figure 6.3(b) exhibits several low intensity features at 450, 664,716,1038,1154, 1390, 1430 and 1500 cm⁻¹. In this case, the signature peak, which occurs at 1622 cm⁻¹, is assigned to ring stretching of C-C mode. All the characteristic peaks were well matched with previous reports [342]. Thus, when these spectra are compared with the Raman spectra of TiN nanoparticle decorated ZnO nanowires presented in figure 6.2(b) shows that the signature peaks of both molecules (NB and MB) are distinct from ZnO and TiN. As a consequence, the SERS effect can be unambiguously studied.

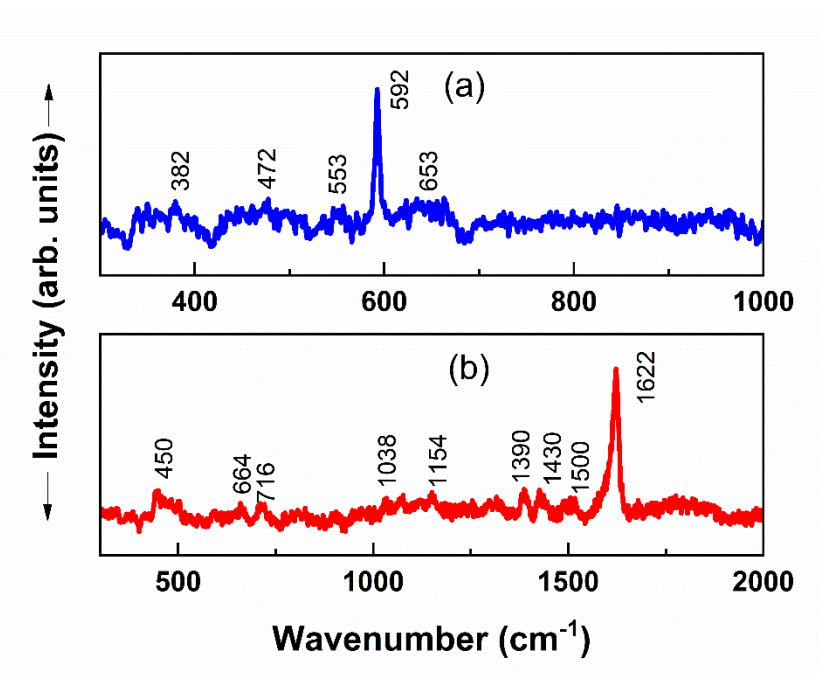


Figure 6.3: Raman spectra of (a) Nile blue (NB) and (b) Methylene blue (MB) on glass slides.

A control experiment to investigate the SERS effect was carried out at 5 μM Nile blue (NB) and Methylene blue (MB) concentrations, directly on ZnO nanowires (ZNW). The NB and MB molecules' Raman spectra were recorded at 10 different, random locations on the ZnO nanowire arrays. However, the spectra did not exhibit any signatures of either the NB or MB molecule at any of these locations. The only peak observed, as shown in a typical Raman spectrum in figure 6.4, appeared at 436 cm⁻¹ corresponding to wurtzite ZnO. The pristine ZNW surface is not suitable as a SERS substrate.

The threshold concentration below which the analyte molecule, NB, is not detected by the TiN nanoparticles decorated ZnO nanowires (termed as T-ZNW) is determined by recording the SERS spectra for different concentrations, as shown in the figure 6.5. It is observed that at a high concentration of 5 µM, there is a decrease in the intensity of the ZnO peak at 438 cm⁻¹. This is accompanied by an increase in the NB signature intensity 592 cm⁻¹, compared to the intensities on ZNW. At an NB concentration of 1 µM, on T-ZNW, there is complete quenching of the Raman modes relating to it, and only one high-intensity peak at 438 cm⁻¹, attributed to wurtzite ZnO is visible. The Raman spectrum of 0.5mM NB dispersed on a glass slide, presented earlier in figure 6.3(a) is also displayed for comparison.

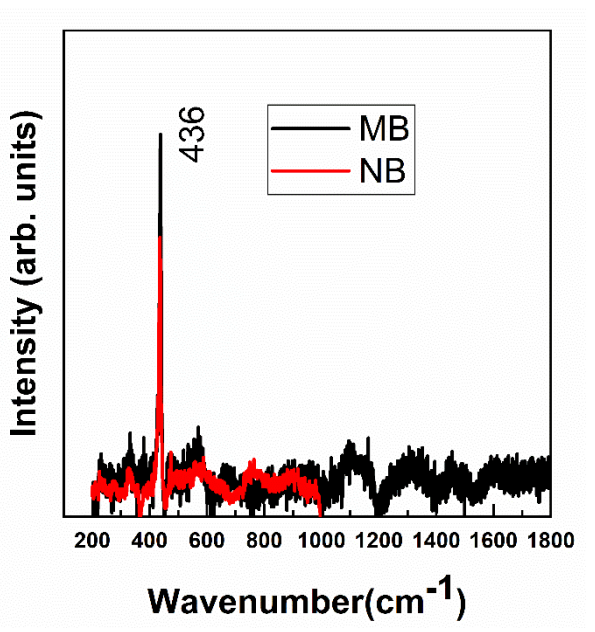


Figure 6.4: Raman spectra of Nile blue (NB) and Methylene Blue (MB) adsorbed directly on ZnO nanowires at $5~\mu M$ concentration.

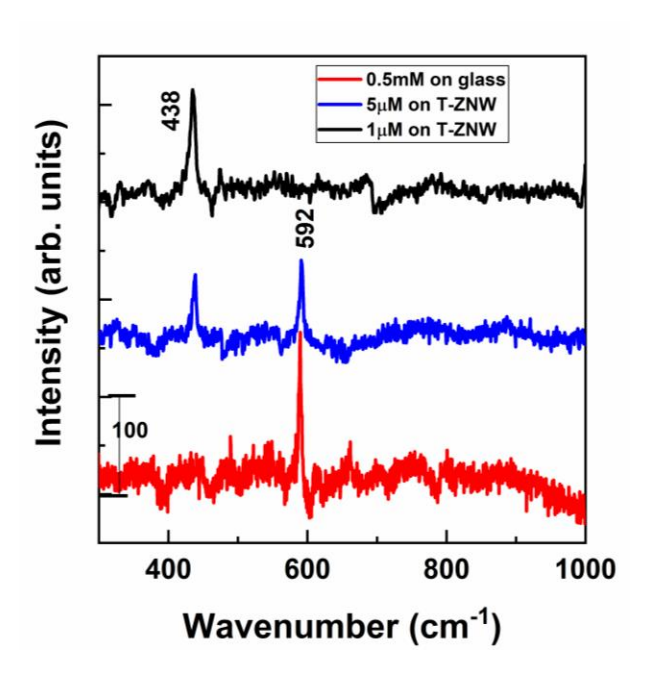


Figure 6.5: SERS spectra of Nile Blue (NB) adsorbed on TiN nanoparticles decorated ZnO nanowires at 1 and 5 μ M concentration. The red curve corresponds to the Raman spectrum of 0.5 mM NB dispersed directly on glass, for comparison.

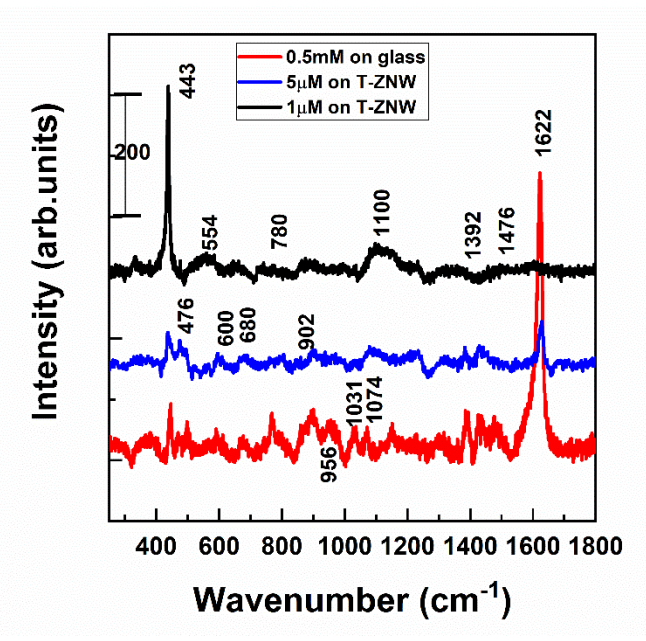


Figure 6.6: SERS spectra of Methylene Blue (MB) adsorbed on TiN nanoparticles decorated ZnO nanowires at 1 and 5 μ M concentration. The red curve corresponds to the Raman spectrum of 0.5mM MB dispersed directly on glass, for comparison.

The results of a similar experiment performed for Methylene Blue (MB) adsorbed on T-ZNW at different concentrations are shown in figure 6.6. At 5 μ M concentration of MB, the intensity of the peak at 1622 cm⁻¹ is significantly increased. Furthermore, there is a decrease in the intensity of the wurtzite ZnO mode, which now occurs at 443 cm⁻¹ compared to the intensity on ZNW shown in figure 6.4. Further decrease in MB concentration to 1 μ M results in suppressing the Raman modes of MB, and only the wurtzite ZnO peak at 443cm⁻¹ is visible. In both cases (i.e., NB and MB), there is enhancement at 5 μ M concentration while the Raman signals of the analyte molecules are quenched at 1 μ M concentration. It is also evident that even at a high concentration of 0.5mM, there is no enhancement of the Raman signals when the analyte molecules are adsorbed directly on the ZnO nanowires. Another exciting aspect is the shift of the most intense peak of ZnO to higher wavenumbers.

The Raman spectra were recorded at ten (10) different, random locations each for 5, 10, 15, and $25 \,\mu\text{M}$ concentration of MB and NB molecules on T-ZNW, and typical spectra are shown in figure 6.7(a) and 6.7(b), respectively. In both cases, there is the enhancement of the signature peaks of the respective molecules, MB at $1622 \,\text{cm}^{-1}$ and NB at $590 \,\text{cm}^{-1}$, with the increase in concentration.

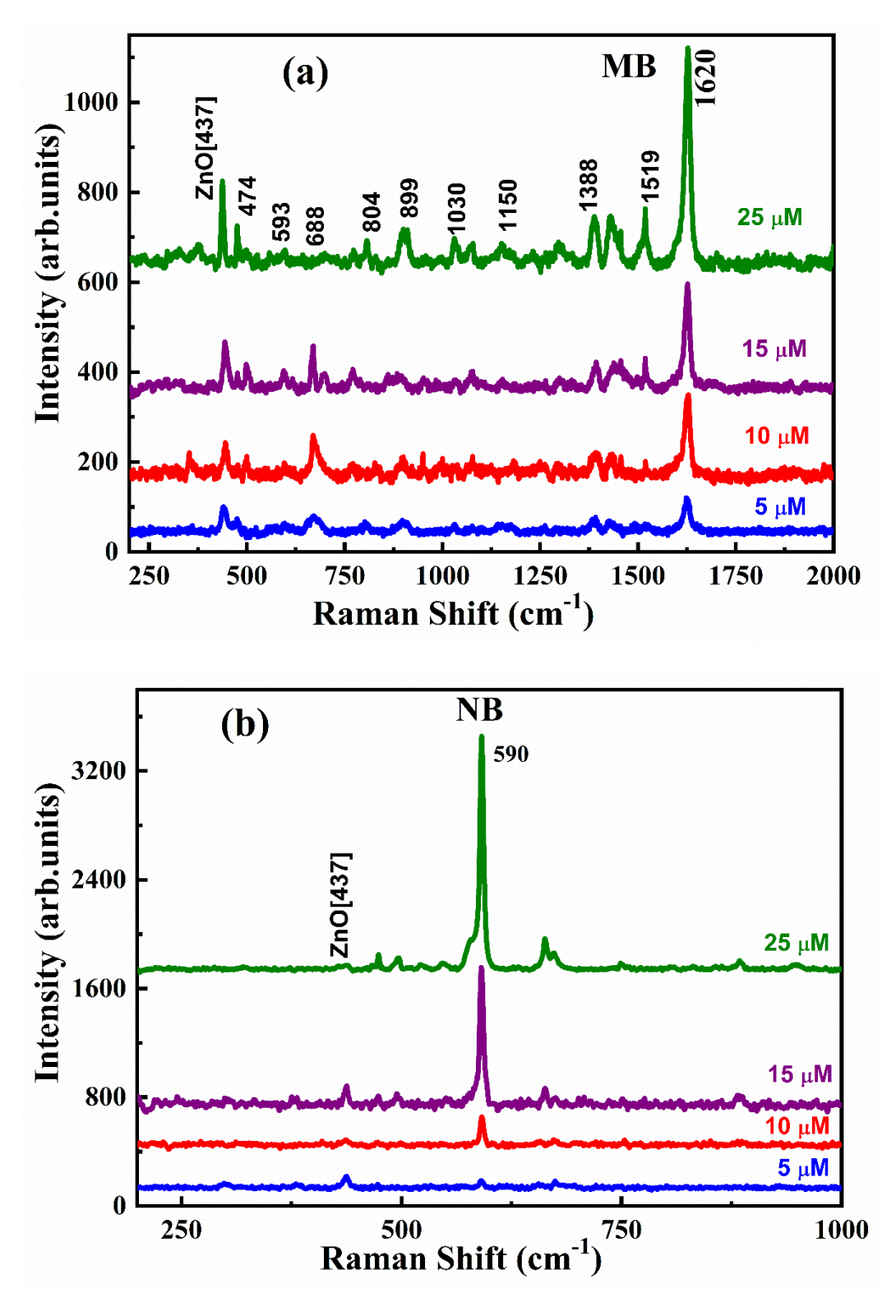


Figure 6.7: SERS spectra of (a) Methylene Blue (MB) and (b) Nile Blue (NB) adsorbed on TiN nanoparticles decorated ZnO nanowires at 5, 10, 15 and 25 μM concentration.

The calculation of the relative standard deviation (RSD %) is based on the Raman spectra recorded at 10 different locations on T-ZNW, for 5 μ M concentration of Methylene Blue (MB) molecule (which is considered the threshold concentration for detection). The results for MB are shown in Figures 6.8(a) and 6.8(b). It is observed that the RSD% for Methylene Blue (MB) molecule is 14.22%.

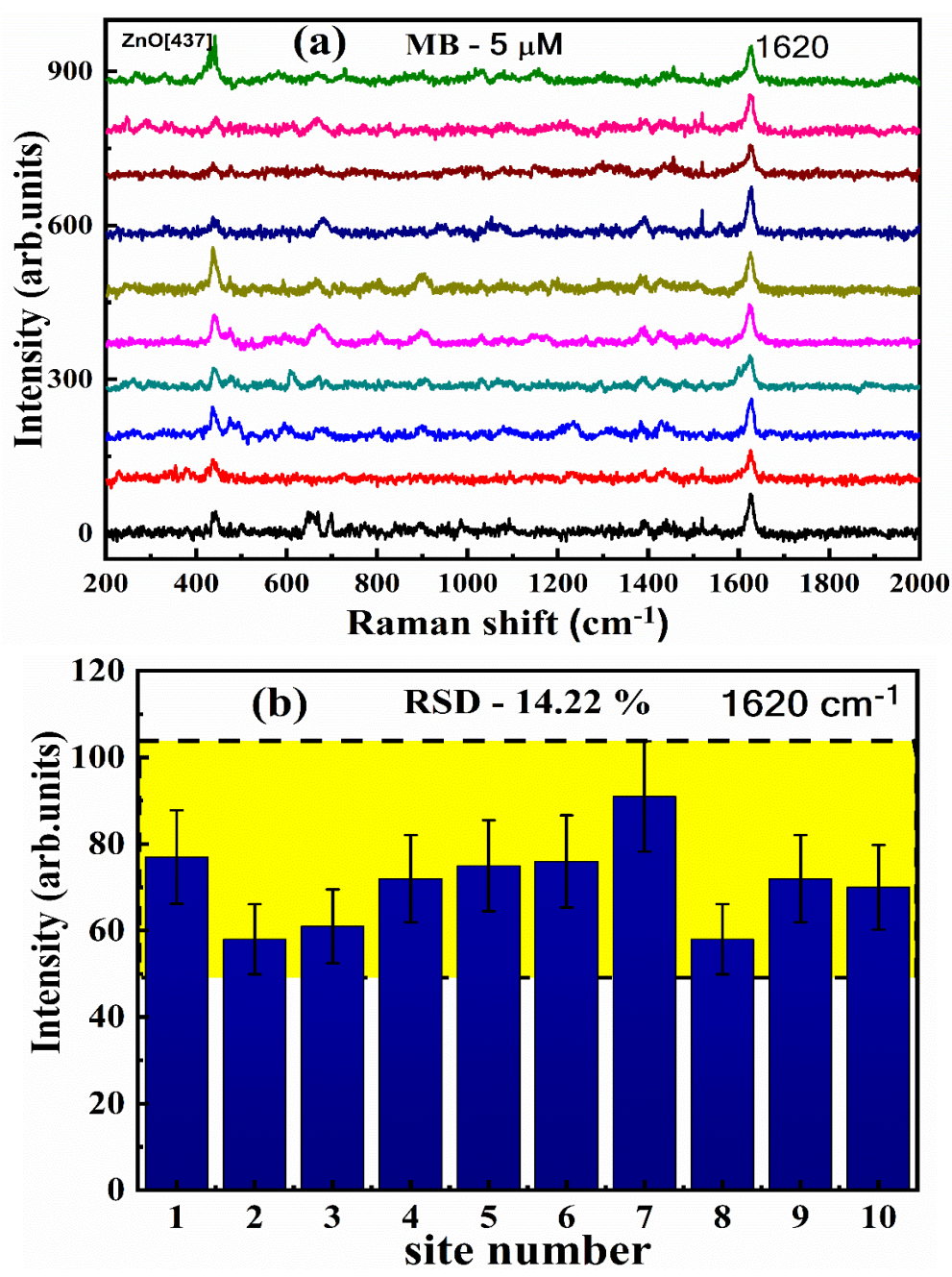


Figure 6.8: SERS spectra of (a) Methylene Blue adsorbed on TiN nanoparticles decorated ZnO nanowires at 5 μM concentration at 10 different locations on the surface and (b) the calculated relative square deviation (RSD %) for the peak at 1620 cm⁻¹.

Similarly, the calculation of the relative standard deviation (RSD %) is based on the Raman spectra recorded at 10 different locations on T-ZNW, for 5 μ M concentration of Nile Blue (NB) molecule(which is considered the threshold concentration for detection). The results for MB are hown in figures 6.9(a) and 6.9(b). It is observed that the RSD% for Nile blue (NB) molecule is 24.87%.

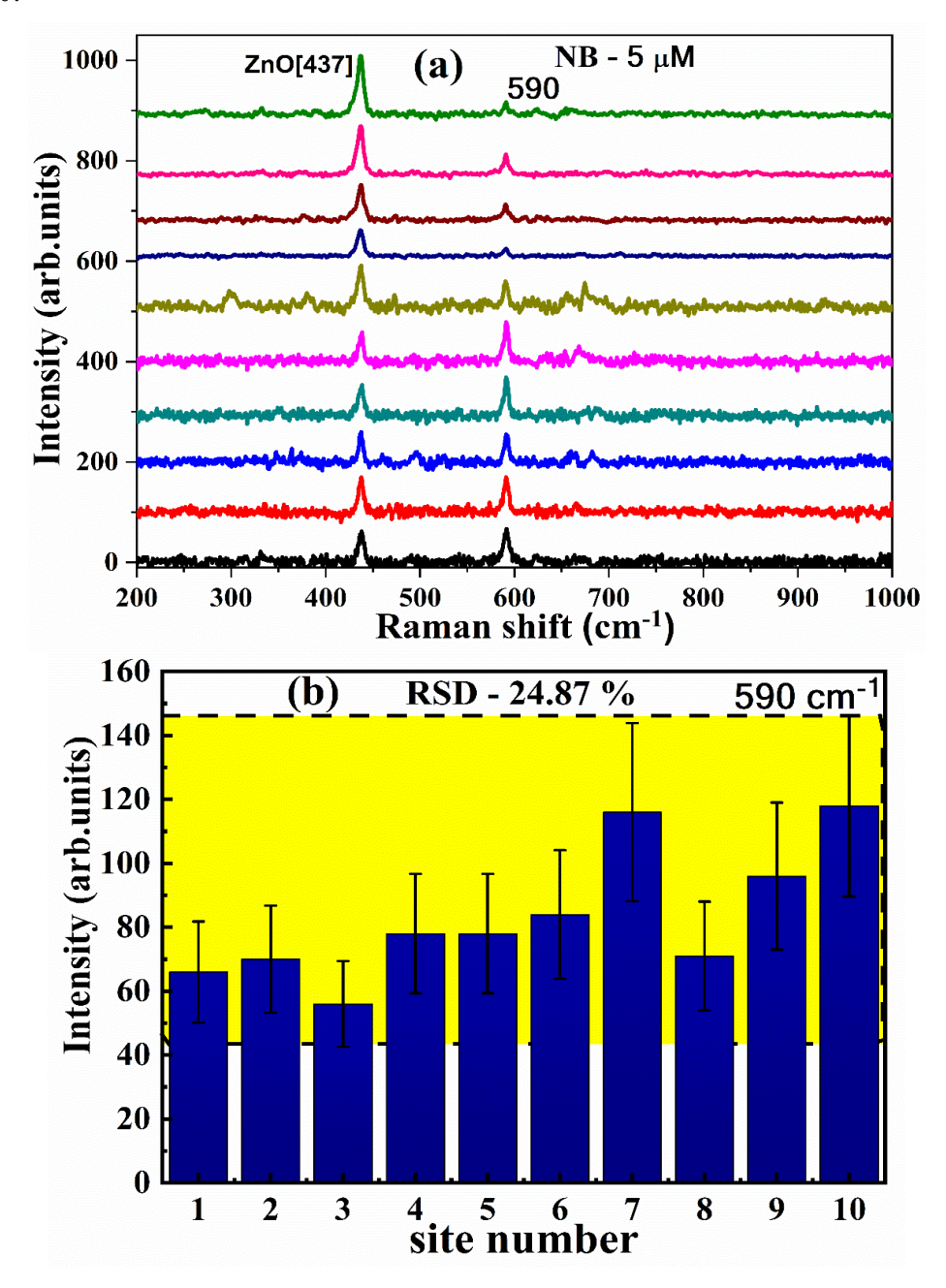


Figure 6.9: SERS spectra of (a)Nile Blue adsorbed on TiN nanoparticles decorated ZnO nanowires at 5 μ M concentration at 10 different locations on the surface and (b) the calculated relative square deviation (RSD %) for the peak at 590 cm⁻¹.

6.2.1. The SERS Enhancement factor calculations

The enhancement factors were calculated for both molecules using the expression [225, 343]

$$E_f = \frac{I_{SERS}}{I_{Raman}} X \frac{C_{Raman}}{C_{SERS}} \rightarrow (6.01)$$

where E_f is the enhancement factor, I_{SERS} is the SERS band intensity of probe molecules [MB (1622 cm⁻¹) and NB (592 cm⁻¹)] using the synthesized TiN-ZnO substrate, I_{Raman} is the Raman intensity of an probe molecule on a glass slide (without using substrate), C_{SERS} represents the corresponding concentration of an probe molecule on a TiN-ZnO substrate (10⁻⁶ M) and C_{Raman} is the concentration of an probe molecule on a glass slide (10⁻³ M, without substrate), which produces the Raman signal, I_{Raman} .

The enhancement factors (EF) values obtained are summarized in table 1 for different concentrations. It is observed that, as the concentration of the dye molecules on the T-ZNW surface is decreased, the E_f of their signature peak also decreases. This is attributed to the reduced adsorption on the T-ZNW surface. Nile blue has the chemical formula $C_{20}H_{20}ClN_3O$ and belongs to the family of phenoxazine and benzo-phenoxazine-based dyes. Methylene blue has the chemical formula $C_{16}H_{18}ClN_3S$ and is also known as methylthioninium chloride. Since the chloride ions are present in both compounds, it is hypothesized that the affinity of TiN to chloride ions might cause the binding of the dye molecules to the nanoparticles, leading to a chemical SERS effect.

It is well established that there are two main surface enhancement mechanisms of Raman signals [225, 343-350]. They are either electromagnetic or chemical in nature. The electromagnetic enhancement of signals involves the coupling of the electric fields related to surface Plasmons of the nanoparticles with incident radiation. The strength of coupling varies as the fourth power of the local electric field. As a result, a minimal variation in the local field can cause very significant changes in the SERS signals. The chemical enhancement is, in contrast, a weaker effect relying on the formation of complexes on the nanoparticle surface, charge transfer, or charge transfer resonances induced by molecular adsorption. Due to the differences in their origins, the enhancement factors observed due to the EM effect are large in magnitude (10⁴ or higher). In contrast, the chemical effect enhancement factors are of the order of 10³, at maximum. Thus, it would appear that the SERS effect is more chemical in nature in the present case. Interestingly, Wei et al. [241] have observed a combination of the electromagnetic and charge transfer effect in the TiN thin film-based SERS substrates used to detect R6G.

Table 1: Enhancement Factors (EF) for Methylene Blue and Nile Blue at different concentrations on TiN-ZnO nanowire array SERS substrates.

Concentration of analyte molecule (µm)	Enhancement factor for	
	Methylene Blue (MB)	Nile Blue (NB)
1	0	0
5	28	94
10	33	110
15	34	360
25	36	369

The origin of the enhancement effect has been deliberated in earlier works [225, 343-350], and it is attributed to three mechanisms:

- 1. The existence of surface Plasmon resonances
- 2. Charge transfer between the metal and conduction band of the adsorbed molecule
- 3. Resonances within the adsorbed molecule leading to single-molecule detection

The charge transfer effect may be due to the differences in Fermi levels of the adsorbed molecule and TiN [344]. It is hypothesized that the chemical enhancement is induced by the interaction between the TiN nanoparticles and the adsorbed molecule leading to the formation of a charge-transfer state. When this state is resonant with the laser wavelength, an additional resonant-chemical effect enhances the SERS. This is possible due to the interaction between the Fermi level of the metal and the molecule's frontier orbitals. Other factors to be considered are postulated by Kudryashov et al. [351] in samples produced by mask-less micro-patterning of thin plasmonic films of Ag, Cu, Al, and Au-Pd alloys for surface-enhanced IR spectroscopy application. The IR

transmission response of micro-hole arrays with varying parameters was studied. In the case of R6G adsorbed on Ag substrates, they find evidence for a donor-like chemical enhancement. This process is sensitive to bonding/ vibration in analyte molecules and contributes to analyte-metal complexing via charge transfer. Thus, the effect of TiN dangling bonds and spectrallyhomogeneous Mie-type SERS enhancement in optically-resonant TiN nanoparticles (either electric dipolar or magnetic dipolar/quadrupolar resonances) also need to be considered in the present case. A third point that needs consideration is that the observed SERS enhancement can be photo-induced in nature. This is inferred from literature wherein it has been shown that TiN is a suitable catalyst for the photodegradation of molecules such as methylene blue [352]. The essential requirement is the adsorption of the molecule to be photodegraded onto the catalyst material. In photocatalysis, the molecule absorbs the incident radiation to generate electron-hole pairs, followed by the separation of the excited charges and charge transfer to the surface of the photocatalyst. Finally, these charges are used for redox reactions [353]. It is assumed that the charge transfer process occurring in the present case is an amalgamation of the three mechanisms (non-photo induced and photo-induced) as described above. However, the individual contributions cannot be isolated from the experimental set-up used in the present study.

The proof-of-concept study presented here indicates promise. Further enhancements will be possible with these substrates by optimizing the size, shape, and inter-particle distance of the TiN nanoparticles. The main advantages are the ease of preparing large-area substrates and the low costs involved. More detailed studies with different analyte molecules (including explosives and pesticides) need to be carried out to test the efficacy of these substrates.

6.3. Summary

TiN nanoparticle decorated ZnO nanowires are synthesized by a simple process. The TiN nanoparticles are 30-100 nm in size and exhibit absorption related features at wavelengths between 400-600 nm. The application of these substrates as surface enhanced Raman scattering substrates is demonstrated by detecting nile blue and methylene blue molecules on the nanoparticles. It is demonstrated that the origin of SERS in this system is chemical in nature. The facile approach to synthesis indicates promise for cost effective scale-up.

Chapter

7

Summary, Conclusions and Scope for future work

7.1. Summary and Conclusions

The main results of the thesis are summarized in this chapter with reference to the objectives formulated which were

1. Investigate the role of precursors, temperature and duration of processing, and seed layers (Au, In, Sn, In_2O_3 , SnO and ZnO) on the growth of ZnO nanostructures.

The results presented in chapters 3 and 4 show that high quality seed layers can be deposited by thermal evaporation in vacuum. The metal films of In, Sn and Au are deposited at room temperature and do not require any post-deposition processing to achieve the crystallinity and microstructure needed to be used as seed layers. This is very attractive for flexible device applications. In the case of oxide seed layer thin films, moderate post deposition annealing is required to achieve the desired crystallinity, microstructure and stoichiometry. The optimal thickness for the growth of ZnO nanostructures in each case, is established. A detailed study of the precursors Zinc acetate and zinc nitrate as well as the role of mineralizers HMTA, NaOH and KOH is presented and it is shown that HMTA is preferred. The threshold temperature and duration of hydrothermal processing to realize nanostructures is also demonstrated.

2. Establish the role of process parameters and surface conditions in the growth of vertically aligned ZnO nanowires and nano/micro rods by hydrothermal synthesis.

In this part of the study, it is shown that HMTA plays a crucial role in vertical alignment of ZnO nanostructures as well as determining the nature of crystallinity. Lower temperature and shorter duration of processing is suitable to produce nanowires with diameters <100 nm while higher temperatures (>120°C) and longer durations (>3hrs) lead to large diameter and longer nano or micro rod arrays. The surface microstructure of seed layer thin films is an important parameter. It is observed that, while ZnO seed layer films support ZnO nanowires, the other seed layer surfaces mostly lead to the growth of hexagonal rods. The density of packing of arrays is strongly dependent on the nature of the seed layer. Independent of the seed layer material, all nano/microstructures are hexagonal shaped when either the temperature is high or the duration of processing is long.

3. Compare the normal and microwave-assisted hydrothermal processes for the growth of ZnO nanostructures.

The main difference between the conventional and microwave assisted hydrothermal synthesis process is that microwave assistance leads to growth of nanostructures at a fairly low temperature (90°C) and short duration (30 min.). However, even in this case it appears, based on the limited experiments carried out, that higher temperatures or longer durations are required to obtain vertically aligned nanostructures. More significantly, in the case of microwave assisted hydrothermal processing a hierarchy of structures is observed, which is absent in conventional hydrothermal processing. This leads to differences in photoluminescence behaviour between the nanostructures processed by the two different techniques.

4. Demonstrate the control of photoluminescence behavior of ZnO nanostructures grown by hydrothermal synthesis.

Two types of structures were studied in the present thesis: (1) Homostructures wherein ZnO nanostructures are grown on ZnO seed layer thin films and (2) Heterostructures wherein the ZnO nanostructures on other seed layers. In both cases, it is observed that the PL features are strongly dependent on the crystallinity and microstructures as well as defects in the seed layer thin films. It is demonstrated that the intensity and position of the defect related peak of ZnO at 500 -600 nm and the near band edge peak at 380 nm are strongly dependent on the seed layer material. Therefore, it is proposed that the emission wavelength of the ZnO nanostructures can be tuned by changing the seed layer. This is very useful for LED applications. A detailed study of defects using Raman scattering is also presented.

5. Demonstrate the use of ZnO nanostructures for wettability and self-cleaning applications

ZnO surfaces are well known for their wettability and self-cleaning applications. In this study, seed layer mediated wettability of the ZnO nano/micro rod arrays is demonstrated. The ZnO nanostructures are hydrophobic independent of the seed layer. However, they are superhydrophobic on the ZnO seed layer thin films. Under the influence of UV irradiation, the nanostructures show transition to (super)hydrophilic state within ten minutes. The rate of this transition is dependent on the seed layer on which the nanostructures are grown. It is thus

evident that the nanostructures can be used for self-cleaning applications. The role of surface defects, oxygen vacancies and adatoms is clearly elaborated by carrying out a detailed correlation between the wettability, PL and Raman data.

6. Demonstrate the use of Titanium nitride (TiN) nanoparticle decorated ZnO nanostructures for sensing applications by the surface enhanced Raman scattering process.

In this study, ZnO nanowire arrays decorated with TiN nanoparticles as surface enhanced Raman scattering (SERS) substrates is demonstrated. TiN nanoparticles were then dispersed in acetone and drop cast on the ZnO nanowire arrays for decoration. Scanning electron microscopy confirmed the presence of TiN nanoparticles on the ZnO nanowires. SERS experiments using different concentrations (5, 10, 15, and 25 μ M) of Nile blue (NB) and Methylene Blue (MB) as the analyte molecules exhibited enhancement in the Raman signals. It is shown that the origin of the SERS effect is chemical in nature, with contribution from different interactions between the analyte molecule and the TiN nanoparticles. Thus, this study represents a simple, cost-effective and facile method for the fabrication of TiN based SERS substrates.

In summary, the most important contributions of the thesis are:

- 1. Deposition and characterization of different metal and metal oxide seed layers and establishing their role in determining the shape evolution and alignment of ZnO nano/micro wire/rod arrays.
- 2. Isolating the contribution of each process parameter on the growth of ZnO nanostructures by hydrothermal synthesis and impact on photoluminescence.
- 3. Comparison of the growth of ZnO nanowires/nanorods by conventional and microwave hydrothermal synthesis.
- 4. Seed layer mediated wettability and wettability transition of ZnO nano/micro-rod arrays.
- 5. ZnO nanowire arrays decorated with Titanium Nitride nanoparticles as surface Enhanced Raman Scattering Substrates.

7.2. Scope for future work

Some possibilities for extending this work in the future are,

- 1. Achieve better and predictable control over the dimensions of the nanowire arrays.
- 2. Investigating the dielectric properties of the vertically aligned metal oxide nanowires and nanorods with different thickness ZnO seed layers at different frequencies (from MHz to GHz).
- 3. To study vertically growing nanostructures on Flexible substrates using different metal and metal-oxide (ZnO, Au, In, Sn) seed layers.
- 4. To study the sensitivity of the metal oxide nanostructures under various gases by fabricating a gas sensor.
- 5. Fabricate different electronic devices with the obtained nanowire arrays.

References

- [1] K.T. Ramesh, Nanomaterials, 1-20 (2009), Springer, Boston, MA.
- [2] Y Gogotsi, Nanomaterials handbook, (2017) CRC press.
- [3] D Vollath, Environ. Eng. Manag. J., 7(6), pp. 865-870 (2008).
- [4] J.N. Tiwari, R.N. Tiwari, and K.S. Kim, *Prog. Mater. Sci*, 57(4), pp. 724-803 (2012).
- [5] G.W.Bryant, In *Science and engineering of one-and zero-dimensional semiconductors*, pp. 243-254(1990), Springer, Boston, MA.
- [6] S. Iijima, Nature 354: 56 Crossref. ISI, Google Scholar(1991).
- [7] S.V.Kuchibhatla, A.S. Karakoti, D. Bera, and S. Seal, *Prog. Mater. Sci*, *52*(5), pp. 699-913 (2007).
- [8] G. Shen, and D.Chen, Front. Optoelectron., 3(2), pp. 125-138 (2010).
- [9] Z. Sun, T. Liao, and L. Kou, *Science China Materials*, 60(1), pp. 1-24(2017).
- [10] M.Fernández- García, and J.A. Rodriguez, *Encyclopedia of inorganic and bioinorganic chemistry* (2011).
- [11] XY.Liu, KX. Wang, JS Chen, Energ StorageMater, 3, pp. 1–17(2016).
- [12] W Li, L Zeng, Y Wu, et al., Sci China Mater, 59, pp. 287–321(2016).
- [13] R.S. Rawat, In J. Phys. Conf., 591(1), pp. 012021(2015), IOP Publishing.
- [14] X. Zhang, Y. Zhang, J. Xu, Z. Wang, X. Chen, D. Yu, P. Zhang, H. Qi, and Y. Tian, Appl. Phys. Lett., 87(12), p. 123111(2005).
- [15] B.D. Yao, Y.F. Chan, and N. Wang, Appl. Phys. Lett., 81(4), pp. 757-759(2002).
- [16] Z.R. Dai, Z.W. Pan, and Z.L. Wang, Adv. Funct. Mater., 13(1), pp. 9-24(2003).
- [17] Y.C. Zhang, X. Wu, X.Y. Hu, and Q.F. Shi, Mater. Lett., 61(7), pp. 1497-1499(2007).
- [18] X. Liu, G. Qiu, Y. Zhao, N. Zhang, and R. Yi, J. Alloy. Compd., *439*(1-2), pp. 275-278(2007).
- [19] K. Lee, W.S. Seo, and J.T. Park, J. Am. Chem. Soc., 125(12), pp. 3408-3409(2003).3
- [20] S. Muthukumar, H. Sheng, J. Zhong, Z. Zhang, N.W. Emanetoglu, and Y. Lu, *IEEE Transactions on Nanotechnology*, 2(1), pp. 50-54(2003).
- [21] Y. Liu, C.R. Gorla, S. Liang, N. Emanetoglu, Y. Lu, H. Shen, and M. Wraback, JEM, 29(1), pp. 69-74(2000).
- [22] A. Huczko, Appl. Phys. A, 70(4), pp. 365-376(2000).
- [23] M. Pérez-Page, E. Yu, J. Li, M. Rahman, D.M. Dryden, R. Vidu, and P. Stroeve, Adv. Colloid Interface Sci., 234, pp. 51-79(2016).
- [24] G. Cao, and D. Liu, Adv. Colloid Interface Sci., 136(1-2), pp. 45-64(2008).

- [25] H.M. Shang, and G. Cao, In *Springer Handbook of Nanotechnology*, pp. 169-186(2010), Springer, Berlin, Heidelberg.
- [26] L. D'Souza, R. Richards, (Rodríguez, J.A., Fernández-García, M; Eds.). Whiley: N. J., Chpt. 3., (2007).
- [27] S. Buzby, R.S. Franklin, S.I. Shah, (Rodríguez, J.A., Fernández-García, M; Eds.). Whiley: N.J., Chpt 4., (2007).
- [28] M. Meyyappan, M. Sunkara, CRC Press, Taylor and Francis Group, Boca Raton, London, New York, (2010).
- [29] R.W. Cahn, the Coming of Materials Science, Pergamon Press: Oxford, UK, 2001.
- [30] P. Anyalebechi, Padnos College of Engineering and Computing: Grand Rapids, MI, USA, 2006.
- [31] W.D. Callister, Fundamentals of Materials Science and Engineering; Wiley: London, UK, 471660817(2000).
- [32] C. Li, Z. Sun, Y. Xue, G. Yao, S.A. Zheng, Adv. Powder Technol., 27, pp. 330–337(2016).
- [33] I. Ismail, M. Jani, A. Mutalib, N. Osman, Mater. Sci. Forum, 917, pp. 78–82(2018).
- [34] T.M. Budnyak, I.V. Pylypchuk, V.A. Tertykh, E.S. Yanovska, D. Kolodynska, Nanoscale Res. Lett., 10, pp. 87(2015).
- [35] K. Kappis, C. Papadopoulos, J. Papavasiliou, J. Vakros, Y. Georgiou, Y. Deligiannakis, G. Avgouropoulos, Catalysts, 9, pp. 138(2019).
- [36] G. Yang, S.J. Park, Electrochim. Acta, 285, pp. 405–414(2018).
- [37] G. Yang, S.J. Park, J. Alloys Compd., 741, pp. 360–367(2018).
- [38] H. Kim, B.N. Popov, J. Power Sources, 104, pp. 52–61(2002).
- [39] J. Morán-Lázaro, E. Guillen-López, F. López-Urias, E. Muñoz-Sandoval, O. Blanco-Alonso, H. Guillén-Bonilla, A. Guillén-Bonilla, V. Rodríguez-Betancourtt, M. Sanchez-Tizapa, M. Olvera-Amador, Sensors, 18, pp. 701(2018). [CrossRef]
- [40] H.R. Ghorbani, F.P. Mehr, H. Pazoki, B.M. Rahmani, Orient. J. Chem., 31, pp. 1219–1221 (2015).
- [41] L. Nejati-Moghadam, A. Esmaeili Bafghi-Karimabad, M. Salavati-Niasari, H. Safardoust, J. Nanostruct., 5, pp. 47–53(2015).
- [42] G. Yang, and S.J. Park, *Materials*, 12(7), pp. 1177(2019).
- [43] D. Polsongkram, P. Chamninok, S. Pukird, L. Chow, O. Lupan, G. Chai, H. Khallaf, S. Park, A. Schulte, Physica B, 403, pp. 3713–3717(2008).
- [44] T. Sekiguchi, S. Miyashita, K. Obara, T. Shishido, N. Sakagami, J. Cryst. Growth, 214, pp. 72–76(2000).
- [45] P.M. Fenn, Can. Miner., 15, pp. 135–161(1977).
- [46] H. Cheng, J. Ma, Z. Zhao, L. Qi, Chem. Mater., 7, pp. 663–671(1995).

- [47] G. Dell'Agli, A. Colantuono, G. Mascolo, Solid State Ion., 123, pp. 87–94(1999).
- [48] J. Zhang, K. Huang, L. Yuan, S. Feng, CrystEngComm., 20, pp. 470–476(2018).
- [49] M. Roble, S. Rojas, R. Wheatley, S. Wallentowitz, A. Cabrera, D. Diaz-Droguett, J. Solid State Chem., 271, pp. 314–325(2019).
- [50] Bharat Newalkar, Johnson Olanrewaju, Sridhar Komarneni, *Chem. Mater.*, 13(2), pp. 552–557(2001).
- [51] A. Pimentel, S.H. Ferreira, D. Nunes, T. Calmeiro, R. Martins, and E. Fortunato, *Materials*, 9(4), pp. 299(2016).
- [52] P. Liu, Y. Li, Y. Guo, Z. Zhang, Nanoscale Res. Lett., 7, pp. 220–222(2012).
- [53] D.C. Kim, B.H. Kong, H.K. Cho, D.J. Park, and J.Y. Lee, *Nanotechnology*, *18*(1), pp. 015603(2006).
- [54] R. Liu, A.A. Vertegel, E.W. Bohannan, T.A. Sorenson, and J.A Switzer, *Chemistry of Materials*, *13*(2), pp. 508-512(2001).
- [55] D. Zhao, C. Andreazza, P. Andreazza, J. Ma, Y. Liu, and D. Shen, Chem. Phys. Lett., 408(4-6), pp. 335-338(2005).
- [56] J. Song, and S. Lim, J. Phys. Chem. C, 111(2), pp. 596-600(2007).
- [57] F. Wang, A. Dong, and W.E. Buhro, Chem. Rev., 116(18), pp. 10888-10933(2016).
- [58] S.M. Roper, S.H. Davis, S.A. Norris, A.A. Golovin, P.W. Voorhees, and M. Weiss, J. Appl. Phys., *102*(3), pp. 034304(2007).
- [59] S.Y. Bae, H.W. Seo, and J. Park, J. Phys. Chem. B, 108(17), pp. 5206-5210(2004).
- [60] J.M. Wu, H.C, Shih, W.T. Wu, Y.K. Tseng, and I.C. Chen, J. Cryst. Growth, *281*(2-4), pp. 384-390(2005).
- [61] A. Umar, S.H. Kim, Y.S. Lee, K.S. Nahm, and Y.B. Hahn, J. Cryst. Growth, 282(1-2), pp. 131-136(2005).
- [62] Q. Ahsanulhaq, A. Umar, and Y.B. Hahn, *Nanotechnology*, 18(11), pp. 115603(2007).
- [63] L. Qin, J. Xu, X. Dong, Q. Pan, Z. Cheng, Q. Xiang, and F. Li, *Nanotechnology*, 19(18), pp. 185705(2008).
- [64] M. Kawakami, A.B. Hartanto, Y. Nakata, and T. Okada, JJAP, 42(1A), pp. L33(2003).
- [65] A. Harano, K. Shimada, T. Okubo, M. Sadakata, J. Nanoparticle. Res., 4, pp. 215(2002).
- [66] L.M. Cao, K. Hahn, Y.Q. Wang, C. Scheu, Z. Zhang, C.X. Gao, Y.C Li, X.Y. Zhang, L.L. Sun, W.K. Wang, and M. RüHLE, *Advanced Materials*, *14*(18), pp. 1294-1297(2002).
- [67] L. M. Cao, X.Y. Zhang, C.X. Gao, W.K. Wang, Z.L. Zhang, and Z. Zhang, *Nanotechnology*, *14*(8), pp. 931(2003).
- [68] N.M. Hwang, and D.K. Lee, *Journal of Physics D: Applied Physics*, 43(48), pp. 483001(2010).

- [69] Y.W. Heo, V. Varadarajan, M. Kaufman, K. Kim, D.P. Norton, F. Ren, and P.H. Fleming, Appl. Phys. Lett., *81*(16), pp. 3046-3048(2002).
- [70] Y.W. Heo, V. Varadarajan, M. Kaufman, K. Kim, D.P. Norton, F. Ren, and P.H. Fleming, *MRS Online Proceedings Library*, 728(1), pp. 3151-3155(2002).
- [71] D. Wang, A. Pierre, M.G. Kibria, K. Cui, X. Han, K.H. Bevan, H. Guo, S. Paradis, A.R. Hakima, and Z. Mi, *Nano letters*, *11*(6), pp. 2353-2357(2011).
- [72] C. Jagadish, and S.J. Pearton, eds., properties, and applications, (2011). Elsevier.
- [73] U. Özgür, Y.I. Alivov, C. Liu, A. Teke, M. Reshchikov, S. Doğan, V.C.S.J. Avrutin, S.J. Cho, and A.H. Morkoç, J. Appl. Phys., 98(4), pp. 11(2005).
- [74] H. Morkoç, and U. Özgür, John Wiley & Sons(2008).
- [75] Z.L. Wang, J. Condens. Matter Phys., 16(25), pp. R829(2004).
- [76] C. Klingshirn, *ChemPhysChem*, 8(6), pp. 782-803(2007).
- [77] W. Mai, (Doctoral dissertation, Georgia Institute of Technology) (2009).
- [78] S. Cho, J. Ma, Y. Kim, Y. Sun, G.K. Wong, and J.B. Ketterson, Appl. Phys. Lett., 75(18), pp. 2761-2763(1999).
- [79] Y.G. Wang, S.P. Lau, H.W. Lee, S.F. Yu, B.K. Tay, X.H. Zhang, and H.H. Hng, **J**. Appl. Phys., *94*(1), pp. 354-358(2003).
- [80] Y.X. Liu, Y.C Liu, D.Z. Shen, G.Z. Zhong, X.W. Fan, X.G. Kong, R. Mu, and D.O. Henderson, J. Cryst. Growth, *240*(1-2), pp. 152-156(2002).
- [81] S.K. Pandey, and S. Mukherjee, In 2013 IEEE 5th International Nanoelectronics Conference (INEC), pp. 205-208(2013). IEEE.
- [82] M.G. Krishna, M. Vinjanampati, and D.D Purkayastha, EPJ AP, 62(3), (2013).
- [83] U.P. Shaik, S. Kshirsagar, M.G. Krishna, S.P. Tewari, D.D. Purkayastha, and V. Madhurima, Mater. Lett., 75, pp. 51-53(2012).
- [84] D.D. Purkayastha, M.G. Krishna, and V. Madhurima, Mater. Lett., 124, pp. 21-23(2014).
- [85] G. Whyman, E. Bormashenko, and T. Stein, Chem. Phys. Lett., 450(4-6), pp. 355-359(2008).
- [86] H.Y. Erbil, and C.E. Cansoy, *Langmuir*, 25(24), pp. 14135-14145(2009).
- [87] E. Bormashenko, Colloids Surf, A Physicochem Eng Asp, 345(1-3), pp. 163-165(2009).
- [88] G. Alberto, S. Meloni, C. Mauro, and C.M. Casciola, (2012).
- [89] E.S. Savoy, and F.A. Escobedo, *Langmuir*, 28(46), pp. 16080-16090(2012).
- [90] W. Ren, Langmuir, 30(10), pp. 2879-2885(2014).
- [91] D. Murakami, H. Jinnai, and A. Takahara, *Langmuir*, 30(8), pp. 2061-2067(2014).
- [92] G. Manukyan, J.M. Oh, D. Van Den Ende, R.G. Lammertink, and F. Mugele, *Phys. Rev. Lett.*, *106*(1), pp. 014501(2011).

- [93] G. Liu, L. Fu, A.V. Rode, and V.S. Craig, *Langmuir*, 27(6), pp. 2595-2600(2011).
- [94] T.N. Krupenkin, J.A. Taylor, E.N. Wang, P. Kolodner, M. Hodes, and T.R. Salamon, *Langmuir*, *23*(18), pp. 9128-9133(2007).
- [95] D. Upadhaya, P. Kumar, and D.D. Purkayastha, J. Mater. Sci.: Mater. Electron., *30*(11), pp. 10399-10407(2019).
- [96] D.D. Purkayastha, and M.G. Krishna, Appl. Surf. Sci., 447, pp. 724-731(2018).
- [97] D.D. Purkayastha, R. Pandeeswari, V. Madhurima, and M.G. Krishna, Mater. Lett., 92, pp. 151-153(2013).
- [98] N. Paul, D.D. Purkayastha, and M.G. Krishna, Superlattices Microstruct., *129*, pp. 105-114(2019).
- [99] T.R. Jensen, M.D. Malinsky, C.L. Haynes, and R.P. Van Duyne, J. Phys. Chem. B, *104*(45), pp. 10549-10556(2000).
- [100] M. Duval Malinsky, K.L. Kelly, G.C. Schatz, and R.P. Van Duyne, J. Phys. Chem. B, *105*(12), pp. 2343-2350(2001).
- [101] T.R. Jensen, M.L. Duval, K.L Kelly, A.A. Lazarides, G.C. Schatz, and R.P. Van Duyne, J. Phys. Chem. B, *103*(45), pp. 9846-9853(1999).
- [102] S. Nie, and S.R. Emory, *science*, 275(5303), pp. 1102-1106(1997).
- [103] K. Fukami, M.L. Chourou, R. Miyagawa, A. Muñoz Noval, T. Sakka, M. Manso-Silván, R.J. Martín-Palma, and Y.H. Ogata, *Materials*, *4*(4), pp. 791-800(2011).
- [104] M.L. Chourou, K. Fukami, R. Miyagawa, T. Sakka, and Y.H. Ogata, *ECS Transactions*, *33*(16), p. 117(2011).
- [105] S.N. Terekhov, A. Yu. PANARIN, K.I. Kholostov, V.P. Bondarenko, and P.Y. TURPIN, In *Physics, Chemistry And Application Of Nanostructures: Reviews and Short Notes* (pp. 507-510) (2009).
- [106] K.V. Artemyeva, H.V. Bondarenko, V.P. Bondarenko, A.Y. Panarin, and S.N. Terekhov, In 2013 23rd International Crimean Conference" Microwave & Telecommunication Technology" pp. 834-835(2013). IEEE.
- [107] M. Kerker, D.S. Wang, and H. Chew, Appl. Opt., 19(24), pp. 4159-4174(1980).
- [108] M.O.L.A.D.S. Kerker, O. Siiman, L.A. Bumm, and D.S. Wang, Appl. Opt., 19(19), pp. 3253-3255(1980).
- [109] D.S. Wang, and M. Kerker, PRB, 24(4), pp.1777 (1981).
- [110] Y. Salinas, R. Martínez-Máñez, M.D. Marcos, F. Sancenón, A.M. Costero, M. Parra, and S. Gil, Chem. Soc. Rev., 41(3), pp. 1261-1296(2012).
- [111] O. Kvítek, J. Siegel, V. Hnatowicz, and V. Švorčík, J Nanomater 2013. *Article ID*, 743684, pp. 15(2013).
- [112] K.B. Biggs, J.P. Camden, J.N. Anker, and R.P.V. Duyne, J. Phys. Chem., *113*(16), pp. 4581-4586(2009).

- [113] S. Kundu, M. Mandal, S.K. Ghosh, and T. Pal, J PHOTOCH PHOTOBIO A, *162*(2-3), pp. 625-632(2004).
- [114] S. Kundu, M. Mandal, S.K. Ghosh, and T. Pal, J. Colloid Interface Sci., 272(1), pp. 134-144(2004).
- [115] K. Kneipp, H. Kneipp, I. Itzkan, R.R. Dasari, and M.S. Feld, J. Condens. Matter Phys., *14*(18), pp. R597(2002).
- [116] H. Zhou, D. Yang, N.P. Ivleva, N.E. Mircescu, S. Schubert, R. Niessner, A. Wieser, and C. Haisch, Anal. Chem., 87(13), pp. 6553-6561(2015).
- [117] M. Kahraman, K. Keseroğlu, and M. Culha, Appl. Spectrosc., 65(5), pp. 500-506(2011).
- [118] Z.L. Wang, J. Nanosci. Nanotechnol., 8(1), pp. 27-55(2008).
- [119] S. Lee, J.W. Peng, and C.S. Liu, APPL SURF SCI, 285, pp. 748-754(2013).
- [120] X. Wang, G. She, H. Xu, L. Mu, and W. Shi, Sens. Actuators B Chem., 193, pp. 745-751(2014).
- [121] G. Sinha, L.E. Depero, and I. Alessandri, ACS Appl. Mater. Interfaces, *3*(7), pp. 2557-2563(2011).
- [122] D.L. Jeanmaire, and R.P. Van Duyne, J. Electroanal. Chem. Interf. Electrochem., 84(1), pp. 1-20(1977).
- [123] P.L. Stiles, J.A. Dieringer, N.C. Shah, and R.P. Van Duyne, *Annu. Rev. Anal. Chem.*, *1*, pp. 601-626(2008).
- [124] J.P. Camden, J.A. Dieringer, J. Zhao, and R.P. Van Duyne, Acc. Chem. Res., *41*(12), pp. 1653-1661(2008).
- [125] S. Nie, and S.R. Emory, *science*, 275(5303), pp. 1102-1106(1997).
- [126] K. Kneipp, Y. Wang, H. Kneipp, L.T. Perelman, I. Itzkan, R.R. Dasari, and M.S. Feld, PRL, 78(9), pp. 1667(1997).
- [127] L. Zhao, L. Jensen, and G.C. Schatz, J. Am. Chem. Soc., 128(9), pp. 2911-2919(2006).
- [128] S.M. Morton, and L. Jensen, J. Am. Chem. Soc., 131(11), pp. 4090-4098(2009).
- [129] S.M. Morton, D.W. Silverstein, and L. Jensen, Chem. Rev., 111(6), pp. 3962-3994(2011).
- [130] P.M.V. Raja, & A.R. Barron, pp. 55670(2021).
- [131] S. Perkowitz, (2012) Elsevier.
- [132] H. Kaftelen, K. Ocakoglu, R. Thomann, S. Tu, S. Weber, and E. Erdem, PRB, 86(1), pp. 014113(2012).
- [133] M. Anpo, and M. Che, Adv. Catal., 44, pp. 119-257(1999).
- [134] J. Lefebvre, S. Maruyama, and P. Finnie, *Carbon Nanotubes*, pp.287-319(2007).
- [135] J. Rodrigues, N.B. Sedrine, M.R. Correia, and T. Monteiro, Mater. Today Chem., *16*, pp. 100243(2020).

- [136] M. Arshad, M.M. Ansari, A.S. Ahmed, P. Tripathi, S.S.Z. Ashraf, A.H. Naqvi, and A. Azam, J. Lumin., *161*, pp. 275-280(2015).
- [137] G. Pathak, S. Pandey, R. Katiyar, A. Srivastava, R. Dabrowski, K. Garbat, and R. Manohar, J. Lumin., *192*, pp. 33-39(2017).
- [138] T. Aoki, Mater. Charact., pp. 1-12(2002).
- [139] Z. L. Wang, J.Song, Science, 312, 242-246(2006).
- [140] M. Willander, O. Nur, N. Bano, K.Sultana, New J. Phys. 11, pp. 125020(2009).
- [141] S. Xu, Z. L. Wang, Nano Res. 4, pp. 1013-1098(2011).
- [142] Y. Lai, M. Meng, Y. Yu, X. Wang, T. Ding, Appl. Catal. B, 105, pp. 335-345(2011).
- [143] E. R. Waclawik, J. Chang, A. Ponzoni, I. Concina, D. Zappa, E. Comini, N. Motta, G. Faglia, G.Sberveglieri, Beilstein J. Nanotechnol., 3,pp. 368-377(2012).
- [144] S. M. Nicaise, J. J. Cheng, A. Kiani, S. Gradecak, K. K. Berggren, Nanotechnology, 26, pp. 075303(2015).
- [145] Y. K. Mishra, R. Adelung, Mater. Today, 21, pp. 631-651(2018).
- [146] J.Wang, R.Chen, L.Xiang, S.Komarneni, Ceram. Int., 44, pp. 7357-7377(2018).
- [147] S. Boubenia, A. S. Dahiya, G. Poulin-Vittrant, F. Morini, K. Nadaud, D. Alquier, Scientific reports, 7, pp. 1-10(2017).
- [148] K. M. Lee, C. W. Lai, K. S. Ngai, J. C. Juan, Water Res., 88, pp. 428-448(2016).
- [149] D. Upadhaya, D. D. Purkayastha, Ceram. Int., 46, pp. 15831–15839(2020).
- [150] S. Baruah, J. Dutta, Sci. Technol. Adv. Mater., 10, pp. 013001(2009).
- [151] W. Shi, S. Song, H. Zhang, Chem. Soc. Rev., 42, pp. 5714-5743(2013).
- [152] T. Demes, C. Ternon, D. Riassetto, V. Stambouli, M. Langlet, J Mater Sci., 51, pp. 10652-10661(2016).
- [153] A. K Radzimska, T. Jesionowski, Materials, 7, pp. 2833-2881(2014).
- [154] S. Xu, C. Lao, B. Weintraub, Z. L. Wang, J. Mater. Res., 23, pp. 2072-2077(2008).
- [155] J. E. Boercker, J. B. Schmidt, E. S. Aydil, Cryst. Growth Des., 9, pp. 2783-2789(2009).
- [156] C. P. Tsangarides, H.Ma, A. Nathan, Nanoscale, 8, pp. 11760-11765(2016).
- [157] Y. Tak, K. Yong, J. Phys. Chem. B, 109, pp. 19263-19269(2005).
- [158] J. Cho, N. Salleh, C. Blanco, S. Yang, C. J. Lee, Y. W. Kim, J. Kim, J. Liu, Nanoscale, 6, pp. 3861-3867(2014).
- [159] X. Wen, W. Wu, Y. Ding, Z. L. Wang, J. Mater. Chem., 22, pp.9469(2012).
- [160] Y.Geng, K.Jeronimo, M.A.B.C. Mahzan, P. Lomax, E. Mastropaolo, R.Cheung, Nanoscale Adv, 2, pp.2814-2823(2020).
- [161] Z.L. Wang, J. Condens. Matter Phys., 16(25), pp. R829(2004).

- [162] S. Singh, P Thiyagarajan, K M. Kant, D Anita, S Thirupathiah, N Rama, B.Tiwari, M Kottaisamy, M S R. Rao, *J. Phys. D: Appl. Phys.*, 40, pp. 6312(2007).
- [163] M Law, L E Greene, J C Johnson, R Saykally, P D Yang, Nat. Mater., 4, pp.455(2005).
- [164] Z R Tian, J A Voigt, J Liu, B Mckenzie, M J Mc Dermott, M A Rodriguez, H Kingishi, Xu H, *Nat. Mater.*, 2, pp. 821(2003).
- [165] X Wang, C J Summers and Z L Wang, *Nano Lett.*, 4, pp. 423(2004).
- [166] S Santra, P K Guha, S Z Ali, P Hiralal, H E Unalan, J A Covington, G A Amaratunga, W I Milne, J W Gardner, F Udrea, *Sens. Actuators, B*, 146, pp. 559(2010).
- [167] U.P.Shaik, S Hamad, M.A. Mohiddon, S V Rao, M Ghanashyam Krishna, *J. Appl. Phys.*, 119, pp. 093103(2016).
- [168] U.P.Shaik, S Kshirsagar, M Ghanashyam Krishna, S P Tewari, D. D. Purkayastha, V. Madhurima *Mater. Lett.*, 75, pp.51(2012).
- [169] F.Rahman, Opt. Eng., 58, pp. 010901(2019).
- [170] H.Sun, Q.Zhang, J.Zhang, T. Deng, J.Wu, Appl. Phys. B, 90, pp. 543(2008).
- [171] M Su, T Zhang, J Su, Z Wang, Y Hu, Y Gao, H Gu, X Zhang, *Opt.Exp.*, 27, pp. A1207(2019).
- [172] V.Kampylafka, A.Kostopoulos, M.Modreanu, M.Schmidt, E.Gagaoudakis, K.Tsagaraki, V.Kontomitrou, G.Konstantinidis, G.Deligeorgis, G.Kiriakidis, E.Aperathitis, *J. Materiomics*, **5**, pp. 428(2019).
- [173] S Baek, Y Porte, Y C Kim, J-M Myoung, J. Mater. Chem. C, 5, pp. 9479 (2017).
- [174] U. P. Shaik, M. G. Krishna, Ceram. Int., 40, pp. 13611-13620(2014).
- [175] B. J. Li, L. J. Huang, N. F. Ren, X. Kong, Y. L. Cai, J. L. Zhang, J. Alloys Compd., 674, pp. 368-375(2016).
- [176] S. Duo, R. Zhong, Z. Liu, J. Wang, T. Liu, C. Huang, H. Wu, J. Phys. Chem. Solids, 120, pp. 20-33(2018).
- [177] S. Nundy, A. Ghosh, T. K. Mallick, ACS omega, 5, pp. 1033-1039(2020).
- [178] T. Kano, T. Isobe, S. Matsushita, A. Nakajima, Mat. Chem. Phys., 217, pp. 192-198(2018).
- [179] H. Li, H. Lu, S. Liu, Q. Li, Q. Liu, Mater. Res. Bull., 114, pp. 85-89(2019).
- [180] C. L. Xu, Y. Z. Wang, Adv. Mater. Interfaces, 4, pp. 1700550(2017).
- [181] J. Wang, B. Weng, P. Larson, Y. Liu, Surf. Interfaces, 16, pp. 188-193(2019).
- [182] U. P. Shaik, D. D. Purkayastha, M. G. Krishna, V. Madhurima, Appl. Surf. Sci., 330, pp. 292-299(2015).
- [183] K. Yadav, B. R. Mehta, S. Bhattacharya, J. P. Singh, Sci Rep., 6, pp. 35073(2016).
- [184] K. Yadav, B. R. Mehta, K. V. Lakshmi, S. Bhattacharya, J. P. Singh, J. Phys. Chem. C, 119, pp. 16026-16032(2015).

- [185] X. Feng, L. Feng, M. Jin, J. Zhai, L. Jiang, D. Zhu, J. Am. Chem. Soc., 126, pp. 62-63(2004).
- [186] C. Mrabet, N. Mahdhi, A. Boukhachem, M. Amlouk, T. Manoubi, J. Alloys Compd., 688, pp. 122-132(2016).
- [187] P. W. Chi, D. H. Wei, S. H. Wu, Y. Y. Chen, Y. D. Yao, RSC Adv., 5, pp. 96705-96713(2015).
- [188] Elmira Velayi, Reza Norouzbeigi, Appl. Surf. Sci., 441, pp. 156-164(2018).
- [189] Y. Liu, Q. Zeng, B. Wang, C. Nie, H. Ma, and H. Yu, J ALLOY COMPD, 874, pp. 159949(2021).
- [190] B. Xia, J.J. Ganem, E. Briand, S. Steydli, H. Tancrez, and I. Vickridge, *Vacuum*, 190, pp. 110289(2021).
- [191] D.E. Yildiz, A. Kocyigit, M.O. Erdal, and M. Yildirim, Bull. Mater. Sci., 44(1), pp. 1-7(2021).
- [192] Z. Wang, H. Kim, and H.N. Alshareef, *Advanced Materials*, 30(15), pp. 1706656(2018).
- [193] M. Kumar, S. Abbas, and J. Kim, ACS Appl. Mater. Interfaces., *10*(40), pp. 34370-34376(2018).
- [194] N.J. Ridha, F.K.M. Alosfur, M.H.H. Jumali, and S. Radiman, *Nanotechnology*, *31*(14), pp. 145502(2020).
- [195] V. Consonni, J. Briscoe, E. Kärber, X. Li, and T. Cossuet, *Nanotechnology*, 30(36), pp. 362001(2019).
- [196] V.S. Bhati, M. Hojamberdiev, and M. Kumar, *Energy Reports*, 6, pp. 46-62(2020).
- [197] J. Theerthagiri, S. Salla, R.A. Senthil, P. Nithyadharseni, A. Madankumar, P. Arunachalam, T. Maiyalagan, and H.S. Kim, *Nanotechnology*, *30*(39), pp. 392001(2019).
- [198] J. Wang, R. Chen, L. Xiang, and S. Komarneni, Ceram. Int., 44(7), pp. 7357-7377(2018).
- [199] D. Selloum, A. Henni, A. Karar, A. Tabchouche, N. Harfouche, O. Bacha, S. Tingry, and F. Rosei, Solid State Sci., 92, pp. 76-80(2019).
- [200] V. Pandiyarasan, S. Suhasini, J. Archana, M. Navaneethan, A. Majumdar, Y. Hayakawa, and H. Ikeda, APPL SURF SCI, *418*, pp. 352-361(2017).
- [201] A.A. Ahmad, A.M. Alsaad, Q.M. Al-Bataineh, and M.A. Al-Naafa, Appl. Phys. A, *124*(6), pp. 1-13(2018).
- [202] H. Chamroukhi, Z.B. Hamed, A. Telfah, M. Bassou, A. Zeinert, R. Hergenröder, and H. Bouchriha, Opt., 84, pp. 703-713(2018).
- [203] H. Beitollahi, S. Tajik, F.G. Nejad, and M. Safaei, J Mater Chem B, 8(27), pp. 5826-5844(2020).
- [204] J.A. Darr, J. Zhang, N.M. Makwana, and X. Weng, Chem. Rev., 117(17), pp. 11125-11238(2017).
- [205] W.Shi, S.Song, and H.Zhang, Chem. Soc. Rev., 42(13), pp. 5714-5743(2013).

- [206] T. Demes, C. Ternon, D. Riassetto, V. Stambouli, and M. Langlet, J. Mater. Sci., *51*(23), pp. 10652-10661(2016).
- [207] Y. Feng, M. Zhang, M. Guo, and X. Wang, Cryst. Growth Des., 10(4), pp. 1500-1507(2010).
- [208] W. Wu, G.Hu, S. Cui, Y.Zhou, and H.Wu, Cryst. Growth Des., 8(11), pp. 4014-4020(2008).
- [209] C. Opoku, A.S. Dahiya, C. Oshman, C. Daumont, F. Cayrel, G. Poulin-Vittrant, D. Alquier, and N. Camara, *Nanotechnology*, 26(35), pp. 355704(2015).
- [210] S. Boubenia, A.S. Dahiya, G. Poulin-Vittrant, F. Morini, K. Nadaud, and D. Alquier, Sci. Rep., 7(1), pp. 1-10(2017).
- [211] P.P.Ortega, C.C. Silva, M.A.Ramirez, G. Biasotto, C.R. Foschini, and A.Z. Simoes, Appl. Surf. Sci., 542, pp. 148723(2021).
- [212] M. Fang, and Z.W. Liu, Ceram. Int., 43(9), pp.6955-6962(2017).
- [213] N.A. Neto, K.N. Matsui, C.A. Paskocimas, M.R.D. Bomio, and F.V. Motta, Mater Sci Semicond Process, *93*, pp. 123-133(2019).
- [214] K.P.S. Parmar, E. Ramasamy, J. Lee and J.S. Lee, ChemComm, 47(30), pp. 8572-8574(2011).
- [215] Z. Xin, L. Li, X. Zhang, and W.Zhang, RSC Adv., 8(11), pp. 6027-6038(2018).
- [216] S.Cho, S.H. Jung, and K.H. Lee, J. Phys. Chem. C, 112(33), pp. 12769-12776(2008).
- [217] J. Huang, C. Xia, L.Cao, and X.Zeng, MSEB, 150(3), pp. 187-193(2008).
- [218] A.P. De Moura, R.C. Lima, M.L. Moreira, D.P. Volanti, J.W.M. Espinosa, M.O. Orlandi, P.S. Pizani, J.A. Varela, and E. Longo, Solid State Ion., 181(15-16), pp. 775-780(2010).
- [219] P.Zhu, J. Zhang, Z.Wu, and Z. Zhang, Cryst. Growth Des., 8(9), pp. 3148-3153(2008).
- [220] I. Bilecka, P. Elser, and M. Niederberger, ACS nano, 3(2), pp. 467-477(2009).
- [221] R. Krishnapriya, S. Praneetha, and A.V. Murugan, New J Chem, *40*(6), pp. 5080-5089(2016).
- [222] R. Krishnapriya, S. Praneetha, and A.V. Murugan, *CrystEngComm*, *17*(43), pp. 8353-8367(2015).
- [223] C. Huang, R. Shi, A. Amini, Z. Wu, S. Xu, L. Zhang, W. Cao, J. Feng, H. Song, Y. Shi, and N. Wang, Sci. Rep., *5*(1), pp.1-5(2015).
- [224] N. Garino, T. Limongi, B. Dumontel, M. Canta, L. Racca, M. Laurenti, M. Castellino, A. Casu, A. Falqui, and V. Cauda, *Nanomaterials*, 9(2), pp. 212(2019).
- [225] J. Langer, D. Jimenez de Aberasturi, J. Aizpurua, R.A. Alvarez-Puebla, B. Auguié, J.J. Baumberg, G.C. Bazan, S.E. Bell, A. Boisen, A.G. Brolo, J. Choo *et al.*, *ACS Nano*, 14, pp. 28-117(2019).
- [226] A.I. Pérez-Jiménez, D. Lyu, Z. Lu, G. Liu, and B. Ren, *Chem. Sci.*, 11(18), pp. 4563-4577(2020).
- [227] J.R. Lombardi, R. L. Birke, Acc. Chem. Res., 42, pp. 734-742(2009).

- [228] E.C. Le Ru, S.A. Meyer, C. Artur, P.G. Etchegoin, J. Grand, P. Lang, F. Maurel, *Chem. Commun.*, 47, pp. 3903-3905(2011).
- [229] E.C. Le Ru, P.G. Etchegoin, MRS Bull., 38, pp. 631(2013).
- [230] G. McNay, D. Eustace, W.E. Smith, K. Faulds, D. Graham, *Appl. Spectrosc.*, 65, pp. 825-837(2011).
- [231] Y. Liu, H. Ma, X. X. Han, B. Zhao, J. Mater. Horiz., 10, pp. 1039(2020).
- [232] Y. Wu, M. Yang, W. U. Tyler, A. M. Martín, C. Zhu, G. C. Schatz, R. P. Van Duyne, *J. Phys. Chem. C*, 123, pp. 29908-29915(2019).
- [233] S.-Y. Ding, J. Yi, J.-F. Li, B. Ren, D.-Y. Wu, R. Panneerselvam and Z.-Q. *Nat. Rev.Mater.*, 1, pp. 16021(2016).
- [234] S. Hamad, G.K. Podagatlapalli, M.A. Mohiddon, S. Venugopal Rao, *Chem. Phys. Lett.*, 621, pp. 171-176(2015).
- [235] G. V. Naik, J. L. Schroeder, X. Ni, A. V. Kildishev, T. D. Sands, A. Boltasseva, *Opt.Mater. Exp.*, 2, pp. 478-489(2012).
- [236] M. Gioti, J. Arvanitidis, D. Christofilos, K. Chaudhuri, T. Zorba, G. Abadias, D. Gall, V.M. Shalaev, A. Boltasseva, P. Patsalas, *J. Opt.*, 22, pp. 084001(2020).
- [237] T. Fu, Y. Chen, C. Du, W. Yang, R. Zhang, L. Sun, D. Shi, *Nanotechnology*, 31, pp. 135210(2020).
- [238] Y. Ma, D. Sikdar, A. Fedosyuk, L. Velleman, D.J. Klemme, S.H. Oh, A.R. Kucernak, A.A. Kornyshev, J.B. Edel, *ACS Nano*, 14, pp. 328-336(2019).
- [239] F. Zhao, X. Xue, W. Fu, Y. Liu, Y. Ling, Z. Zhang, *J. Phys. Chem. C*, 123, pp. 29353-29359(2019).
- [240] A.A. Popov, G. Tselikov, N. Dumas, C. Berard, K. Metwally, N. Jones, A. Al-Kattan, B.Larrat, D. Braguer, S. Mensah, A. Da Silva, *Sci. Rep.*, 9, pp. 1-11(2019).
- [241] H. Wei, M. Wu, Z. Dong, Y. Chen, J. Bu, J. Lin, Y. Yu, Y. Wei, Y. Cui, R. Wang, *J. Raman Spectrosc.*, 48, pp. 578-585(2017).
- [242] I. Lorite, A. Serrano, A. Schwartzberg, J. Bueno and J.L. Costa-Krämer, *Thin Solid Films*, 531, pp. 144-146(2013).
- [243] J. Zhao, J. Lin, H. Wei, X. Li, W. Zhang, G. Zhao, J. Bu, Y. Chen, *Opt. Mater.*, 47, pp. 219-224(2015).
- [244] N. Kaisar, Y.T. Huang, S. Jou, H.F. Kuo, B.R. Huang, C.C. Chen, Y.F. Hsieh, Y.C. Chung, *Surf. Coat. Technol.*, 337, pp. 434-438(2018).
- [245] K. Vasu, M. Ghanashyam Krishna, K.A. Padmanabhan, *Appl. Surf. Sci.*, 257, pp. 3069-3074(2011).
- [246] F. JCPDS, *ICDD*, *Philadelphia*, (1977).
- [247] J. Tauc, In *Amorphous and liquid semiconductors*, Springer, Boston, MA. pp. 159-220, (1974).

- [248] J. Tauc, and A. Menth, J NON-CRYST SOLIDS, 8, pp. 569-585(1972).
- [249] A.L. Subramaniyan, J. Sabareswaran, M. Kottaisamy, and R. Ilangovan, J. Nanoelectron. Optoelectron, *10*(1), pp. 24-27(2015).
- [250] A. Sáenz-Trevizo, P. Amézaga-Madrid, P. Pizá-Ruiz, W. Antúnez-Flores, and M. Miki-Yoshida, Mater. Res, 19, pp. 33-38(2016).
- [251] M.A. Mohiddon, L.V. Sangani, and M.G. Krishna, Chem. Phys. Lett., 588, pp. 160-166(2013).
- [252] S.V. Rao, G. K. Podagatlapalli, and S. Hamad, J. Nanosci. Nanotechnol., *14*(2), pp. 1364-1388(2014).
- [253] K. Y. Foo, and B.H. Hameed, Chem. Eng. Sci., 156(1), pp.2-10(2010).
- [254] Y. Geng, K. Jeronimo, M.A.B.C. Mahzan, P. Lomax, E. Mastropaolo, and R. Cheung, Nanoscale Adv., 2(7), pp. 2814-2823(2020).
- [255] T. Demes, C. Ternon, D. Riassetto, V. Stambouli, and M. Langlet, J. Mater. Sci., *51*(23), pp. 10652-10661(2016).
- [256] T. Demes, C. Ternon, D. Riassetto, H. Roussel, L. Rapenne, I. Gélard, C. Jimenez, V. Stambouli, and M. Langlet, J. Phys. Chem. Solids, *95*, pp. 43-55(2016).
- [257] S. Vyas, P. Giri, S. Singh, and P. Chakrabarti, J. Electron. Mater, 44(10), pp. 3401-3407(2015).
- [258] Y. X. Liu, Y.C. Liu, D.Z. Shen, G.Z. Zhong, X.W. Fan, X.G. Kong, R. Mu, and D. O. Henderson, Solid State Commun., *121*(9-10), pp. 531-536(2002).
- [259] Y.X. Liu, Y.C. Liu, C. L. Shao, and R. Mu, j. phys. D. appl. phys., *37*(21), pp. 3025(2004).
- [260] S.D. Kshirsagar, U.P. Shaik, M.G. Krishna, and S.P. Tewari, J. Lumin., *136*, pp. 26-31(2013).
- [261] V.Strelchuk, O. Kolomys, S.Rarata, P.Lytvyn, O.Khyzhun, C.O.Chey, O.Nur, M.Willander, *Nanoscale Res. Lett.*, 12, pp. 351(2017).
- [262] H. K. Yadav, K. Sreenivas, V. Gupta, and R.S. Katiyar, *Journal of Raman Spectroscopy: An International Journal for Original Work in all Aspects of Raman Spectroscopy, Including Higher Order Processes, and also Brillouin and Rayleigh Scattering*, 40(4), pp. 381-386(2009).
- [263] S. Guo, Z. Du, and S. Dai, Phys. Status Solidi B, 246(10), pp. 2329-2332(2009).
- [264] H.Siegle, G.Kaczmarczyk, L.Filippidis, A. P.Litvinchuk, A.Hoffmann, C.Thomsen, *Phys. Rev. B*, 55, pp. 7000(1997).
- [265] Y. Huang, M. Liu, Z. Li, Y. Zeng, and S. Liu, Mater. Sci. Eng. B: Solid-State Mater. Adv. Technol., *97*(2), pp. 111-116(2003).
- [266] S B Yahia, L Znaidi, A Kanaev, J P Petitet, *Spectrochim. Acta A Mol. Biomol. Spectrosc.*, 71, pp. 1234(2005).

- [267] Z.W. Zhao, B.K. Tay, J.S. Chen, J.F. Hu, X.W. Sun, and S.T. Tan, Appl. Phys. Lett., 87(25), p. 251912(2005).
- [268] S. Zhang, and G. Lu, Mater. Lett., 155, pp. 65-67(2015).
- [269] D. Gogova, L.K. Thomas, B. Camin, Thin Solid Films, 517, pp. 3326–3331(2009).
- [270] G. Geng, P. Chen, B. Guan, Y. Liu, C. Yang, N. Wang, and M. Liu, RSC Adv., 7(82), pp. 51838-51846(2017).
- [271] S. Baruah, and J. Dutta, Sci Technol Adv Mater (2009).
- [272] M.C. Akgun, Y.E. Kalay, and H.E. Unalan, Mater. Res., 27(11), pp. 1445(2012).
- [273] C.P. Tsangarides, H. Ma, and A. Nathan, *Nanoscale*, 8(22), pp. 11760-11765(2016).
- [274] A. Sugunan, H.C. Warad, M. Boman, and J. Dutta, J Solgel Sci Technol J Sol-Gel. Sci. Techn., 39(1), pp. 49-56(2006).
- [275] C. Lausecker, B. Salem, X. Baillin, H. Roussel, E. Sarigiannidou, F. Bassani, E. Appert, S. Labau, V. Consonni, *Nanotechnology*, 30, pp. 345601(2019).
- [276] R. D. Vispute, V. Talyansky, S. Choopun, R. P. Sharma, and T. Venkatesan, M. He, X. Tang, J. B. Halpern, M. G. Spencer, Y. X. Li, L. G. Salamanca-Riba, A. A. Iliadis, K. A. Jones, Appl. Phys. Lett. 73, pp. 348(1998).
- [277] S. Cho, J. Ma, Y. Kim, Y. Sun, G. K. Wong, and J.B. Ketterson, Appl. Phys. Lett., *75*(18), pp. 2761-2763(1999).
- [278] B. K. Meyer, H. Alves, D. M. Hofmann, W. Kriegseis, D. Forster, F. Bertram, J. Christen, A. Hoffmann, M. Straßburg, M. Dworzak, U. Haboeck, A. V. Rodina, Phys. Stat. Solidi B, 241, pp. 23(2004).
- [279] M. Rajalakshmi, A.K. Arora, B.S. Bendre, and S. Mahamuni, Int. J. Appl. Phys., 87(5), pp. 2445-2448(2000).
- [280] T.C. Damen, S.P.S. Porto, and B. Tell, Phys. Rev., 142(2), pp. 570(1966).
- [281] K. Samanta, A.K. Arora, and R.S. Katiyar, J. Phys. D J PHYS D APPL PHYS, *45*(18), pp. 185304(2012).
- [282] R. Cuscó, E. Alarcón-Lladó, J. Ibanez, L. Artús, J. Jiménez, B. Wang, and M.J. Callahan, Phys. Rev. B, *75*(16), p. 165202(2007).
- [283] J. Serrano, A.H. Romero, F.J. Manjon, R. Lauck, M. Cardona, and A. Rubio, Phys. Rev. B, *69*(9), pp. 094306(2004).
- [284] G.J. Exarhos, and S.K. Sharma, Thin Solid Films, 270(1-2), pp. 27-32(1995).
- [285] Y.J. Xing, Z.H. Xi, Z.Q. Xue, X.D. Zhang, J.H. Song, R.M. Wang, J. Xu, Y. Song, S.L. Zhang, and D.P. Yu, Appl. Phys. Lett., *83*(9), pp. 1689-1691(2003).
- [286] S.H. Jeong, B.S. Kim, and B.T. Lee, Appl. Phys. Lett., 82(16), pp. 2625-2627(2003).
- [287] H. Sun, Q. Zhang, J. Zhang, T. Deng, and J. Wu, Appl. Phys. B, 90(3), pp. 543-546(2008).

- [288] M. Su, T. Zhang, J. Su, Z. Wang, Y. Hu, Y. Gao, H. Gu, and X. Zhang, Opt. Express, 27(16), pp. A1207-A1215(2019).
- [289] V. Kampylafka, A. Kostopoulos, M. Modreanu, M. Schmidt, E. Gagaoudakis, K. Tsagaraki, V. Kontomitrou, G. Konstantinidis, G. Deligeorgis, G. Kiriakidis, and E. Aperathitis, J. Materiomics, *5*(3), pp. 428-435(2019).
- [290] S.D. Baek, Y. Porte, Y.C. Kim, and J.M. Myoung, J. Mater. Chem. C, *5*(36), pp. 9479-9487(2017).
- [291] D.K. Kwon, Y. Porte, and J.M. Myoung, J. Mater. Chem. C, *122*(22), pp.11993-12001(2018).
- [292] G. Wang, S. Chu, N. Zhan, Y. Lin, L. Chernyak, and J. Liu, Appl. Phys. Lett., 98(4), pp. 041107(2011).
- [293] F. Rahman, Opt. Eng., 58(1), pp. 010901(2019).
- [294] Z. Zhang, and J. Mu, J. Colloid Interface Sci., 307(1), pp. 79-82(2007).
- [295] V.S. Bhati, M. Hojamberdiev, and M. Kumar, Energy Rep., 6, pp. 46-62(2020).
- [296] J. Theerthagiri, S. Salla, R.A. Senthil, P. Nithyadharseni, A. Madankumar, P. Arunachalam, T. Maiyalagan, and H.S. Kim, *Nanotechnology*, *30*(39) pp. 392001(2019),.
- [297] J. Wang, R. Chen, L. Xiang, and S. Komarneni, Ceramics International, 44(7), pp. 7357-7377(2018).
- [298] D. Selloum, A. Henni, A. Karar, A. Tabchouche, N. Harfouche, O. Bacha, S. Tingry, and F. Rosei, Solid State Sci., 92, pp. 76-80(2019).
- [299] V. Pandiyarasan, S. Suhasini, J. Archana, M. Navaneethan, A. Majumdar, Y. Hayakawa, and H. Ikeda, Appl. Surf. Sci., *418*, pp. 352-361(2017).
- [300] A.A. Ahmad, A.M. Alsaad, Q.M. Al-Bataineh, and M.A. Al-Naafa, Optical and structural investigations of dip-synthesized boron-doped ZnO-seeded platforms for ZnO nanostructures, *Applied Physics A*, 124(6) (2018), pp. 1-13.
- [301] H. Chamroukhi, Z.B. Hamed, A. Telfah, M. Bassou, A. Zeinert, R. Hergenröder, and H. Bouchriha, Opt. Mater., *84*, pp.703-713(2018).
- [302] H. Beitollahi, S. Tajik, F.G. Nejad, and M. Safaei, J Mater Chem B, 8(27), pp. 5826-5844(2020).
- [303] T. Demes, C. Ternon, D. Riassetto, V. Stambouli, and M. Langlet, J. Mater. Sci., *51*(23), pp. 10652-10661(2016).
- [304] Y. Feng, M. Zhang, M. Guo, and X. Wang, Cryst. Growth Des., 10(4), pp.1500-1507(2010).
- [305] W. Wu, G.Hu, S. Cui, Y.Zhou, and H.Wu, Cryst. Growth Des., 8(11), pp.4014-4020(2008).
- [306] C. Opoku, A.S. Dahiya, C. Oshman, C. Daumont, F. Cayrel, G. Poulin-Vittrant, D. Alquier, and N. Camara, , *Nanotechnology*, 26(35), p.355704(2015).
- [307] R.L. Penn, and J.F. Banfield, *Science*, 281(5379), pp.969-971(1998).

- [308] C.J. Dalmaschio, C. Ribeiro, and E.R. Leite, *Nanoscale*, 2(11), pp.2336-2345(2010).
- [309] J. Zhang, F. Huang, and Z. Lin, *Nanoscale*, 2(1), pp.18-34(2010).
- [310] B.B. Salzmann, M.M. van der Sluijs, G. Soligno, and D. Vanmaekelbergh, Acc. Chem. Res., *54*(4), pp. 787-797(2021).
- [311] U.P. Shaik, P.A. Kumar, M.G. Krishna, and S.V. Rao, Mater. Res. Express, *1*(4), p.046201 (2014).
- [312] U. Ozgur, Ya. I. Alivov, C. Liu, A. Teke, M. A. Reshchikov, S. Dogan, V. Avrutin, S.-J. Cho. H. Morkoç, J.Appl.Phys. 98, 041301 (2005).
- [313] M. Lucas, W. Mai, R. Yang, Z.L. Wang, and E. Riedo, *Nano Lett.* 7(5), pp. 1314-1317 (2007).
- [314] E. H. Martins Ferreira, Marcus V. O. Moutinho, F. Stavale, M. M. Lucchese, Rodrigo B. Capaz, C. A. Achete, A. Jorio, Phys. Rev. B, 82,pp. 125429 (2010).
- [315] A. Mang, and K. Reimann, 94(4), pp. 251-254 (1995).
- [316] D.C. Reynolds, D.C. Look, B. Jogai, C.W. Litton, G. Cantwell, and W.C. Harsch, Phys. Rev. B, *60*(4), p. 2340 (1999).
- [317] C. Boemare, T. Monteiro, M.J. Soares, J.G. Guilherme, and E. Alves, Phys. B: Condens. Matter, *308*, pp. 985-988 (2001).
- [318] S.S. Xiao, L. Zhao, Y.H. Liu, and J.S. Lian, Appl. Surf. Sci., 283, pp. 781-787 (2013).
- [319] S. Kunj, and K. Sreenivas, *Curr. Appl. Phys.*, 16(7), pp. 748-756 (2016).
- [320] L.W. Wang, F. Wu, D.X. Tian, W.J. Li, L. Fang, C.Y. Kong, and M. Zhou, *J. Alloys Compd.* 623, pp. 367-373 (2015).
- [321] M.G. Krishna, M. Vinjanampati, and D.D. Purkayastha, EPJ Appl. Phys., 62(3) (2013).
- [322] R.N. Wenzel, *Ind. Eng. Chem.*, 28(8), pp. 988-994 (1936).
- [323] A.B.D. Cassie, and S. Baxter, J. Chem. Soc. Faraday Trans. 40, pp. 546-551 (1944).
- [324] C.V. Suciu, T. Iwatsubo, K. Yaguchi, and M. Ikenaga, *J. Colloid Interface Sci.*, 283(1), pp. 196-214 (2005).
- [325] L. Afferrante, and G. Carbone, Soft Matter, 10(22), pp. 3906-3914 (2014).
- [326] E. Bormashenko, 222, pp.92-103 (2015).
- [327] D.D. Purkayastha, and M.G. Krishna, Appl. Surf. Sci., 447, pp.724-731 (2018).
- [328] C. Mrabet, N. Mahdhi, A. Boukhachem, M. Amlouk, T. Manoubi, J. Alloys Compd.688 122-132 (2016).
- [329] C. Mrabet, N. Mahdhi, A. Boukhachem, M. Amlouk, T. Manoubi, J. Alloys Compd.725, pp. 765-772 (2017).
- [330] X.Q. Meng, D.X. Zhao, J.Y. Zhang, D.Z. Shen, Y.M. Lu, L. Dong, Z.Y. Xiao, Y.C. Liu, X.W. Fan, Chem. Phys. Lett., 413, pp. 450–453 (2005).

- [331] J. Zhang, Y. Liu, Z. Wei, J Zhang, Appl. Surf.Sci., 265, pp. 363–368 (2013).
- [332] G.V.Naik, J.L.Schroeder, X. Ni, A.V. Kildishev, T.D. Sands, and A.Boltasseva, Opt. Mater. Express, 2(4), pp. 478-489 (2012).
- [333] M. Gioti, J. Arvanitidis, D. Christofilos, K. Chaudhuri, T. Zorba, G. Abadias, D. Gall, V.M. Shalaev, A. Boltasseva, and P. Patsalas, *J. Opt.*, 22(8), pp. 084001 (2020).
- [334] T. Fu, Y. Chen, C. Du, W. Yang, R. Zhang, L. Sun, D. Shi, *Nanotechnology* 31,135210 (2020).
- [335] F. Zhao, X. Xue, W. Fu, Y. Liu, Y. Ling, Z. Zhang, J. Phys. Chem. C 123, pp. 29353-29359 (2019).
- [336] I. Lorite, A. Serrano, A. Schwartzberg, J. Bueno and J.L. Costa-Krämer, *Thin Solid Films* 531, pp. 144-146 (2013).
- [337] J. Zhao, J. Lin, H. Wei, X. Li, W. Zhang, G. Zhao, J. Bu, Y. Chen, *Opt. Mater.* 47, 219-224 (2015).
- [338] C. P. Constable, J. Yarwood, W.-D. Münz, Surf. Coat. Technol. 116, pp. 155-159 (1999).
- [339] B. Subramanian, M. Jayachandran *J. Appl. Electrochem.* 37, pp. 1069-1075 (2007).
- [340] C. Zhang, Y. Xu, J.Liu, J. Li, J. Xiang, H.Li, J. Li, Q. Dai, S. Lan, A.E. Miroshnichenko, *Nat Commun* **9**, 2964 (2018).
- [341] M.S.S. Bharati, C. Byram, S. Venugopal Rao, *Bull. Mater. Sci.* 43.1, 53 (2020).
- [342] M.S.S. Bharati, C. Byram, S. Venugopal Rao, RSC Adv. 9, pp. 1517-1525 (2019).
- [343] A.I. Pérez-Jiménez, D. Lyu, Z. Lu, G. Liu, and B. Ren, *Chem. Sci.* 11.18, pp. 4563-4577 (2020).
- [344] J.R. Lombardi, R. L. Birke, Acc. Chem. Res. 42, pp. 734-742 (2009).
- [345] E.C. Le Ru, S.A. Meyer, C. Artur, P.G. Etchegoin, J. Grand, P. Lang, F. Maurel, *Chem. Commun.* 47, pp. 3903-3905 (2011).
- [346] E.C. Le Ru, P.G. Etchegoin. MRS Bull. 38, 631 (2013).
- [347] G. McNay, D. Eustace, W.E. Smith, K. Faulds, D. Graham, *Appl. Spectrosc.* 65, pp. 825-837(2011).
- [348] Y. Liu, H. Ma, X. X. Han, B. Zhao, (2020). https://doi.org/10.1039/D0MH01356K
- [349] Y. Wu, M. Yang, W. U. Tyler, A. M. Martín, C. Zhu, G. C. Schatz, R. P. Van Duyne, *J. Phys. Chem. C*, 123, pp. 29908-29915 (2019).
- [350] S.-Y. Ding, J. Yi, J.-F. Li, B. Ren, D.-Y. Wu, R. Panneerselvam and Z.-Q. Tian, *Nat. Rev. Mater.*, 1, pp. 16021 (2016).
- [351] S.I. Kudryashov, P.A. Danilov, A.P. Porfirev, I.N. Saraeva, T.H.T. Nguyen, A.A. Rudenko, R.A.Khmelnitskii, D.A. Zayarny, A.A. Ionin, A.A. Kuchmizhak, S.N. Khonina, O.B. Vitrik, *Appl. Surf. Sci.*, 484, pp. 948-956 (2019).

- [352] J.B. Yoo, H.J. Yoo, H.J. Jung, H.S. Kim, S. Bang, J. Choi, H. Suh, J.H. Lee, J.G. Kim, and N.H. Hur, *J. Mater. Chem. A* 4, pp. 869-876 (2016).
- [353] S. Zhu, D. Wang, Adv. Energy Mater. 7, 1700841 (2017).

"Studies on Hydrothermally processed Zinc Oxide nanostructures for Optical, wettability and sensing applications"

by Yalambaku Rajesh

Submission date: 21-Dec-2021 04:39PM (UTC+0530)

Submission ID: 1734623183

File name: Rajesh thesis Final2.pdf (14.38M)

Word count: 35405

Character count: 180375

"Studies on Hydrothermally processed Zinc Oxide nanostructures for Optical, wettability and sensing applications"

ORIGINALITY REPORT

SIMILARITY INDEX

INTERNET SOURCES

STUDENT PAPERS

PRIMARY SOURCES

Yalambaku Rajesh, Debarun Dhar

Purkayastha, M. Ghanashyam Krishna. "Seed layer mediated wettability and wettability transition of ZnO nano/micro-rod arrays", Journal of Alloys and Compounds, 2021

Publication

This is the student's own

m. Thanas

Yalambaku Rajesh, Santanu Kumar Padhi, M. Ghanashyam Krishna. "ZnO thin filmnanowire array homo-structures with tunable photoluminescence and optical band gap", RSC Advances, 2020

Publication

own publicut

Yalambaku Rajesh, Md. Ahamad Mohiddon, M. Ghanashyam Krishna. "Shape evolution and optical response of ZnO nanostructures grown on thermally evaporated ZnO and Au thin films", Materials Chemistry and Physics, 2022

Publication

lowu student's publication

Prof. M. GHANASHYAM KRISHNA Centre for Advanced Studies in Electronics Science & Technology School of Physics, University of Hyderabad HYDERABAD-500 046. Telangana, India.

Yalambaku Rajesh, M. S. S. Bharati, S. 8% Venugopal Rao, M. Ghanashyam Krishna. "ZnO nanowire arrays decorated with titanium nitride nanoparticles as surface-This is the Smdent's own enhanced Raman scattering substrates", Publication M. Hackarlyan Applied Physics A, 2021 **Publication** Y. Rajesh, Debarun Dhar Purkayastha, M. Ghanashyam Krishna. "Seed layer mediated wettability and wettability transition of ZnO Thus is the Shident's nano/micro-rod arrays", Journal of Alloys and own zublicahan. Compounds, 2020 Publication www.epjap.org Internet Source Submitted to University of Hyderabad, Hyderabad Student Paper Y. Rajesh, Md. Ahamad Mohiddon, M. 8 Ghanashyam Krishna. "Shape evolution and optical response of ZnO nanostructures This is the shident's grown on thermally evaporated ZnO and Au Own publication thin films", Materials Chemistry and Physics, M. Thanashyon 2021 Prof. M. GHANASHYAM KRISHNA Publication Centre for Advanced Studies in

baadalsg.inflibnet.ac.in

Internet Source

Electronics Science & Technology

School of Physics, University of Hyderabad HYDERABAD-500 046 Telangana, India.

10	Guijun Yang, Soo-Jin Park. "Conventional and Microwave Hydrothermal Synthesis and Application of Functional Materials: A Review", Materials, 2019	<1%
11	www.acrhem.org Internet Source	<1%
12	Forat H. Alsultany, Z. Hassan, Naser M. Ahmed, Nezar G. Elafadill, Hassnen R. Abd. "Effects of ZnO seed layer thickness on catalyst-free growth of ZnO nanostructures for enhanced UV photoresponse", Optics & Laser Technology, 2018 Publication	<1%
13	Ummar Pasha Shaik, Syed Hamad, Md. Ahamad Mohiddon, Venugopal Rao Soma, M. Ghanashyam Krishna. "Morphologically manipulated Ag/ZnO nanostructures as surface enhanced Raman scattering probes for explosives detection", Journal of Applied Physics, 2016 Publication	<1%
14	"Encyclopedia of Nanotechnology", Springer Nature, 2016 Publication	<1%
15	onlinelibrary.wiley.com Internet Source	<1%

16	Saurabh Kunj, K. Sreenivas. "Defect mediated ferromagnetism in cluster free Zn 1–x Ni x O nanopowders prepared by combustion method", Journal of Industrial and Engineering Chemistry, 2018 Publication	<1%
17	pubs.rsc.org Internet Source	<1%
18	Soaram Kim, Giwoong Nam, Kwang Gug Yim, Jewon Lee, Yangsoo Kim, Jae-Young Leem. "Effects of post-heated ZnO seed layers on structural and optical properties of ZnO nanostructures grown by hydrothermal method", Electronic Materials Letters, 2013 Publication	<1%
19	J. P. Kar, S. N. Das, S. W. Lee, M. H. Ham, J. H. Choi, J. M. Myoung. "SURFACE MODIFICATION OF HYDROTHERMALLY GROWN ZnO NANOSTRUCTURES WITH PROCESS PARAMETERS", Chemical Engineering Communications, 2009 Publication	<1%
20	"ZnO Nanocrystals and Allied Materials", Springer Science and Business Media LLC, 2014 Publication	<1%

21	Ravi K Biroju, Nikhil Tilak, Gone Rajender, S Dhara, P K Giri. "Catalyst free growth of ZnO nanowires on graphene and graphene oxide and its enhanced photoluminescence and photoresponse", Nanotechnology, 2015 Publication	<1%
22	pubs.acs.org Internet Source	<1%
23	Yalambaku Rajesh, Debarun Dhar Purkayastha, M. Ghanashyam Krishna. "Seed layer mediated wettability and wettability transition of ZnO nano/micro-rod arrays", Journal of Alloys and Compounds, 2020 Publication	<1%
24	cdn.intechopen.com Internet Source	<1%
24		<1 _%
242526	Submitted to IIT Delhi	<1% <1% <1%

28	www.swinburne.edu.au Internet Source	<1%
29	EUNJUNG KO. "Inverse Capacitance-Voltage Characteristics of Bi 3.25 La 0.75 Ti 3 O 12 Thin Film Pulsed Laser Deposited on Thermally Oxidized n-Type Si Substrates", Integrated Ferroelectrics, 1/1/2004 Publication	<1%
30	Kenanakis, G "Light-induced reversible hydrophilicity of ZnO structures grown by aqueous chemical growth", Applied Surface Science, 20080715 Publication	<1%
31	S. K. Padhi, S. N. Gottapu, M. Ghanashyam Krishna. "Electron-beam irradiation induced transformation of Cu (OH) NO nanoflakes into nanocrystalline CuO ", Nanoscale, 2016 Publication	<1%
32	Submitted to Universiti Teknologi MARA Student Paper	<1%
33	Submitted to University of Sheffield Student Paper	<1%
34	Md. Ahamad Mohiddon, M. Ghanashyam Krishna. "Nanocrystalline wurtzite Si-nickel silicide composite thin films with large band gap and high resistivity", Journal of Materials Science, 2010	<1%

35	Yangyang Zhang, Manoj K. Ram, Elias K. Stefanakos, D. Yogi Goswami. "Synthesis, Characterization, and Applications of ZnO Nanowires", Journal of Nanomaterials, 2012	<1%
36	iopscience.iop.org Internet Source	<1%
37	etheses.whiterose.ac.uk Internet Source	<1%
38	Submitted to Pacific University Student Paper	<1%
39	Ida Marie Høiaas, Andreas Liudi Mulyo, Per Erik Vullum, Dong-Chul Kim et al. "GaN/AlGaN Nanocolumn Ultraviolet Light-Emitting Diode Using Double-Layer Graphene as Substrate and Transparent Electrode", Nano Letters, 2019	<1%
40	R. Nandi, R.S. Srinivasa, S.S. Major. "Morphology and photoluminescence of ZnO nanorods grown on sputtered GaN films with intermediate ZnO seed layer", Materials Chemistry and Physics, 2016 Publication	<1%
41	digitalcommons.mtu.edu Internet Source	<1%

42	R. Brahma, M.Ghanashyam Krishna. "Optical behavior of silver/dielectric and gold/dielectric bilayer thin films", Physica E: Low-dimensional Systems and Nanostructures, 2011 Publication	<1%
43	Ummar Pasha Shaik, M. Ghanashyam Krishna. "Single step formation of indium and tin doped ZnO nanowires by thermal oxidation of indium–zinc and tin–zinc metal films: Growth and optical properties", Ceramics International, 2014 Publication	<1%
44	Busi Kumar Babu, Siddhartha Ghosh, Sabyasachi Chakrabortty. "Recent developments in smart window engineering: from antibacterial activity to self-cleaning behavior", Elsevier BV, 2020 Publication	<1%
45	Submitted to Nanyang Technological University, Singapore Student Paper	<1%
46	etd.uwc.ac.za Internet Source	<1%
47	worldwidescience.org Internet Source	<1%
48	Nguyen Thanh Son, Jin-Seo Noh, Sungho Park. "Role of ZnO thin film in the vertically aligned	<1%

growth of ZnO nanorods by chemical bath deposition", Applied Surface Science, 2016

Publication

Publication

Saurabh Kunj, K. Sreenivas. "Residual stress <1% 49 and defect content in magnetron sputtered ZnO films grown on unheated glass substrates", Current Applied Physics, 2016 Publication chemistry-europe.onlinelibrary.wiley.com <1% 50 Internet Source J F Conley. "Directed assembly of ZnO 51 nanowires on a Si substrate without a metal catalyst using a patterned ZnO seed layer", Nanotechnology, 02/01/2005 Publication Ming Wei. "Self-catalysed growth of zinc oxide <1% 52 nanowires", Nanotechnology, 08/01/2005 Publication Submitted to PEC University of Technology <1% 53 Student Paper Rendón-Angeles, J.C., Z. Matamoros-Veloza, J. 54 López-Cuevas, R. Perez-Garibay, J. Diaz-Algara, and K. Yanagisawa. "Rotaryhydrothermal method assisting the conversion of celestine into scheelite SrWO4 in alkaline solutions", International Journal of Mineral Processing, 2016.

55	Submitted to Universiti Teknologi Malaysia Student Paper	<1%
56	Zhang, Z "Facing-target sputtering deposition of ZnO films with Pt ultra-thin layers for gasphase photocatalytic application", Journal of Hazardous Materials, 20100415	<1%
57	dr.ntu.edu.sg Internet Source	<1%
58	mjs.uomustansiriyah.edu.iq Internet Source	<1%
59	scholar.uwindsor.ca Internet Source	<1%
60	O Akhavan. "Hydrothermal synthesis of ZnO nanorod arrays for photocatalytic inactivation of bacteria", Journal of Physics D Applied Physics, 11/21/2009 Publication	<1%
61	P. Dash, A. Manna, N.C. Mishra, Shikha Varma. "Synthesis and characterization of aligned ZnO nanorods for visible light photocatalysis", Physica E: Low-dimensional Systems and Nanostructures, 2018 Publication	<1%
62	etd.lib.metu.edu.tr Internet Source	<1%

63	ethesis.nitrkl.ac.in Internet Source	<1 %
64	repositorium.sdum.uminho.pt Internet Source	<1%
65	Christine M. R. Clancy, J. Brian Nofsinger, R. Kyle Hanks, John D. Simon. "A Hierarchical Self-Assembly of Eumelanin", The Journal of Physical Chemistry B, 2000 Publication	<1%
66	Submitted to International Institute of Information Technology, Hyderabad Student Paper	<1%
67	Kunj, Saurabh, and K. Sreenivas. "Residual stress and defect content in magnetron sputtered ZnO films grown on unheated glass substrates", Current Applied Physics, 2016. Publication	<1 %
68	Sridevi Yerra, Bharat Kumar Tripuramallu, Samar K. Das. "Decavanadate-based discrete compound and coordination polymer: Synthesis, crystal structures, spectroscopy and nano-materials", Polyhedron, 2014 Publication	<1%
69	Submitted to Universiti Sains Islam Malaysia Student Paper	<1%
70	duepublico.uni-duisburg-essen.de:443	<1%

71	hdl.handle.net Internet Source	<1%
72	"Sensors Set", Wiley, 1995 Publication	<1 %
73	Submitted to Gautam Buddha University Student Paper	<1%
74	Jawwad A. Darr, Jingyi Zhang, Neel M. Makwana, Xiaole Weng. "Continuous Hydrothermal Synthesis of Inorganic Nanoparticles: Applications and Future Directions", Chemical Reviews, 2017 Publication	<1%
75	Tawfik A. Saleh. "Protocols for synthesis of nanomaterials, polymers, and green materials as adsorbents for water treatment technologies", Environmental Technology & Innovation, 2021 Publication	<1%
76	Submitted to Universiti Tunku Abdul Rahman Student Paper	<1%
77	dspace.lboro.ac.uk Internet Source	<1%
78	link.springer.com Internet Source	<1 %

79

Chen, Z.. "A facile route to ZnO nanorod arrays using wet chemical method", Journal of Crystal Growth, 20060801

Publication

80

epub.uni-regensburg.de

Internet Source

<1 % <1 %

export.arxiv.org

Internet Source

Exclude quotes

On

Exclude matches

< 14 words

Exclude bibliography

Plagiarism-free statement

This is to certify that the thesis titled "Studies on hydrothermally processed Zinc Oxide nanostructures for optical, Wettability and sensing applications" has been screened by the Turnitin software at the Indira Gandhi Memorial Library of the University of Hyderabad. The software shows a 53% similarity index, out of which 45% came from the candidate's own research articles related to this thesis, which are already published and available online. Thus, the effective similarity index excluding his research articles is 53% — 45%= 8%, which is lower than the 10% stipulated by the university guidelines. Therefore, this thesis maybe considered free from plagiarism as per guidelines.

M. Manadyoun Prof. M.Ghanashyam Krishna

Prof. M. GHANASHYAM KRISHNA
Taggis (Superarised Studies in
Electronics Science & Technology
School Mohysigs Howersity of Hyderabad
HYDERABAD-500 046. Telangana, India.

University of Hyderabad

List of publications

- 1. **Y. Rajesh,** Padhi, S.K. and Krishna, M.G., 2020. ZnO thin film-nanowire array homostructures with tunable photoluminescence and optical band gap. *RSC Advances*, *10*(43), pp.25721-25729.
- 2. **Y. Rajesh,** Purkayastha, D.D. and Krishna, M.G., 2021. Seed layer mediated wettability and wettability transition of ZnO nano/micro-rod arrays. *Journal of Alloys and Compounds*, 857, p.157617.
- 3. **Y. Rajesh,** Bharati, M.S.S., Rao, S.V. and Krishna, M.G., 2021. ZnO nanowire arrays decorated with titanium nitride nanoparticles as surface-enhanced Raman scattering substrates. *Applied Physics A*, 127(4), pp.1-8.
- Y. Rajesh, Md. Ahamad Mohiddon., and Krishna, M.G., "Shape evolution and optical response of ZnO nanostructures grown on thermally evaporated ZnO and Au thin films" Materials Chemistry and Physics, 125448 (2021).
 [https://doi.org/10.1016/j.matchemphys.2021].

Conferences and workshops attended

- ❖ Y. Rajesh, L.V. Sangani, U.P. Shaik, A. Gaur, M.A. Mohiddon, and M.G. Krishna, 2017, visualizing the optical field strengths in Au/dielectric nanostructures and its correlation to SERS enhancements. The 61th DAE Solid State Physics Symposium, (*DAE-SSPS-2016*). (*Poster presentation*).
- ❖ Y. Rajesh, Md Ahamad Mohiddon, M. Ghanashyam Krishna "Precursor and seed layer thickness controlled microwave hydrothermal synthesis of ZnO nanostructures for sensing applications" International Conference on Nano Science and Technology, *ICONSAT 2018*. (*Poster presentation*).
- ❖ Y. Rajesh, S K Padhi, Pranitha Sharma, M. Ghanashyam Krishna "Effect of ZnO and Au seed layers on the growth of ZnO nanorods" 5th International Conference on Nano Science and nanotechnology, *ICONN- 2019. (Poster presentation)*.
- **❖ Workshop on** "Formulation and Development of Nanoparticles" March 20-25, 2017, HRDC- UOH-Hyderabad.

- ❖ Workshop on "Bringing the Nano world Together (BTNT-2017) Oxford Instruments Nanotechnology" Dec 05-06, 2017, UOH-Hyderabad.
- **❖ Workshop on** "Processing and Characterization of Thin films" Jan 03-09, 2018, UGC-NRC, UOH-Hyderabad
- ❖ Workshop on "Principles and applications of Transmission Electron Microscopy" Nov 27-28, 2018, SRM Institute of science and technology, Kattankulathur.

Brief Bio-Data

Yalambaku Rajesh

Centre for Nanotechnology

School of Physics

University of Hyderabad

Gachibowli, Hyderabad, Telangana

India- 500046

Email: rajeshphd15@uohyd.ac.in; yalambakurajesh@gmail.com